2017

Micro-Electro-Mechanical System for Measuring Mechanical Properties of Cell Aggregates

Negar Moghimi
Lehigh University

Micro-Electro-Mechanical System for Measuring Mechanical Properties of Cell Aggregates

by

Negar Moghimi

A Dissertation

Presented to the Graduate and Research Committee

of Lehigh University

in Candidacy for the Degree of

Doctor of Philosophy

in

Electrical Engineering

Lehigh University

January 2017

Approved and recommended for acceptance as a dissertation in partial fulfillment of the requirements for the degree of Doctor of Philosophy

Negar Moghimi
Micro-Electro-Mechanical System for Measuring Mechanical Properties of Cell Aggregates

_____

Defense Date

_____

Dr. Svetlana Tatic-Lucic, Dissertation Director

_____

Approved Date

Committee Members:

_____

Dr. Miltiadis Hatalis

_____

Dr. D. Richard Decker

_____

Dr. Richard Vinci

_____

Dr. Sabrina Jedlicka

ACKNOWLEDGMENTS

I would like to thank my advisor, Professor Tatic-Lucic for her constant support and training not only for me to be a better scientist but also a better person. Her valuable feedback on my work has made my scientific and personal advancement possible. I would like to thank Professor Hatalis, Professor Decker, Professor Vinci and Professor Jedlicka for their valuable help and support. I am grateful for having a great committee and I thank them for their advice throughout this research. I specifically acknowledge Professor Hatalis's support in providing access to his laboratory for fabrication of this device. I appreciate Professor Vinci's valuable feedback in design and characterization of the device. I am very grateful to my parents and my brother, Dr. Saeed Moghimi, for their unconditional support and encouragement. I would like to thank Dr. Markus Gnerlich, Grant Reed, Bill Muschock, David Morrisette, Ted Bowen, Ray Filozof, and William Fowl for their training and technical support. I would like to thank Christopher Hassan for editing parts of this dissertation. Finally, I would like to thank my undergraduate thesis adviser at University of Tehran, Professor Mohajerzadeh, who introduced me to microfabrication and nanotechnology. This research was financially supported by Lehigh University, and Pennsylvania Infrastructure Technology Alliance (PITA) and I would like to thank them for their support.

TABLE OF CONTENTS

LIST OF FIGURES

LIST OF TABLES

ABSTRACT

Developing microelectromechanical system (MEMS) for the characterization of biological cells can advance the capabilities of medical professionals to diagnose and treat different diseases. This dissertation presents the design, modeling, fabrication process and characterization of a BioMEMS for mechanical characterization of cell aggregates. This actuator is intended to provide a set of large predefined lateral displacements. This device has a high aspect ratio and is fabricated using deep reactive ion etching (DRIE). The actuator includes five different pairs of comb drives translating five independent displacements to a central shuttle. The successful operation of the actuator is verified in air and examined in deionized (DI) water.

The device is designed to measure the mechanical properties of cell aggregates. The target aggregates consist of human mesenchymal stem cells and are of great importance in regeneration studies for the treatment of cardiovascular disease. This integrated micro-actuator could provide actuation in micro-optics or microfluidics applications, allowing for large displacements.

1.Introduction

1.1. Motivation and Significance

The application of microelectromechanical systems (MEMS) in biomedical devices has expanded vastly over the last few decades, with MEMS devices being developed to measure different characteristics of cells such as a device for measuring electrical conductivity of cells [1], and a BioMEMS for measuring mechanical properties of cells [2].The study of cell mechanics offers a valuable understanding of cell viability and functionality [3, 4]. Cell biomechanics approaches also facilitates the characterization of important cell and tissue behaviors [5, 6]. The study of cell biomechanics has a great importance in biomedicine since it can improve the knowledge of the cause, progression and cure of diseases. Furthermore, the biomechanical responses of the cells may play an important role in metastasis and invasiveness of cancerous cells [6, 7]. More deformable cancerous cells can propagate easier in body [8]. These studies may provide assistance with diagnostic approaches for potential cancerous cells [9].

The key motivation is to develop systems for controlled mechanical stimulation and characterization of cells. This study is focused on a novel system to provide actuation in order to measure mechanical properties of cell aggregates such as embryoid bodies (EBs). Using a culture technique known as embryoid body formation, human mesenchymal stem cells (hMSCs) have been shown to spontaneously form a cell aggregate and differentiate into cardiogenic cells [10]. The common technique used to culture EBs is known as the hanging drop method, which is performed by placing a droplet of cell suspension on a flat surface such as the inner surface of a petri dish lid. EBs can be formed after inverting the lid due to the balance of gravitational and surface tension forces. This produces a hanging droplet of cell suspension and it will cause the formation of a 3-dimensional aggregate called EB. EBs are entities which emulate the conditions during early stages of development of an embryo. Cardiac muscle cells are one type of cells that hMSCs can form

through differentiation [11] and EBs promote necessary conditions for hMSCs to differentiate into cardiac muscle cells [12].

The biomechanical measurement of cell aggregates such as EB is important because cellular mechanical properties not only change with age [4], but also change with differentiation. For instance, there is a hypothesis that chondrogenic or osteogenic differentiations might be caused by mechanical strain in undifferentiated hMSCs [13]. These mechanical changes could potentially be predictive in nature indicating if the cells are in a state that could be subject to differentiation protocols, or if they are the proper type of cell for transplantation. In fact, studying the cellular mechanical properties in cell aggregates is important to the questions of how cellular mechanical properties ultimately affect downstream cell properties. Using the mechanical properties, if we could differentiate the cells into specific phenotypes more reproducibly, we could potentially use the cells for transplantation to replace cells that had degenerated such as damaged cardiac muscle cells in heart disease [14]. Studying mechanical properties of hMSC cells can have a great impact in cartilage regeneration and cartilage tissue engineering [15].

The first step to study hMSC cells involves characterization of the mechanical environment of single cells and single cell biomechanics. Several methods have been developed to study the biomechanics of single cells. Micropipette aspiration, AFM method, cytoindentation, optical traps and cell compression are among the most important ones [2, 16-18]. We have also utilized another method previously and measured mechanical characteristics of single suspended hMSC cells with our developed BioMEMS device [19]. The previous generation of BioMEMS which consists of an on-chip sensor and actuator allowed us to measure biomechanical characteristics of single hMSC cells. The new generation of BioMEMS device discussed in this dissertation will let us measure the viscoelastic properties of embryoid bodies (EBs) i.e. human mesenchymal stem cells which are differentiated into cardiomyocytes. Studying mechanical properties of these cells of different passages will help in finding the optimum cell culture conditions. Therefore, one of the future applications of this device is to find the best culture conditions correlated with mechanical properties of EBs of different passages. This will finally benefit the studies about cardiomyocyte regeneration [20] and thus cardiovascular disease treatments. In fact,

the fabrication and characterization of this novel BioMEMS device will pave the way for future biomedical applications.

Apart from the biomedical perspective, the system can be used for mechanical characterization of other materials such as polymers. The novel high aspect ratio microactuator which provides multiple predefined large displacements, can be utilized to provide on-chip actuation for other applications such as micro-optics or microfluidics. It can also be used to provide cyclic strain for mechanical testing of different elastic and viscoelastic materials or thin films that is hard to measure with conventional methods.

1.2. Objectives and Challenges

Our main goals include design, fabrication and characterization of a novel BioMEMS device. This BioMEMS device is designed for mechanical characterization of embryoid bodies (EBs) *in vitro*. A list of the objectives is given below and each objective is explained in the following section.

1. The first objective is to design an on-chip actuator which provides motion in a series of discrete steps ranging from 5 % to 25 % of the EB diameter (up to 100 μm).
2. The second objective is to extend the design of a piezoresistive force sensor to measure the reaction force from EB.
3. The third objective is related to the need to have a positioning system incorporated into the chip to place the target in designated area for compression.
4. The fourth objective is the fabrication of the MEMS device with the previously mentioned components.

The objectives are explained in the following section.

1- The average diameter of EBs is 250 μm to 290 μm. In order to do mechanical characterization without permanently deforming the target, we intend to provide displacements from 5 % to 25 % of the EB diameter. Therefore, the micro actuator needs to provide five different predefined displacements up to around 100 μm. The previous actuator design in our group was only capable of one to six microns of displacement and it was designed for single-cell characterization but the current design

requires relatively larger displacements because the average size of a cell aggregate is more than 10 times larger than a single cell. This novel electrostatic actuator can provide a large displacement and it is also compatible with micromachining techniques and thus easy to integrate on-chip. The first challenge is to obtain a large displacement with actuator. The other challenge is due to biomedical application of this system and operation of actuator in ionic media (cell medium).

2- We have applied the idea of a piezoresistive force sensor from our previously designed BioMEMS for single cell characterization [19]. This force sensor utilizes piezoresistive silicon transducers to measure the reaction force of the target during compression. The reaction force results in a stress distribution along the sensor cantilever beam and transducers are located in the area with the maximum stress. The applied stress will cause a change in resistance in piezoresistive elements and a voltage difference will be measured. Force is related to voltage according the calibration of the device.

3- Our designed quadruple DEP structure that has been experimentally verified and modeled for trapping a single cell [21] was accordingly modified in the new generation for positioning EBs. DEP positioning is a contactless method that uses dielectrophoretic force to trap the body to the center which in this case is the EB characterization area between actuator and force sensor plates.

4- In order to accommodate EBs with minimum of 250 μm in diameter, device height of 150 μm is envisioned. Therefore, the fabrication process of this device involves etching 150 μm of silicon using deep reactive ion etching (DRIE) method. Fabrication of a high aspect ratio MEMS structure could be challenging. Moreover, as a result of a long etching time, over- or under-etching and undercut of the structure can change main characteristics of the device such as the electrostatic force or stiffness values of the actuator. The fabrication process is given after explaining the details for specifications and design of the device.

After fabrication, characterization of the novel on-chip actuator is performed to determine the characteristics of the actuator such as static displacement and resonant frequency. Characterization of the bank of actuators will be first done in the air. The future application

of this actuator is intended to be in cell medium. Producing large and repeatable displacements can be challenging specially in cell medium, because it is an ionic environment and may require additional fabrication steps. Exploring the application of the developed device in measuring viscoelastic parameters of EBs is one of the future goals. The goal is to try to extend the mechanical measurements from single hMSC cells to EBs using our novel BioMEMS device. The elastic and viscoelastic properties of EBs could be measured by step compression tests.

A picture of the MEMS device is given in Fig. 1.

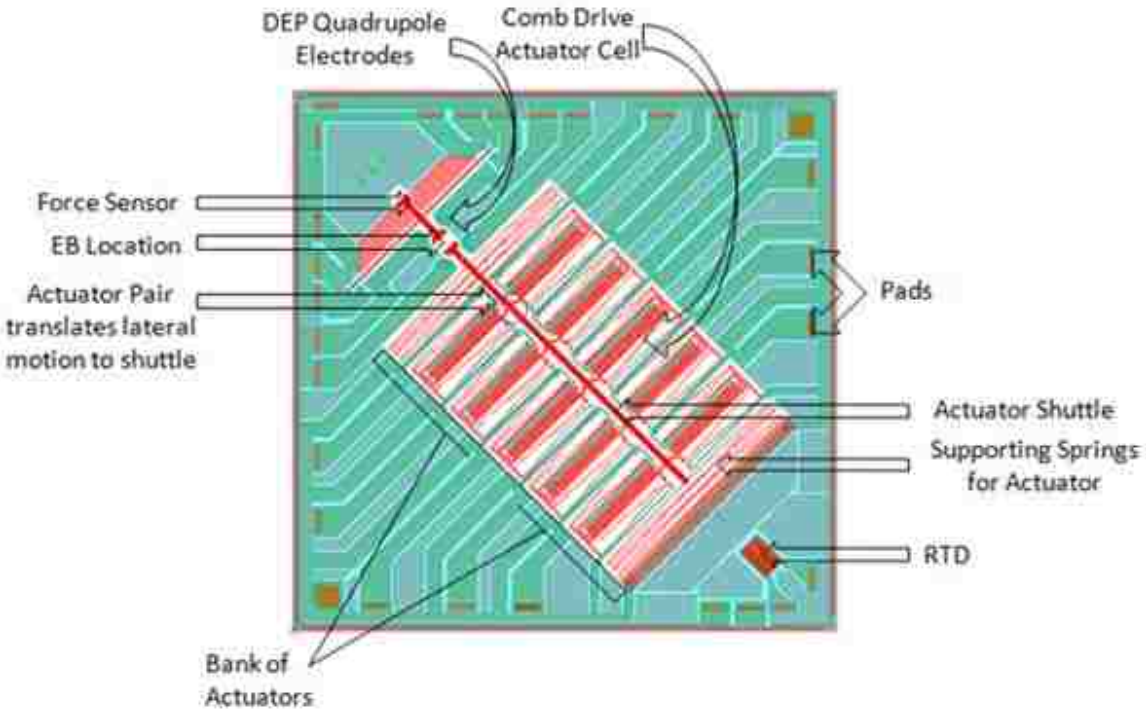

Figure 1. BioMEMS device with integrated actuator and sensor on-chip, the die size is 12 mm by 12 mm.

2. Actuator Design and Modeling

2.1. Different Actuation Methods

Different methods of actuation have been used in MEMS and microfluidics such as electrostatic [22], magnetic [23], piezoelectric [24], thermal [25], chemical [26] and pneumatic [27]. The advantages of pneumatic, thermal and chemical expansion methods are large displacements and high energy densities (or pressures), but they have slow response times (typically >1 ms and often >1 s) [28]. Piezoelectric actuation provides a faster response at the cost of smaller displacement and energy density [28]. Magnetic actuators are comparable to piezoelectric devices in terms of energy densities and response times, magnetic devices can provide much larger displacements [28] . The problem with magnetic actuators is that the current material choices for micromagnets are limited. Also a limited number of those materials can be micromachined in conventional cleanrooms [29] .

Electrostatic actuators on the other hand, are capable of relatively large displacements (10–100 μm with interdigitated comb drives) at fast response times (typically μs to ms in vacuum or air, and limited only by damping in liquids). Electrostatic energy densities in air are slightly lower than piezoelectric and magnetic actuation, but electrostatic actuation gains two orders of magnitude in high dielectric constant fluids such as water. Electrostatic actuators such as comb drives have a proven reliability [28]. Their design and fabrication are simpler than most of the other actuation mechanisms, and they require only silicon-based materials. They are quickly and easily integrated into microsystems because they can be fabricated with standard IC micromachining processes and materials [28] . It is also possible to achieve high forces and high displacements by optimizing the shape of comb drive designs [29].

One of the challenges for electrostatic actuators is the limitation of stable traveling range due to the electromechanical side instability. Side instability happens when the movable comb fingers move perpendicular to the actuation direction and then make contact with the

fixed comb fingers. As the overlapping area between fingers increases with the forward displacement of the actuator, the cross-axis force becomes larger and larger that causes the fingers to suddenly snap over the sideway. The other challenge is that the performance of electrostatic actuators will degrade in liquids with higher conductivities due to electrochemical reactions and ionic environment [30]. Also an optimal actuation method for mechanical excitation of living cells should offer a high degree of accuracy in the control of the applied force or displacement. The advantages and disadvantages of different actuation methods are listed in Table 1.

Table 1: The advantages and disadvantages of different actuation methods

	Advantages	Disadvantages	Reference
Electrostatic	- Compatibility with standard IC micromachining processes and materials - Easy to integrate into micro devices - Large displacements - Fast response time - Large forces	- Limited stable range of movement due to side instability - Change in performance and initial stroke in conductive liquids - Electrolysis in liquid environment	[22, 31, 32]
Magnetic	Large displacements	- Small energy density - Requires specific material and might not be easy to integrate	[23, 29]
Piezoelectric	Fast response time	- Small displacements - Small energy densities - Limitation in materials and achievable geometries	[24, 29]
Electro-thermal	- Large displacements - High energy densities	- Slow response time - Electrolysis in liquids - High temperatures not good for cells	[25]
Chemical	- Large displacements - High energy densities	- Slow response time	[26]
Pneumatic	- Large displacements - High energy densities	- Slow response time - Harder to integrate on chip	[27]

Different type of actuators could be compared based on energy density that represents output energy per actuator volume. Output energy of the actuator can be calculated by the following expression [33].

$$E = \frac{1}{2}.F.y \quad (1)$$

where E is output energy, F is force and y is the output displacement. A comparison between energy densities of different actuators is given in Table 2 [34]. The energy density value for our actuator based on finite element analysis (FEA) modeling is also shown in the table. According to modeling which will be discussed in details in the following section, our device will provide up to displacement of 110 μm and force of 275 μN. Using equation (1), output energy for the actuator in our design was calculated and then divided by volume of the actuator to determine the energy density. An overview of performances for different actuation methods both in terms of displacement and force is given in Table 3.

Table 2. Comparison of different actuators with respect to energy density values [34].

Actuator Type	Elastic Energy Density (J/cm^3)
Electroactive Polymer Artificial Muscle Acrylic Silicone (CF19-2186)	 3.4 0.75
Electrostrictor Polymer P(VDF-TrFE)	0.3
Electrostatic Devices (Integrated Force Array) Our actuator*	0.0015 0.0366
Electromagnetic (Voice Coil)	0.025
Piezoelectric Ceramic (PZT) Single Crystal (PZN-PT) Polymer(PVDF)	 0.10 1.0 0.0024
Shape Memory Alloy (TiNi)	>100
Shape Memory Polymer	2
Thermal (Expansion)	0.4
Electrochemo-mechanical Conducting Polymer (Polyaniline)	23
Mechano-chemical Polymer/Gels (polyelectrolyte)	0.06
Mechano-chemical Polymer/Gels (polyelectrolyte)	0.025
Natural Muscle (Human Skeletal)	0.07

* Energy density for our comb drive actuator based on FEA results

Table 3. Comparison of different MEMS actuation means for characterization of living cells [33].

Actuation technique	Displacement (max)	Displacement (min)	Force (max)	Force (min)
Positioning Stages	>1 mm	10 pm	>1 N	10 pN
Piezo& Polymers	700 µm	1 µm	10 mN	0.1 µN
Electrostatic	250 µm	0.8 µm	10 mN	10 µN
Electrothermal	300 µm	1 µm	10 mN	50 µN
Air pressure	10 µm	10 nm	100 nN	10 pN
Magnetic fields	200 µm	1 nm	400 µN	0.01 pN
Electrical fields	10 µm	10 nm	400 µN	0.01 pN
Optical gradients	100 µm	1 nm	40 nN	0.01 pN

2.2. Actuator Design Overview

As described earlier, the actuator role is to provide mechanical stimulation for the EB inside the cell medium. To this end, the actuator system is expected to provide rather a large displacement to compress the target to 25 % strain. The required displacement will be around 72.5 µm for characterization of an EB with 290 µm diameter. Integration on the MEMS device and compatibility with microfabrication techniques utilized in the fabrication process are also required. As it was mentioned in the previous section, the electrostatic actuators have various advantages such as large displacements and forces, speed, and ease of on-chip integration. Another advantage of using electrostatic actuator in liquid media is that the electromechanical efficiency increases with the dielectric constant of the medium and the energy density is at least 80 times larger in water relative to air.

One of the characteristics of the actuator system is operation in physiological conditions; this means the actuator which is integrated on-chip will be immersed into cell medium which is an ionic environment. The key challenges of operating electrostatic actuator in

conducting media are electrostatic shielding, electrode polarization, and electrochemical reactions [28].

2.3. Actuation in Ionic Media

Most of the applications of electrostatic actuators have been in environments such as air or vacuum. During the last decade, devices have been utilized in ionic media using high frequency signals to avoid electrostatic shielding and electrochemical reactions [28, 35]. Sounart et al. were the first to demonstrate AC actuation in ionic media [28]. This method was used to operate electrostatic actuators in order to characterize cells in ionic solutions [36, 37]. High frequency signals and low voltages were utilized to prevent the electrostatic shielding, electrolysis and electrochemistry [28, 37]. The frequency of AC square waves should be high enough so that the ions do not have time to accumulate at the electrodes. The electric field will then be uniform since the electrostatic force is independent of the polarity of the applied voltage. As reported in [28], more conductive solutions require a higher frequency signal for actuation. However, at frequencies above 1 MHz attenuation due to parasitic impedances prevents actuation. A differential drive electrode design was utilized to overcome parasitic impedance losses in ionic media [37]. Although differential design minimized high frequency losses, the limitation of drive electronics happened at 5 MHz and signal distortions were observed for higher frequencies. The maximum displacement achieved in ionic media in previous works was less than 10 μm [29, 37]. Using our novel actuator design which will be discussed in the following sections we intend to achieve significantly larger displacements.

Our approach for actuation will be the on-chip electrostatic actuation. We will apply differential electrode configuration to our custom-designed actuator. The differential electrode configuration is the method of applying voltages with 180 degrees out of phase to stators of a pair of actuators. This method will basically make it possible to use high frequency signals which are needed to provide the large displacement in ionic media. The use of 180 degrees out of phase voltages for a pair of comb drives will result in zero current

through the actuator shuttle and thus will decrease the loss and temperature effects which are the main obstacles for increasing frequency of signal [37].

Our other approach for providing displacement is using off-chip actuation. There is a place designed for a probe tip that could be driven by an external off-chip piezo driver in the actuator moving plate. Using piezo driver motion, the lateral displacement with 10 nm accuracy can be obtained. With feedback control enabled ("servo" mode), exact position is monitored with 10 nm precision, but in practice the accuracy is limited by the calibration of the device [14].

2.4. Electrostatic Comb Drive Actuators

Electrostatic actuators are based on the force between capacitor plates with an applied voltage. The actuators considered in this work are actuated by an integrated comb drive actuator [38]. Comb drive actuator is one of the most common electrostatic actuator used in MEMS applications. Comb drive actuators have been used as resonators [38], electromechanical filters [39], optical shutters [40], micro grippers [41], voltmeters [42] and micromechanical gears [43] . Comb drive actuator is chosen because of relatively large displacements of the actuator in contrast to the actuators based on a close-gap configuration. One of the other beneficial features of the comb drive is that the force provided by the actuator is independent of the actuator displacement. This simplifies the design and operation of the device and eliminates the undesired electrostatic pull-in instability in the direction of the actuation. However, the structures actuated by a comb drive are still prone to the lateral pull-in instability, which is often the main factor limiting the stable displacement range [44].

Comb drive actuator consists of two interdigitated finger structures, where one comb structure is fixed and the other one is movable and connected to a suspension. The suspension must be compliant in the direction of displacement and stiff in the orthogonal direction. The driving voltage between the comb structures causes the movable comb to move towards the fixed fingers by an attractive electrostatic force. The movable comb

fingers are connected to the ground in order to prevent electrostatic pull-down forces to the substrate. A comb drive actuator schematic is shown in Fig. 2.

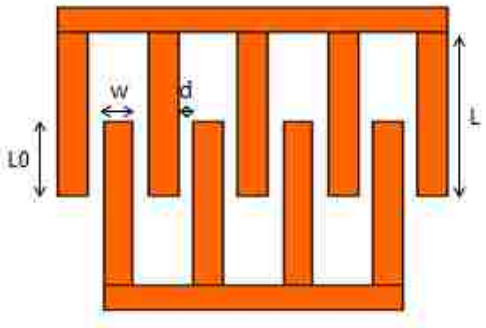

Figure 2. Electrostatic comb drive actuator, L is the length of finger, L_0 is the initial finger overlap, w is the finger width and d shows the finger spacing.

The electrostatic force between the fixed comb and the movable comb is given in (2)

$$F = \frac{n\epsilon\varepsilon_0 t V^2}{d} \tag{2}$$

where n is the number of fingers, ε is the relative permittivity of the medium between the comb fingers, $\varepsilon_0$is the permittivity of free space, t is the thickness of the comb fingers, l_0 is the initial comb finger overlap, d is the gap spacing between the fingers and V is the applied voltage between the fixed and movable electrodes. Mechanical force is generated through the spring of the suspension structure.

For allowing the actuator to have a large displacement the spring attached to the combs should be properly designed. Different types of spring designs such as clamped-clamped beam, crab leg flexure and folded flexure have been applied in comb drive actuators [38, 39, 41-43, 45-48], and they are shown in Fig. 3.

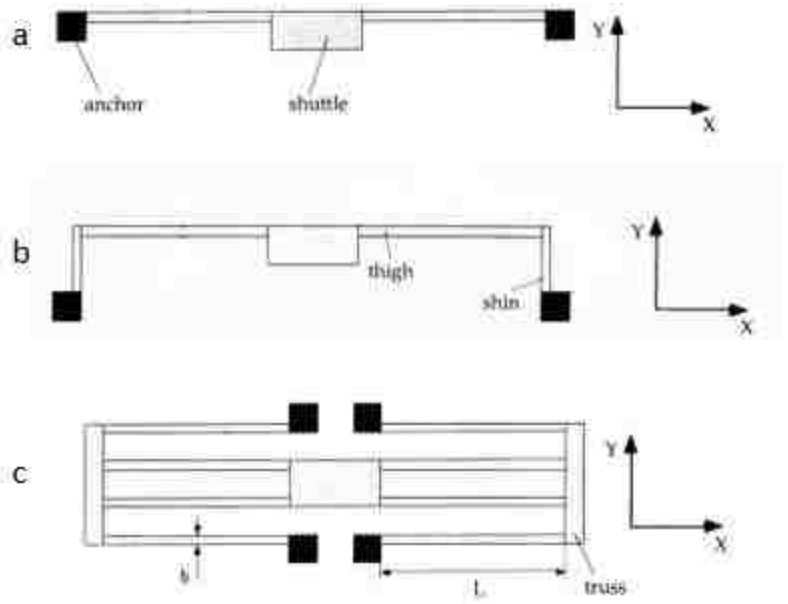

Figure 3. Different spring designs, clamped-clamped beam (a), crab leg flexure (b) and folded flexure (c) [45].

The spring stiffness generated from beam designs used in comb drive actuator needs to be relatively small in the direction of movement and large enough in the other direction. The folded flexure design with initially bent beams was found to be more advantageous in applications with large displacement because of great compliance in lateral direction, great axial stiffness, lower side instability and minimal area usage [45, 49].

A folded flexure consists of fixed-guided beam which is fixed on one end and is confined to move at the other end. The two fixed-guided beams are connected by a rigid truss that translates the displacement at the end of one to the other. The truss member is designed to be much stiffer than the beam so as to act as a rigid bar. Under this condition, the folded beams act as two springs in series, thus creating a more compliant system. The folded flexure is designed with the same length on the two legs.

The folded flexure design strongly reduces the development of axial forces and exhibits a much larger linear deflection range [45]. The springs remain within 1% of linearity for deflections up to around 10% of the beam length [50]. After this the Euler beam theory is

not valid anymore and non-linear stiffness and spring softening effects arise. In this design the maximum deflections are within the linear range of deflection, thus the Euler beam theory is true for the displacement range.

Some of the previously designed comb drive actuators were explored. The first comb drive actuator was designed by Tang et al. [38] and is shown in Fig. 4. The original comb-drive actuator had a folded-flexure suspension design and was symmetric along x and y directions and provided two microns of displacement.

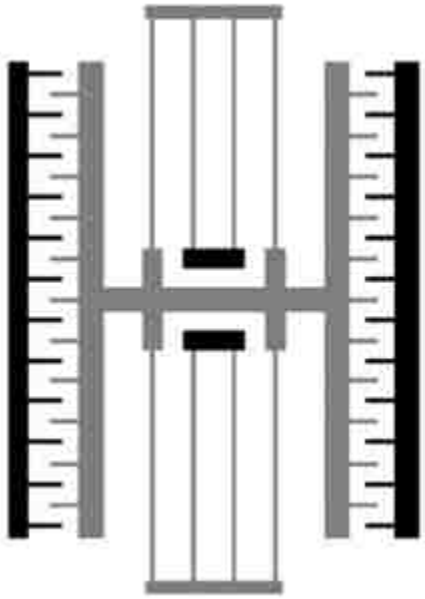

Figure 4. The first comb drive designed by Tang [38].

Gerson et al. in [44] introduced design of multistable comb drive actuators with large displacements. These actuators allowed stable displacements up to 100 μm. The multistable actuators had a number of curved beams going through buckling events. The beam snap events created a non-linear and hysteresis form of displacement voltage curve which was not suitable for our application. Grade et al. [49] introduced a comb drive design which was 50 % smaller than Tang's design and was only symmetric about the y-axis (Fig. 5). With half the combs and half the suspension beams of the traditional design, the actuator deflection and fundamental resonant frequency remained unchanged. By placing

the folded suspension outside of combs the rotational stiffness was also increased. This design was proved to be capable of displacements up to 110 μm while biased with almost 150 volts. Since the displacement voltage characteristic for this design is close to a linear relation, a similar design can be used for our application. Our design for a comb drive unit will be symmetric along y axis but we are going to use folded flexure design with initially-bent suspension beams to delay the electrostatic instability. The use of pre-bent beam reduces development of the axial forces perpendicular to the direction of actuator movement and thus will increase the stable range of displacement for the actuator. Besides electrostatic forces along the actuation direction, there are also electrostatic forces pulling the stator and rotor fingers together. Normally the forces on both sides of the comb fingers cancel each other. However, when the first derivative of the electrostatic force becomes larger than the restoring spring constant in the y-direction, side instability of the comb drive is introduced. This incident could be delayed by the proper design of the spring and will lead to larger stable displacements.

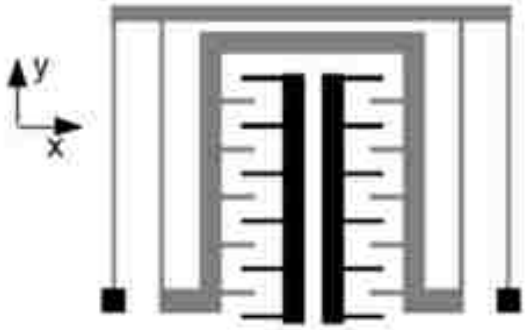

Figure 5. The comb drive designed by Grade [49].

2.5. Lateral Displacement of Comb Drive Actuator

The position of the movable finger structure is controlled by a balance between the electrostatic force and the mechanical restoring force of the compliant suspension. The capacitance between the fixed comb and the movable comb can be expressed as:

$$C = \frac{2n\epsilon\varepsilon_0 t(y + l_0)}{d} \tag{3}$$

where n is the number of fingers, ε is the relative permittivity of the medium between the comb fingers, $\varepsilon_0$is the permittivity of free space, t is the thickness of the comb fingers, l_0 is the initial comb finger overlap, y is the comb displacement and d is the gap spacing between the fingers. The lateral electrostatic force in the y-direction is equal to the negative derivative of the electrostatic co-energy with respect to y [45]:

$$F = \frac{1}{2}\frac{\partial C}{\partial y}V^2 = \frac{n\epsilon\varepsilon_0 t V^2}{d} \tag{4}$$

where V is the applied voltage between the fixed and movable electrodes. Mechanical force is generated through the spring of the suspension structure.

$$F = k_y.y \;\Rightarrow y = \frac{n\epsilon\varepsilon_0 t V^2}{k_y.d} \tag{5}$$

where k_y in the spring stiffness and y is the static displacement of the comb drive and α,the slope of displacement-voltage incorporates all the effects of the actuator geometry and material properties. The electrostatic force and static displacement of the comb drive are proportional to the square of the applied potential. The electromechanical efficiency of a comb-drive actuator can be characterized by replacing with an empirical constantα.

$$y = \epsilon\alpha V^2 \tag{6}$$

In the derivation of equation 5, a uniform electric field was implicitly assumed. This behavior is modified if the operating medium contains mobile charges as in the case of ionic/polar solutions. The presence of mobile ions leads to the well-known problems of electrolysis, electrochemical corrosion and ionic screening. Therefore, equations 5 and 6 only apply to a comb drive actuated in a homogeneous dielectric of negligible conductivity. In a leaky dielectric which supports an ohmic current, ions accumulate in an electrical double layer (EDL) at the electrode interface, thus reducing or eliminating the applied force and actuator displacement [28].

2.6. Critical Frequency for Actuation in Ionic Media

It was reported that in all liquids, electrostatic comb drive displacement is zero below a medium-dependent critical frequency, above which the displacement reaches a frequency-independent maximum value [28]. Critical frequency is defined as

$$f_c = \frac{\sigma b}{\varepsilon_{ox}\varepsilon_0 d} \tag{7}$$

Where b is the oxide thickness and σ is the local electrical conductivity. The theory suggests that the critical frequency can be adjusted higher or lower by growing or preventing growth of the native oxide respectively. Minimizing the oxide layer thickness will reduce the actuation frequency thus unoxidized electrode materials can do actuation in higher conductivity electrolytes. On the other hand, very low thickness of native oxide and high voltages might lead to corrosion of electrodes due to leakage currents [36]. Thus lowering native oxide thickness can be a method to decrease the critical frequency which means with applying lower frequencies actuation in ionic media can be achieved, however magnitude of the applied AC signals should be low enough not to cause electrochemical reactions at the electrodes. This suggests that there is a limitation for both frequency and voltages applied in ionic media dependent on the electrical properties of medium. One other method for enabling higher voltages could be coating electrodes with 1-3 nm Al2O3 which is deposited by atomic layer deposition (ALD). For on-chip actuation method we are going to compare different coating conditions for electrodes such as electrodes without native oxide, with a couple of nanometers of native oxide and electrodes coated with ALD Al2O3.

Critical frequency inside NIH3T3 medium (conductivity=1.6 S/m) based on the gap size will be the following:

g = 6.5 μm => f = 12 MHz

g = 8 μm => f = 10 MHz

2.7. Dynamic Behavior

In a comb-drive electrostatic actuator the electrostatic force F is balanced by the suspension of stiffness k_y in the actuation direction and depends on the applied voltage V as

$$F = \frac{n\epsilon\varepsilon_0 tV^2}{d} = k_y.y \tag{8}$$

where n is the number of fingers, ε is the relative permittivity of the medium between the comb fingers, $\varepsilon_0$is the permittivity of free space, t is the thickness of the comb fingers, y is the comb displacement and d is the gap spacing between the fingers. However, this is not true in the case of a conducting liquid medium where the electric field is not uniform and is shielded by the interface capacitance due to the formation of the electrical double layer (EDL). In this case, AC signals with high frequency need to be applied to prevent the EDL formation. Thus, the electrostatic force depends upon the frequency of the actuation signal since the extent of shielding depends on the time available for the mobile ions to accumulate at the electrode medium interface. By modeling the electrode-electrolyte interface as a thin layer of capacitance and all components of the circuit as linear components, the overall impedance of the electrode system (Z) and actuator gap impedance (Z_M) are expressed as [51].

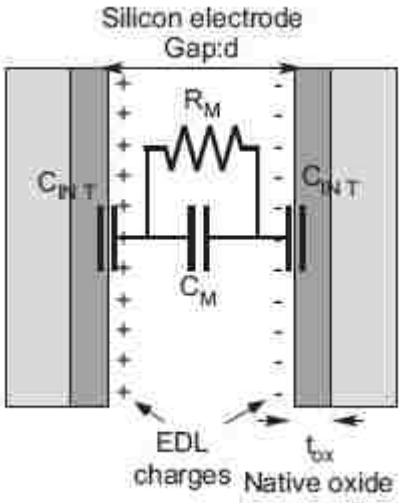

Figure 6. Circuit model for comb drive inside liquid [51].

The total impedance of the actuator system which is shown in Fig. 6 can be expressed as:

$$Z = \frac{2}{jwC_{INT}} + \frac{R_M}{1 + jwR_M C_M} \tag{9}$$

The impendence of the actuator gap is the second term in the above expression which is

$$Z_M = R_M/(1 + jwR_M C_M) \tag{10}$$

When an AC voltage is applied between the combs, the voltage across the actuator gap in terms of the total gap can be expressed as below

$$V_{AC} = V_0 \exp(jwt) \tag{11}$$

$$Vm = Re\left\{|\frac{Z_M}{Z}|V_0 \exp(jwt + \varphi)\right\} \; where \; \varphi = \arg\left(\frac{Z_M}{Z}\right) \tag{12}$$

$$V_m = \left\{|\frac{Z_M}{Z}|V_0\right\}\cos\ (wt + \varphi) \tag{13}$$

The assumptions for derivation of harmonics is that the voltage drops across all components are sinusoidal without non-linear distortions. These assumptions are valid for the range of concentrations and frequencies we are using here. Substituting V_m in the force equation we obtain the electrostatic force as

$$F = \frac{Nt\varepsilon_m\varepsilon_0}{d}\left\{|\frac{Z_M}{Z}|V_0\right\}^2 \cos^2(wt + \varphi) \tag{14}$$

Therefore, the electrostatic force has a DC component superposed with second order harmonics. ($cos^2\,\theta = (1 + cos2\theta)/2$) If we consider mechanical systems with natural frequencies much less than the actuation signal, the mechanical response filters out the higher harmonics (For such systems the actuator responds quasi-statically to the average force determined by the root-mean square voltage). This is true in particular for the class of actuators which their natural frequencies are lower than 1 KHz, while the actuation signals are going to be above 10 KHz. Thus the electrostatic force for a sinusoidal signal can be written as

$$F = \frac{Nt\varepsilon_m\varepsilon_0}{d}\left|\frac{Z_M}{Z}\right|^2 V_{RMS}^2 \quad (15)$$

Since the term $\left|\frac{M}{Z}\right|^2$ is a function of frequency the electrostatic force can be expressed as

$$F = \frac{Nt\varepsilon_m\varepsilon_0}{d} f(w) V_{RMS}^2 \quad (16)$$

2.8. Actuator Design Parameters

This device is designed for a cell aggregate of 250 μm in diameter. There is a tradeoff between accommodating the target and fabrication process limits for a high aspect ratio structure. A device height of 150 μm is chosen to accommodate 60 % of the target diameter. The starting material is SOI wafer with device layer of 150 μm, 2 μm silicon oxide and handle layer of 500 μm. Five variations of dies were designed to use in the wafer layout. Differences are in design parameters of combs, finger spacing, spring length and finger pairs. This will lead to different displacement capabilities as well as some fabrication differences. For instance, the displacement will be larger for smaller values of finger spacing but the structure with smaller gap has a higher aspect ratio and therefore will be more challenging to fabricate. The design parameters are given in Table 4.

The minimum feature size is the finger width in our design which is 8 μm. Different dies are capable of various displacements that are brought in Table 5. Displacements in set1 corresponds to 5% to 25% of a cell aggregate with maximum diameter of 290 μm. Displacements in set 2 corresponds to 5% to 25% of a cell aggregate with diameter of 250 μm. 40 μm is added to these numbers because the gap for target placement is 290 μm and the device needs to move 40 μm to touch the cell aggregate first.

Electrostatic force increases with decreasing the gap and increasing the number of comb fingers. However, due to fabrication process and Deep Reactive Ion Etching (DRIE) limitations, dimensions are limited by the minimum feature size i.e. the minimum beam width and gap spacing. The minimum feature size was derived based on aspect ratio of 20 for DRIE and thickness of 150 μm for device layer of the wafer. This means the minimum beam width can be equal or greater than 8 μm. Therefore, the minimum feature size was chosen to be 8 μm as well as the gap between comb drive fingers. Only 10 dies out of 75

dies have comb drives with finger spacing of 6.5 µm (these structures were replaced with 8 µm ones later due to fabrication limitations). The displacement and number of pairs of fingers in certain length highly depends on the finger spacing. However due to possible over-etching problem dies with 10µm minimum feature size were also incorporated into the layout. There are also two type of dies with actuators providing only the maximum displacement. Overall, there are total of six different designs on the wafer layout according to the mentioned different actuators and minimum feature size.

Table 4: Design parameters for different types of dies

Design Parameter	**Type 1**	**Type 2**	**Type 3**	**Type 4**	**Type 5**	**Type 6**	**Test Die**	**Total**
Finger Width (µm)	8	10	8	10	8	10		
Designed Displacement (µm)	Set2	Set1	Set2	Set2	100	100		
Actuator Length (µm)	7861	7861	7861	7861	2961	2961		
Finger Length (µm)	120	120	120	120	120	120		
Finger Spacing (µm)	6.5	6.5	8	8	8	i8		
Finger Pairs	70	62	70	63	70	63		
Spring length (µm)	2100	2100	2310	2310	2310	2310		
Initial overlap (µm)	10	10	10	10	10	10		
Beam Length (µm)	1888	1888	1888	1888	1888	1888		
Yoke Width (µm)	120	120	120	120	120	120		
Number of Dies	5	5	30	25	5	5	1	76

Table 5: Different designed set of displacements

Designed Displacements (hard stops)	**25%**	**20%**	**15%**	**10%**	**5%**
Set 1 (µm)	72.5	58	43.5	29	14.5
Set 2 (µm)	100	90	77.5	65	52.5

2.9. Spring Design

Different types of spring designs such as clamped-clamped beam, crab-leg flexure and folded-flexure have been applied in comb-drive actuators. The spring stiffness generated from beam designs used in comb drive actuator needs to be relatively small in the direction of movement and large enough in the other direction. Folded flexure design with initially bent beams as shown in Fig. 7 was found advantageous in applications with large displacement because of great compliance in lateral direction, great axial stiffness, lower side instability and minimal area usage [45, 49].

Figure 7. Folded flexure design with initially bent beams [45], the gray part is movable and the black part is fixed. There are two fixed-guided beams on each side of the structure.

Deflection of a cantilever beam with a point force applied on the tip is derived in the following section. The moment equation is given in (17) and Euler bending equation is expressed in (18). Equation 19 is derived from substituting equation 17 in equation 18.

$$M(x) = F(l - x) \tag{17}$$

$$\frac{\partial^2 y}{\partial x^2} = \frac{M(x)}{EI} \tag{18}$$

$$\frac{\partial^2 y}{\partial x^2} = \frac{F(l - x)}{EI} \tag{19}$$

where y is the direction of the beam, l is the length of the beam, F is the point force, I is the moment of inertia, and x is the perpendicular direction to y. The boundary conditions are the following

$$y = 0 \ @x = 0 \tag{20}$$

$$\frac{\partial y}{\partial x} = 0 \ @x = 0 \tag{21}$$

Therefore, integration of equation 19 results in displacement and spring stiffness of

$$y = \frac{F}{3EI} l^3 \tag{22}$$

$$k_y = \frac{3EI}{l^3} \tag{23}$$

For a rectangular beam of width b and thickness t, $I = \frac{bt^3}{12}$ the spring stiffness will be

$$k_y = \frac{Ebt^3}{4l^3} \tag{24}$$

A folded flexure consists of two fixed-guided beams which are fixed on one end and confined to move on the other end. The stiffness of this beam can be obtained in a similar fashion as above while changing the boundary conditions for deflection at the free end.

$$k_y = \frac{12EI}{l^3} = \frac{Ebt^3}{l^3} \tag{25}$$

A folded flexure has two fixed-guided beams connected by a rigid truss that translates the displacement at the end of one to the other. The truss member is designed to be much stiffer than the beam so as to act as a rigid bar. Under this condition, the folded beams act as two springs in series, thus creating a more compliant system. The folded flexure is designed with the same length on the two legs. The combined stiffness of such a flexure is given as

$$k_y = \frac{Ebt^3}{2l^3} \tag{26}$$

The stiffness of folded flexure in the axial direction is

$$k_x = \frac{Ehb}{2l} \tag{27}$$

And the stiffness ratio is

$$\frac{k_y}{k_x} = \left(\frac{l}{b}\right)^2 \tag{28}$$

The folded flexure design strongly reduces the development of axial forces and exhibits a much larger linear deflection range [45]. The springs remain within 1% of linearity for deflections up to around 10% of the beam length [50]. After this the Euler beam theory is

not valid anymore and non-linear stiffness and spring softening effects arise. In this design the maximum defections are within the linear range of deflection, thus the Euler beam theory is true for the displacement range. The actuator design incorporates five pairs of comb drive cells. Each actuator cell has a folded flexure beam structure which allows large displacement while reduces side instability.

2.10. Side-instability

Comb drives inherently suffer from electromechanical instability called lateral or side instability. Besides electrostatic forces along the y-axis, there are also electrostatic forces pulling the stator and rotor fingers together. Normally the forces on both sides of the comb fingers cancel each other. However, when the first derivative of the electrostatic force with respect to x becomes larger than the restoring spring constant in the x-direction side instability of the comb drive is introduced. When the driving voltage exceeds the so-called side instability voltage V_{SI} the comb drive becomes unstable leading to side sticking of the rotor and stator fingers. Assuming $k_x >> k_y$, the maximum deflection that can be obtained is:

$$y_{max} = d\sqrt{\frac{k_x}{2k_y}} - \frac{L_0}{2} \tag{29}$$

From this equation it can be seen that the side-instability voltage and maximum deflection are proportional to the gap spacing and increase with the spring stiffness ratio.

2.11. FEA Modeling of Actuator

In order to verify the design, the actuator design layout was sketched in CoventorWare (Coventor, Inc.), MEMS design and finite element analysis (FEA) software. The fabrication process was defined and a solid model was built and analyzed using the built-in MemMech solver (mechanical simulation) and CoSolve solver (coupled electromechanical simulation). The material is modeled as anisotropic silicon which is an anisotropic crystalline material with cubic symmetry and thus three independent values

should be used to explain the stiffness behavior. The silicon material properties used for the simulation are shown in Table 6 while the axis are aligned along silicon fundamental [100] directions. Due to more compliant Silicon crystal structure in the 110 direction, the design beams are aligned in <110> directions and therefore at a 45-degree angle to the wafer flat. (See Fig. 8).

Table 6: Silicon Material Properties used in CoventorWare FEA tool

Parameter	**Element**	**Value**
Stiffness	C_{11}	1.657e5 MPa
	C_{12}	6.39e4 MPa
	C_{44}	7.96e4 MPa
Poisson ratio	ν_{12}	2.78e-1
	ν_{13}	2.78e-1
	ν_{23}	2.78e-1
Shear Modulus	G_{12}	7.964 MPa
	G_{13}	7.964 MPa
	G_{23}	7.964 MPa
Density	D	2.331e-15 kg/μm^3
Conductivity	P	5.556e+1 pS/μm
Piezoresistivity	π_{11}	-5.300e-4 MPa
	π_{12}	2.77e4 MPa
	π_{44}	-7.05e-5 MPa^{-1}

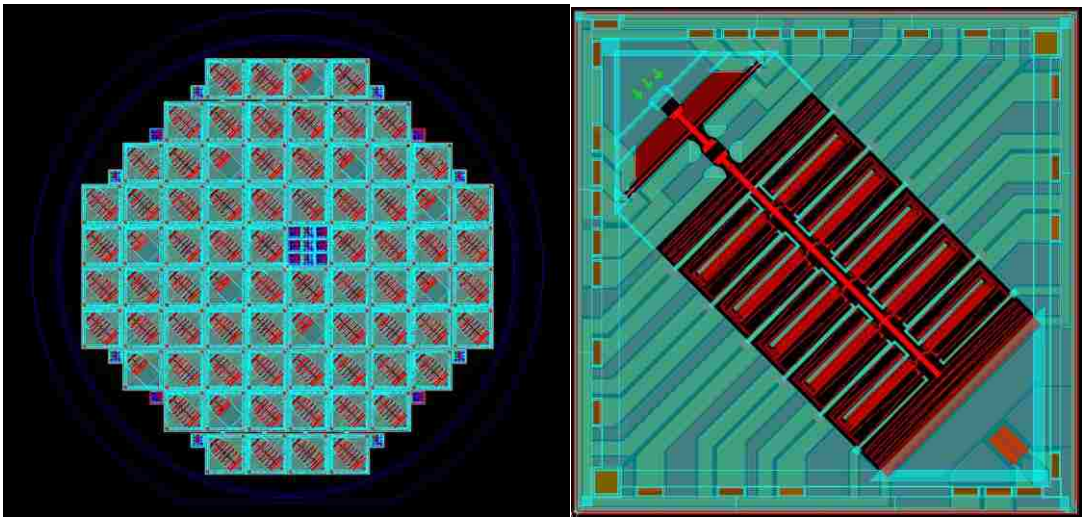

(a) (b)

Figure 8. Design orientation versus wafer flat which is located at the bottom of the wafer layout (a), layout of one die is shown on the right which has a force sensor and a bank of actuators (b)

The actuator bank consists of a shuttle and five pairs of comb drive actuator units capable of five different displacements. Comb drive unit and bank of actuator sketch are shown in Fig. 9 and Fig. 10 respectively. Comb drive units in one bank of actuator are similar in design parameters which were listed in Table 4, the only difference between them is the anchor spacing with the moving comb. Thus each bank of actuator provides a set of five different displacements designed to be 5 % to 25 % of an average embryoid body diameter which are set 1 and set 2 displacements as previously shown in Table 5.

FEA analysis was done for a unit comb drive in CoSolve solver which performs electromechanical simulation. The simulation results for actuation in vacuum for 150 V is shown in Fig. 9. Maximum displacement of 95 μm was obtained in simulation for vacuum condition when applying 150 volts between combs. Four types of comb drive actuator designs were simulated and used in the layout. The parameters and simulation results for displacement and electrostatic force are given in Table 7. Since both displacement and force values are measured to be larger after fabrication than design specifications, four types of actuators should be capable of characterization of embryoid bodies according to simulation results.

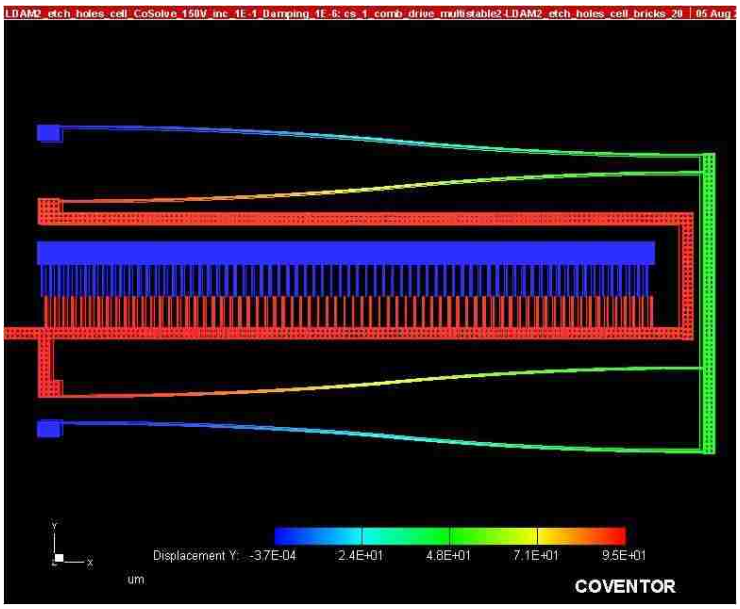

Figure 9. Comb drive unit electromechanical simulation results, displacement of 95 µm while applying 150 volts in vacuum.

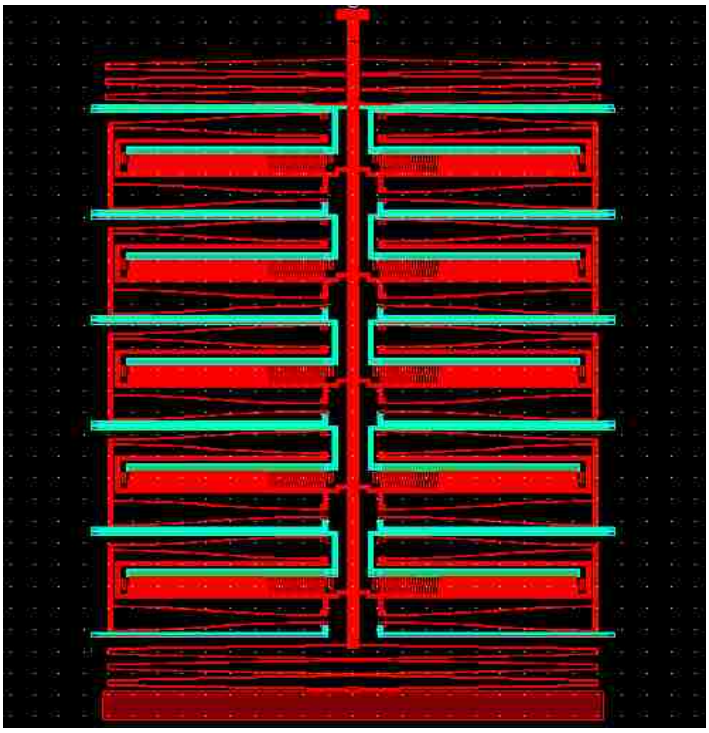

Figure 10. Bank of actuators showing 5 different pairs of comb drive units in the actuator which provides 5% to 25 % displacement of embryoid body diameter.

Table 7: Displacement and the maximum force for actuators from FEA simulations

Actuator Types	Finger Width (µm)	Finger Spacing (µm)	Finger Pairs	Spring Length (µm)	Finger Length, (µm)	Initial Overlap (µm)	Electrostatic Force (µN)	Displacement (µm)
Type 1	8	6.5	70	2100	120	10	116	95
Type 2	10	6.5	63	2100	120	10	225	73
Type 3	8	8	70	2310	120	10	275	110
Type 4	10	8	63	2310	120	10	218	78

The meshing type is extruded bricks and the element size is 20 by 20 by 20. The iteration method used in simulation is Newton. Buckling parameters such as numerical damping coefficient and initial increment in software should be adjusted to 10^-6 and 0.1 respectively. The initial increment indicates the initial size of the increment used in the iteration process towards a solution. As the solver tries to converge, the current increment will be adjusted using the minimum and maximum increment sizes, which are defined separately. The initial increment size has a default setting of 1.0. For complex problems this setting may be changed to a small number to increase the solver efficiency. Numerical Damping Coefficient is used for nonlinear static problems that are unstable, such as buckling or oscillation. If the instability is localized, there will be a local transfer of strain energy from one part of the model to the neighboring parts. This setting can be used to add volume-proportional damping to stabilize the problem. The optimum value for this setting has to be determined by previous simulations. The value must be equal to or greater than zero. Large deflection actuator modeling without buckling parameters result in divergence. Simulation results including displacement magnitude, displacement in actuation direction, reaction force, and Mises stress for the first type of comb drive actuator unit is shown in Fig. 11.

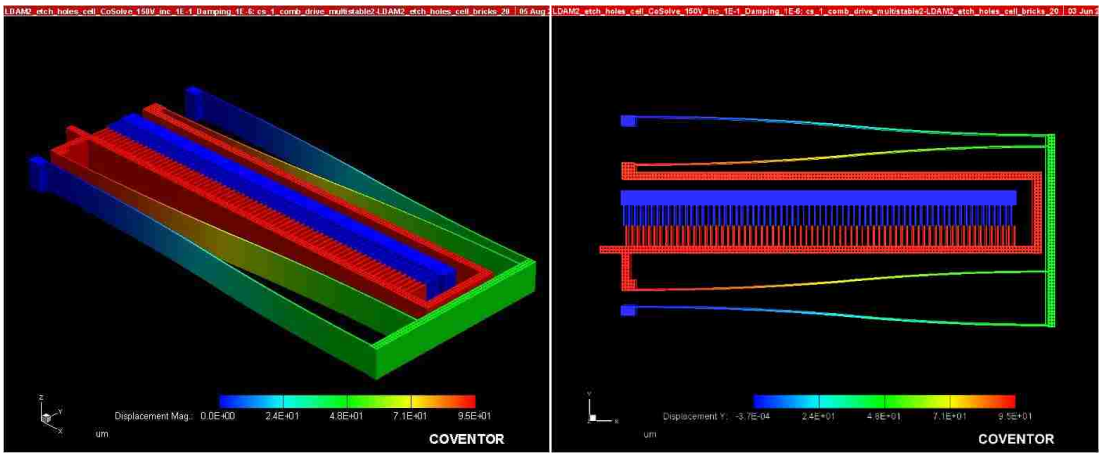

(a) **(b)**

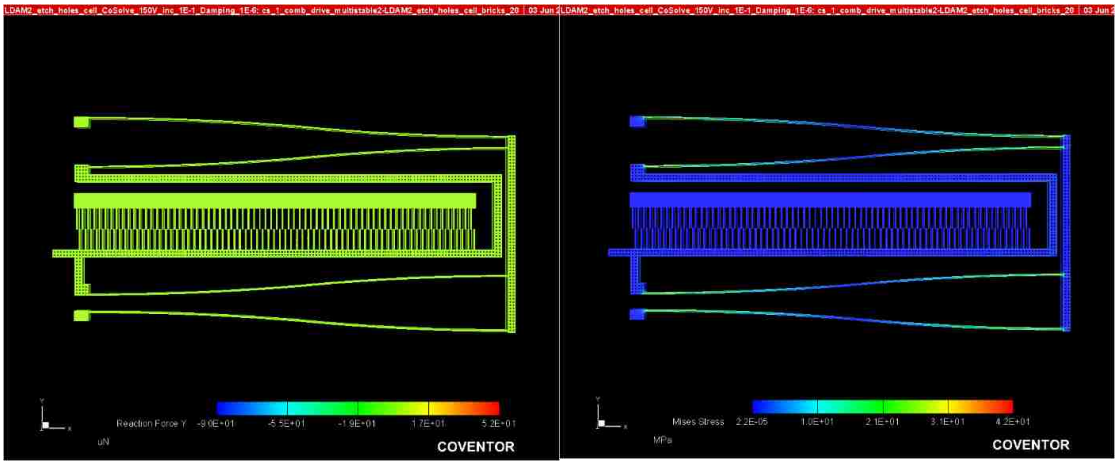

(c) **(d)**

Figure 11. Type1 of comb drive design, displacement magnitude (a) displacement in actuation direction (b), reaction force (c), and Mises stress.

2.12. Actuator Modes

The first four natural frequencies of the comb drive actuator unit are shown in Fig. 12. The first eigen mode corresponds to the actuation in y direction and the device is more compliant while moving in this mode. The device generates small displacements when moving in the other modes. This indicates stiffness of the device in x direction which, protects the design from side-instability.

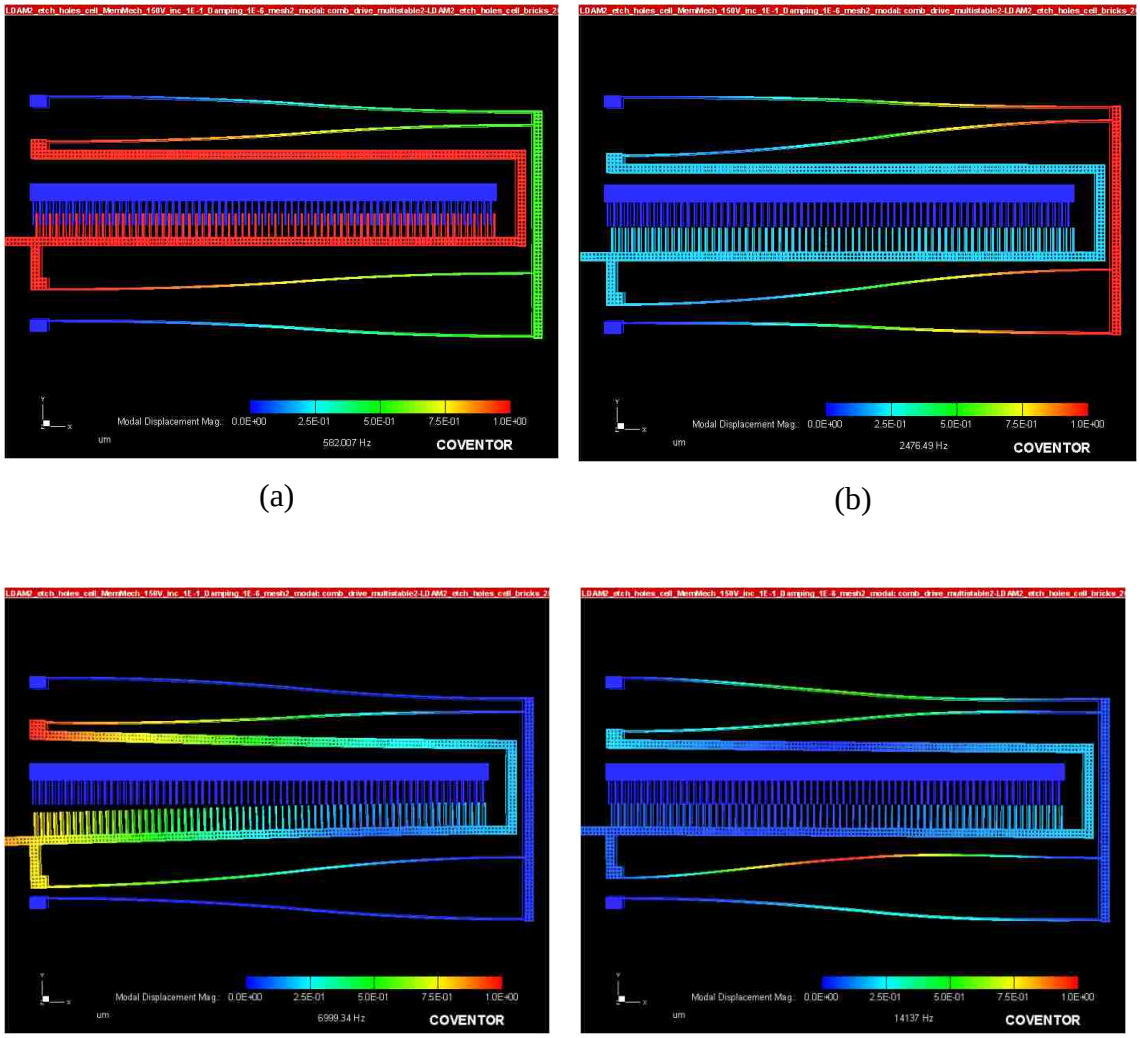

Figure 12. First four vibrational modes of the actuator. The first mode which is 582 Hz (a) is the one where the actuator has maximum displacement in y direction. The displacements are exaggerated to 50 times larger to demonstrate the modes.

2.13. Actuator Shuttle Model

Another series of simulations were done to compare different designs in order to find the proper actuator shuttle and springs connected to it. The springs should be compliant enough to allow for large displacement of around 100 μm displacement. Displacements for different designs are displayed in Fig. 13. The design with maximum displacement was

found to be more compliant based on displacement results for an equal force applied in the actuation direction.

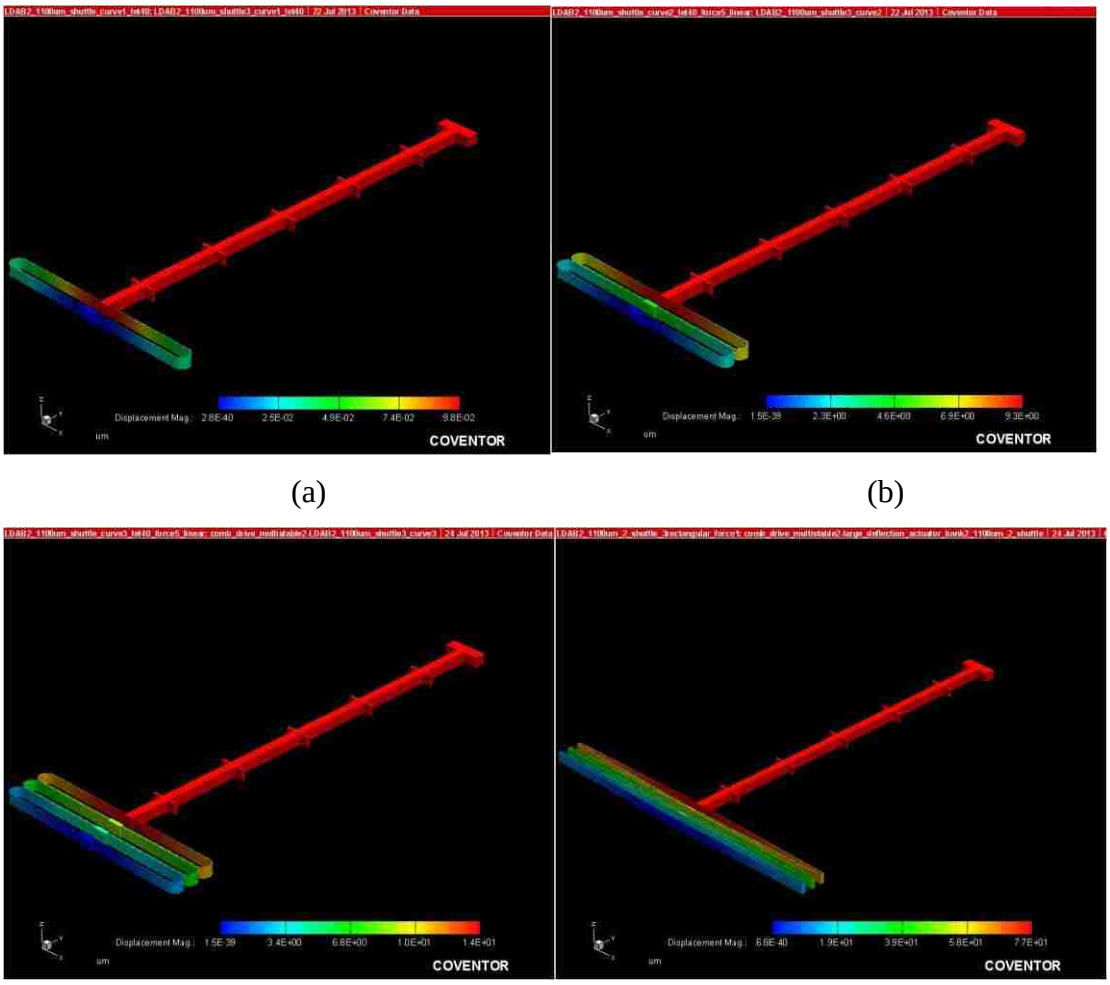

(a) (b)

(c) (d)

Figure 13. Displacement results for different designs of actuator shuttle while applying an equal force of 20 μN in actuation direction, the design in (d) shows maximum displacement of 77 μm.

The design also should be stable agaist forces in direction perpendecular to actuation direction (x-direction in this case). The selected design was compared to a design with springs placed on the top of the shuttle and displacements in x direction were simulated for an equal force of 50 μN. The results are shown in Fig. 14.

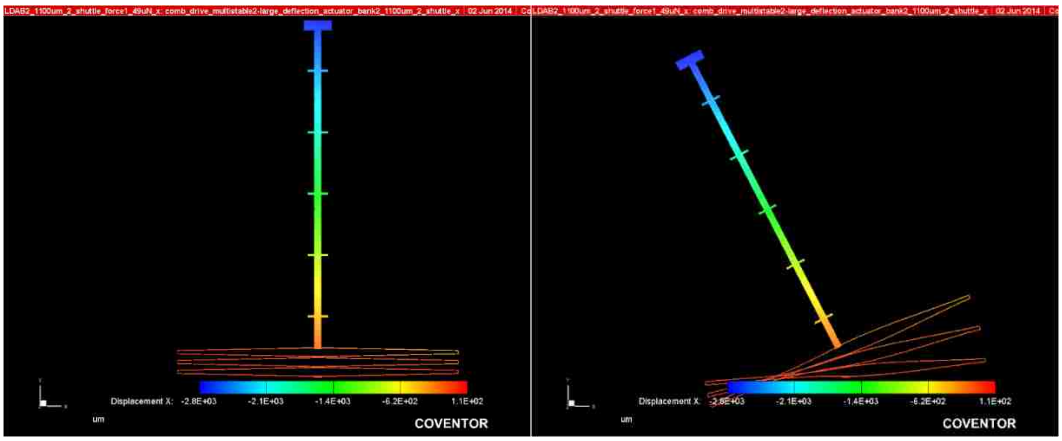

(a) (b)

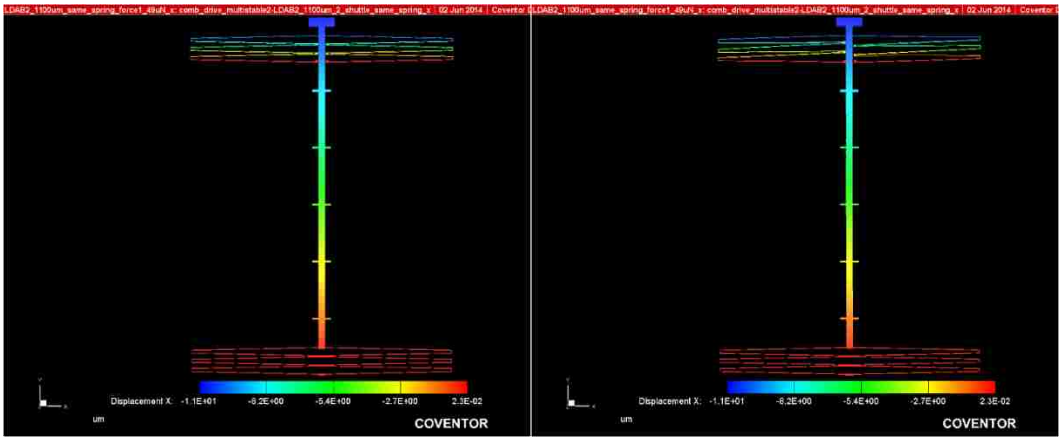

(c) (d)

Figure 14. Displacement results for two different designs (a) and (c) of actuator shuttle while applying an equal force of 49 μN perpendicular to the actuation direction, (b) and (d) show the deformed shapes. Design (c) shows more stability against perpendicular.

A comparison between the selected design vs. folded flexure spring for the top springs shows the folded flexure spring is less compliant and therefore not proper for this application which requires large displacement. The displacement results for both are shown in Fig. 15. The first four vibrational modes of actuator shuttle are shown in Fig. 16. The first mode will be important in determining the resonant frequency and ultimately stiffness of structure.

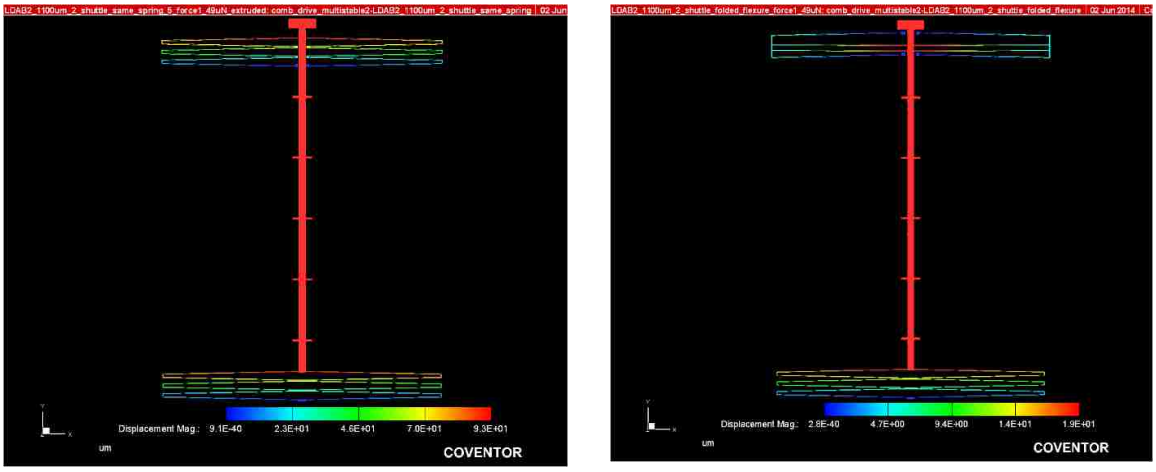

(a) (b)

Figure 15. Comparison between rectangular springs and folded flexure springs for actuator shuttle. Displacements are shown for an equal force of 49 μN in y direction.

(a) **(b)**

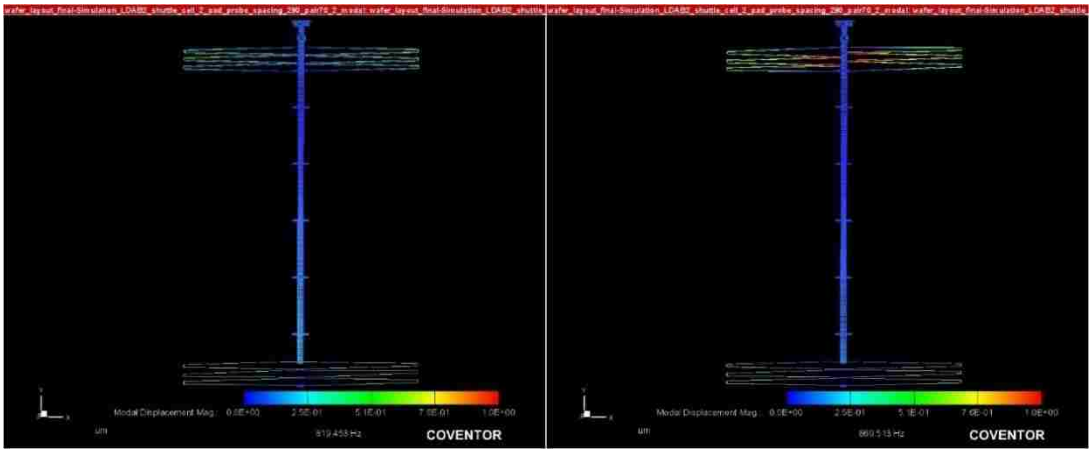

(c) **(d)**

Figure 16. First four vibrational modes of the actuator shuttle.

3. Force Sensor Design and Modeling

The force sensor is based on a free-standing cantilever beam combined with piezoresistive transducers made of silicon. Four transducers on each side of the force sensor make a full bridge which helps measuring the force due to calibration of the device. Increasing device height to find biomechanical characteristics of embryoid body and fabrication limitation in DRIE implies changes in minimum width of transducers in full bridge but the principle remains the same as the previous design for single cells [14].

Using Euler-Bernoulli beam theory the overall sensitivity of the force sensor can be estimated.

When a fixed-free cantilever beam is subjected to a force at the free end, the free end deflects and stress is created along the edges of the beam. This stress is greatest at the base of the cantilever where it is fixed and the piezoresistive transducers are placed in the region of maximum stress and oriented so that they are in the pathway of electrical current so the resistance can be measured. The structural regions and the sensing regions are made from the same piezoresistive material in integral sensors used in this design and the sensing direction is lateral direction. The direction of the force to be measured is also lateral to the plane of the silicon wafer. The integral piezoresistive transducer design simplifies the fabrication process to just one mask by defining the piezoresistive regions [14]. The electrically separated mechanical structures will be formed using DRIE on a silicon-on-insulator (SOI) wafer. The force sensor design schematic and design parameters such as beam length, beam width, transducer length, transducer width and yoke length are shown in Fig.17 and specified in Table 8.

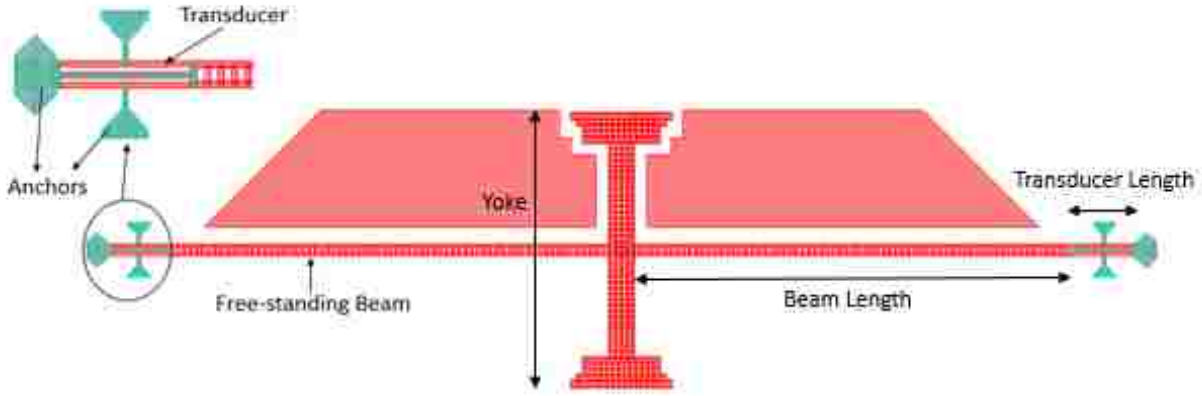

Figure 17. Schematic showing the force sensor design.

Table 8: Die types and different force sensor design parameters

FS Type	Minimum Feature size (µm)	Beam Length (µm)	Beam Width (µm)	TD Length (µm)	TD Width (µm)	Yoke Length (µm)	Number
Type 1	8	1888	40	128	8	600	40
Type 2	10	1888	50	128	10	600	35

The reaction force from compressed body will be applied to the yoke and causes the maximum stress in transducer region. The strain in the transducer region creates a change in resistance due to piezoresistivity. The change in resistivity will be measured with change in voltage in a full bridge because the resistors (transducers) are connected in a full-bridge configuration. As long as the central yoke at the center is significantly less stiff than the two symmetric cantilevers, the two cantilevers can behave as a pair of fixed-free beams which increases the stress at the base compared to a fixed-fixed cantilever of equal length. The governing equations based on Euler–Bernoulli beam theory can be found in the next section.

The electrical potential is applied to the anchors. Two opposite anchors on both sides at the very end of the force sensor will be connected to drive voltage V_s and V_0 through metal traces coming from pads. The voltage is sensed from the other two anchors which are

located at the opposite ends of the pair of cantilevers. Each pair of anchors on both sides of force sensor are connected through traces to make a full bridge. The difference in electrical potential will be measured while an applied force unbalances the full bridge and produces a voltage difference (V_1- V_2) which is the output voltage (See Fig. 18). Based on calibration of the force sensor this value will be used to calculate the applied force.

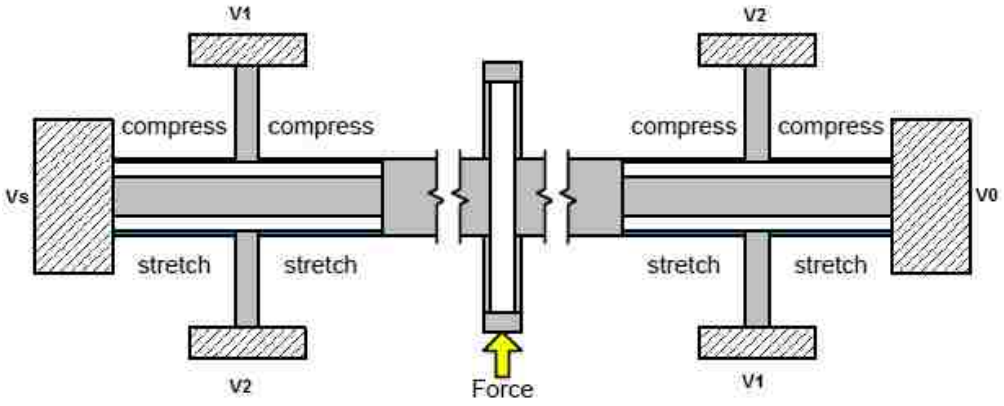

Figure 18. Transducers stretch or compress due to the applied force to the central yoke of force sensor (12).

3.1. Linear Beam Bending

Force sensor can be modeled based on Euler-Bernoulli beam theory. Displacement and thus spring stiffness of the structure due to applied force can be predicted using this model. The change in resistance in piezoresistive transducers and thus the expected voltage of full bridge can be calculated using predicted stress values. The force sensor as shown in Fig. 18 consists of two regions, one transducer region which is connected to three anchors to substrate and the other one the relatively longer beam region with cut-out regions. The area moment of inertia is different for two regions, the displacement in two regions will be derived separately considering boundary conditions. The cut-out regions are incorporated to facilitate the release step of the free-standing force sensor. In the case of point force loading at the end of cantilever beam under fixed-free bending condition, the equations for applied force will be the following [14].

$$\frac{d^3y(x)}{dx^3} = \frac{F}{EI_X(x)} \tag{30}$$

Where y is displacement, F is force, E is young modulus and I_x is moment of inertia around the x-axis. Moment and stress are given in equations 31 and 32.

$$M(x) = F\ (L - x) \tag{31}$$

$$\sigma(x, y) = \frac{M(x).y}{I_X(x)} \tag{32}$$

The deflection and the corresponding moment of inertia around x-axis in the two regions are shown in equation 33 and equation 34. $x = 0$ is at the base, $x = l2$ is where the two regions meet and $L = l1 + l2$ is the total length of the beam.

$$y(x) = \begin{Bmatrix} y_2(x), x \le l2 \\ y_1(x), x > l2 \end{Bmatrix} \tag{33}$$

$$I(x) = \begin{Bmatrix} I_{x2}(x), x \le l2 \\ I_{x1}(x), x > l2 \end{Bmatrix} \tag{34}$$

The boundary conditions are given by equations 35 and 36.

$$\frac{d^2y_1}{dx^2}\Big|_{x=L} = 0, \frac{dy_1}{dx}\Big|_{x=L} = 0, y_1\Big|_{x=L} = 0 \tag{35}$$

$$\frac{d^2y_2}{dx^2}\Big|_{x=l2} = \frac{d^2y_1}{dx^2}\Big|_{x=l2}, \frac{dy_2}{dx}\Big|_{x=L} = \frac{dy_1}{dx}\Big|_{x=L}, \ y_2\Big|_{x=L} = y_1\Big|_{x=L} \tag{36}$$

Integrating equation 32 two times considering boundary conditions will result in deflection which is given in equations 37 and 38.

$$y_1(x) = y_2(x)\Big|_{x=l2} + + \frac{F}{E}\left(\left(\frac{\frac{1}{6}}{I_{x2}}\right)x^3 - \left(\frac{\frac{L}{2}}{I_{x1}}\right)x^2 + \left(\frac{Ll2 - \frac{1}{2}l2^2}{I_{x1}} + \frac{E}{F}\frac{dy_2}{dx}\Big|_{x=l2}\right)x\right) - \frac{F}{E}\left(\left(\frac{\frac{1}{6}}{I_{x1}}\right)l2^3 - \left(\frac{\frac{L}{2}}{I_{x1}}\right)l2^2 + \left(\frac{Ll2 - \frac{1}{2}l2^2}{I_{x1}} + \frac{E}{F}\frac{dy_2}{dx}\Big|_{x=l2}\right)l2\right) \tag{37}$$

$$y_2(x) = + \frac{F}{E}\left(\left(\frac{\frac{1}{6}}{I_{x2}}\right)x^3 - 1/2\left(\frac{L - l2}{I_{x1}} + \frac{l2}{I_{x2}}\right)x^2\right) \tag{38}$$

3.2. Piezoresistive Force Sensor

The change in resistivity ($\Delta\rho/\rho$) due to stress can be expressed using the piezoresistive coefficient (π_{11}) for n-type silicon is given in equation 39.

$$\frac{\Delta\rho}{\rho} = \pi_{11}\sigma_{11} \tag{39}$$

The four piezoresistive transducers in the force sensor are arranged in a full bridge so the ratio of output voltage to drive voltage V/Vb is directly proportional to $\Delta R/R$ [14]. The sensitivity of the force sensor is measured as volts per volt per newton ((V/V)/N) since the output of the bridge is measured as the ratio of the bridge offset voltage to the bridge driving voltage in response to an applied force.

3.3. FEA Modeling of Force Sensor

Finite Element simulations were performed in MemMech solver (mechanical simulation) and MemPZR solver (piezoresistive simulation) in CoventorWare software. Design parameters such as beam length and transducer length were varied, stress values were determined and the sensor sensitivity was derived. The maximum sensitivity and the corresponding design values was determined and used. The beam length should be maximized and transducer width minimized to reach the maximum sensitivity.

The displacement and stress in force sensor for an applied force of 100 μN was determined using FEA simulations (see Fig. 19). The displacement and stress will cause a change in resistance of piezoresistive transducers. Applying a constant voltage to the electrodes, the change in current density is obtained from the software. Therefore, the change in resistance and sensitivity can be calculated. The displacement, stress, electrical potential and current density simulation results in transducer region for the same applied force and 0.5 V, 0.5 V and 0 V applied voltages in electrodes are shown in Fig. 20.

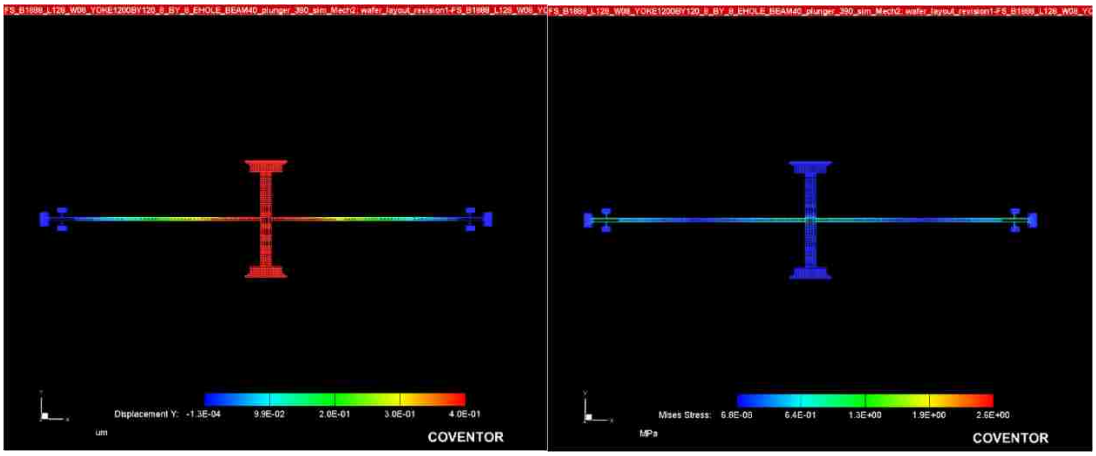

(a) (b)

Figure 19. Displacement (a) and stress (b) of the force sensor (type 1) for 100 μN applied force.

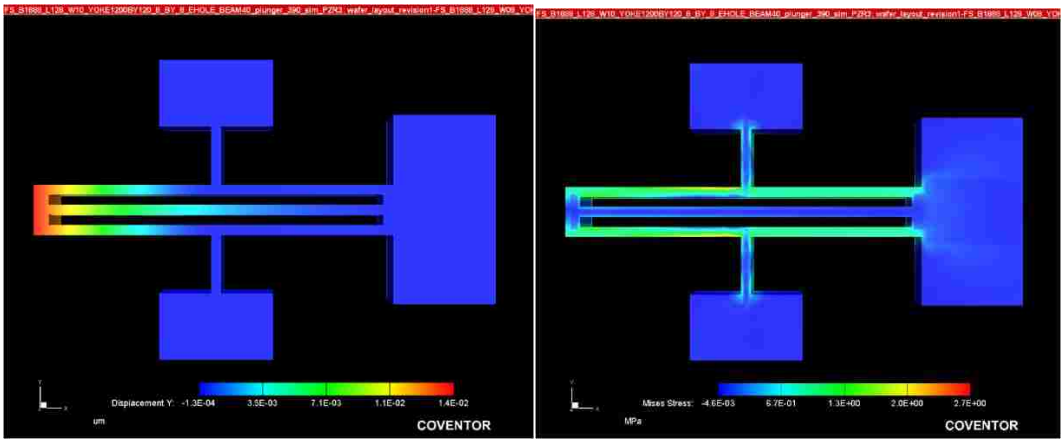

(a) (b)

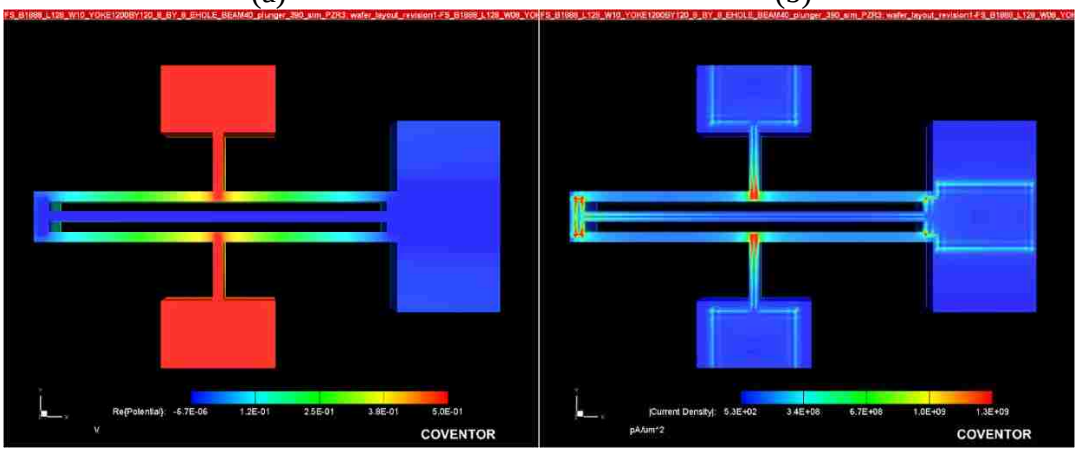

(c) (d)

Figure 20. Displacement (a), stress (b), electrical potential (c) and current density (d) in transducer region of the force sensor, the applied force 100 μN, and voltages are 0.5, 0.5 and 0 V.

The sensitivity values calculated from the simulations are shown in Table 9. The required sensitivity was determined according to previous design sensitivity and the minimum force (See Table 10).

Table 9: Simulation results and calculated sensitivity of force sensor

Patch Voltage (V)	Patch Current	%Change in Current	I (A)	Δi	R(Ω)	ΔR(Ω)	ΔR/R	Sensitivity ((Ω/Ω)/N)
0.5	1.69969E+11	0.016392	0.169969	2.7861E-05	2.941707 23	-0.00048212	-0.00016 3891	1.638908626
0.5	1.69919E+11	-0.01637	0.169919	-2.7816E-05	2.942576 18	0.00048178	0.00016 3729	1.637287127

Table 10: Different sensitivity of the force sensor design

	Min Force	Sensitivity ((Ohm/Ohm)/N)	Device Height (µm)	Beam Length (µm)	Transducer Width (µm)
Design for single cell	15 nN	102	10	450	1 or 2
Design for embryoid body	1 µN	1.52	150	1888	8 or 10

3.4. Force sensor modes

The first four vibrational modes from modal mechanical simulation are given in Fig. 21. The modes will be important in determining resonant frequency of the sensor.

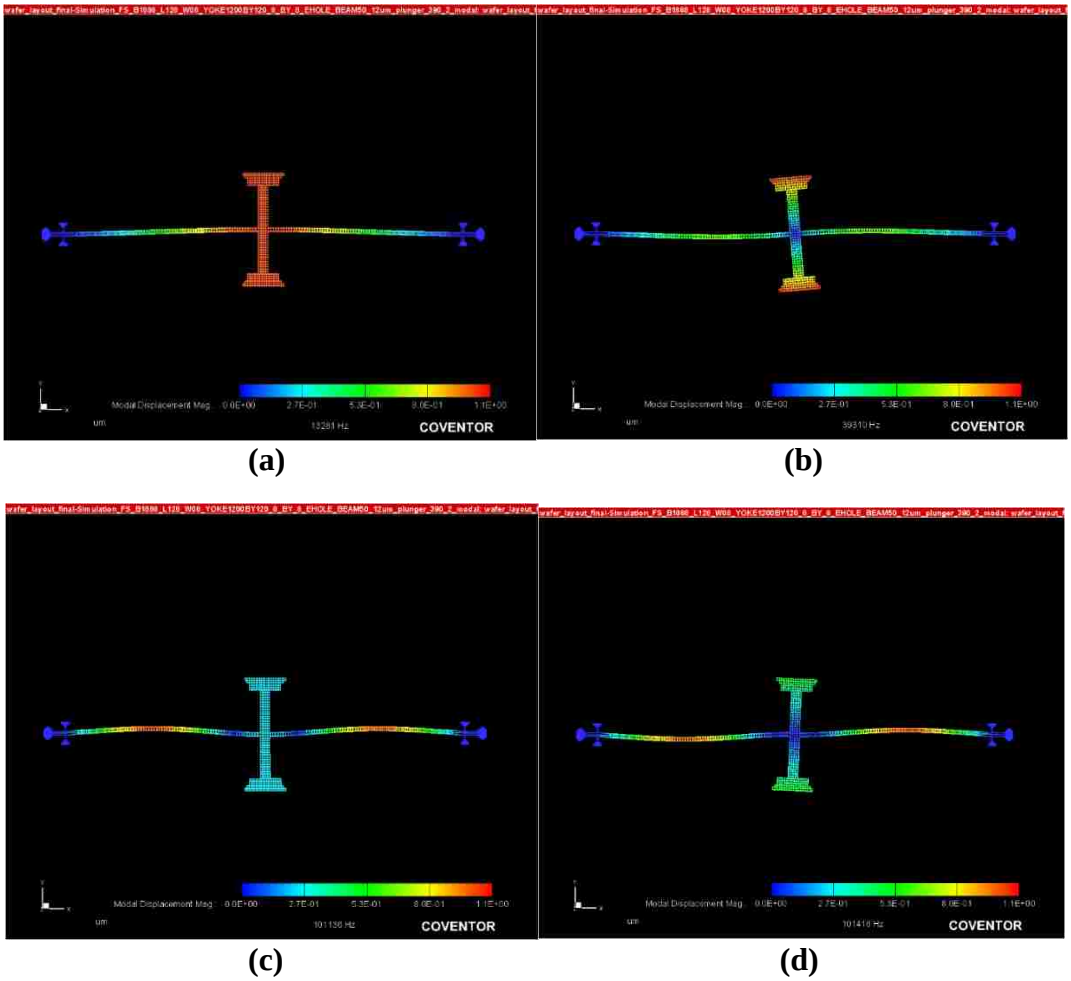

(a) **(b)**

(c) **(d)**

Figure 21. The first four vibrational modes of the force sensors, deformed shaped are demonstrated (with exaggeration).

4. Dielectrophoretic Positioning System

We have included a quadrupole electrode configuration to position the embryoid body in the proper place for characterization. The embryoid body should be placed between the force sensor and the actuator in order to be mechanically characterized. We have successfully demonstrated trapping of a single cell with a similar configuration. This method is using dielectrophoresis force as a contactless way to position the dielectric target in the desired position. This method is explained in this chapter.

Dielectrophoresis is used more and more frequently in MEMS, most often as a method to trap particles in predefined positions [52, 53]. Notable applications of this technique are utilization of DEP for multielectrode arrays (MEAs) [54], and as an element of a microsystem for determining mechanical properties of biological cells [2]. In fact, dielectrophoretic trapping has been one of the most popular methods of manipulating biological particles. Positioning the cell in the proper area of MEMS device to perform different experiments without changing the characteristics of the cell is an important issue. One of the advantages of this method is that it is a contactless approach to position cells in predetermined places [55-57]. However, it is difficult to design an effective DEP trap. Whereas some traps are functional for certain cell types, they do not work for other cell types. Here we present a modeling approach verified by experiment where the cell trajectories, type of dielectrophoresis (positive vs. negative), as well as the forces acting on the cells during the DEP trapping process can be anticipated. This methodology can greatly help in design of DEP positioning and trapping systems. Using negative dielectrophoresis in quadrupole electrode configuration (very frequently used), microspheres can be trapped in the center. In this work, we have investigated two types of particles: polystyrene microspheres and mouse fibroblasts (NIH3T3). We have developed a MATLAB algorithm to model the motion of the microspheres during the trapping process.

Modeling movement of a cell due to dielectrophoresis inside a microfluidic channel was reported in [58], which we have used as starting point in developing our code.

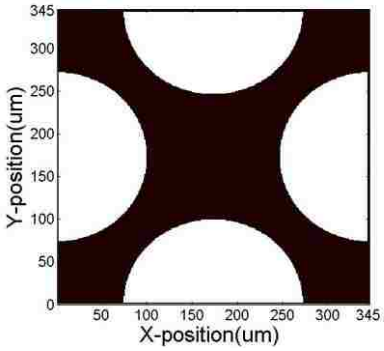

Figure 22. The DEP quadrupole electrodes, adjacent electrodes are powered with opposite polarities, this results in electric field minimum at (172.5μm, 172.5μm), the point that corresponds to the center in our coordinate system.

In this section, we model the dielectrophoretic force and the trajectories of the microspheres while being trapped in the quadrupole electrode configuration which is shown in Fig. 22. The adjacent electrodes will be powered with sinusoidal voltage with the equal amplitude but 180 degrees of phase difference. This electrode configuration will result in the electric field minimum in the center point and will cause the microspheres to move towards the center.

4.1. Theoretical Background

The dielectrophoretic force is exerted on a particle when it is placed in a non-uniform electric field surrounded by a medium with different dielectric constant. Dielectrophoresis can be either negative or positive. In the former case, the particle will be attracted to the electric field minimum while in the latter it will be attracted to the electric field maximum. The time averaged dielectrophoretic force acting on a homogenous spherical particle of radius r is given by [59]

$$F = 2\pi r^3 \varepsilon_m \mathrm{Re}[k] \nabla |E|^2 \qquad (40)$$

where ε_m is the permittivity of medium at zero frequency is, $\mathrm{Re}[K]$ is the real part of Clausius–Mossotti factor K, and E is the RMS value of the electric field. Both of the microspheres were modeled as spheres. The Clausius-Mossotti factor for a simple sphere is given by [60]

$$K(\omega) = (\varepsilon_p^* - \varepsilon_m^*)/(\varepsilon_p^* + 2\varepsilon_m^*) \quad (41)$$

where ε_m^* is the complex permittivity of the medium surrounding the particle and ε_p^* is the complex permittivity of the particle. The dielectrophoresis is called negative when $\mathrm{Re}[K] < 0$ and is positive when $\mathrm{Re}[K] > 0$. The complex permittivity as a function of frequency is

$$\varepsilon^* = \varepsilon + \sigma/i\omega \quad (42)$$

where ε is the permittivity at zero frequency, σ is conductivity and ω is the field frequency. It can be seen from equations 41 and 42 that the Clausius-Mossotti factor is a function of electrical characteristics of both the particle and the medium as well as frequency of the electric field.

The forces incorporated in our model are the dielectrophoretic force and the drag force. Other forces such as electrothermal force are considered to be negligible in this model. The gravity is assumed to be in equilibrium with buoyancy force and all the motion equations were solved in the plane of electrodes. Considering the forces mentioned above, Newton's second law can be written as

$$F_{DEP} - F_{Drag} = ma \quad (43)$$

where m is the mass of the spherical particle, a is acceleration and F_{Drag} is the Stokes' drag force. The Stokes' drag force can be described with the following equation for a sphere

$$F_{Drag} = 6\pi\eta r v \quad (44)$$

where η is the fluid viscosity, v is the particle velocity and r is the radius of the spherical particle. From the equations listed above we can form a set of differential equations as follows.

$$m\frac{d^2x}{dt^2} = F_{DEP,X} - 6\pi\eta r\frac{dx}{dt} \quad (45)$$

$$m\frac{d^2y}{dt^2} = F_{DEP,Y} - 6\pi\eta r\frac{dy}{dt} \quad (46)$$

where $F_{DEP,X}$ is the dielectrophoretic force component in x direction and $F_{DEP,Y}$ is the dielectrophoretic force component in y direction, This set of equations was used in the modeling efforts described in the following section.

4.2. Modeling

The goal of our modeling efforts is to find the DEP forces, trajectories, and velocities of our microspheres that we are trying to trap. The first step in our modeling process is to determine the gradient of the electric field from the potential distribution, and then we incorporate it in equation 40 and determine the DEP force. Subsequently we can solve the differential equations and determine the trajectories and the velocities which are our remaining goals. In order to model the microsphere motion, first the electrical potential distribution as a function of position in the quadrupole electrode configuration was derived using the relaxation method [61], [0.5μm grid resolution] in MATLAB (version R2010a, MathWorks). In the relaxation method, the solutions to Laplace's equation are found by setting the V value at each point equal to the average of its nearest neighbors. The potential solution is found by cycling through the points on the grid and assigning to each one the average of its neighbors. On each subsequent pass, the updated values are used. After a few iterations, the values change less on each subsequent pass. Eventually, the changes are negligible and a numerical solution will be reached. After finding the electrical potential, the electric field was calculated by taking the gradient of the electrical potential. The gradient of the electric field squared was obtained after this step and the dielectrophoretic force was derived for each point from equation 40. In the following step, the differential equations 45 and 46 were solved and the trajectory and the velocity of the microsphere were calculated. A MATLAB algorithm was developed to solve our differential equations by using the proper trapezoidal rule solver [62].

The inputs for the algorithm are the initial velocity and position of the microsphere, the amplitude and frequency of the voltage applied to the electrodes and the electrical properties of the microsphere and the medium. The electrical properties found from the literature are conductivity of $1.6\ S/m$ and relative permittivity of 80 for the NIH3T3 cell medium [63], [64], conductivity of $10^{-16} S/m$ and relative permittivity of 2.5 for the polystyrene microspheres, and the conductivity of $0.6\ S/m$ and relative permittivity of 82 for NIH3T3 cells [63].

In each time step, the dielectrophoretic force components $F_{DEP,X}$ and $F_{DEP,Y}$ will be calculated based on the previous position. Also, the drag force components will be calculated from the velocity determined from the previous time increment. The differential equations for motion will be solved and the outputs will be the new x and y positions and velocities. Modeling results show that for a given initial condition inside the electrodes, x and y position will converge to the x and y of the center and velocity components are going to zero which means the microsphere will move toward the center and eventually will be trapped. Similar results were observed in the experiments as well.

Figure 23.The experimental setup. Four probe tips were used to apply desired voltages to four Ti/Pt electrodes located on Si substrate.

4.3. Experimental Setup

We have designed the experiments to verify our modeling efforts. Experiments were done to trap both polystyrene microspheres and cells. First we have trapped the polystyrene microspheres (L14822 Molecular Probes) with a radius of 3 μm suspended in DI water which had conductivity of $6.25 * 10^{-6}\ S/m$ as measured by conductivity meter EC410 (Extech Instrument). The second set of experiments was done on the NIH3T3 mouse fibroblasts with an average radius of 10 μm. Cells were suspended in high glucose Dulbecco's Modified Eagle Medium *(*DMEM), supplemented with 10% bovine calf serum (BCS) and 1% Penicillin Streptomycin (PenStrep). We have trapped the microspheres by applying the sine voltages using a signal generator (33521A Agilent Technologies). The

frequency of the voltage was within the range of 400 KHz-2 MHz with amplitude of 10-15 Vp-p. The experimental set-up is shown in Fig. 23.

For the range of frequencies used, the sign of the real part of the Clausuis-Mossotti factor is negative for polystyrene spheres in DI water, as well as NIH3T3 cells in the cell medium. This negative sign leads to a negative dielectrophoresis, where microspheres are repelled from the electrodes to the electric field minimum. The real part of the Clausuis-Mossotti factor for NIH3T3 cells in cell medium and for the polystyrene microspheres in DI water were calculated to be approximately -0.26 and -0.48 respectively at the frequencies we used. Therefore, negative dielectrophoresis was observed and verified in our experiments. As a result, the microspheres are attracted to the center of the trap where the minimum of electric field is located. The trapping process was captured by Motic Image Plus 2.0 (Motic PSM-1000) [65]. The experimental data was then analyzed and compared with the modeling results.

4.4. Comparison of Modeling and Experimental Results

We analyzed the experimental data using CellTrack software [65] and MATLAB to find the trajectories, the velocities and subsequently the DEP force. The trapping videos were converted to time-stamped images using an image processing algorithm in MATLAB.

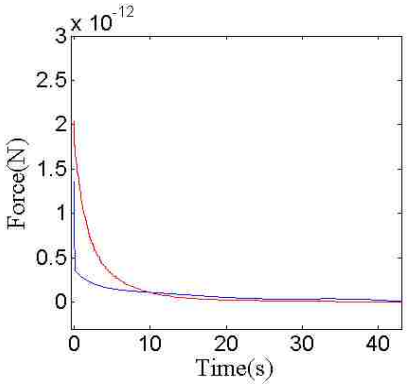

Figure 24. The magnitude of the measured DEP force (blue line) and the magnitude of the modeled DEP force (red line) for a polystyrene microsphere. The time axis indicates the experimental time. Both modeled and measured forces are plotted for the same position of the microsphere. The voltage frequency was 400 KHz with amplitude of 6 V and the initial position was (131 μm, 198 μm). The zero DEP force corresponds to the microsphere being trapped at the center.

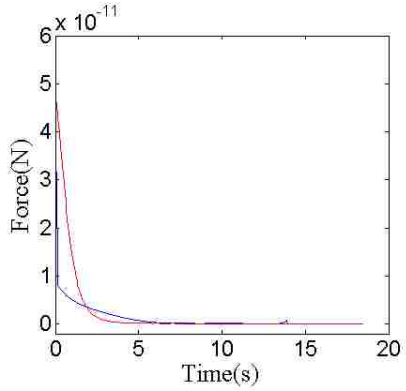

Figure 25. The magnitude of the measured DEP force (blue line) and the magnitude of the modeled DEP force (red line) for a NIH3T3 cell. The time axis indicates the experimental time. Both modeled and measured forces plotted for the same position of the cell. The voltage frequency was 1 MHz with amplitude of 5 V and the initial position was (107 μm, 237 μm). The cell started moving towards the center of the trap until the DEP force became zero and the cell was trapped at the center [65].

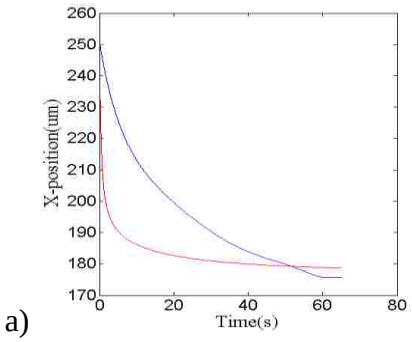

a)

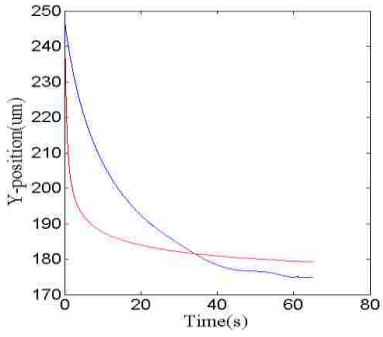

b)

Figure 26. The experimental trajectories (blue line) and the modeled trajectories (red line) along x (a) and y (b) directions while the polystyrene microsphere moves from initial position (247.5 μm, 244.5 μm) in the upper right corner of our trap to the trapping center (172.5 μm, 172.5 μm) in the middle of the trap-see Fig. 22.

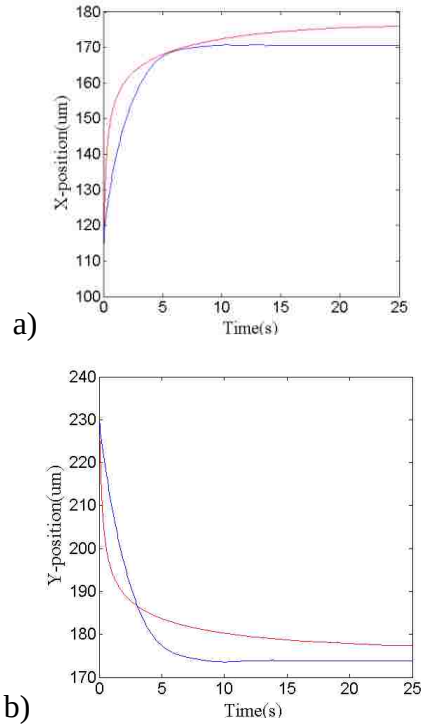

Figure 27. The experimental trajectories (blue line) and the modeled trajectories (red line) along x (a) and y (b) directions for a NIH3T3 cell in cell medium with the initial position of (113 μm, 227.5 μm).

The microsphere trajectories were traced using Optical Flow Tracking option of CellTrack considering the same coordinate system as the experiment. The tracking information was imported to MATLAB to determine the velocities and subsequently the DEP force by another user-defined MATLAB routine. In order to be able to measure the DEP force, velocities and accelerations were determined from the experimental trajectories. In the next step, the drag force was calculated and the DEP force was determined according to equation 43.

Comparison between DEP forces from modeling and experiments are shown in Figs. 24 and 25. It can be seen that the general agreement is obtained between the experimental and modeling results for the DEP force. The trajectories obtained from the simulations and the experiments were also compared. Modeling results for x and y trajectories are close to the experimental data for the trapped microspheres (Figs. 26 and 27). The initial position for the polystyrene microsphere is (247.5 μm, 244.5 μm) which is located in the upper right

section of our coordinate system (See Fig. 22), and the initial position for the cell is (113 μm, 227.5 μm) which is located in its upper left section.

5. Fabrication and Characterization

The fabrication process was done on 6-inch SOI wafers in Sherman Fairchild Center (SFC), Lehigh University. The properties of SOI wafers is given in Table 11.

Table 11: SOI wafer specifications

Device Layer	**Specifications**
Diameter:	150+/-.2 mm
Type/Dopant:	P/Boron
Orientation:	<100>+/-.5 deg
Thickness:	150+/-1 µm
Resistivity:	.001-.005 Ohmcm
Particles:	<10@.2 µm
Flats:	Semi std
Edge Exclusion:	<5mm
Finish:	Polished
Buried Thermal Oxide	
Thickness:	2µm+/-5%
Handle Layer	
Type/Dopant	P/Boron
Orientation	<100>+/-.5 deg
Resistivity:	1-20 Ohmcm
Thickness:	500+/-15 µm
Overall TTV:	<2 µm
Finish:	Polished

Fabrication of the device involves a set of three masks. Metal deposition, deep reactive ion etching and atomic layer deposition are the main steps of the fabrication. Fabrication of high aspect ratio (HAR) MEMS structures is challenging. Also simple microfabrication techniques such as lithography might not work over the HAR structures. The fabrication process for building the device could be performed in two methods based on the order of release and atomic layer deposition (ALD) steps. The first approach will be to release the free-standing structures after deposition of Alumina with ALD. In this case, after lamination of dry resist we pattern it to open the pads and windows to later etch silicon oxide underneath the alumina layer. Based on application of the dry resist, we could get

side walls covered with alumina to have them insulated. The second fabrication approach is to release the structure before ALD deposition of Alumina. However, this will cause the high aspect ratio structures to become very fragile and the following patterning steps will damage the structure. Therefore, the first method was chosen for fabrication.

Three masks were designed for the fabrication process. The first mask is to define the metal pads and connect them to proper part of the design such as electrodes. The second mask is to provide a masking layer of photoresist for deep reactive ion etching of silicon. The third mask is to pattern insulation layer which is intended to provide electrical isolation for operation in an ionic environment.

The fabrication process steps are listed in the following. The fabrication process flow with the corresponding device cross sections is depicted in Fig. 28.

1- Starting material is SOI wafer with 150 μm device layer, 2 μm buried oxide and 500 μm handle layer.
2- Photolithography with AZ nLOF 2020 using mask 1
3- Metallization, Cr-50nm, Au-250nm, Cr-10nm
4- Lift-off
5- Photolithography with SPR 220-7 using mask 2
6- DRIE for etching 150 μm device layer
7- Stripping the resist
8- Atomic layer deposition (ALD) of Al2O3
9- Patterning dry resist using mask 3 (Lamination of resist in DEVCORP with ADEX 5 photoresist)
10- Etching isolation layer with SF6 plasma
11- Removing dry resist
12- Release of free-standing structures with vapor hydrofluoric acid

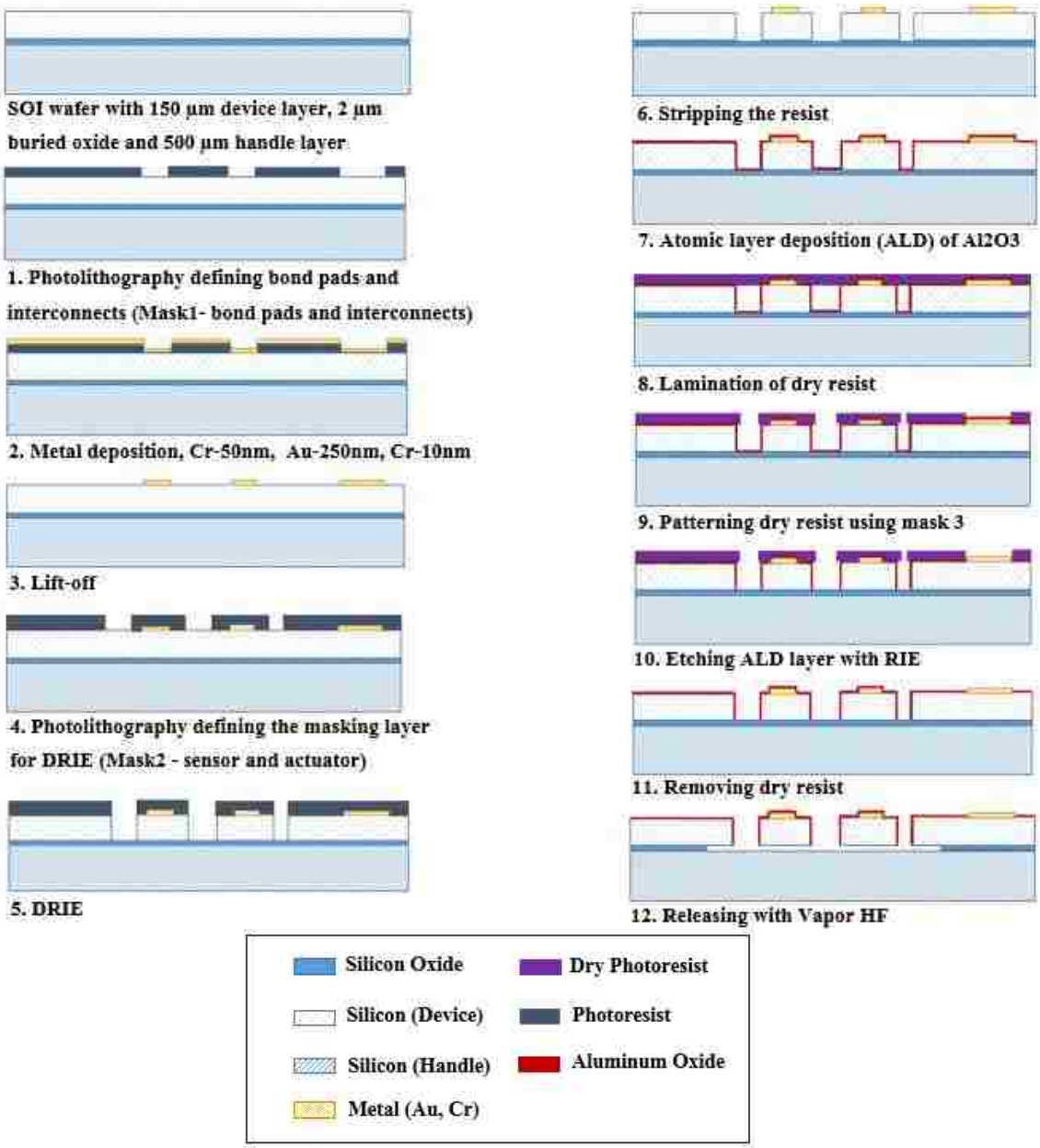

Figure 28. Schematic cross-sectional view of the fabrication process flow.

5.1. Metallization and Lift-off

Developing the fabrication process and instructions e.g. exposure dose, photoresist treatments, baking times, and rehydration time between the steps was performed for AZ2020 negative lift-off resist. This step was crucial to for lift-off of stack of 310 nm

chrome gold as the first layer. The metal structure after lift-off in the test and device area of the wafer is shown in Figs. 29.a and 29.b.

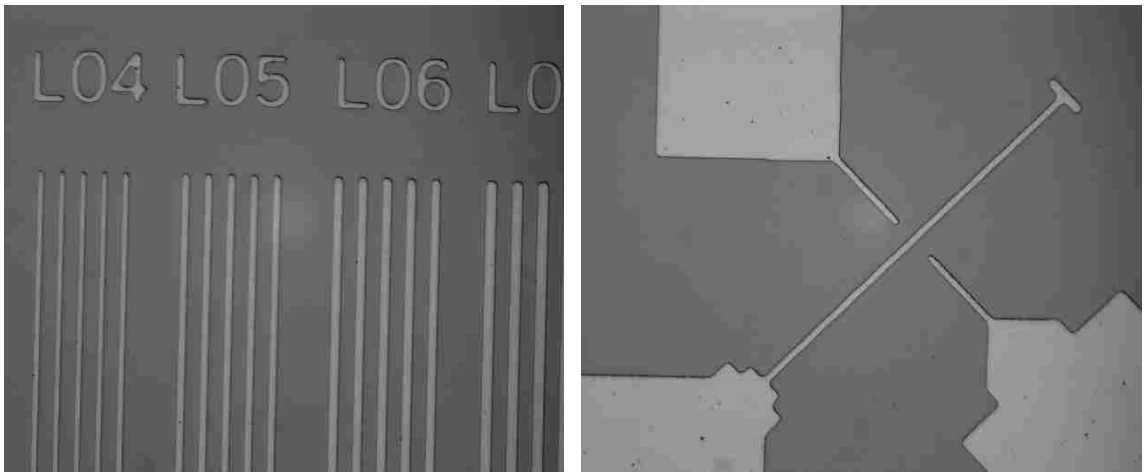

(a) (b)

Figure 29. (a) Line pattern test showing metal lines from 4 μm to 7 μm after lift-off. (b) Minimum feature size for metal layer is 4μm and located in transducer area of force sensor

5.2. Process Development for Photolithography

SPR 220 was used as a masking layer for deep etching of silicon. Fabrication instructions were developed for this resist in order to avoid cracking, bubbling and being able to act as a mask for two hours of etching in the chamber. Photoresist profile tuning was also done in order to provide almost 90-degree angle sidewalls. A series of experiments were conducted to minimize the sidewall angle by changing the space between wafer and mask in the mask aligner after the optimum exposure was determined. Once the photoresist was properly patterned (Figs.30.a and 30.b), we started the etching experiments. The details of photolithography conditions will be discussed in section 5.4.

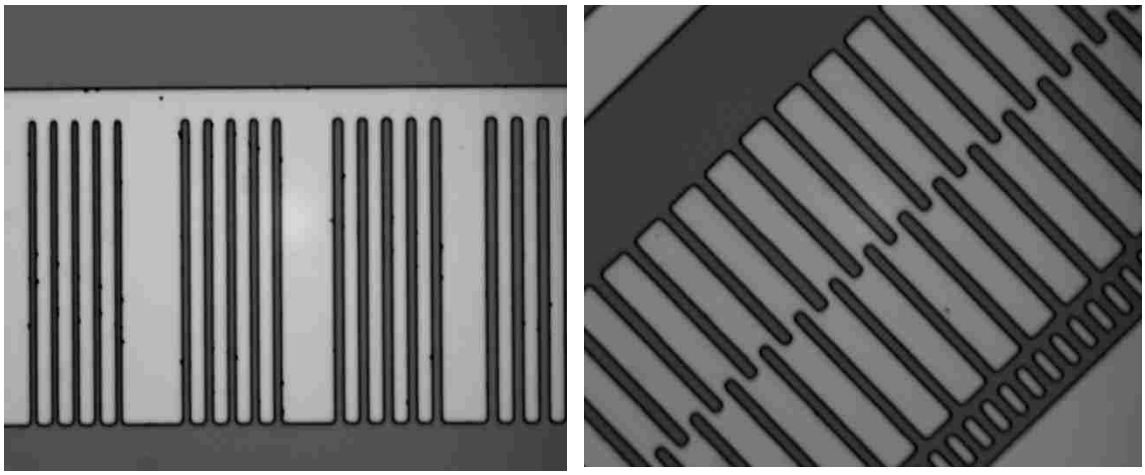

(a) (b)

Figure 30. (a) Line pattern showing 4 µm to 7 µm lines of photoresist focus shift. (b) Comb drive fingers had the minimum feature width covered by photoresist mask i.e. 8µm.

5.3. Bosch Process

Deep reactive ion etching (DRIE) of silicon provides the ability to create vertical sidewalls and make complex structures on silicon. As opposed to wet etching, which is isotropic etch, DRIE using Bosch process is highly anisotropic allowing for creation of 3D structures.

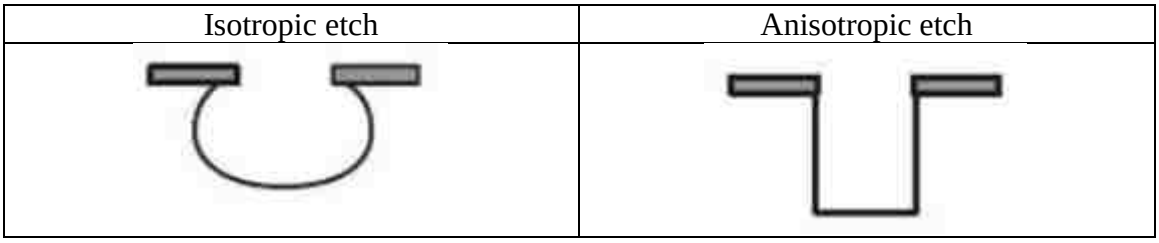

Figure 31. Comparison of isotropic and anisotropic etch [66].

Silicon etch with fluorine is naturally isotropic. In order to get isotropic etching, two gases for etching and passivation need to be alternating.

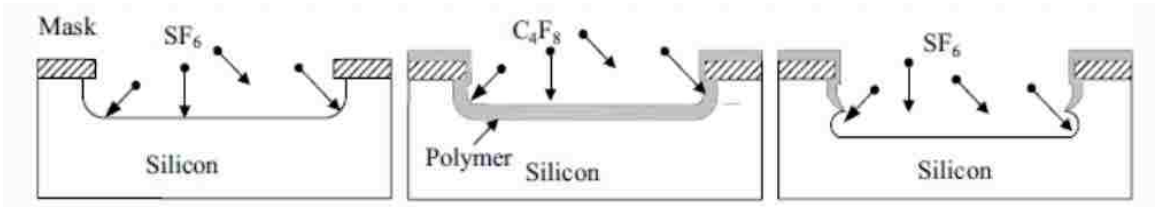

Figure 32. Bosch process [66].

Two common gases in Bosch process are SF6 for etching and C4F8 for passivation. In each cycle, fluorine ions etch the bottom of trenches followed by C4F8 polymer deposition on the bottom of trenches and sidewalls. During the following cycle, passivation on the bottom of the trenches will be removed by SF6 and etching will create deeper trenches into silicon while maintaining the sidewalls ideally intact from etching. Main parameters in etching are source power, pressure, bias power, gas flow and duration. Source power is usually kept at 13.56 MHz generating the plasma. Bias power can be either radio frequency (13.56 MHz) or low frequency (280-320 kHz) intended to accelarate ions inside plasma and provides directionality. Gas flow and times for etching and passivation are also important factors in Bosch process and need to be taylored for the requirements of the structure.

Aspect Ratio Dependent Etching

The trenches with different size get etched differently, with larger features getting etched more than the smaller openings. This effect is called aspect ratio dependent etching and therefore etch stops such as oxide are used in SOI wafer.

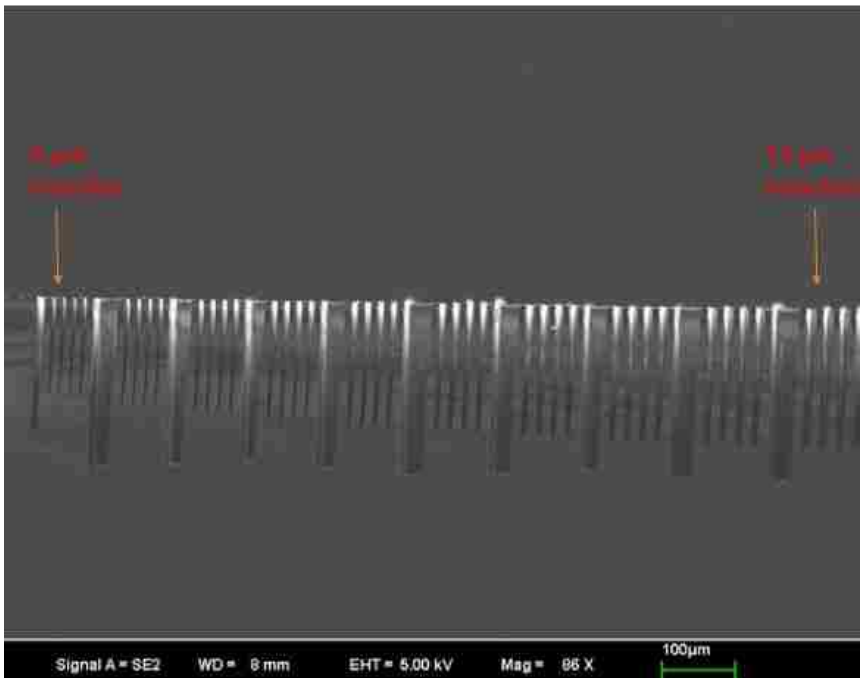

Figure 33. Aspect ratio dependent etching is shown. Narrower trenches are etched less than the wider ones, width of trenches increase from left to right and there are four trenches of each width.

5.4. DRIE Tests and SEM Characterization Results

A number of deep reactive ion etching experiments were performed in order to find the proper etching recipe for our experiment using Adixen AMS 100 (Alcatel) etching system. Our process utilizes a single mask etching step for etch depth of 150 μm in silicon with photoresist as a masking layer. Since the masking layer of photoresist should protect the underlying layer up to two hours in etching chemistry, photolithography parameters needed to be adjusted accordingly. This is important in order to avoid damage to the structure to the end of etching time (See Fig. 34).

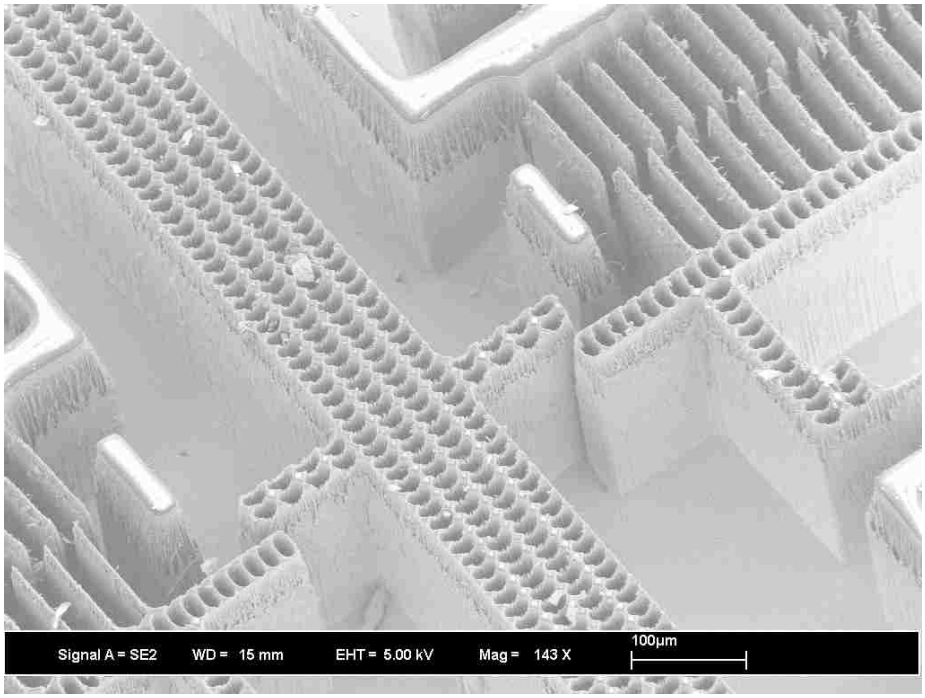

Figure 34. Damage to top of features due to lack of photoresist mask.

The photolithography parameters include resist thickness, exposure dose, bake time and required time for rehydration to avoid cracking and bubbling in the resist. Initial photolithography parameters and final parameters that was established with process development after the device mask revision are given in Table 12 and Table 13.

Photolithography with mask 1 was done using a projection system (ASML Projection Aligner Model 700). The starting recipe and the derived parameters for etching are given in the following sections.

Table 12: Photolithography parameters for SPR 220 as a masking layer for DRIE

Surface Preparation	Spin Speed (rpm)	Target Thickness (μm)	Measured Thickness (μm)	Exposure Dose (mJ)	Soft Bake Time (sec)	PEB Time (sec)	Dehydration
HMDS Treatment	2000	8	8-8.5	400-550	2-5 min 115 C	2-5 min 115 C	Overnight

Table 13: Revised photolithography parameters for SPR 220 as a masking layer for DRIE

Surface Preparation	Spin Speed (rpm)	Target Thickness (μm)	Measured Thickness (μm)	Exposure Dose (mJ)	Soft Bake Time (sec)	PEB Time (sec)	Dehydration
HMDS Treatment	1500	11	11-11.1	500	2 min 50 C 5 min 110 C	2 min 50 C 5 min 110 C	Overnight

To avoid resist bubbling, baking was adjusted to be done in two steps instead of one. This will eliminate an abrupt change in temperature of the resist in one step and solve the bubble formation. The thickness of resist was increased to resist more etching time. Exposure dose was adjusted by multiple experiments and measurements of line pattern width in the center and edge and according to the average vales for desired measurements for 10 μm lines.

In order to be able to release the free standing sensor and actuator, there are etch holes designed throughout their structures. However, the etch holes need to be completely opened to the oxide for the structure to be released. For this to happen, the holes need to get etched 150 μm. Etching experiments were designed to reach that goal. The first DRIE experiment was done with the default substrate temperature of 10 C. The test wafer was then cleaved along the test structure to be characterized by SEM pictures taken by Hitachi TM1000 and Zeiss 1500. The SEM pictures were taken from cross section of the trenches with different depth designed in the test pattern. The SEM picture of a test wafer etched

for 72 min in 10 C is shown in Fig. 35. The images were analyzed in ImageJ to find out the depth of the trenches. The measured etch depth for different trenches from 4 µm to 13 µm is given in Fig. 36.

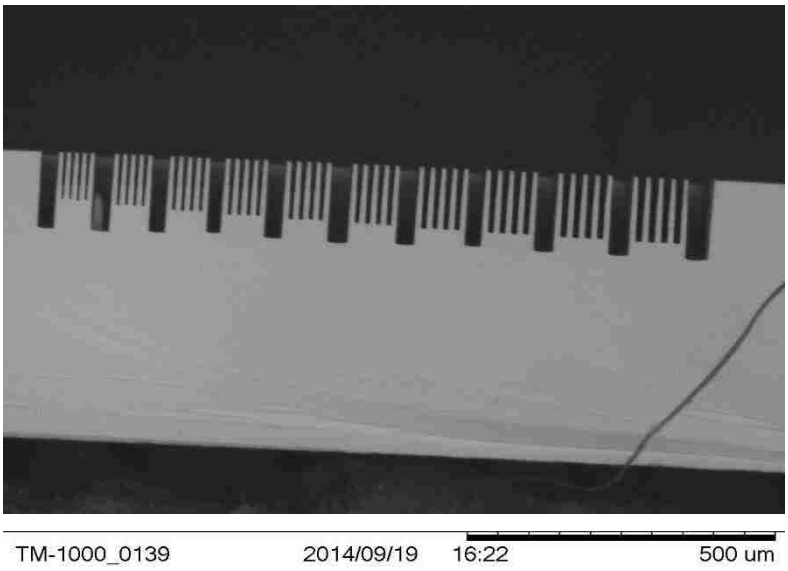

Figure 35. SEM picture of a test wafer etched for 72 min in 10 C.

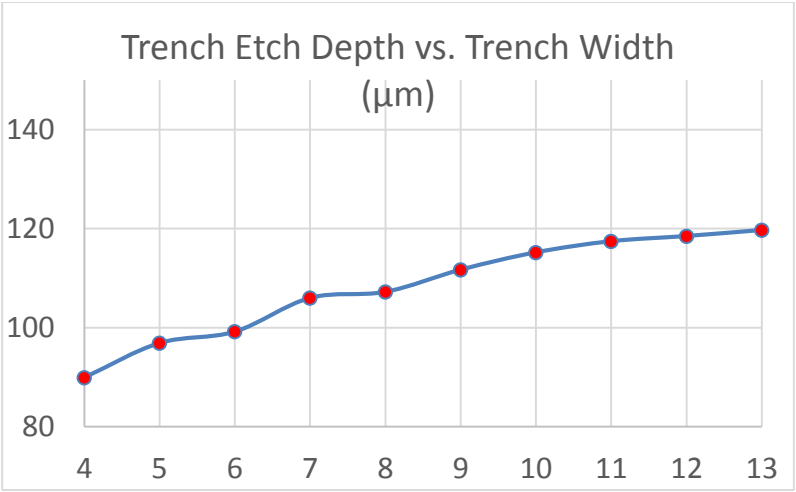

Figure 36. Trench etch depth vs. trench width.

The next experiment was carried out at -10 C to avoid RIE lag i.e. lower etch rate in the narrower trenches [67]. The thickness of photoresist mask was increased to 10 µm and the etch time was increased to 1.5 hour trying to find the maximum etch depth in the narrowest

etch hole of 8 μm by 10 μm. The etch depth measured in the wide areas, between fingers and inside of the smallest etch hole in the free standing structure (8 μm by 10 μm) is given in the Table 14. In the SEM picture in Fig. 37, different trenches with widths from 4 μm to 13 μm are shown. This shows with the revised DRIE parameters, mainly the lower temperature, trenches with 8-μm width can get etched down to 150 μm (Fig. 38) but the depth of the 8 μm by 10 μm etch hole is still less than 150 μm (Fig. 39), and therefore it would not reach the oxide in a SOI wafer to be released. The etch depth of finger spacing was also measured to be larger than 150 μm. The DRIE parameters are given in section 5.6.

Table 14: Etch depth for different openings on the wafer

Etch Depth	**Size of the opening**
110 μm	Etch hole (8 μm by 10 μm)
161 μm	Finger Spacing (8 μm)
210 μm	Wide area (~200 μm)

Lower temperatures such as -20 C was also experimented but the etch rate of silicon was very low and therefore it was not suitable for etching 150 μm of silicon. The test that was done at -10 C lead to the best results in terms of etch rate in the narrow holes and uniformity of etch throughout the wafer. In addition, this temperature results in the minimum resist etch rate which is important in maintaining the masking layer to the end of the experiment. The following SEM pictures show more details on the profile of trench pattern, line pattern and the etch depth in 8-μm trench which is our narrowest trench in the structure.

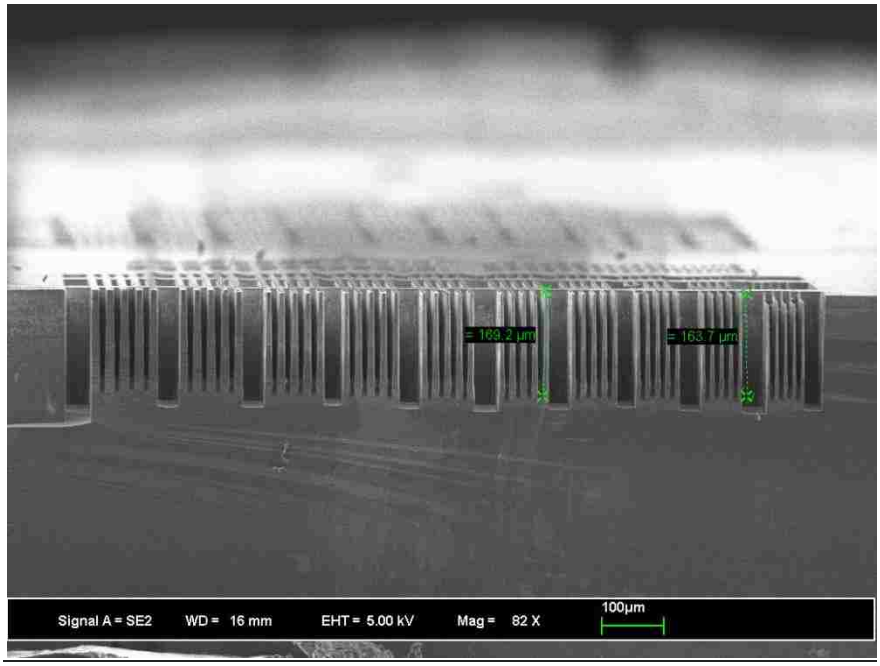

Figure 37. SEM graph of trench pattern with 4 µm to 13 µm width (width of trench increases from left to right).

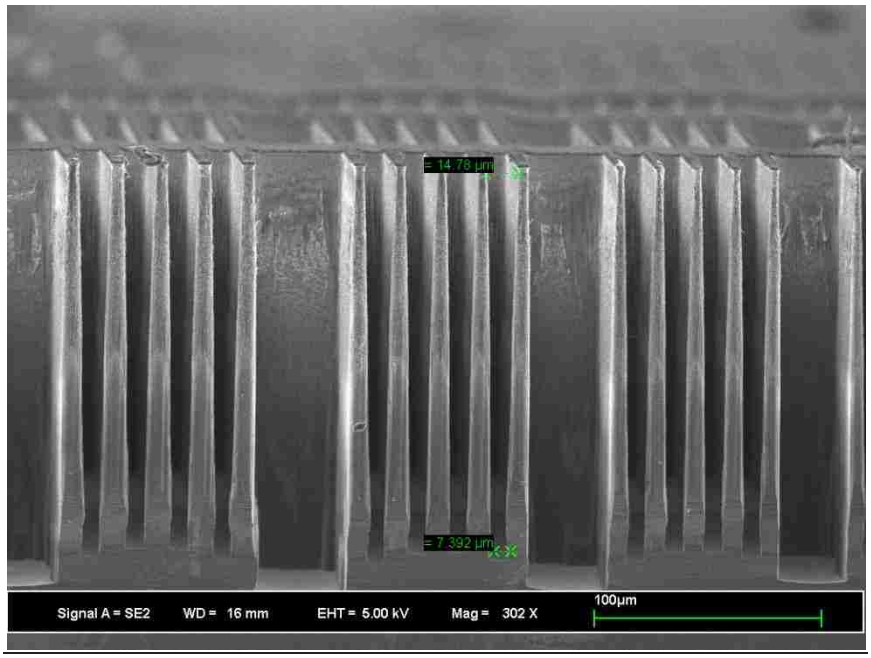

Figure 38. Trench pattern in the center of wafer is shown. 8-µm trench reached more than 160 µm.

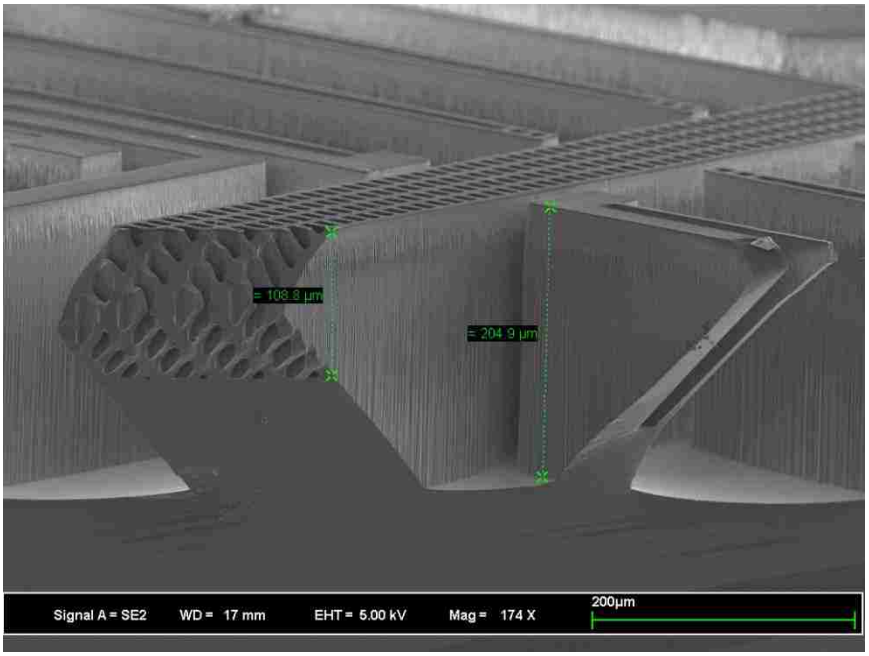

Figure 39. This picture shows etch depth in wide area and in the shuttle etch hole of 8 µm by 10 µm.

5.5. Generation #1 Layout and Revision of Device Mask

Since the smallest etch holes in the structures would have not been etched deep enough to reach the oxide with the current mask, we had to redesign the device mask. In addition, a number of revisions were done to improve the design that will be discussed in details. The device mask was redesigned with enlarged etch holes in the free standing structure and also added test structures for more effective and less time consuming characterization of etch depth. Also different comb drive test structures were added. Also, some of the modifications were related to the effect of fabrication over etching. The layout design was optimized to ensure it will be released and finger spacing minimum was also increased from 6.5 µm to 8 µm to make it more feasible.

The previous layout dimensions were given in Table 4. The design dimensions in the new layout is given in Tables 15 and 16. The die distribution in the wafer is given in Table 17.

Major revisions to the device mask are listed below:

1- Etch holes were adjusted in force sensor, comb drive actuators and shuttle. Previously they were 8 μm by 10 μm (min), 15 μm by 20 μm, and 8 μm by 20 μm they got etched to 110 μm. based on design and shapes they were maximized throughout free standing structures. Now it is 30 μm by 52 μm, 35 μm by 48 μm, 20 μm by 72 μm, New test structures
2- In 10 dies spring width increased 2 μm due to over etching in wide areas.
3- 10 dies with 6.5 μm finger spacing replaced with 8 μm finger spacing, less number of pairs.
4- Stress concentrators were reduced in the design of actuator springs in order to avoid breaking
5- In the free standing structures, beam width was increased to 12 μm everywhere instead of being 10 μm to avoid over etching problems (The minimum anchor width is 20 μm)

6- Test structures were modified in the center (details are given in the following section)

7- 12 μm trenches for force sensor were included for 15 dies (in addition to 10 μm and 8 μm in the previous design)

8- All spring widths are increased to 10 μm or 12 μm instead of 8 μm and 10 μm which were used in the previous mask respectively

9- Variations for initial finger overlap of 18 μm for 10 dies and 14 μm for 30 dies was added instead of all 10 μm

10- More space for trapping EBs were added to Die 1, Die 2 and Die 8 types.

Table 15: Design dimensions of actuator (AT) in the revised layout

Die Type	Minimum Si Width (µm)	AT Designed Displacement (µm)	AT Spring Width (µm)	AT Length (µm)	Comb Finger Spacing (µm)	Comb Finger Pairs	Spring length (µm)	Initial overlap (µm)	Count
Die 1	8	Set*	12	7861	8	63	2100	18	5
Die 2	8	Set	12	7861	8	63	2110	18	5
Die 3	8	Set	10	7861	8	70	2310	14	15
Die 4	8	Set	10	7861	8	70	2310	14	10
Die 5	10	Set	12	7861	8	63	2310	10	25
Die 6	10	Set	12	7861	8	63	2310	10	5
Die 7	8	100	8	2961	8	70	2310	14	5
Die 8	10	100	10	2961	8	63	2310	10	5
Test Die									1
Total									76

*Set means the bank of actuators provides a set of five displacements including 100 µm, 90 µm, 77.5 µm, 65 µm, and 52.5 µm.

Table 16: Design dimensions of force sensor in the revised layout

Die Type	Min Si Width(µm)	FS Beam Width (µm)	FS Beam Length (µm)	FS Yoke Width (µm)	Plunger length (µm)	Count
Die 1	8	54	1888	120	435	5
Die 2	8	54	1888	120	435	5
Die 3	8	40	1888	120	435	15
Die 4	8	50	1888	120	435	10
Die 5	10	50	1888	120	435	25
Die 6	10	54	1888	120	435	5
Die 7	8	40	1888	120	435	5
Die 8	10	50	1888	120	435	5
Test Die						1
Total						76

Table 17: Die distribution in the wafer after revision (See Tables 15 and 16 for color codes)

		T	D19	D18	A17	A18	T		
	T2	D17	D16	D15	A14	A15	A16	T2	
T	D14	D13	D12	D11	A10	A11	A12	A13	T
D10	D09	D08	D07	D06	A05	A06	A07	A08	A09
D05	D04	D03	D02	D01	Test	A01	A02	A03	A04
C05	C04	C03	C02	C01	B01	B02	B03	B04	B05
C10	C09	C08	C07	C06	B06	B07	B08	B09	B10
T	C14	C13	C12	C11	B11	B12	B13	B14	T
	T2	C17	C16	C15	B15	B16	B17	T2	
		T	C19	C18	B18	B19	T		

Test structures for DRIE were designed to help with the characterization of the etch process (Figs.40-42). Trench pattern and line pattern with varied widths from 4 μm to 13 μm are included in the test die1. The characterization process involves cleaving through the test die to measure the etch depth. The arrangement of lines and trenches in this test die, in addition to the special way the test dies are located in a larger test area are carefully designed to increase the probability of at least one structure in the proper area to coincide with any random cleaving line (Fig. 40). This design maximizes the probability of cleaving through the proper area of trench pattern to be able to measure the depth and therefore obtaining successful characterization results from SEM.

In order to make sure our revised structure will provide the expected performance we ran the FEA simulations and made sure results are within the required range. Displacement which is one of the important goals was increased in simulations after the modifications. The coupled electromechanical simulation results for the new comb drive design is given in the Fig. 43.

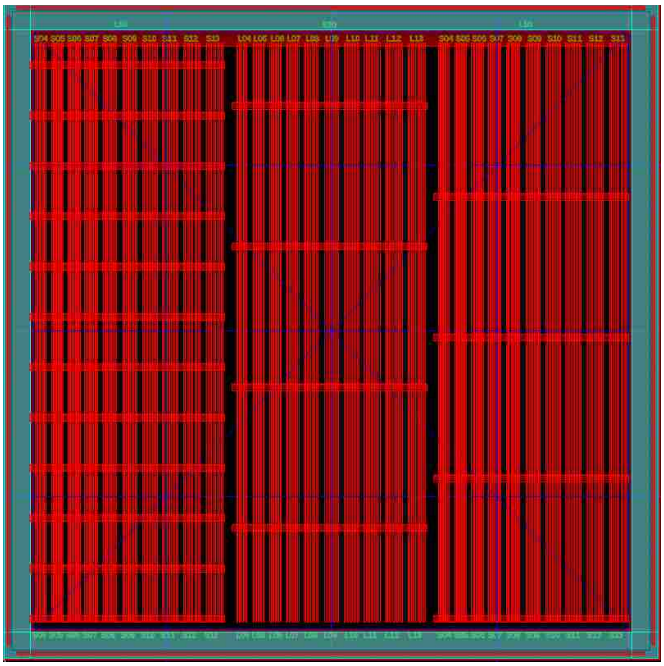

Figure 40. This picture shows trench and line pattern. Trenches are from 4 µm to 13 µm wide. Making a cut with scribe through trenches is necessary for SEM characterization, however the previous test structures needed cleaving line to be in one millimeter margin which is a very narrow line and easy to miss. With inclusion of this structure, two parallel trench patterns on the left and right will increase the chance of cleaving in the right place to happen at least in one of them.

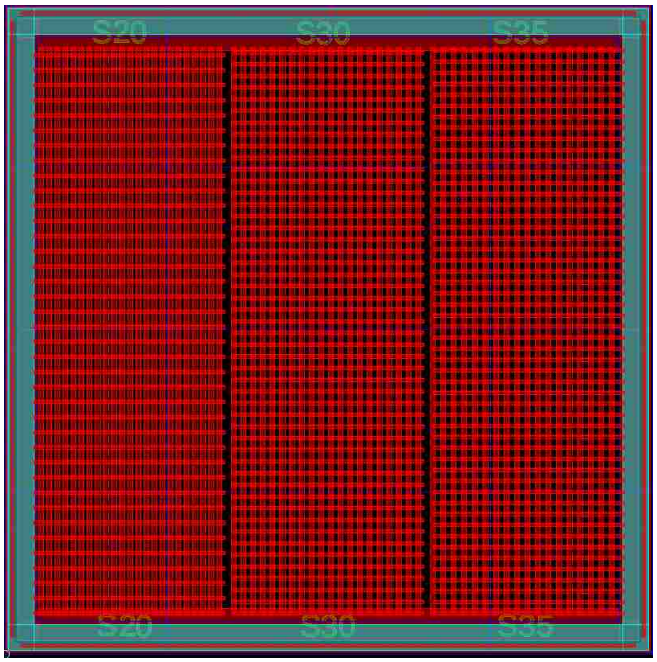

Figure 41.This test structure is a DRIE test structure for holes and includes the three smallest holes in the structure 30 µm by 52 µm, 35 µm by 48 µm, 20 µm by 72 µm.

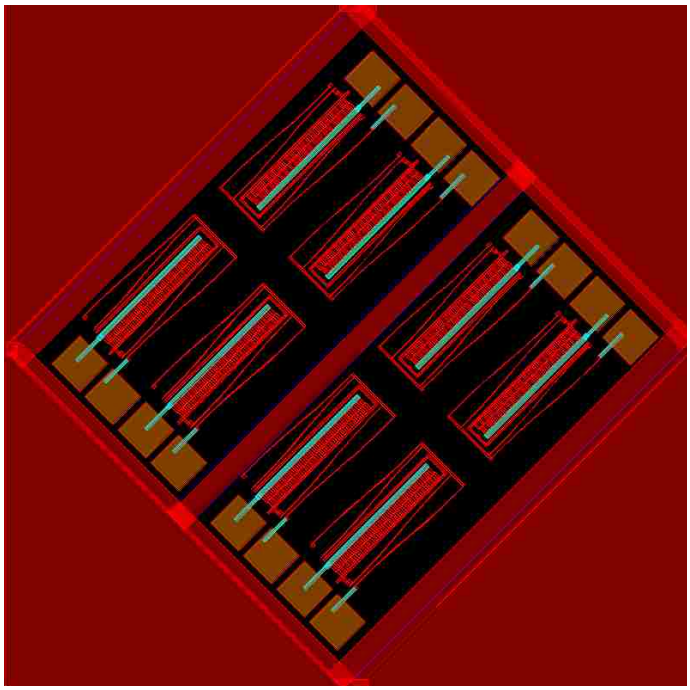

Figure 42. This structure has different comb drives with different spring widths (8 µm, 10 µm, and 12 µm) and different number of pairs that are currently in the design (63 pair and 70 pair).

Figure 43. Displacement of 130 µm is the result of applying 150 V instead of 120 µm for 150 V in the previous design.

After revision of mask, in order to find the conditions for achieving uniform etching everywhere on the wafer especially in narrow trenches we performed a series of experiments. Substrate at temperatures from -20 C to 10 C were experimented and etch depth of wide and narrow trenches were characterized using SEM images (Figs. 44 and 45). There is a trade-off between etch uniformity in trenches with different width and silicon etch rate. The uniformity of etch increases in trenches with different width by decreasing the temperature but the silicon etch rate decreases at the same time. For instance, after characterization of the wafer etched at -20 C, the etch depth is around 25 μm in the widest area which is well below the target etch depth of 150 μm. The etch rate of the resist do not considerably change and considering there is 5 μm resist left, the maximum etch depth to achieve in silicon will be only 50 μm and therefore this recipe do not achieve the etch depth target.

Etch rate of silicon and resist as well as selectivity were determined for different temperatures. Based on the etch rate of silicon in different areas for different temperatures (Table 18) and especially the etch rate in the trench with the minimum width of 8 μm, the required etching time of two hours was calculated for the etch depth of 150 μm.

Table 18: Etch rate of silicon and resist selectivity in different temperatures

	T=10 C	T=-10 C	T=20 C
Etch rate of silicon, wide area	2.5 μm /min	2.4 μm /min	<0.4 μm/min
Etch rate of silicon, 8-μm trench	1.6 μm /min	1.9 μm /min	Very small
Etch rate of silicon, etch holes	1.21 μm /min	1.26 μm /min	Very small
Etch rate of resist	0.086 μm /min	0.079 μm /min	0.079 μm /min
Selectivity	29	30	30

In the following experiments, -10 C was found to be the optimum temperature for this etching process. Center of the wafer had the least thickness of resist after etching. Thickness of resist in the center of the wafer (4 μm) is 2.3 μm thinner than the flat of the

wafer (6.3 μm). This measurement was done for a wafer that was etched at 10 C for 72 min. The lithography error might have contributed only 0.2 μm towards that difference in thickness of the resist.

A test wafer patterned with 11 μm resist was etched for 2 hours at -10 C. The result later shows the aspect ratio was reached and wafer was etched 150 μm everywhere up to etch-stop layer. By optimization of lithography and temperature we will be able to etch minimum required amount of 150 μm in all trenches including the minimum feature size of 8 μm trench.

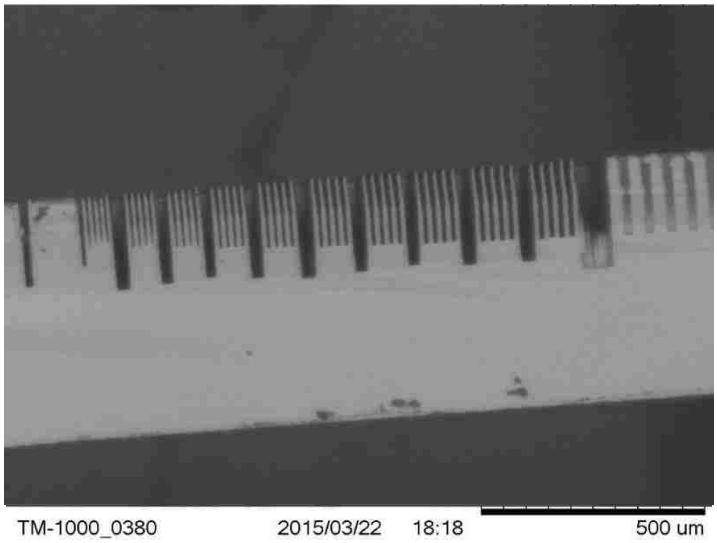

Figure 44. SEM picture of trench pattern in test wafer etched at -10 C.

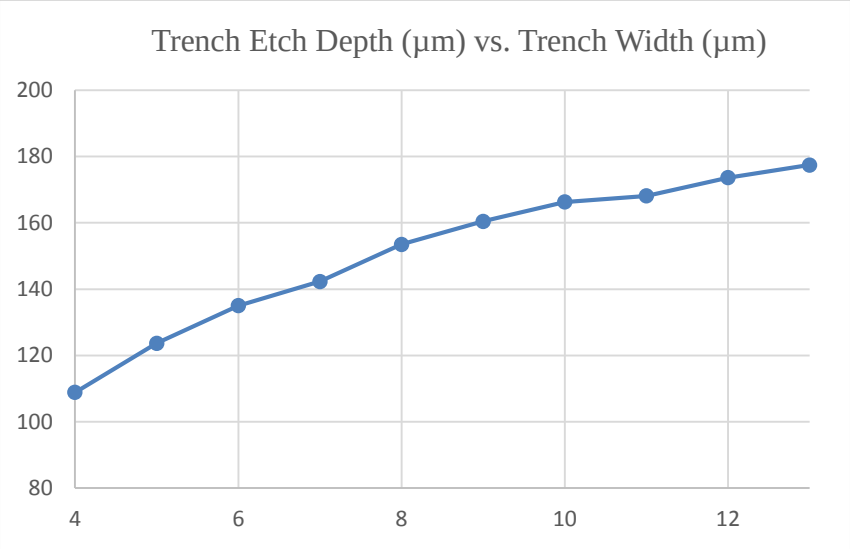

Figure 45. Trench etch depth vs. trench width.

Table 19: Etch depth for different trenches in test pattern

Trench Depth(µm)	**Trench Width(µm)**
109	4
124	5
135	6
142	7
153	8
160	9
166	10
168	11
174	12
177	13

It was also confirmed that the revised etch holes (corresponding test die was shown in Fig. 41) were etched more than 150 µm in this process. SEM pictures from the etch holes located in the center of the wafer is shown in Fig.46. The results were confirmed with SEM instrument (Zeiss, Inc.) and are shown in Figs. (47-49).

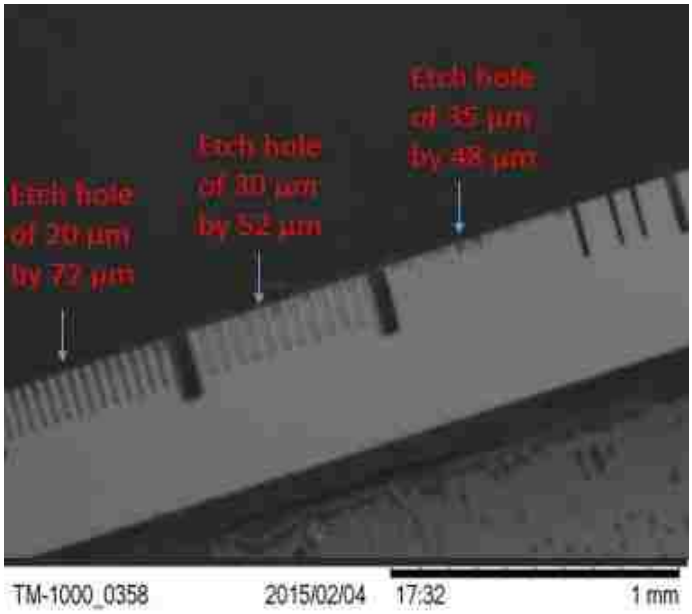

Figure 46. Three types of etch holes similar to the ones in the device structure are etched down more than 150 µm. The smallest etch hole which is 20 µm by 72 µm is etched more than 151 µm. This confirms the release of free standing structures for the revised design.

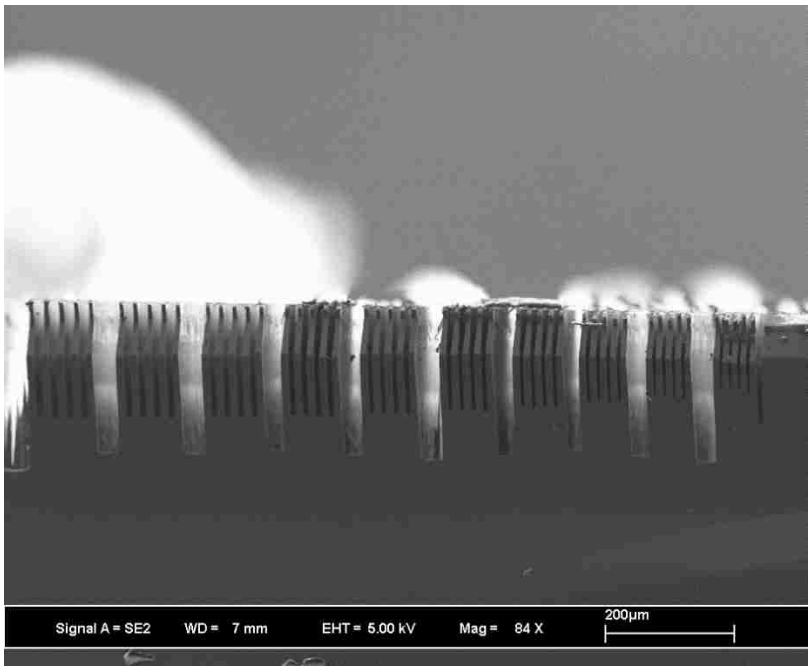

Figure 47. SEM picture of trench pattern in a test wafer etched at -10 C, 4 µm to 13 µm from right to left.

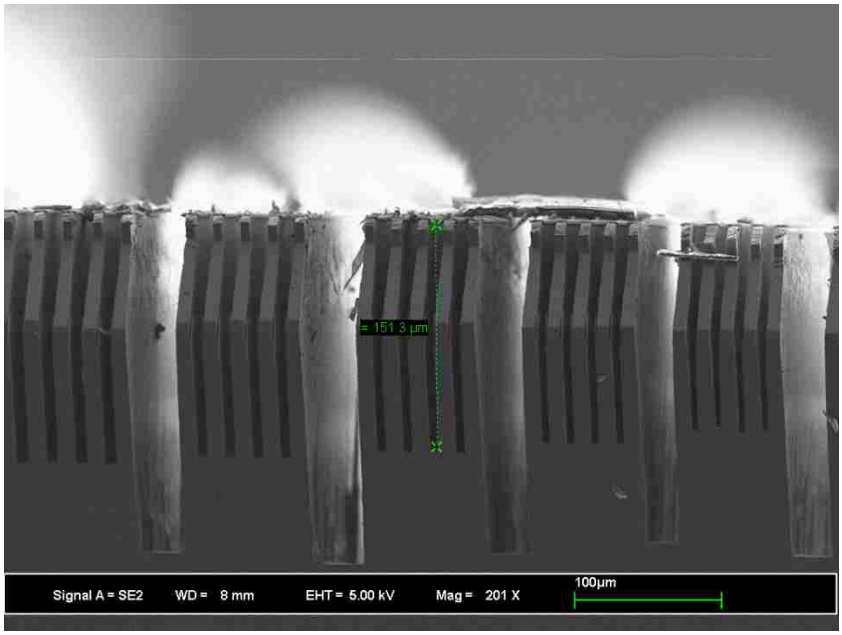

Figure 48. SEM picture showing etch depth of an 8µm-trench in a test wafer etched at -10 C.

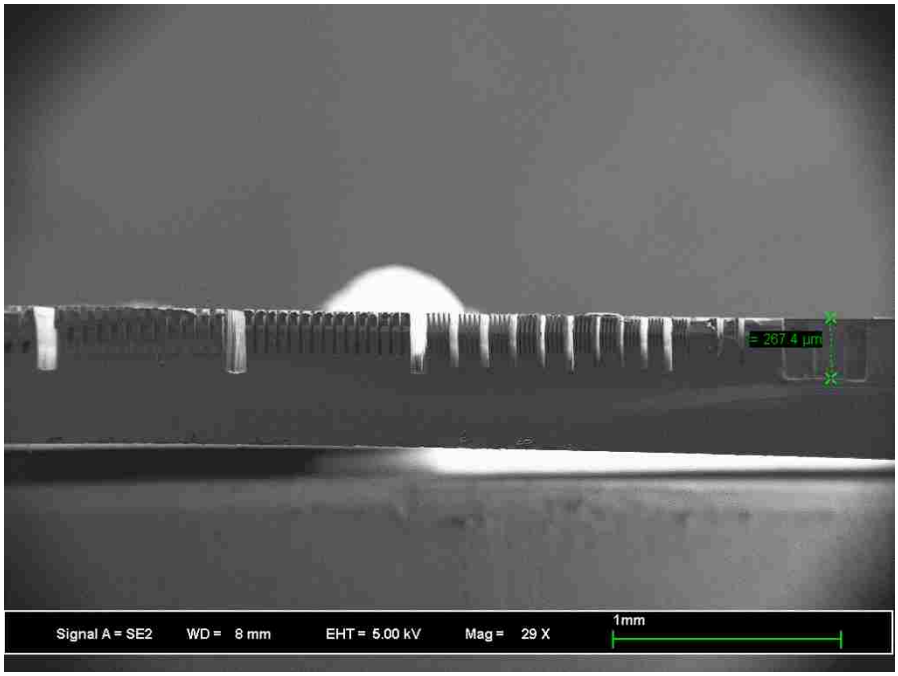

Figure 49. SEM picture showing the etch depth of wide area for a test wafer etched at -10 C.

Fabrication process for the device wafer was executed afterwards. After patterning metal layer with lift off, SPR 220 was patterned as a masking layer for DRIE. The first device wafer (SOI wafer) was then etched with the revised mask and recipe for 2 hours at -10 C.

The SEM pictures are given in the following figures. SEM images from different sites of the SOI wafer are shown in Figs. (50-55).

The test pattern in Fig.53 shows the 8-μm trench was etched down to oxide (depth of etch around 150 μm). In the zoomed-in photo (Fig. 54), some post-etch residue can be seen on the side walls of the patterned structure. Part of this residue is fluorocarbon residue possibly coming from the products of polymer deposition step (C4F8) of Bosch process. There is also silicon grass residue on top of the oxide (Fig.55). We tried to clean the polymer residue from the silicon test wafers by ashing and oxygen plasma cleaning and the results are given in the following section.

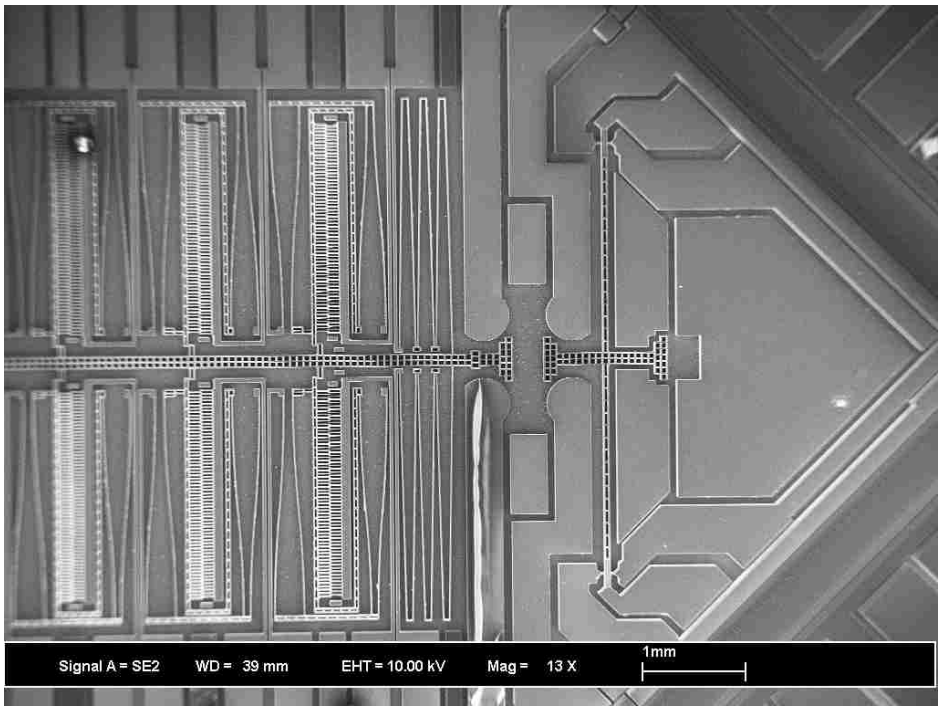

Figure 50. SEM image of SOI wafer etched for 2 hours at -10 C, 3 pair of comb actuators, DEP electrodes and force sensor are shown.

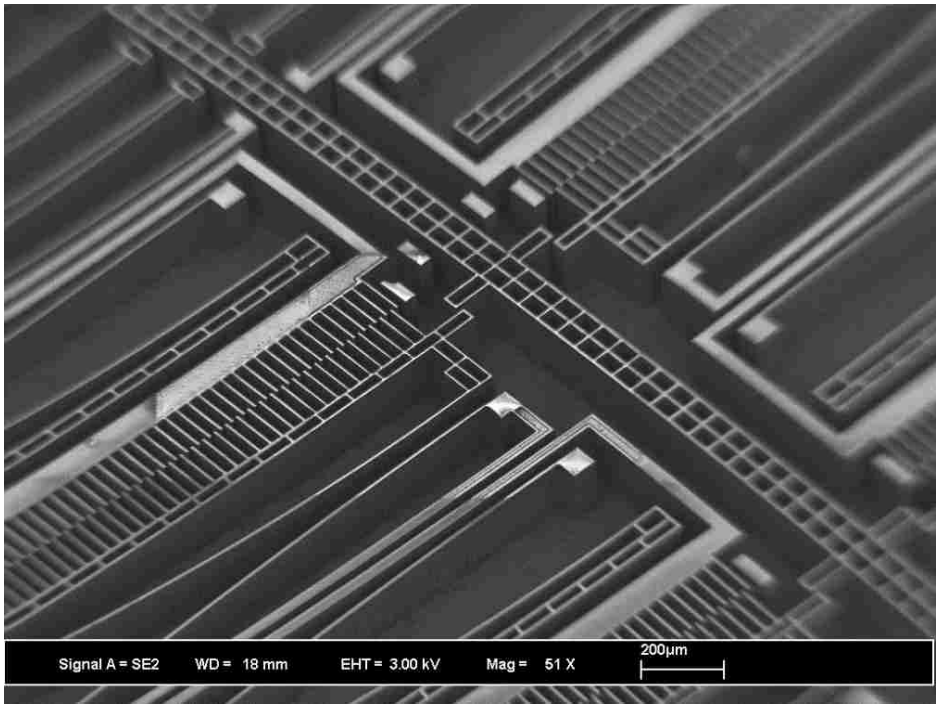

Figure 51. SEM image of SOI wafer etched for 2 hours at -10 C, actuator shuttle and comb drive actuators are shown.

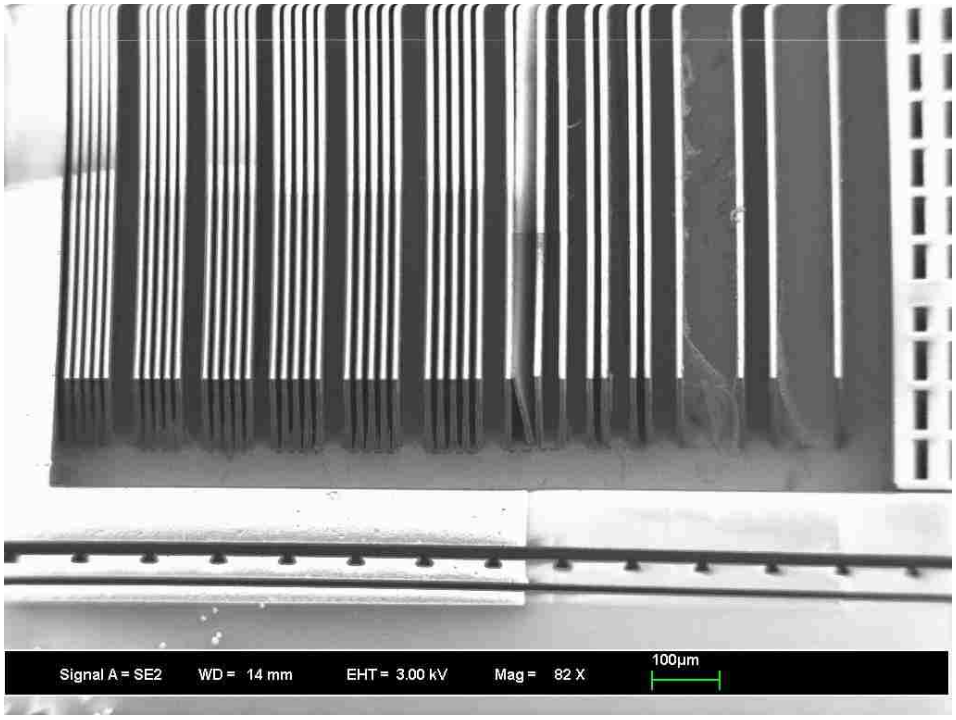

Figure 52. SEM image of SOI wafer etched for 2 hours at -10 C, trench pattern on the test die is shown, each five group of 10 µm features are spaced from 4 µm (left) to 13 µm (right). Over etching increases from left to right.

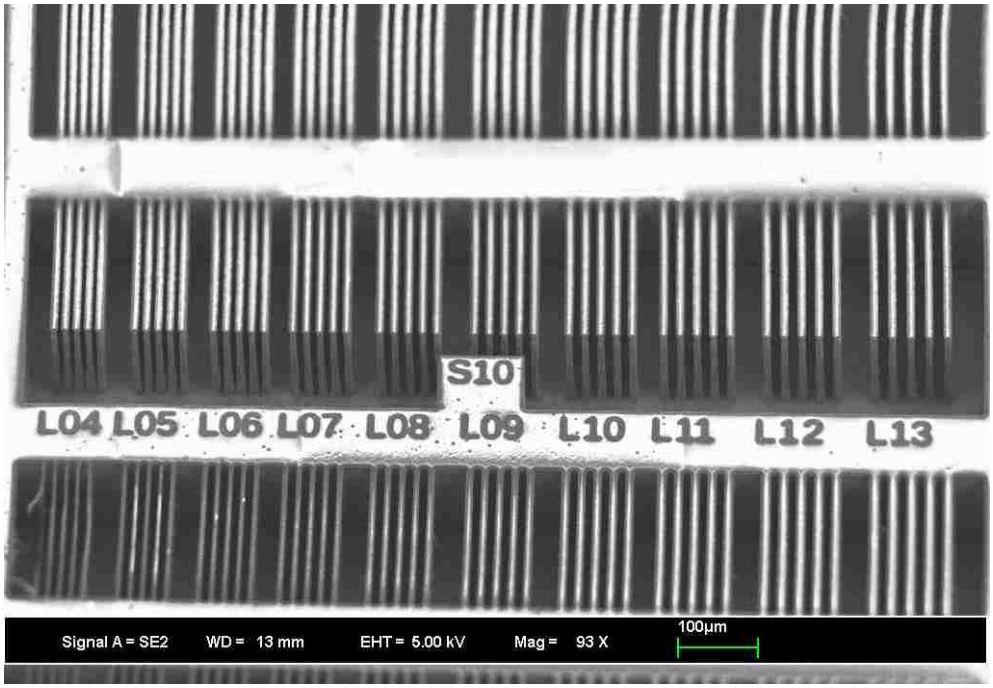

Figure 53. SEM image of SOI wafer etched for 2 hours at -10 C, line pattern is shown on the bottom and trench pattern is shown on the top.

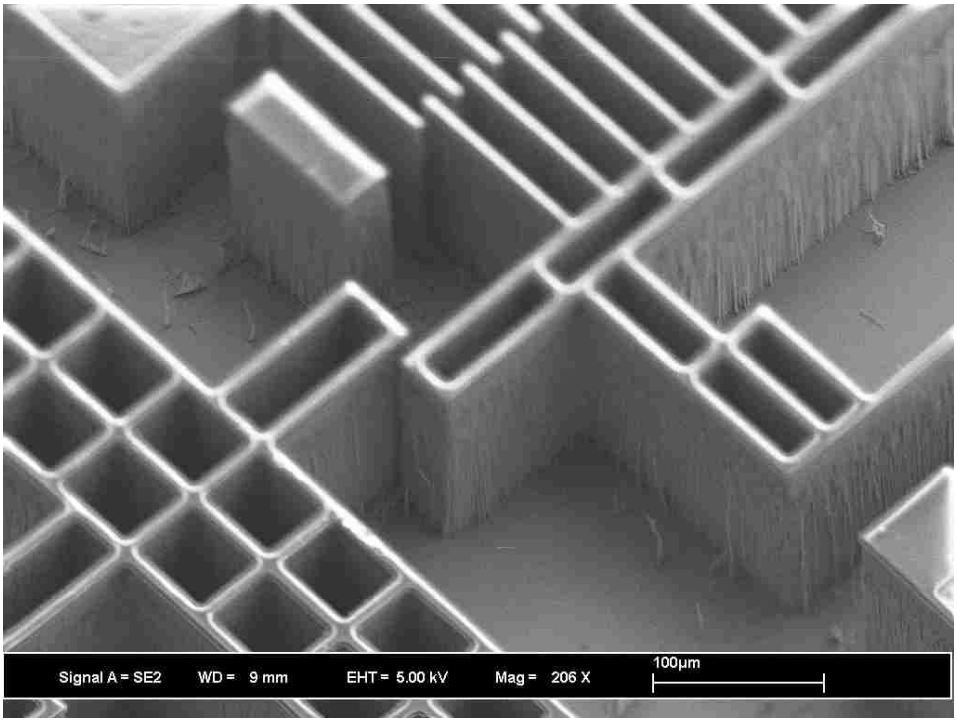

Figure 54. SEM image of SOI wafer etched for 2 hours at -10 C, zoomed in photo from the actuator area shows residue on the sidewalls.

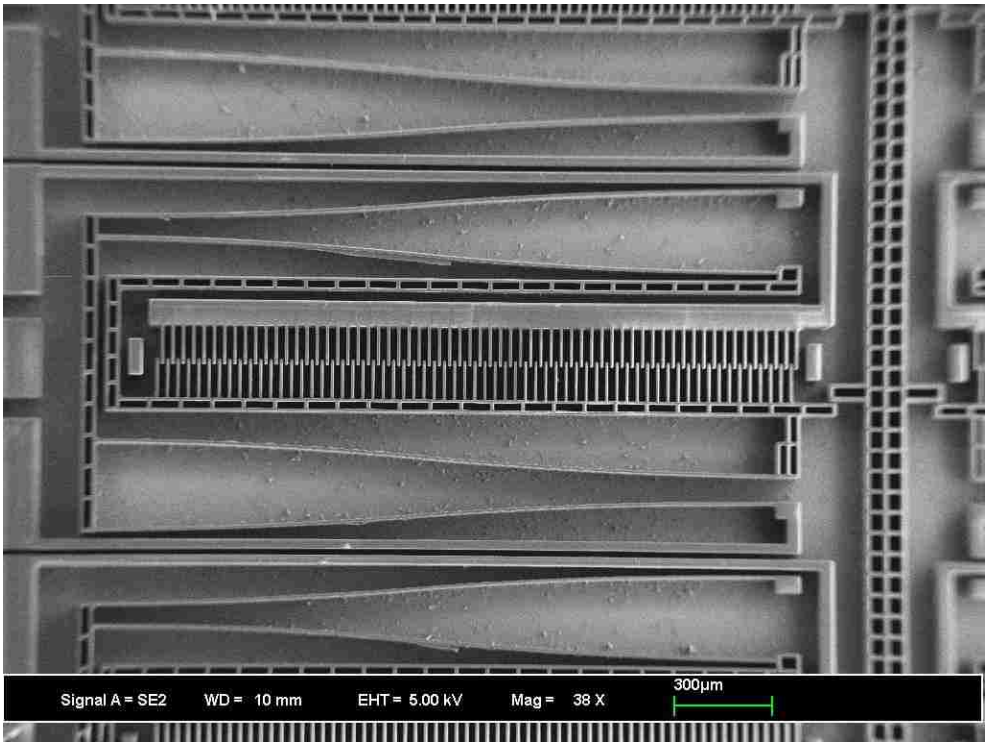

Figure 55. SEM image of SOI wafer etched for 2 hours at -10 C, dots on the surface of the wafer are silicon grass residue on oxide.

5.6. Developed DRIE recipe

The DRIE tool that was used was Alcatel Adixen AMS-100. The starting DRIE recipe was the following

1. Thermalization

Wafer Temperature: 10 C
Center He Pressure: 8 mbar

2. Temporization 30 sec

3. Process

Table 20: Starting DRIE recipe process parameters

	Flow (sccm)	Priority	Time (Sec)
SF6	200	2	2
C4F8	150	1	1

The flow of SF6 and C4F8 gases and duration of each gas are given in Table 20. Priority shows which gas enters the chamber first in each cycle.

Power/Pressure:

Source Generator (Inductively Coupled Power): 1500 W

Substrate Holder Bias, Low frequency (Pulsed): 80 W for 10 ms, 0 W for 90 ms

Center He Pressure: 8 mbar

Process Time: 5 min

The above recipe was used for creating 10 μm etch depth

The DRIE process steps used for etching 150 μm in all trenches with width equal or greater than 8 μm on Adixen AMS 100 (Alcatel) are the following. The etching time is relatively long for this process (two hours).

1. Thermalization

Wafer Temperature: - 10 C
Center He Pressure: 8 mbar

2. Temporization for 30 sec

3. Process

Table 21: DRIE recipe Process parameters

	Flow (sccm)	Priority	Time (Sec)
SF6	200	2	2
C4F8	100	1	1

Power/Pressure:

Source Generator (Inductively Coupled Power): 1500 W

Substrate Holder Bias, Low frequency (Pulsed): 80 W for 10 ms, 0 W for 90 ms

Center He Pressure: 8 mbar

Process Time: 2 hours

The above recipe was used for creating 150 μm etch depth in narrowest trench with 8 μm width

Differences between two recipes are given below**:**

- C4F8 flow was changed from 150 sccm to 100 sccm because of the flow meter limitation/malfunction at 150 sccm.
- Substrate temperature was changed from 10 C to -10 C to avoid RIE lag i.e. [67] to be able to etch faster in narrow trenches, also to increase etch rate selectivity of Si to photoresist i.e. photoresist tends to etch slower at -10 C compared to 10 C (details were mentioned in section 6.4).
- Process time increased from 5 minutes to 2 hours to increase the etch depth from 10 μm to 150 μm.

In the next section, we will talk about our method to remove a major part of the residue called silicon grass.

5.7. Silicon Grass

Needlelike surfaces produced in c-DRIE are referred to as silicon grass (See Fig. 56). Effect of different parameters in silicon grass formation are discussed in literature [68-71] and summarized here. Etching experiments that were done to remove the silicon grass are presented in the following section.

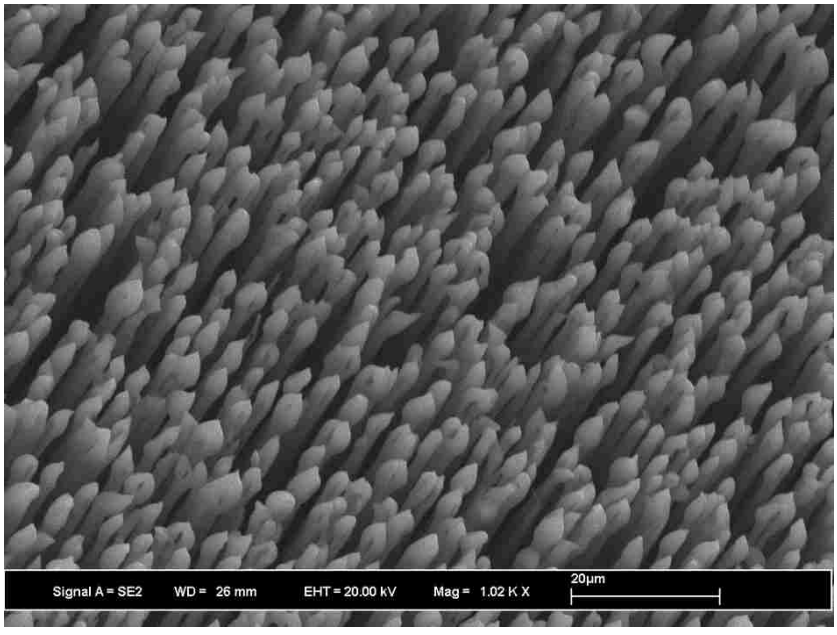

Figure 56. Silicon grass that looks like needle-shape silicon on our wafers is mostly formed at the bottom of the wide etched areas on the substrate.

What is the main reason for formation of silicon grass?

The main reason behind the formation of silicon grass is found to be micromasking effect, which is caused by the presence of micrometer-size foreign particles. In many cases, some undesired foreign particles used to be present on the wafer surface. These micrometer-size particles start acting like a mask and protect the silicon area (See Fig. 57). In almost all cases, this foreign material particle has a slower etching rate than silicon and hence, the surrounding silicon surface etches faster and the needle-shaped silicon structure starts growing. During passivation cycle, a thin coating of Teflon-like polymer keeps on depositing on this silicon grass structure, further reducing the etching rate of this grass structure.

What are the causes?

These foreign particles impurities may come from four possible sources: incompletely removed natural oxide on the silicon-wafer surface during the wafer cleaning process, involatile photoresist mask material, polymer deposited during the passivation step, and aluminum atoms caused by plasma sputtering on an aluminum clamping ring.

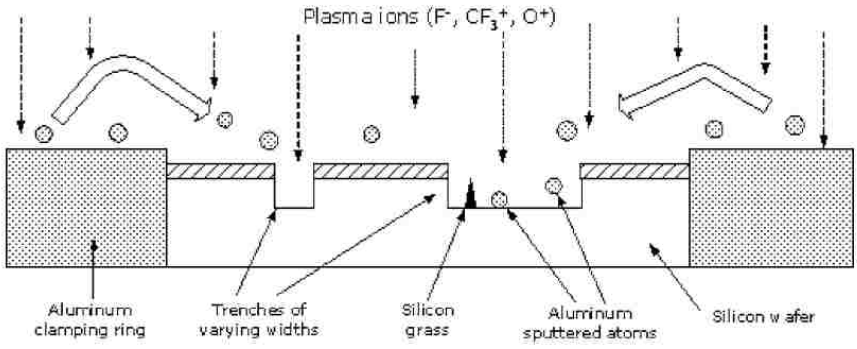

Figure 57. Schematic diagram showing an example of a micro-mask, i.e. aluminum atoms sputtered from clamping ring used to hold the wafer [91].

Main solutions to try?

1- Using ceramic ring instead of aluminum ring

2- Increasing SF6 flow time and therefore ratio of SF6 time to C4F8 time (ratio should not exceed a certain number to avoid grass formation, the recommended maximum ratio for etching to passivation time before is specified as 3) [69]
3- Increasing chuck power and duty cycle

What is the physics behind it?

1- The etching tool uses an aluminum clamping ring to provide the electrical contact to the silicon wafer. During DRIE operation, highly directed ions O+, CF3+, and neutral atoms are directed toward the substrate. Being a conductive metal, the aluminum ring is also polarized along with the wafer, and hence, these highly energized ions start bombarding the aluminum clamping ring. This continuous ion bombardment results in a minor sputtering process in which some aluminum atoms leave the clamping ring and redeposit on the wafer. These deposited micrometer-size aluminum atoms act as a micromasking layer and result in silicon grass formation.
2- Due to short etching period, bottom polymer layer is not completely etched away and the remaining polymer layer acts as a secondary mask and protects bottom silicon from etching. This results in long needle kind of silicon 'grass' structures
3- If the chuck power increases, the ion energy increases as well. Ion energy supplies directional kinetic energy to silicon wafer for etching. Therefore, as the chuck power increases, the amount of silicon grass decreases as expected.

Effect of chamber on silicon grass

A clean chamber will help creating less micro masks and therefore less silicon grass. There are methods that are typically used for cleaning chambers which two of them are the following.

1- The first method starts with performing a 1-hour oxygen plasma cleaning. If chunks of material remain, they have to be removed with a plastic wedge. After this step, the remaining material needs to be vacuumed out. Chamber needs to be cleaned with IPA followed by a half hour oxygen plasma cleaning.

2- The second method in addition to run the oxygen plasma cleaning, conditions the chamber by running the etching process with a dummy Si wafer for about 20 minutes. If the wafer comes out grassy, then another run of etch for 5-10 minutes is recommended. If it's still looking grassy, then it is recommended to modify the process parameters.

Chamber cleaning was performed and a DRIE test was done with the original recipe mentioned previously (C4F8 150 sccm, Temperature 10 C) on a test wafer for two hours after an oxygen plasma cleaning for chamber (200 sccm 15 min 2000 W,100 W pulsed) was performed.

Results of this test showed a lot of silicon grass, (Fig 58). The trenches were full of grass. This could be due to several factors including micromasking of aluminum particles released due to cleaning of the surface of aluminum ring inside the chamber or other organic particles released by IPA cleaning. In the following experiments, the process parameters were modified to remove the silicon grass.

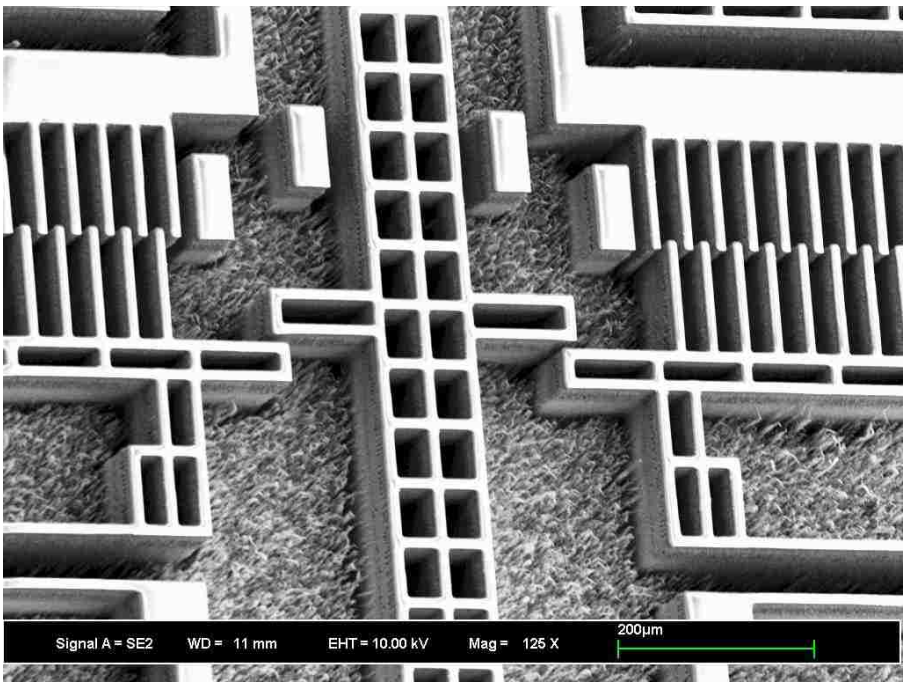

Figure 58. Result of etching after chamber cleaning, lots of silicon grass is present on the substrate.

5.8. Post Etch Residue and Cleaning Methods

Traditional residue removal methods typically are a combination of vapor and liquid processing. Vapor processing includes oxygen-reactive ion etching and oxygen ashing. Liquid chemistries include treatments in an aqueous sulfuric acid/hydrogen peroxide mixture, hydroxylamine, aqueous ozone with additives, and solvent-based solutions. Liquid solutions routinely require temperatures between 50 and 80°C for effective removal. Both dry etch and wet etch methods are recommended in literature. Dry methods such as oxygen plasma cleaning are less corrosive to the metals so they are examined first. However, there might be a need to try wet etching methods to remove the remaining residue. Piranha cleaning is one of the wet etch methods that could be tried, but because we have Cr as an adhesive layer for gold and there is an etch rate of > 16 nm/min for Cr, piranha can damage the metal layer in our structure.

In order to clean the residue, we have used oxygen ashing on Technics PE II-A plasma etching system. The power was set to 200 W and we have tried 10 minutes. After that step, sample was exposed to oxygen plasma cleaning at 250 W for 20 minutes in RIE system (high frequency 13.56 MHz).

Sidewalls of structure on the test wafer that were etched for 2 hours at -10 C are shown in Fig. 59, these images show the structure both before (left) and after (right) ashing and oxygen plasma cleaning were performed. (Note: these two processes are both done in plasma etching machine, with oxygen as a gas, but on different power levels and frequencies)

Color of metal structures (gold) covered with photoresist was visibly changed after this process which means that photoresist was partially removed from the metal layer and thus the sample. The SEM images (Figs.59.d and 59.e) show that the most of the residue including the delaminated fluorocarbon from sidewalls is removed after the oxygen plasma cleaning process.

The remaining silicon sidewall has vertical striations on the sidewalls that can be seen after oxygen plasma cleaning. There is a difference in the first ~ 20 μm of the sidewall that might be related to the high reflected power which is more than 50 % of the forward power in the

first few minutes. During rest of the etching time, the reflected power will decrease but it keeps overshooting sometimes to ~ 25 % of the forward power. (The forward power is 80 W).

As mentioned before, temperature was decreased from 10 C in original recipe to -10 C in current recipe to avoid the RIE lag. We have compared SEM images from two tests previously done at -10 C and 10 C to investigate if there is a correlation between temperature and residue.

SEM images of a test wafer previously etched at 10 C for 72 mins is also shown (Fig.60.a and 60. d). We have noticed that SEM images of previously etched samples both at 10 C and -10 C look cleaner on the sidewalls than current samples. This suggests temperature might not be the reason for the residue because we did not observe it in our earlier experiments with either of the temperatures. That led us to believe that we have to clean the etching chamber, because that might be part of the reason for the residue buildup.

SEM images of a silicon test wafer before cleaning, etching time = 2hrs at -10 C, the etch depth is measured to be 267 μm in wide areas.	SEM images of a silicon test wafer after cleaning, ashing at 200 W 10 mins + Oxygen plasma cleaning at 250 W 15 mins
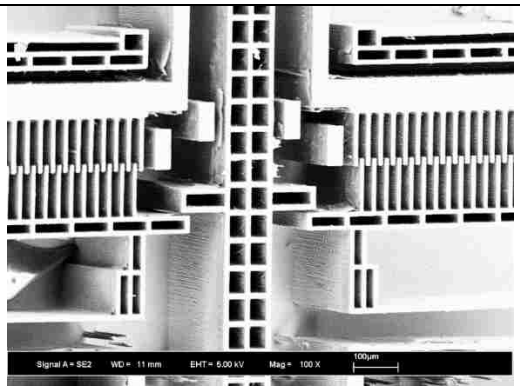	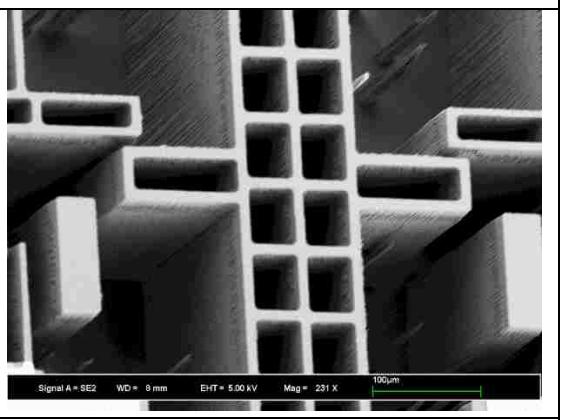
(a)	(d)
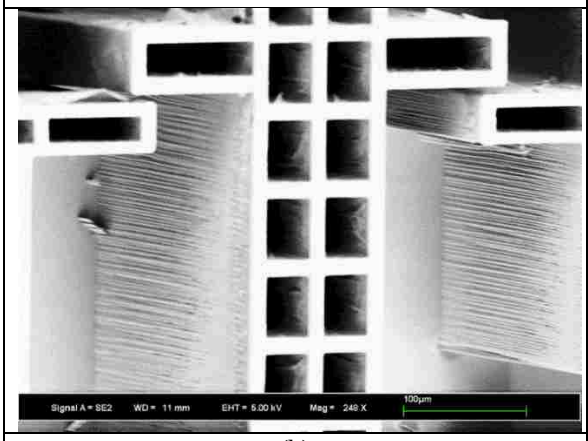	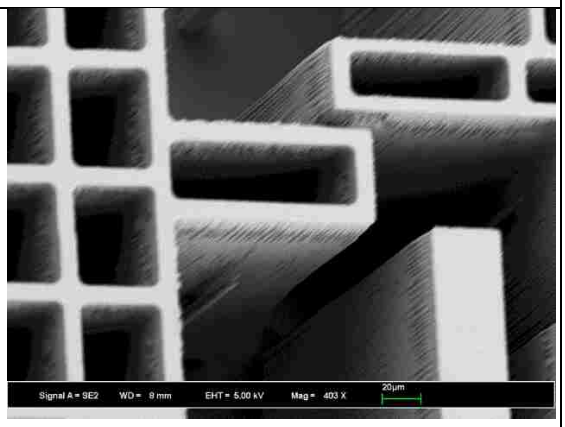
(b)	(e)
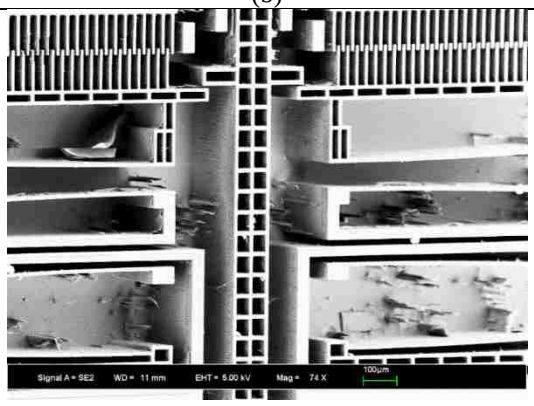	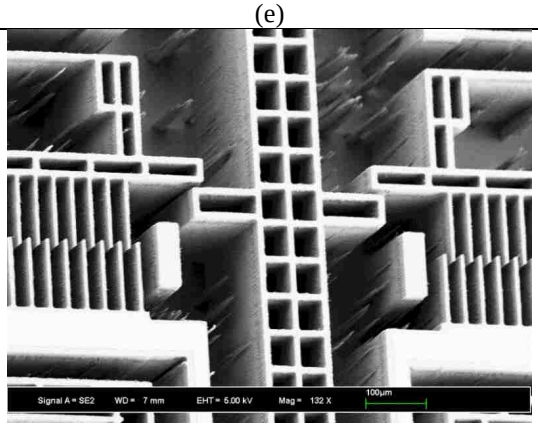
(c)	(f)

Figure 59. SEM images of sample before cleaning (a) delaminated residue on the sidewalls (b) delaminated residue and horizontal lines on sidewalls can be seen (c) silicon grass is seen on the surface, SEM images of sample after oxygen plasma cleaning (d) delaminated residue on sidewalls is almost gone (e) delaminated residue on sidewalls is almost gone, horizontal marks on sidewalls are more visible (f) silicon grass is still seen on the surface.

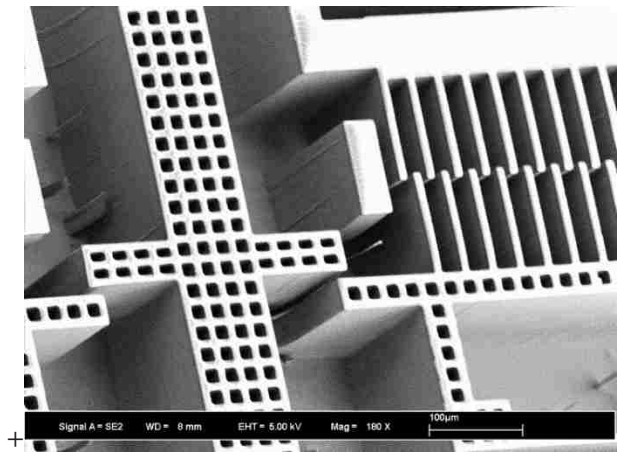

(a)

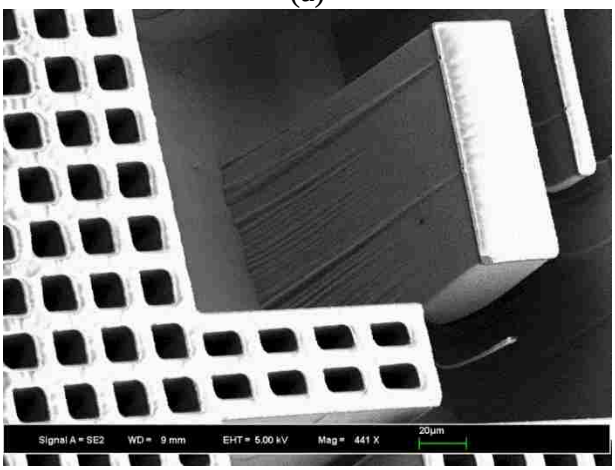

(b)

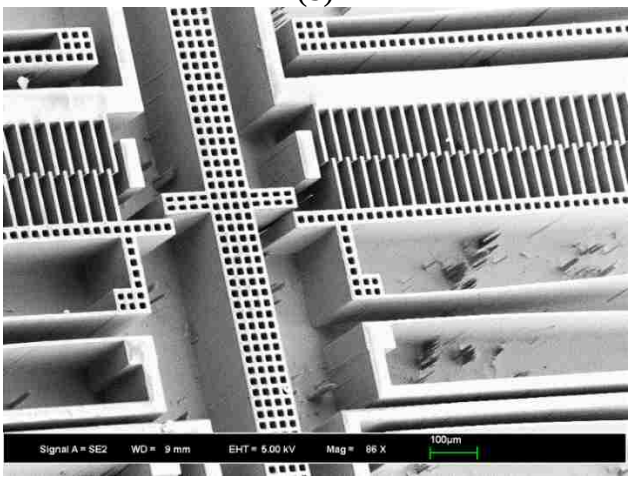

(c)

Figure 60. SEM images of test wafer previously etched at 10 C, Etch time = 72 mins. (a) actuator area shows no residue (b) zoomed in photo of anchor (c) silicon grass in wide areas near the actuator.

In order to confirm whether the temperature is the reason for creating the residue we have performed an etching test with current situation of etching system on a silicon test wafer at 10 C for 1.7 hrs. while the rest of the parameters of DRIE recipe kept the same. After the test, we could still see some residue on the sidewalls and grass on the surface therefore residue was not due to temperature.

In order to clean the remaining residue, another oxygen plasma cleaning experiment was done for a sample that was etched 2 hours at -10 C. An increased power of 300 W was used for 20 minutes (after 10 minutes of ashing at 200 W) in order to remove the residue. The SEM images showing the comparison before and after the oxygen plasma cleaning are given in Fig.61. The final determined conditions for oxygen plasma cleaning are given in Table 22.

Table 22: Conditions for oxygen plasma cleaning.

Gas	Flow	Power	Time	Frequency
Oxygen	20 sccm	300 W	20 min	13.56 MHz

SOI Wafer after Oxygen Plasma Cleaning

In order to clean the sidewalls, an oxygen plasma cleaning procedure that was confirmed on the test wafers was performed on the SOI wafer. The result is shown in Figs. 62 and 63.

Some of the fluorocarbon residue on sidewalls has been cleared using ashing and oxygen plasma cleaning methods. However, there is still some residue left. A liquid cleaning step might remove the rest but considering we have chromium on the structure, acidic liquids might also attack the metal. For removing some of the silicon grass, buffered HF might be a way but might cause stiction for movable parts. The summary of the residue cleaning methods that were tried are given in the following section.

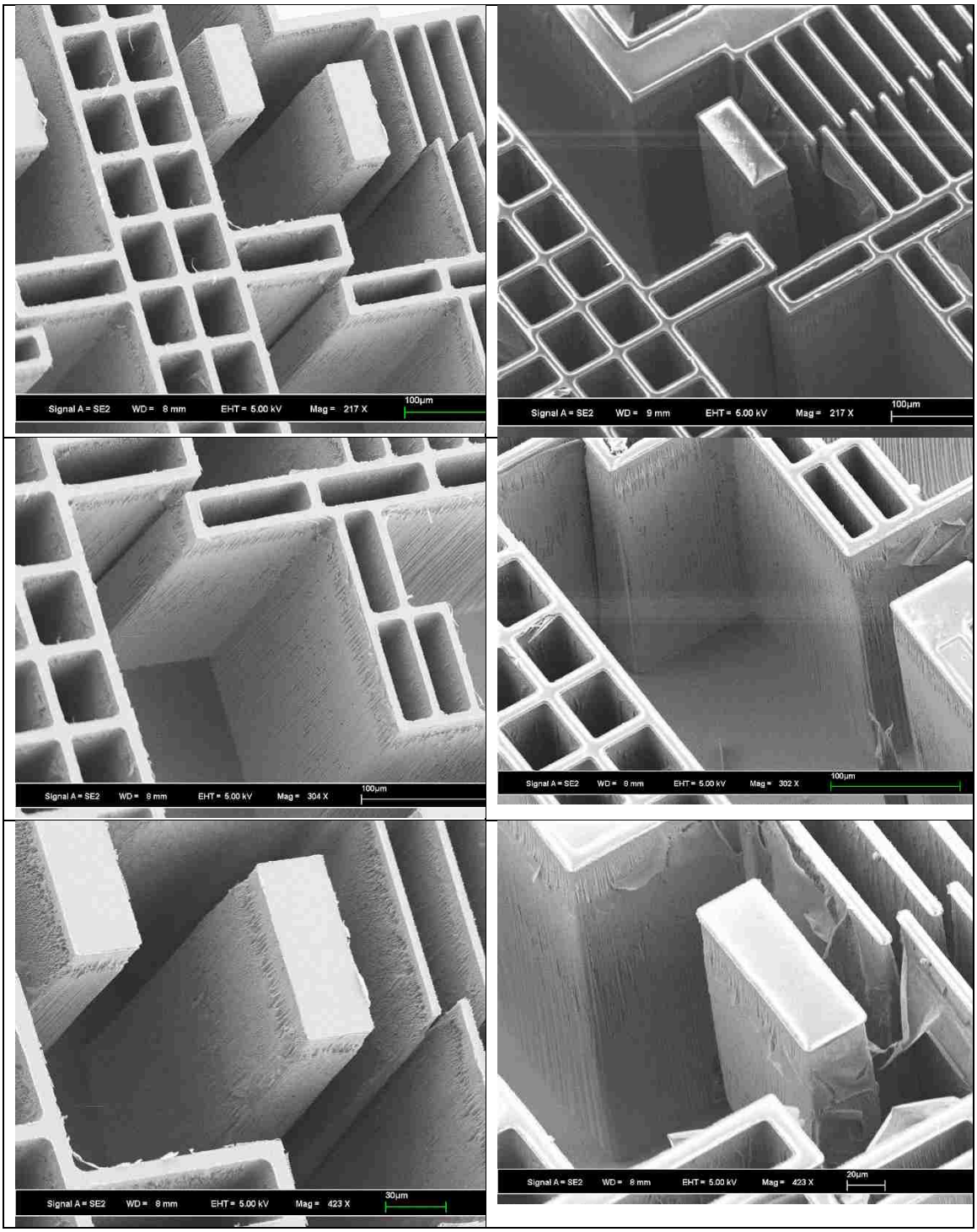

Figure 61. SEM images of a sample that was etched 2 hours at -10 C before (column on the right) and after cleaning (column on the left) are shown.

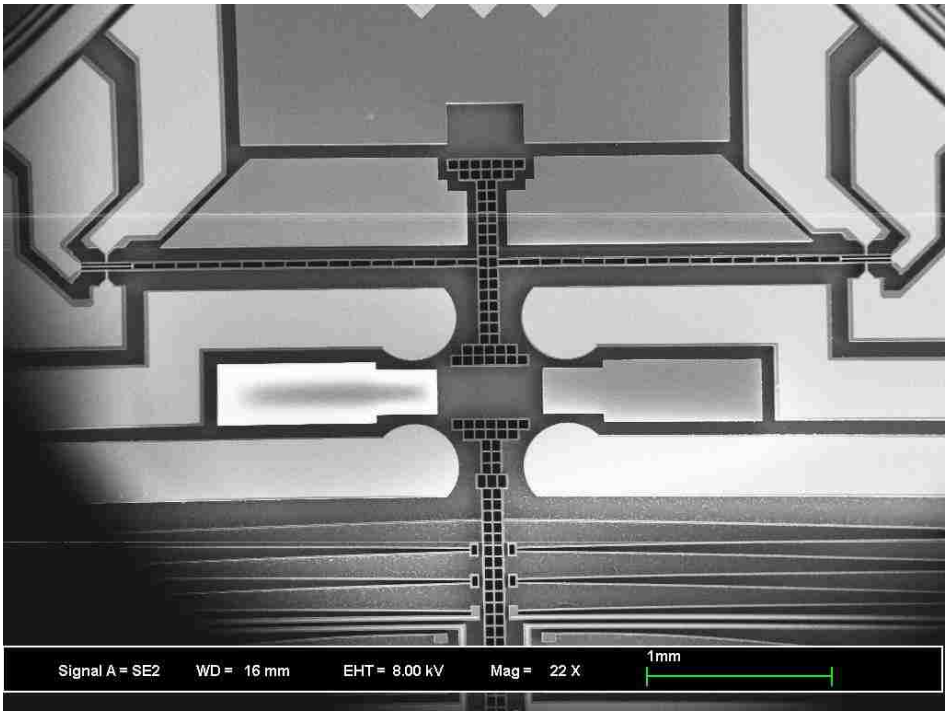

Figure 62. SOI wafer after oxygen plasma cleaning, some of the residue has been cleared.

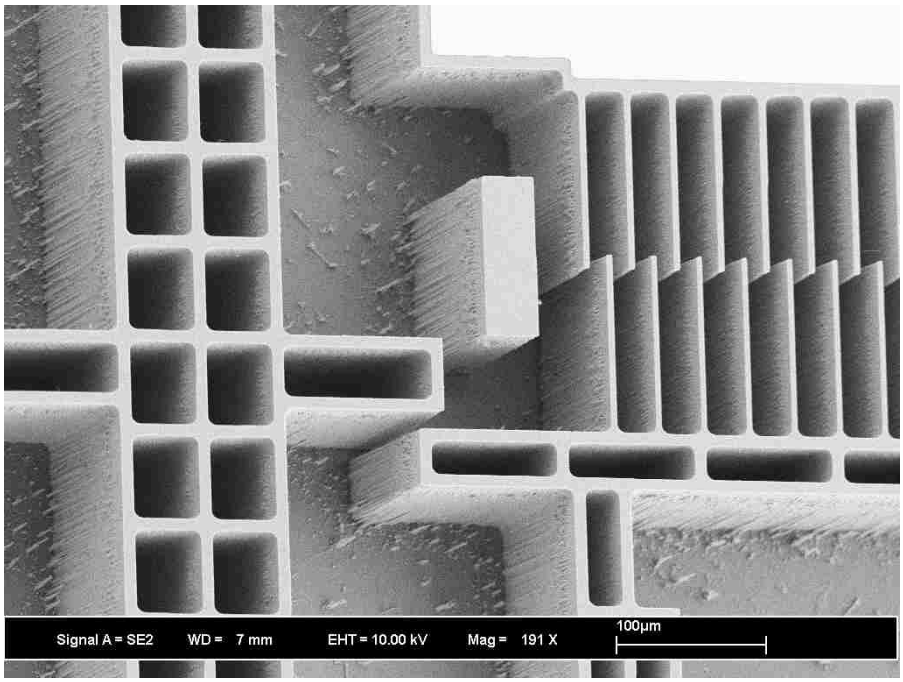

Figure 63. Some residue is still seen on the sidewalls, they might be fluorocarbon materials generated in passivation cycles.

DRIE tests performed to investigate how to clean the structure

A few DRIE tests was done in order to investigate cleaning of the structure after deep etching. They are listed in the following

1- Test with higher temperature for substrate 10 C Instead of -10 C

Characterization result: same residue and silicon grass

2- Test after chamber cleaning

Characterization result: a lot of silicon grass

3- Test with original recipe, i.e. 150 sccm of C4F8 instead of 100 sccm and temperature 10 C

Characterization result: Very low etch rate and therefore not applicable

Liquid Cleaning Methods

For removing silicon residue, there are some wet etching methods such as HNA (acetic, nitric, hydrofluoric mixture) which are not suitable in our case because they attack chromium or oxide. Chromium was used as an adhesion layer for gold, titanium was used in the previous generations and caused delamination of metal layer in release step.[14] Piranha cleaning is another method which is again not suitable in our case because it also attacks chromium.

In order to remove the effect of the etching tool on the results, we have run etching experiments with other DRIE tools in University of North Carolina (UNC) and University of Michigan (UMICH). Comparison between different deep reactive ion etching that was done at Lehigh, UNC and UMICH are given in the following section.

The first recipe that was tried at Lehigh is DRIE recipe 1 with the following details.

DRIE recipe 1:

SF6: 200 sccm, 2 second

C4F8: 150 sccm, 1 second

Temperature: -10 C

Time: 2 hours

In order to decrease the silicon grass, flow of SF6 gas was increased to 3 seconds as opposed to 2 seconds in the previous recipe while the C4F8 gas flow remained 1 second. The result of experiment show silicon grass was almost removed. The reason could be that the longer time of etching will etch the bottom polymer away and does not allow the polymer particles to act as micro masks. According to the SEM pictures such as Fig. 64, silicon grass density was reduced to a great extent.

DRIE recipe 2 parameters are given below.

SF6: 200 sccm, 3 second

C4F8: 100 sccm, 1 second

Temperate: -10 C

Time: 1 hour

Result of etching with DRIE recipe 2 is given in the Fig. 64.

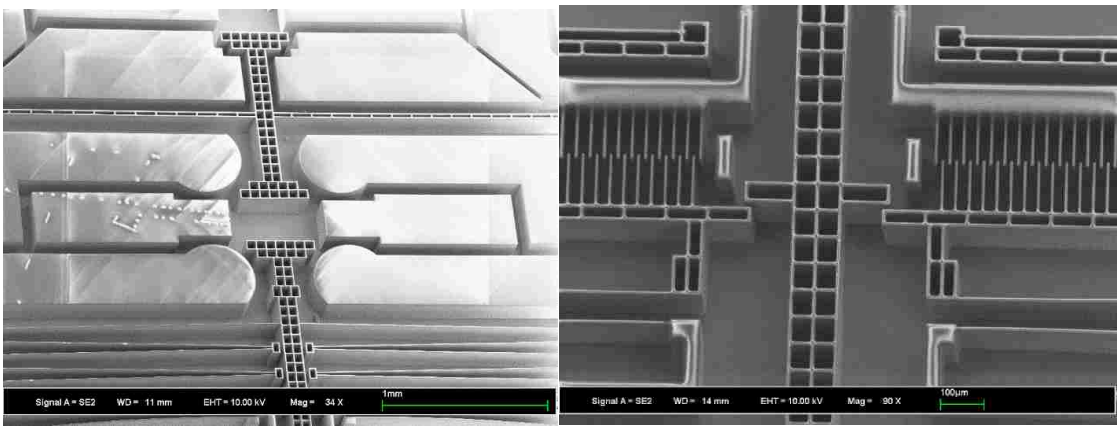

Figure 64. SEM images showing little or no grass

Depth of etch in wide areas vs 8-µm trench can be calculated according to the measurements (see Fig. 65). In order to have more accurate measurements, the wafer was cleaved later along the trenches to find out the depth of the etch.

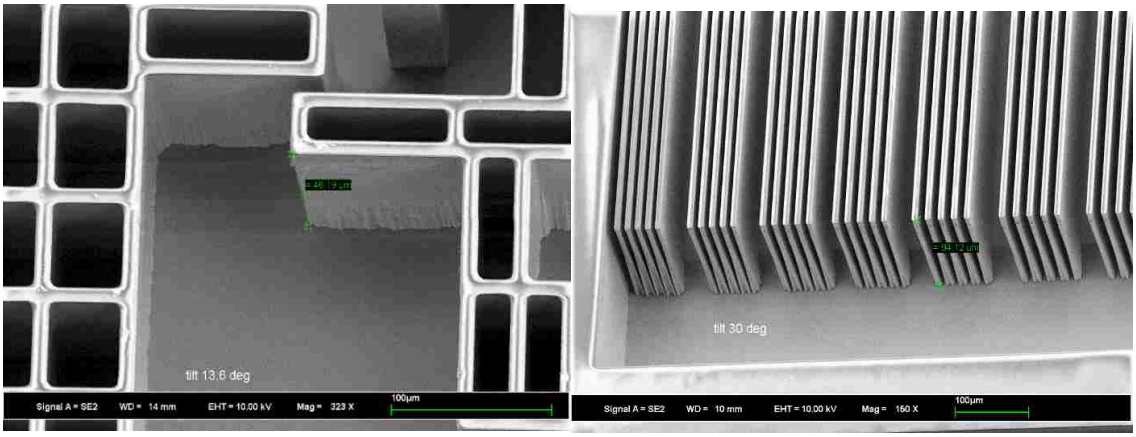

Figure 65. SEM images indicating depth of etch for wide areas 46.19/ sin (13.6) = 196.43 µm (left) and depth of etch for 8-µm trench is 94.12/ sin (30) = 188.24 µm (right)

DRIE etching was performed previously with a similar tool in University of North Carolina and results are given in Fig. 66. The main problem with this etch was that the process etched all the resist in the center of the wafer leaving the silicon exposed to ion bombardment. A very thick layer of photoresist creates photolithography non-uniformities and large dimension errors and therefore it was avoided.

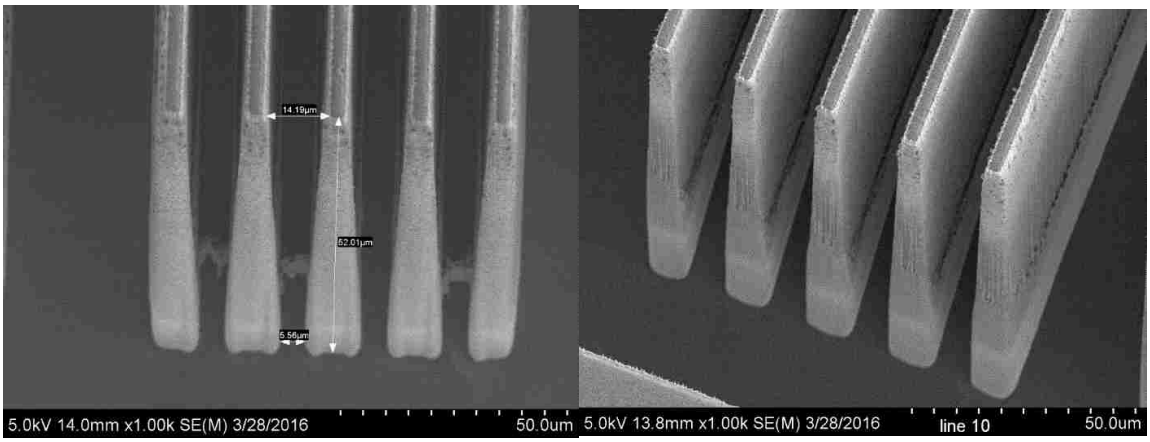

Figure 66. Depth of etch = 52/ sin (tilt angle=17deg) = 177 µm, Sidewall angle= Arctan {177µm/ {(14.19-5.56)/2= 4.315 µm}} = 88.6 degrees (left), the resist is etched away in some areas of the wafer (right).

The DRIE results from University Michigan looks good in terms of sidewall angle and sidewall roughness but there is some residue between the trenches. If the residue that exists

in narrow trenches is conductive, the fingers of comb drive might have been shorted out this way.

The DRIE recipe in this case is creating the minimum undercut and better uniformity for different size features. It consists of a quick Ar descum, 20 min of etching to get straight sidewall with ramping the etch rates, 20 minutes with another step with different etch rates to maintain straight sidewalls.

The following are the etch rates of different features in this recipe:

2μm feature is 3μm/min

10μm feature is 4.5μm/min

100μm feature is 5.6μm/min

Undercut about 180nm

After DRIE, oxygen plasma cleaning and XeF2 treatment was performed to remove the residue. SEM images indicate the residue is still present as can be seen in Fig. 67.

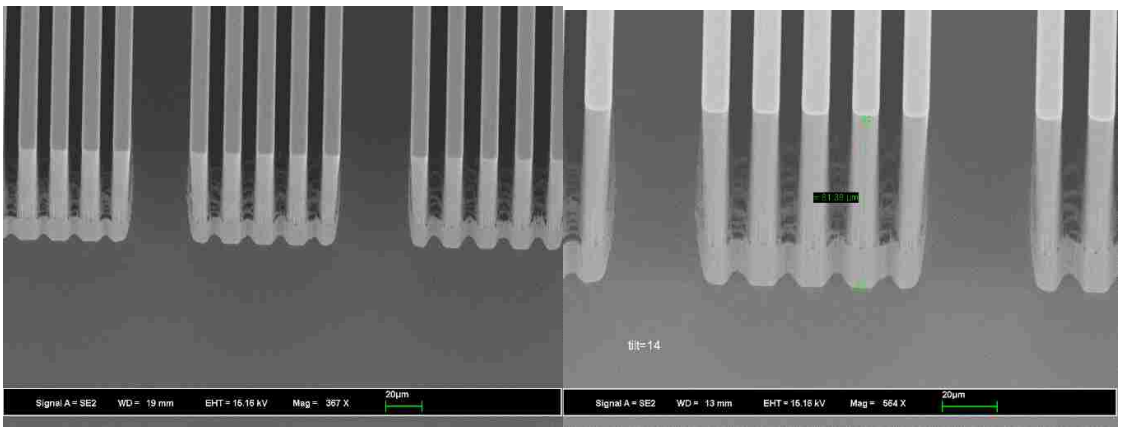

Figure 67. SEM image of 7 μm, 8 μm and 9 μm trenches on the test pattern. The residue exists in between these narrow trenches (left), depth of etch is 61.38/ sin (14) = 253.71 μm (right).

EDS experiments was utilized to characterize the residue, the top of the feature and in between the trenches were examined. The result for the characterization of the top of the feature shows the material is mostly silicon and also a bit of carbon is present. On the area between the trenches with more residue, the amount of carbon is more in spectrum (Fig. 68).

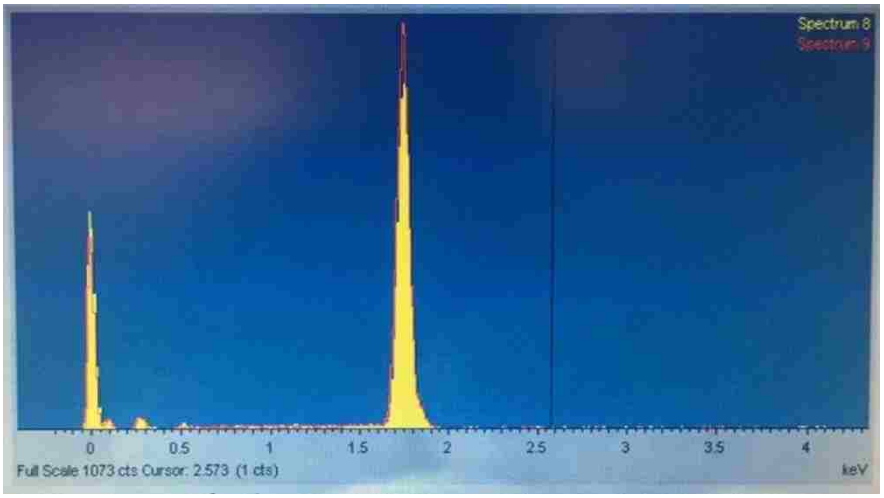

(a)

Figure 68. X-ray characterization to identify elements in residue. (a) Comparison of spectrums. Spectrum 8 was showing more carbon and less silicon that spectrum 9. Spectrum 8 was from the residue and spectrum 9 was from the top of the feature.

The etched wafer with the new DRIE recipe that removed the silicon grass was cleaved on the trench test pattern area to measure the depth of etch for the minimum feature size i.e. 8 µm trench. SEM was done at 90-degree tilt and SEM images indicated the depth is about 118 µm for the 8 µm trenches as indicated in the Figs. 69 and 70. Two areas of the wafer were measured and are in good agreement.

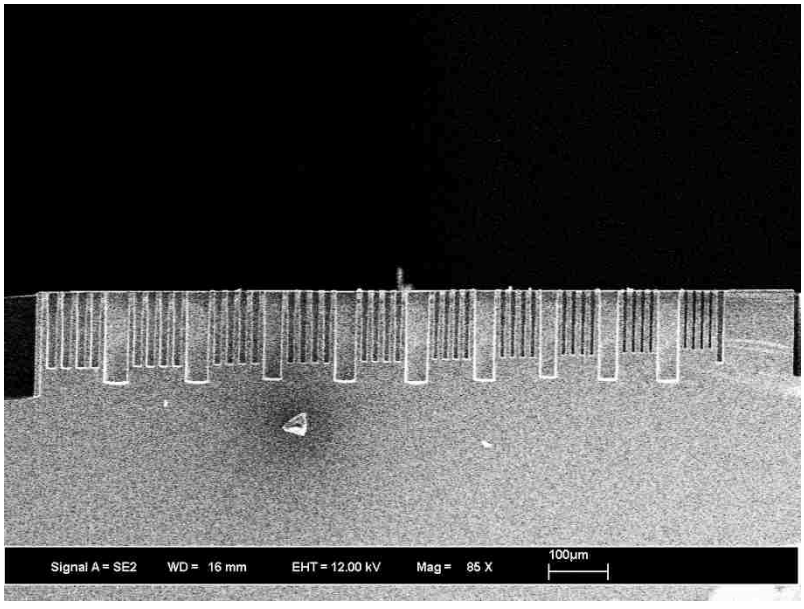

Figure 69. Trench pattern showing 13 µm to 4 µm trenches from left to right.

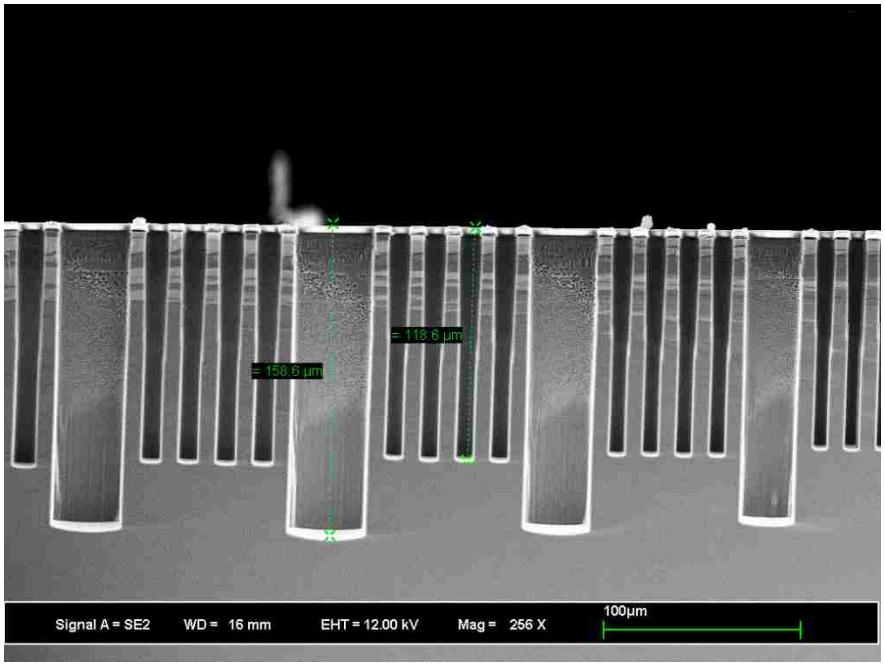

Figure 70. SEM image showing 7 µm, 8 µm and 9µm trenches. 8 µm trench is etched 118 µm and therefore more etching time is required

Photoresist thickness was measured to be 4.6 µm on the edge of the wafer Measurement was also done using profilometer on the edge and center of the wafer. Following calculations indicates that the time of the test needs to be increased at least 16 minutes and the maximum possible increase time according to the photoresist etch rate is 23 minutes considering half a micron margin for the resist left to cover the device.

Additional etching depth:150 -118 = 32 µm left

Photoresist thickness in the center = 3.5 µm and edge= 4.5 µm

Average resist etch rate = 11.5 - 3.5 µm / 60 min= 0.133 µm/min

Resist extra holding time = (3.5 µm- 0.5 µm)/0.133= 23 min

Average silicon etch rate = 1.97 µm/min Minimum etch time = 1 h+ 32/1.97 = 1 h 16 min

Estimation of depth of etch in 23 min:

Max etch rate ~1.2 * 1.97 = 2.364 µm/min => 2.364*23= 54 µm

Min etch rate ~ 0.8 * 1.97 = 1.576 µm/min => 1.576* 23= 36 µm

These calculations show the extra 23 minutes should be enough to reach the desired depth.

5.9. Releasing the device

In fabrication of the previous generation of BioMEMS, the release step was performed by a manual vapor HF method. The etching is done on a beaker of liquid HF while back of the wafer is heated by a lamp [14]. The method was very slow and it took 3 to 4 hours to release the structure. In this fabrication process, we have utilized a vapor HF process that is more accurate and controllable and at the same time faster and safer approach for device release.

Because of the previous long etching step, the oxide underneath the device layer was attacked during etching and created undercut that is called DRIE footing. The amount of DRIE footing is maximum in the center of the wafer because of the maximum etch rate in this area. Measurements before releasing the free standing structure was done in order to find out the minimum width and maximum width of structure to be released (Fig. 71). Also the minimum width of the anchor was measured to make sure etching will not release the over-etched anchors (Fig. 72).

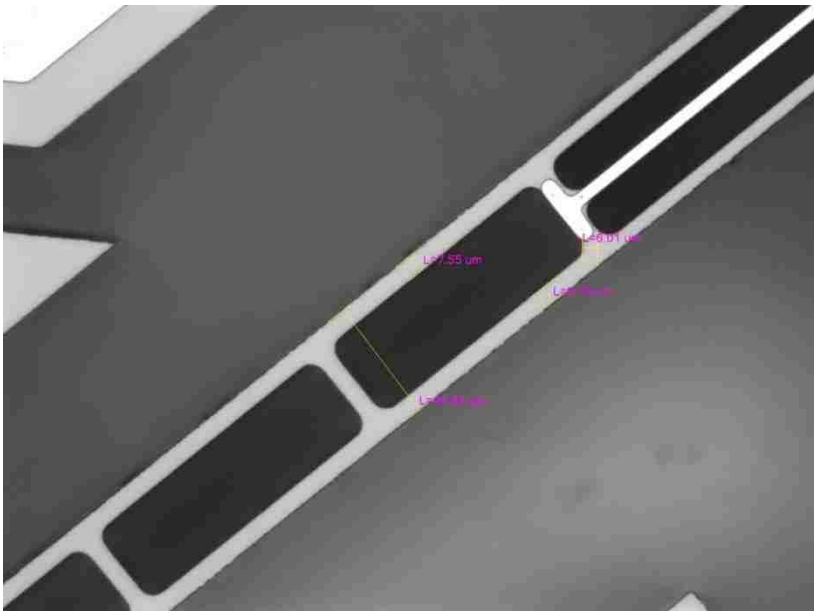

Figure 71. Measurements of force sensor beam and cantilevers. Beams appear to be over-etched specially on top of the structure.

Measurements show over etching of beams during etching. For instance, beam with design width of 12 µm is measured to be 8.2 µm. Considering over-etching measurements and an estimate of undercut, an initial etching time of 40 minutes was calculated.

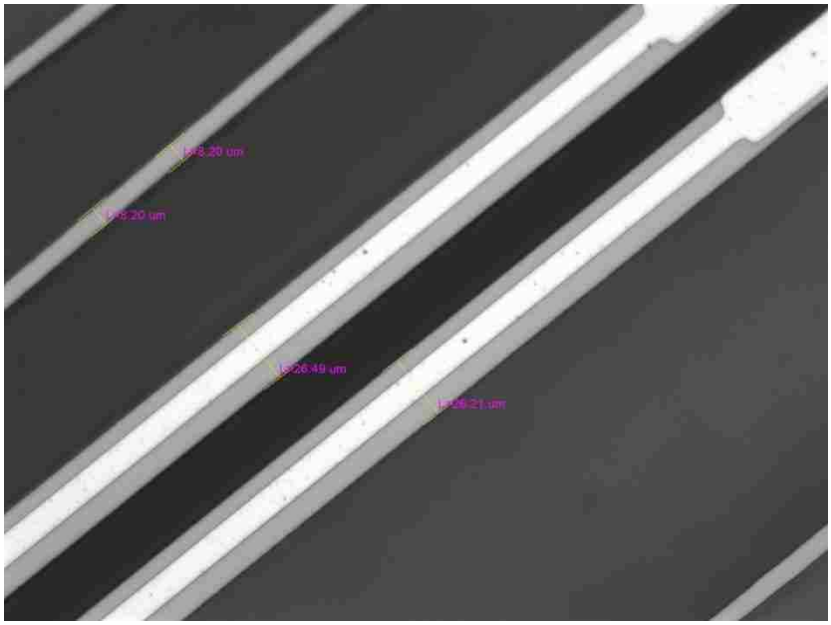

Figure 72.The maximum beam width to be released is measured. Also the width of the narrowest anchor that should not be released is measured. These two measurements determined the minimum and the maximum etching time.

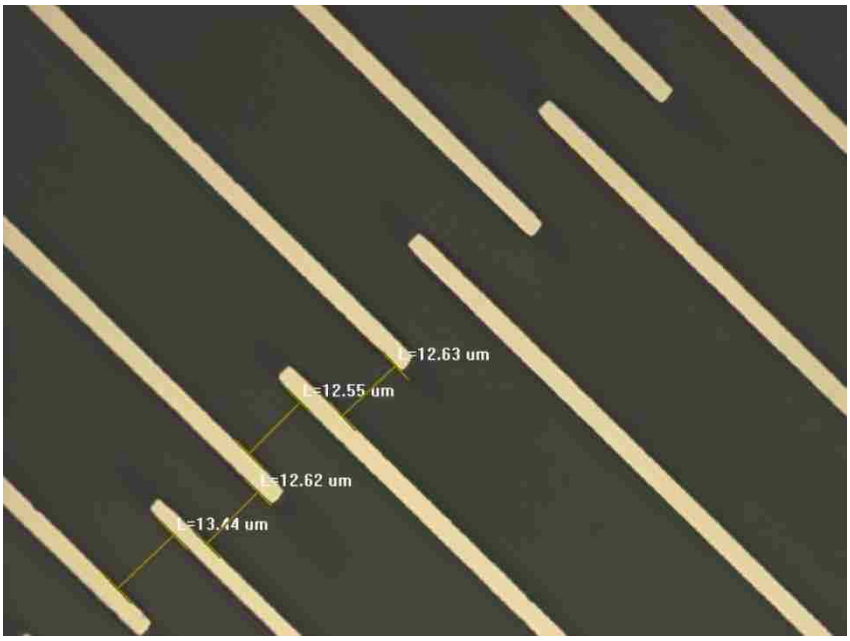

Figure 73. Measurements of finger spacing before release. The movable comb may move slightly after release and this could be an indication of release.

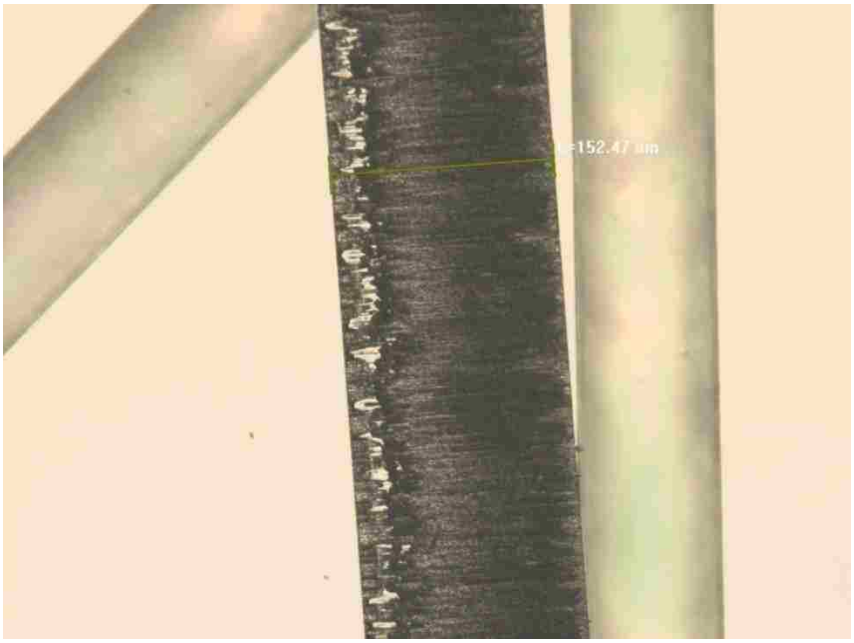

Figure 74. Sidewall of a broken beam which is released and lying flat on top of silicon substrate, the beam height is around 152 μm.

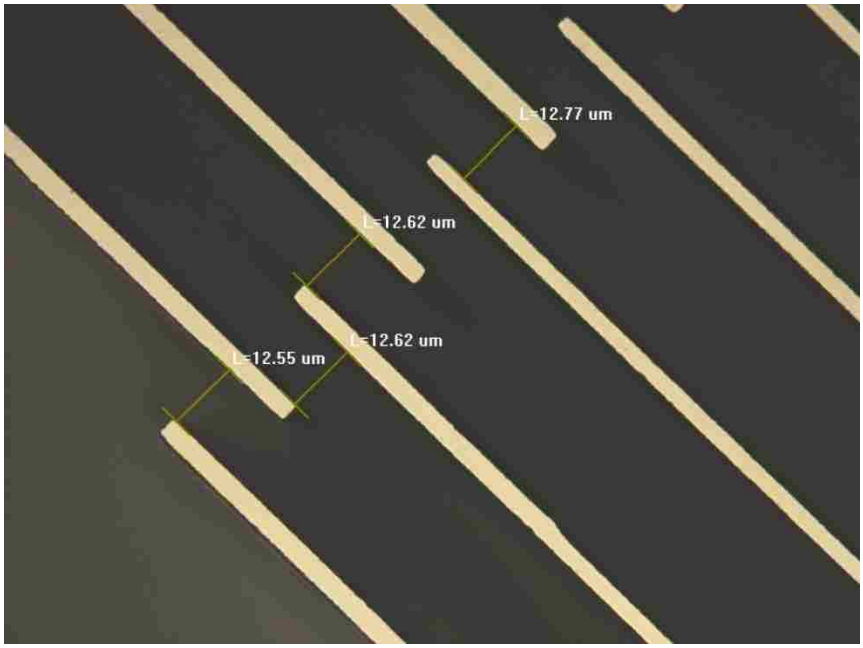

Figure 75. Measurements of the spacing between comb fingers after 40 minutes of etching. It does not show much difference; therefore, it is probably not released.

SiO2 was etched with the etch rate of 1000 A per minute in uEtch vapor HF tool (SPTS Technologies). After this step, some of the detached silicon grass was observed on the silicon surface. The silicon grass was observed to be increasing radially towards the edge of the wafer.

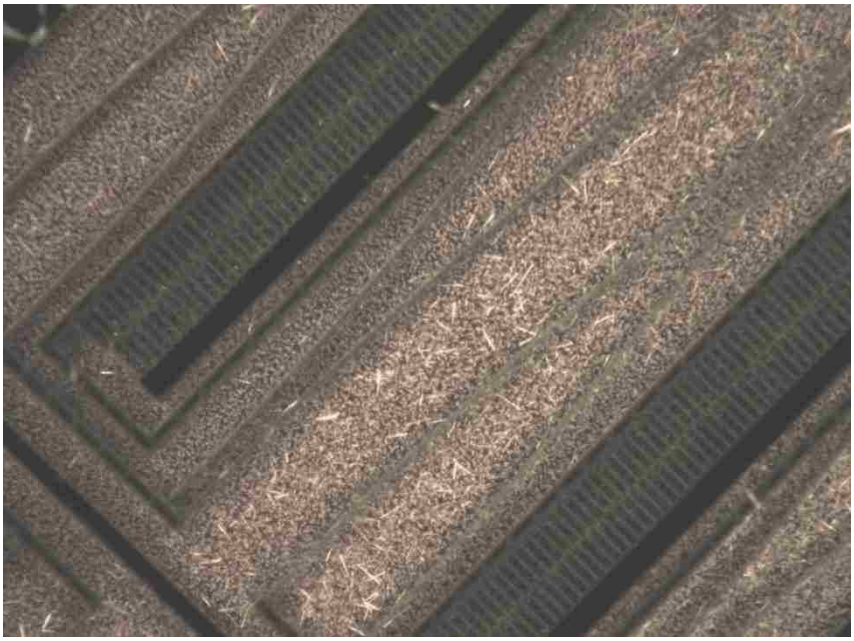

Figure 76. Released silicon grass is shown at the bottom of the structure near the edge (dark field image).

In order to verify the absence or presence of the underlying oxide layer, infrared technology is normally used. However, because of the thickness of this structure (150 μm), the conventional infrared test to monitor the presence of oxide underneath the structure was not possible. After inspection under the microscope, a tape test was done in order to find out if the structure is released. A small piece of tape was used to remove part of a dummy die. Some parts of the structure such as force sensor or actuator beam were fully released and removed with tape (See Figs. 77-80). The bright spots seen on the back of the structure are indicating the areas that were actually released. These areas are making less than one-third of the total free standing beam; the rest of the beam was detached from oxide in the DRIE step because of footing.

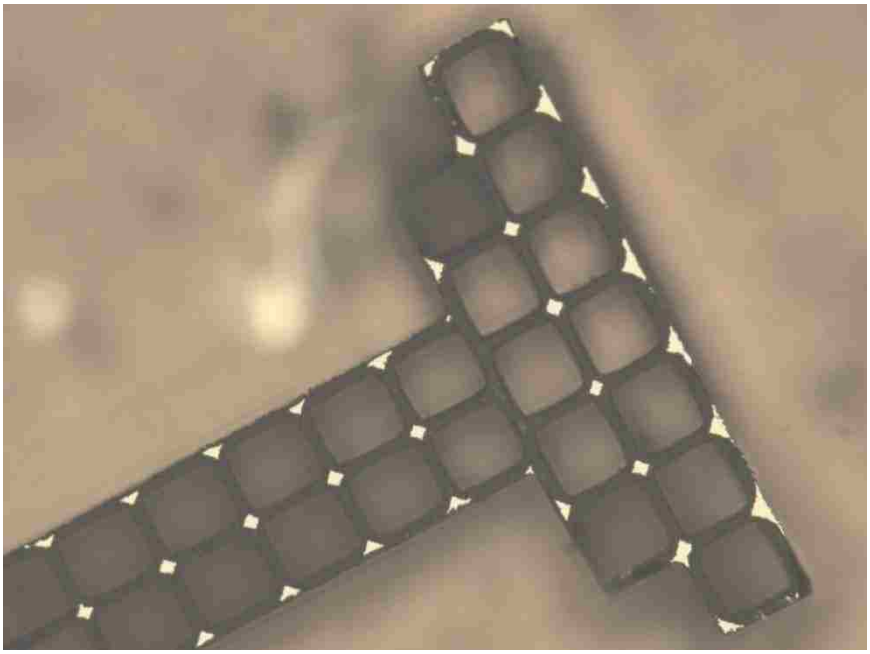

Figure 77. The bottom of the force sensor attached to the tape is shown here. The bright area was the only part that was released by VHF while the darker area was undercut during DRIE step.

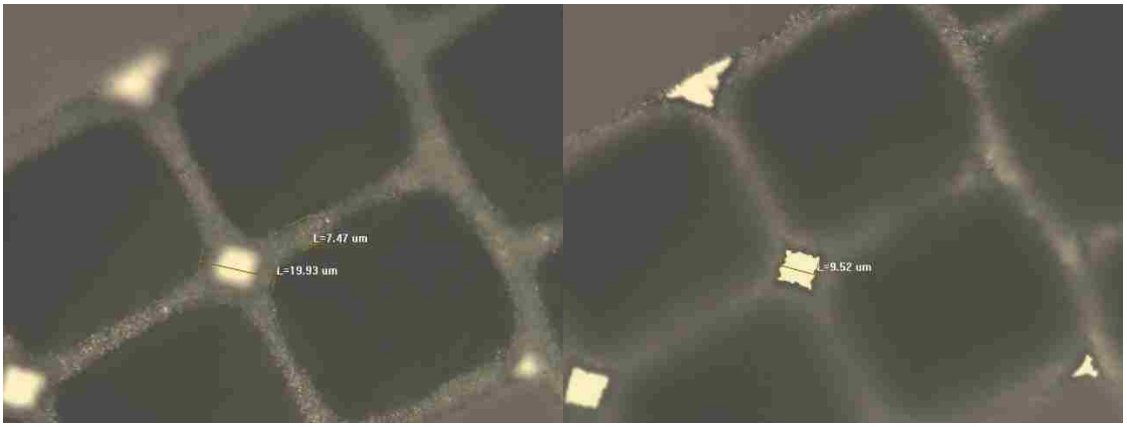

Figure 78. Tape test confirming release of the actuator shuttle, the bottom of the shuttle removed with tape is shown, the total area that would have been etched was around 20 μm (left picture) but almost half of it is already detached by DRIE footing.

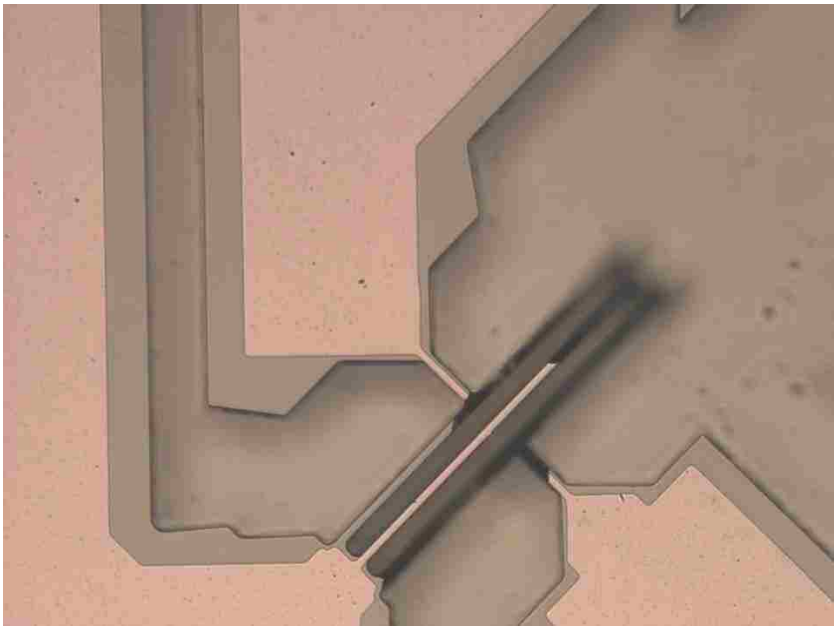

Figure 79. Tape test showing force sensor is not fully released and could not be removed by tape in the transducer area after 50 mins of VHF. Therefore, more time was added in the next step.

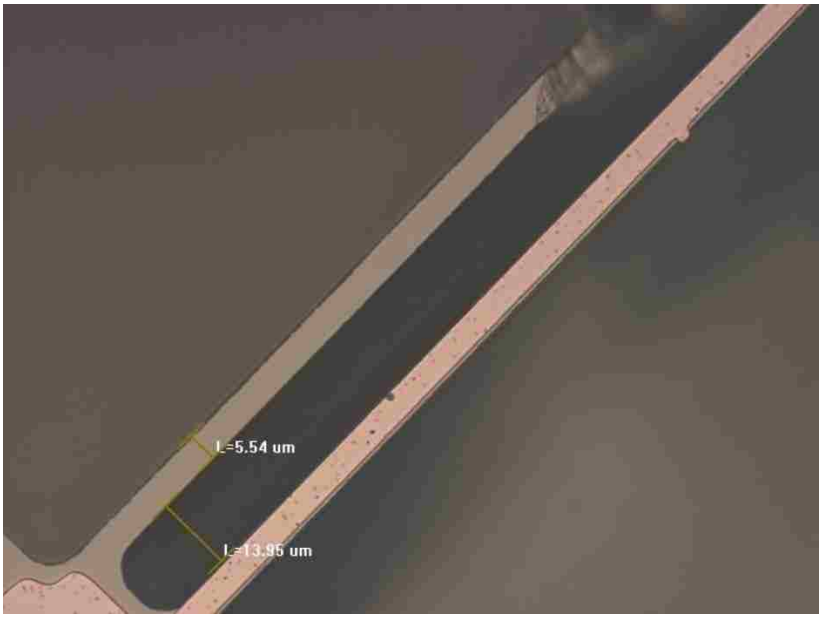

Figure 80. The narrowest trench in the structure is located on the force sensor transducer area. This results in the minimum undercut in this area which requires more etching time.

However, some areas such as transducers were not fully released in some areas because they could not be fully detached from oxide. Therefore, 10 more minutes of etching was

added in uEtch etching tool. At this point, broken comb drives was seen to be displaced and finger spacing were not symmetric anymore (Fig. 81).

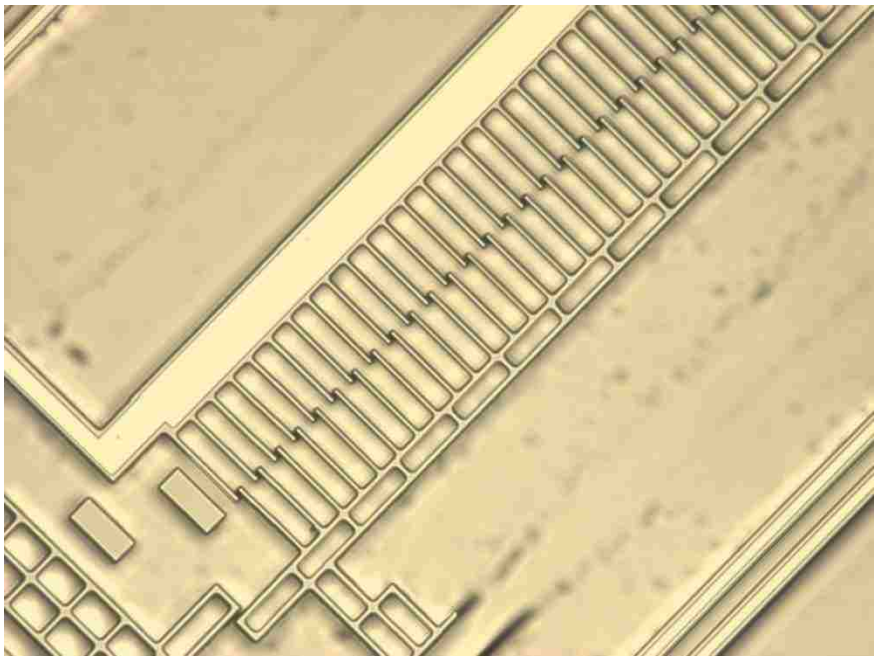

Figure 81.The movable comb that was not attached to anchor is relocated after release. The change in finger spacing is even visible with eyes indicating the release of this structure.

A probe test was done afterwards to confirm the structure is fully released. The test includes applying a little force on the probe tip to the force sensor plunger and observing movement of four transducers (Fig. 82). The beam bending test was recorded in a video. Analyzing the recorded video shows no bending in the area of the transducer which was close to the anchors, which means they were not released (Fig. 83).

In the next step, 15 more minutes of Vapor HF was added. The release of free standing structures was examined under probe station. A probe tip was used and by micromanipulator, lateral force was applied to the force sensor. The transducer area is the last part of the structure to release because of the minimum undercut in this area. The minimum undercut happens in transducer area because of the presence of the minimum trench size in this area of the free standing beam. Therefore, the release of this part indicates the completion of releasing step.

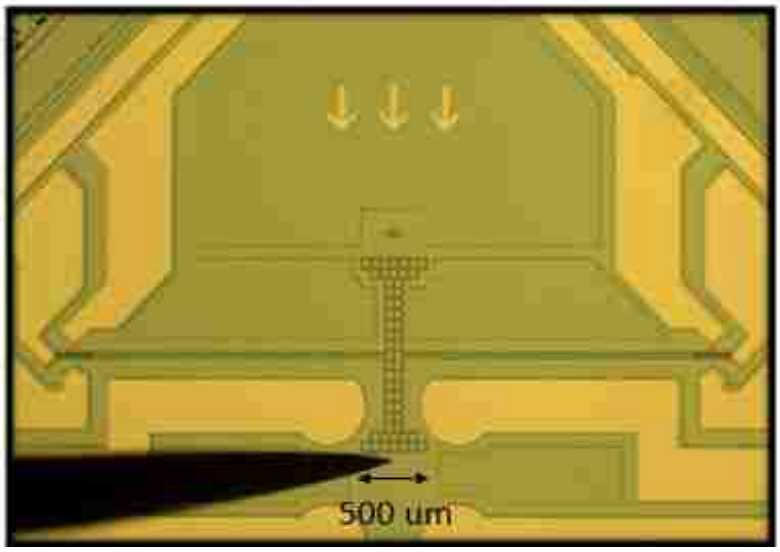

Figure 82. Release test on probe station is shown, free standing force sensor is being poked by a probe.

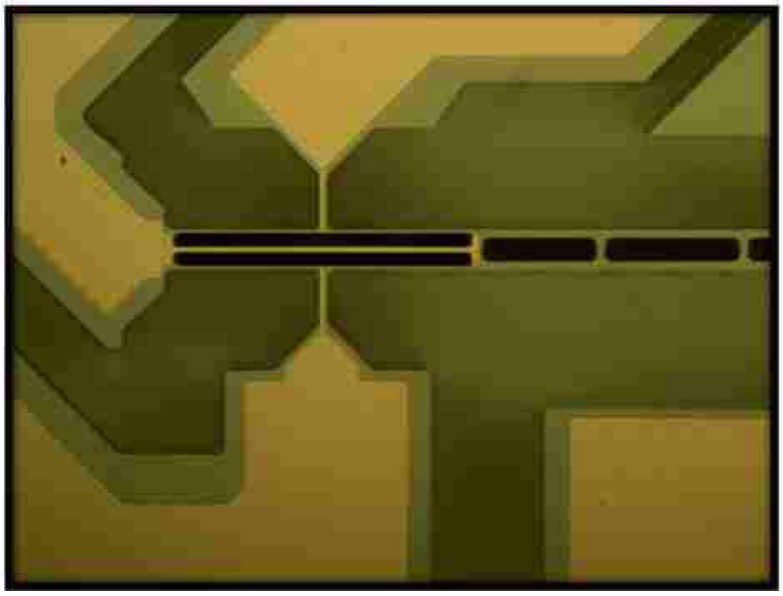

Figure 83. Force sensor transducers have the minimum trench size i.e. average of 10 μm, this area will be the last area to release in the free standing structure and therefore videos were taken from this area while poking at the tip of the sensor.

5.10. Inspection Results

Dies were examined for grass, crack or broken beams and are listed in color coded Table 23. Green dies have silicon grass and red dies have actuators with one or few broken beams. There are 36 functional dies on this wafer.

Table 23: Inspection results for SOI1 after release for 65 minutes in vapor HF showing color coded dies with silicon grass (green) and dies with one or more broken beams (red). Letter g indicates grassy, c indicated cracked areas and b indicates broken.

		T	D19,g	D18,g	A17,g	A18,g	T		
	T2	D17,g	D16,g	D15,g	A14,g	A15,g	A16,g	T2	
T	D14,g	D13,g	D12	D11	A10	A11	A12,g	A13,g	T
D10,g	D09,g	D08,g	D07	D06	A05	A06	A07	A08,g	A09,g
D05,g	D04,g	D03,gc	D02,c	D01	Test,c	A01,b	A02,cb	A03,gb	A04,gp
C05,g	C04,g	C03,g	C02,gc	C01,bc	B01,b	B02,cb	B03,cb	B04,gcb	B05,gcbp
C10,g	C09,g	C08,gc	C07,gc	C06,b	B06,cb	B07,b	B08,cb	B09,gcb	B10,gcp
T	C14,gc	C13,g	C12,gb	C11,gcb	B11,gcb	B12,gcb	B13,gcb	B14,gcb	T
	T2	C17,g	C16,gc	C15,gcb	B15,gb	B16,gcb	B17,gcb	T2	
		T	C19,gc	C18,gc	B18,gcb	B19,gcb	T		
		T	D19,gc	D18,gc	A17,gc	A18,gc	T		
	T2	D17,gc	D16,gcb	D15,gc	A14,gc	A15,gc	A16,gc	T2	
T	D14,gc	D13,gcb	D12,cb	D11,c	A10,c	A11,c	A12,gc	A13,gc	T
D10,gc	D09,gb	D08,gcb	D07,cb	D06,c	A05,cb	A06,c	A07,b	A08,gc	A09,gcap
D05,gc	D04,gcb	D03,gc	D02,c	D01	Test,c	A01,b	A02,cb	A03,gb	A04,gp
C05,gc	C04,gc	C03,gc	C02,gc	C01,bc	B01,b	B02,cb	B03,cb	B04,gcb	B05,gcbp
C10,gc	C09,gc	C08,gc	C07,gc	C06,b	B06,cb	B07,b	B08,cb	B09,gcb	B10,gcp
T	C14,gc	C13,g	C12,gb	C11,gcb	B11,gcb	B12,gcb	B13,gcb	B14,gcb	T
	T2	C17,g	C16,gc	C15,gcb	B15,gb	B16,gcb	B17,gcb	T2	
		T	C19,gc	C18,gc	B18,gcb	B19,gcb	T		

5.11. Characterization of Al_2O_3 and TiO_2 thin films deposited using Atomic Layer Deposition (ALD) after vapor HF treatment

Atomic Layer Deposition (ALD) thin films are used in microelectronics and as a controllable, biocompatible insulation layer for Micro-Electro-Mechanical Systems (MEMS). In order to investigate the application of two types of ALD layers for MEMS applications, we have measured the etch rate of ALD Al_2O_3 and TiO_2 thin films in vapor HF which is an important step in fabrication of MEMS devices with free-standing structures. The materials on the surface were characterized after vapor HF treatment. The low etch rate of the ALD alumina n vapor HF shows it could be a reliable protective insulator material for MEMS and BioMEMS applications.

ALD deposition has advantages in comparison with other deposition techniques. This method provides a conformal coverage for high aspect ratio devices and can be performed at relatively low temperatures as opposed to other techniques such as Chemical Vapor Deposition (CVD). The benefits of ALD include thickness control at the atomic scale, production of highly conformal films, low temperature growth, and wide-area uniformity [72].

ALD technology has been utilized in microelectronics to deposit high-k gate oxides such as HfO_2 and TiO_2 in addition to fabrication of dynamic random access memories (DRAMs) where the control of ultrathin films and conformality are essential [73]. The Al_2O_3 and TiO_2 layers show promise for example as etch-stops in deep silicon etching, as protective layers, and as high-dielectric constant materials for RF-MEMS [74, 75]. TiO_2 ALD films grown on polysilicon cantilever beam arrays and sidewall friction testers demonstrate self-assembled monolayer stiction performance and superior wear resistance [76]. The first application of ALD Al_2O_3 film as a protective coating in MEMS devices was described in [77] where the ALD film was used to prevent mechanical wear and electrical shorting between contacting parts of a released cantilever MEMS. ALD Al_2O_3 was utilized as wear-resistant coating for a MEMS micro-engine [78] and as a low temperature electrical insulation in a 3D magnetometer aimed for portable devices because it provides conformal, pinhole-free uniform layers at relatively low temperatures [74]. The possible application

of ALD film may allow BioMEMS to operate in aqueous environments and prevent electrolysis and corrosion of electrodes [36].

One of the important steps in fabrication of MEMS devices with free standing structures is the release step. Conventional liquid HF is normally used to release the structure, rinsing and drying steps are usually required after wet release step. Dry releasing the structure with vapor HF eliminates the need and cost for rinsing and drying steps in addition to reducing the stiction and undesirable adhesion of free standing structures to the substrate [79]. Vapor HF also shows better selectivity to some of the materials used in standard IC micromachining in comparison with liquid HF [80].

We have characterized for the first time the etch rate of ALD Al_2O_3 and TiO_2 in vapor HF. X-ray photoelectron spectroscopy (XPS) characterization was done to confirm the resulting materials on the surface. Therefore, ALD Al_2O_3 and TiO_2 thin films can be used as reliable protective and insulation coatings in MEMS and BioMEMS devices.

ALD Deposition

Atomic layer deposition was carried out in an Ultratech Cambridge Nanotech S100 thermal ALD instrument. Aluminum oxide was grown at 100 C using trimethylaluminum and water (1000 cycles).

TiO_2 was grown at 100 C using tetrakis dimethylamido titanium (TDMAT) and water (2500 cycles). All precursors were held at room temperature except TDMAT which was heated to 75 C.

Vapor HF Etching Experiments

The etching experiments were done at SPTS Technologies, (an Orbotech company), using uEtch vapor HF etching tool to characterize the etch rate of ALD titania and alumina oxides that could be used for insulation purposes.

Thickness of samples were measured by a Filmetrics thickness measurement tool. Half of the samples were baked prior to the experiment. Baking is done before etching to avoid water on the surface. Silicon dioxide samples were also included to make sure that the conditions were calibrated. Samples Al_2O_3 #1, TiO_2 #2, and SiO_2 #1 were baked 25 min at

310 C on a hotplate prior to etching. All of the samples were etched in a uEtch tool for 5 minutes with recipe given in Table 24. Thickness of samples were measured after the experiment.

Table 24: Vapor HF recipe details.

Temp (C)	Pressure (Torr)	HF (sccm)	EtOH (µl/min)	N2 (sccm)	Steps	Step Time (min)	Etch Time (min)
45	125	525	400	1000	2	30	60.00

X-ray Photoelectron Spectroscopy

XPS analysis was performed with a Scienta ESCA-300 spectrometer. An excitation energy of 1486.6 eV, Al(k-alpha) was used with analysis performed of electrons escaping in a direction normal to the sample surface. Survey spectra were collected using a pass energy of 300 eV, while high resolution spectra used a pass energy of 150 eV. Energy resolution was on the order of 0.6 eV at full width half maximum. Sampling depth was on the order of 3 nm. Charge compensation with an electron flood gun was invoked during analyses.

Analysis was performed on the "baked" member of each pair (Al_2O_3 #1 and TiO_2 #2).

Samples of each material pressed onto conductive tape with moderate pressure and transferred to a sample holder. This was performed in a glove page under a N_2 atmosphere. A brief (< 30 s) exposure to air for the samples was necessary during the transfer of the sample holder to the XPS system.

Thickness measurements and etch rates for Al_2O_3 and TiO_2 in Vapor HF

Thickness of the ALD TiO_2, ALD Al_2O_3 and thermal SiO_2 and the resulting etch rates for 5 minutes of vapor HF treatment are given in Table 25.

The measured etch rate for thermal SiO_2 was in agreement with the expected calibration value of 0.1 µm per minute for the same recipe in uEtch tool. Since thickness of both Al_2O_3 and TiO_2 samples almost did not change and slightly increased, the increase in thickness was confirmed by performing an hour long etching with the same recipe.

Samples were etched for one hour in uEtch tool (SPTS Technologies) with the same conditions. Measurement of thickness for samples were done before and after etching and etch rates (A/min) calculated. One of the important observations of this experiment was TiO_2 "migration". TiO_2 migrated to different spots on the sample and sample holder. It was noted that the TiO_2 sample surfaces were "speckled" with bright spots, suggesting an incomplete film on the substrate surface.

Table 25. Etch rate of ALD TiO2, ALD Al2O3 and thermal SiO2 after 5 minutes of vapor HF treatment.

	Al_2O_3 #1	**Al_2O_3 #2**	**TiO_2 #2**	**TiO_2 #3**	**SiO_2 #1**	**SiO_2 #2**
Starting Thickness (Å)	829	825	1385	1388	9473	9488
Thickness After Vapor HF(Å)	830	829	1386	1394	4311	4156
Etch Rate (Å /min)	-0.22	-0.86	-0.26	-1.14	1032.28	1066.46
Bake Condition	Baked	Not baked	Baked	Not baked	Baked	Not baked

Al_2O_3 had no overall thickness change, but some pinholes were observed with a thickness gradient around them. A thickness gradient which was visible by a change in color was also observed near the edges of the film. Baking did not have any noticeable effect on the etching results. The etch rates are given in Table 26. Pictures of ALD Al_2O_3 and TiO_2 samples after etching are given in the Fig. 84 and Fig. 85 respectively.

Table 26: Etch rate of ALD TiO_2 and ALD Al_2O_3 after an hour of vapor HF treatment.

	Al_2O_3 #1	**Al_2O_3 #2**	**TiO_2 #2**	**TiO_2 #3**
Starting Thickness (Å)	838	839	1390	1400
Thickness After Vapor HF(Å)	851	842	1545**	1560**
Etch Rate (Å /min)	-0.18	-0.10	-2.2**	-2.3**
Bake Condition	baked	not baked	baked	not baked

*The single measurement error for thickness is typically ~10 A. For small thicknesses (<500 A), the fitting can become very sensitive to noise in the spectrum. Very small thicknesses tend to "snap" to a value of zero.

** Values near the center of the sample. The measurements indicated TiO_2 migrated on the surface.

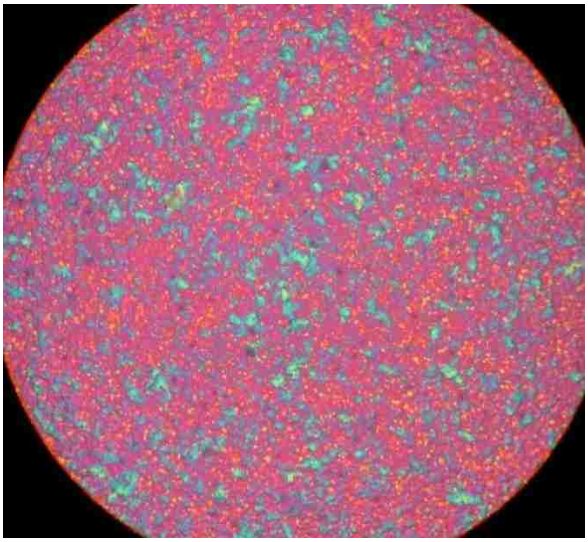

Figure 84. Close-up view of TiO_2 sample after etching. Blue areas are thicker than pink or orange according to the measurements. Possibly indicates TiO_2 migrates from edges toward the center of the sample. Thickness is measured to be ~ 1545 A in the center and ~1438 A near the edges.

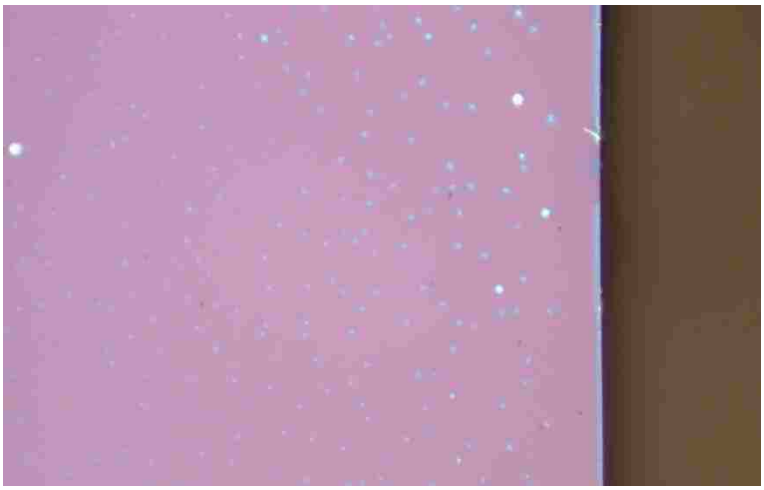

Figure 85. Al_2O_3 sample after etching. Color changes to blue near the edges of the film and around pinholes which indicates a thickness gradient.

In order to do material characterization on the surface of etched samples, experiment was repeated, and Al_2O_3 and TiO_2 samples were vacuumed immediately after etching. Some desiccants were also added to the package before vacuuming.

XPS analysis of ALD TiO2 and Al2O3 films following etching in vapor HF

A survey spectrum from Al_2O_3 sample #1 which was baked is shown in Fig.86. The spectrum is dominated by F features due to 1s photoelectrons and KLL Auger electrons.

Also clearly present are features associated with O, Al, C and trace N. High resolution spectra associated with these elements are found in Fig. 87. Approximate compositional quantitation is shown in Table 27. Generally, these are calculated by measuring the area of an element's characteristic peak and then adjusting that value by a literature-based relative sensitivity factor (RSF) for that specific feature. The regions used for these calculations are illustrated in the high resolution spectra and indicated within Table 27.

Table 27: Apparent sample composition (at %).

Sample	Al (2p)	Ti (2p)	O (1s)	C (1s)	Si (2p)	F (1s)	N (1s)
1: Al-2	25	-	17	14	-	42	1.3
2: Ti-2	-	0.7	19	11	68	1.2	0.3

The surface of TiO_2 sample #2 appears to be dominated by the presence of Si and O, as seen in Fig.88. Smaller features correspond to Ti, F, and C. The detailed spectra from this sample shown in Fig. 89 also indicates trace N. Compositional values determined for these samples are also shown in Table 27. It would appear that almost all of the TiO_2 had been removed during the HF treatment. One might also suspect that the residual F and N are associated with the residual Ti on the basis of compositional correlations seen in the Table. A qualitative summary of some of the peak characteristics is presented in this section. The C spectra from samples #1 and 2 can be each deconvoluted to at least 3 features. This is shown in Figs.87 and 89. Table 28 presents the center energy of each component and its relative composition. The largest feature for each likely corresponds to C bond solely to other C or H, with a typical literature value near 285.5 eV. On this basis, it would appear that the XPS peaks for sample #1 may be shifted by 1.7 eV due to sample electrostatic charging.

The Al (2p) spectrum in Fig. 87 can be deconvoluted to at least 2 peaks at 78.4 eV (68%) and 76.8 eV (32%). From literature values, adjusting for sample charging, the former peak is most likely associated with Al bonded to F, while the latter to Al associated with O [81]. There are likely at least two O (1s) features, here calculated to be at 535.2 (78%) and 533.5 eV (22%), with former likely associated with aluminum oxide and the latter with carbon-containing species. The F (1s) spectrum does not clearly evince more than one state.

Table 28: C spectral components.

	Peak energies (eV) and % composition		
Sample #	C I	C II	C III
1	287.2 – 81	289.0 – 10	291.7 – 10
2	285.5 – 73	287.1 – 18	289.3 – 10

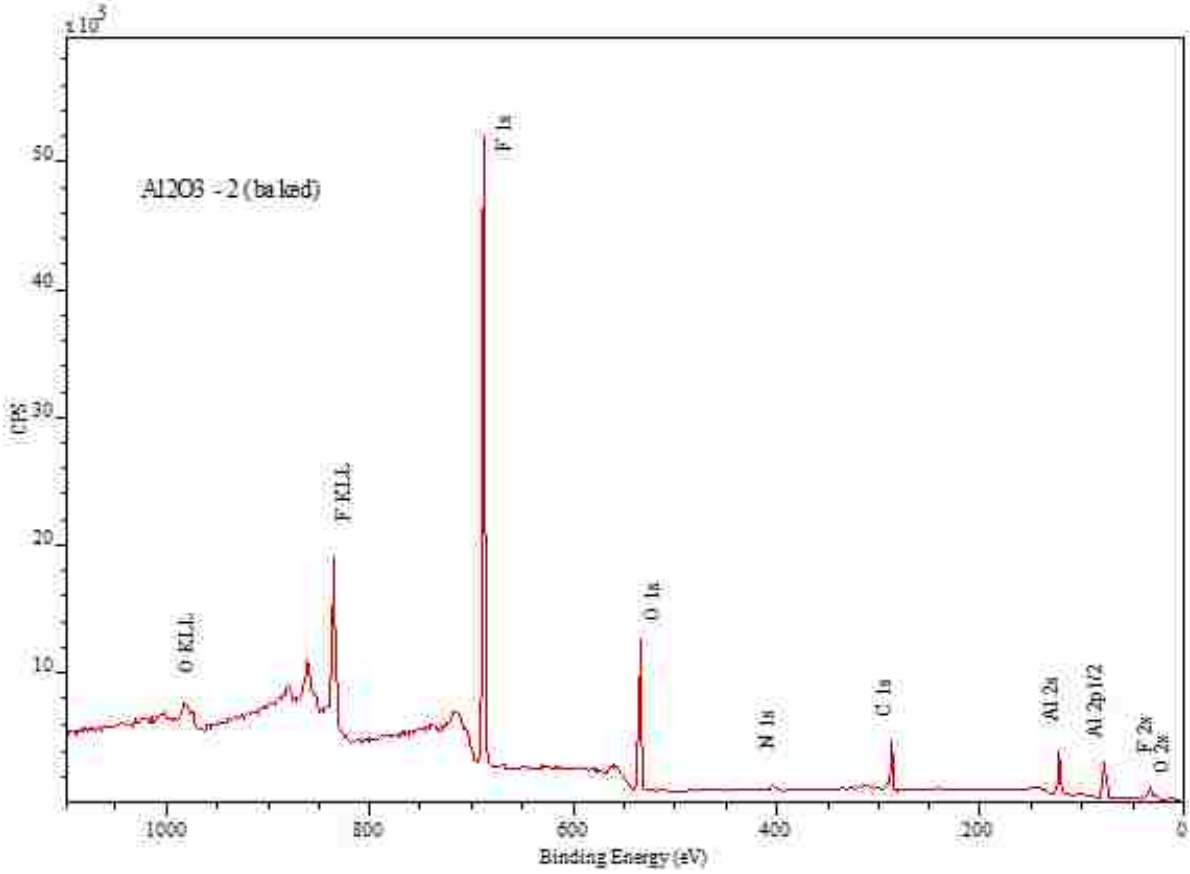

Figure 86. XPS survey spectrum of sample #1 (Al_2O_3, baked)

The Si (2p) spectrum for sample #2 (Fig. 89) has at least 2 features at 99.6 (93%) and 103.7 eV (7%), likely associated with elemental and oxidized Si, respectively. The two peaks in the Ti (2p) spectrum are largely a result of spin-orbit electron coupling that typically produces separate features for $2p_{3/2}$ and $2p_{1/2}$ photoelectrons, and do not indicate different chemical environments. The F (1s) suggests multiple chemical states, but have not been deconvoluted here. Similar results are seen for non-baked sample.

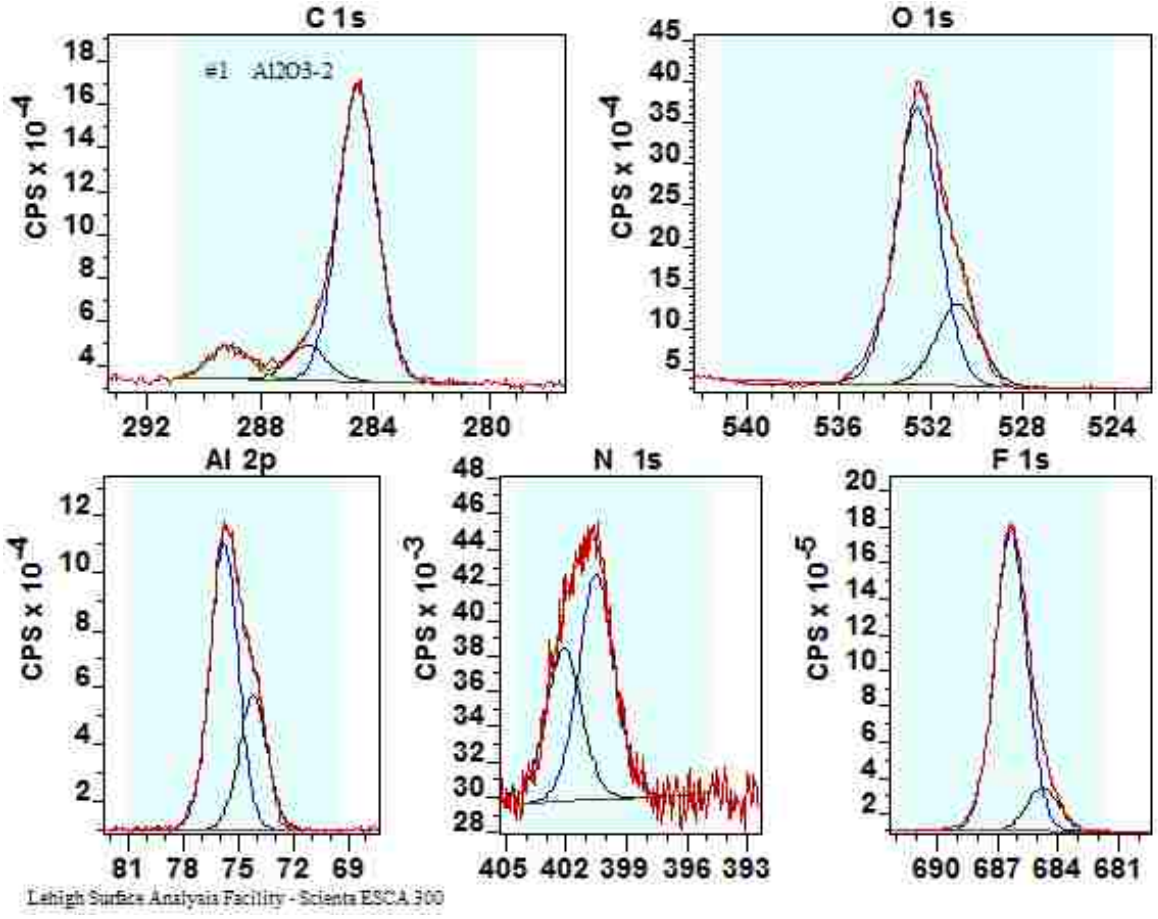

Figure 87. XPS detailed spectra of sample #1 (Al_2O_3, baked)

There likely remains some residual sample charging during the analysis of the three samples, resulting in a uniform shift of the energy scales. It is common practice to adjust such spectra such that the major C (1s) feature is set to 284.6 eV, the typical literature value for C (1s) for C bonded to C and/or H alone. This has been done for all three of the samples in the following analysis. As it is not known for certain if the chemical environment corresponding to the major C line is the same for all samples, some offset error may remain. The C spectra from samples can be each deconvoluted to at least 3 features as shown in the attached C high resolution spectra. Similarly, the somewhat asymmetric O (1s) spectra are best fit by using at least two components. Table 29 presents the center energy of each C(1s) and O (1s) component and its relative composition. The largest feature for each likely corresponds to C bond solely to other C or H, with a typical literature value near 285.5. eV

[81]. On this basis it would appear that the XPS peaks for sample #1 may be shifted by 1.7 eV due to sample electrostatic charging.

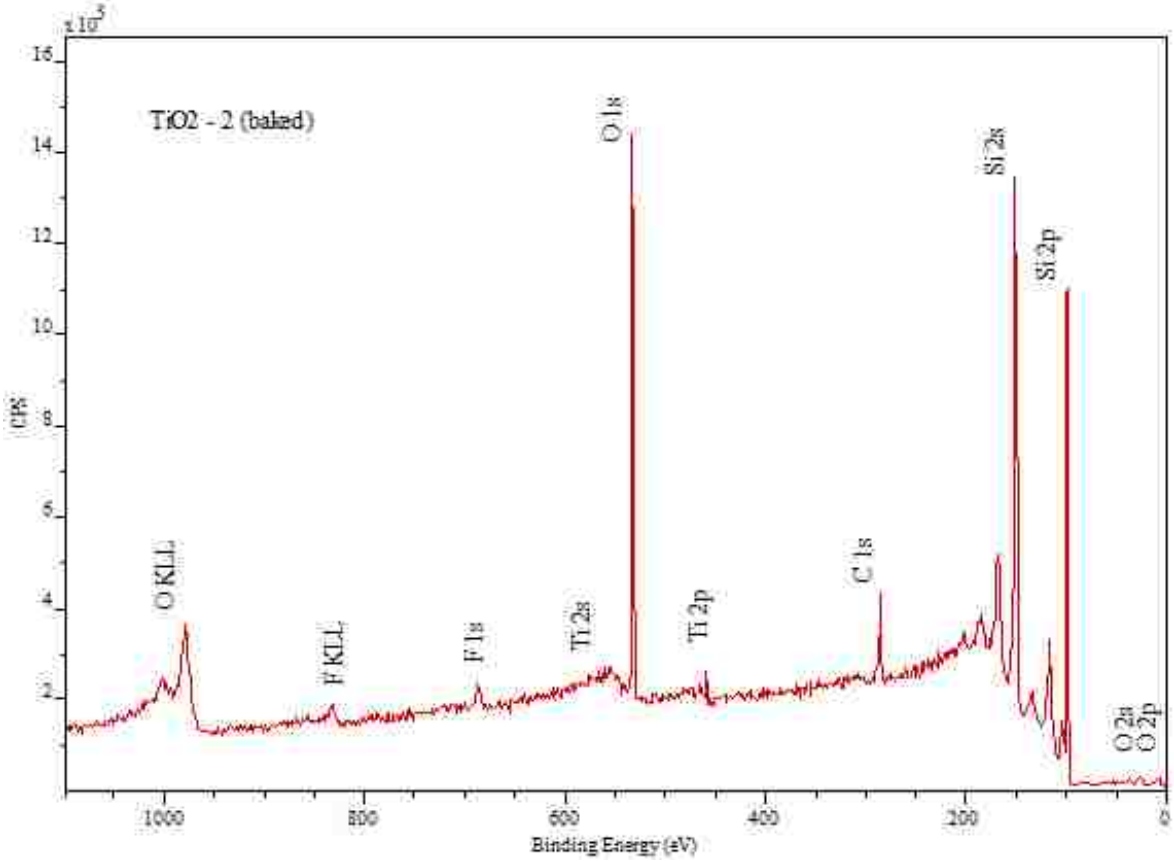

Figure 88. XPS survey spectrum of sample #2 (TiO_2, baked)

Table 29: C (1s) and O (1s) spectral components.

	Peak energies (eV) and % composition				
Sample #	C I*	C II	C III	O I	O II
1	284.6 81	286.4 10	289.1 9	532.6 77	530.8 23
2	284.6 73	286.3 18	288.5 10	532.2 92	530.4 8

(* Each spectra is offset to have its C I feature at 284.6 eV.)

The samples also have the presence of F and N in common, with a particularly greater concentration of F for #1. Two F (1s) lines are apparent with #1, while at least three each for #2. The N (1s) spectrum for #1 is deconvoluted to two states in Fig. 87, while the signal intensity is too weak for the other sample to ascertain the value of separating its signal.

Derived peak energies for F (1s) and N (1s) are given in Table 30. The remaining elements that have been observed are given in Table 31.

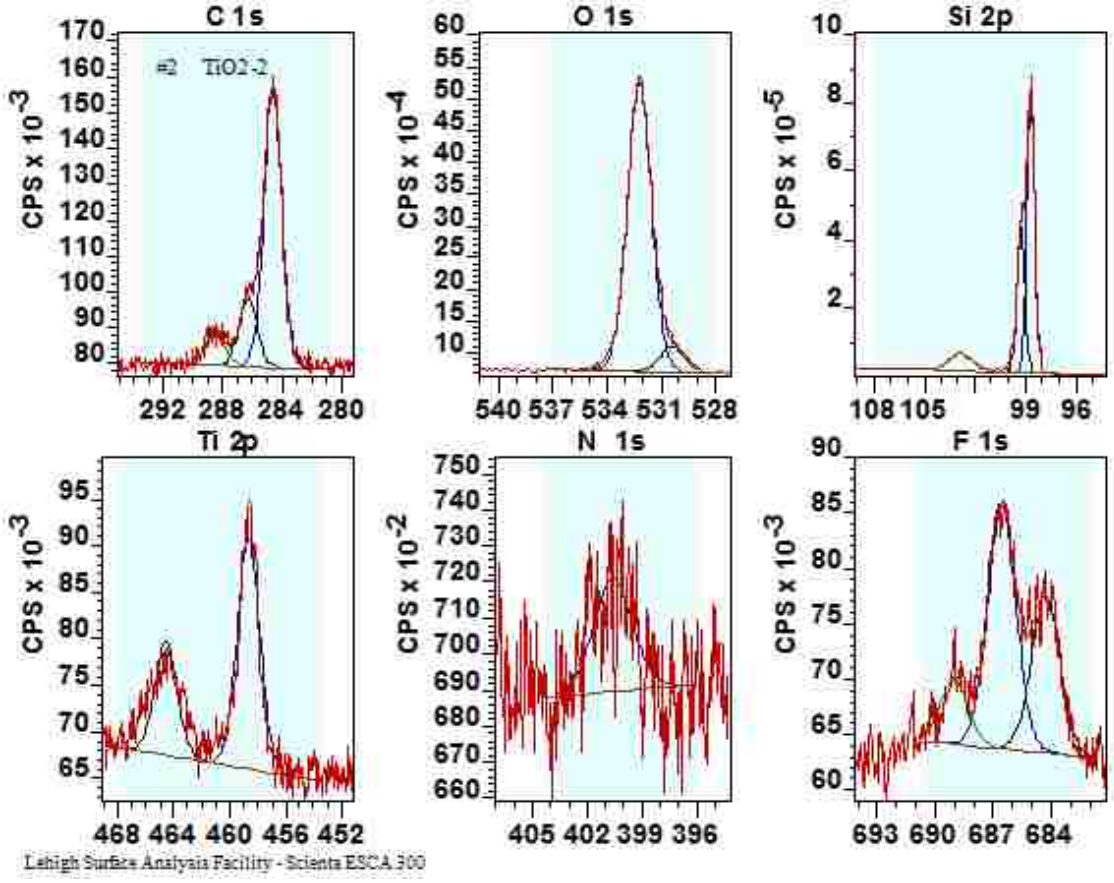

Figure 89. XPS detailed spectra of sample #2 (TiO_2, baked)

Table 30: F (1s) and N (1s) spectral components. (Each spectra has been offset to have its C I feature at 284.6 eV.)

	Peak energies (eV) and % composition				
Sample #	F I	F II	F III	N I	N II
1	686.3 87	684.7 13	-	400.5 60	402.1 40
2	686.5 52	684.3 34	689.0 14	400.6 100	-

As noted previously, the C I component for each spectrum (Table 28) has been set to coincide closely with the literature values for carbon in graphene and hydrocarbons. On that basis, the energy of the C II features might be assigned to C atoms having an associated

single C-O bond. The C (1s) bonding energies associated with C III may be associated with carbonyl (C=O) or single fluorocarbon (C-F) bonds. The highest value for C III associated with sample #1 potentially indicates some doubly fluorinated C atoms, coinciding with the greater F concentration.

Table 31: Al (2p), Si (2p) and Ti ($2p_{3/2}$) spectral components. (Each spectra has been offset to have its C I feature at 284.6 eV.)

	Peak energies (eV) and % composition				
Sample #	Al I	Al II	Si I	Si II	Ti
1	75.8 68	74.2 32	-	-	-
2	-	-	98.6 89	102.8 11	458.6 100

The O I states noted in Table 29 have energies consistent with literature values for O in SiO_2 and Al_2O_3 [82]. The lower energy component O II in sample 2 may be associated with O bonded to Ti. However, this does not explain the presence of a similar peak in sample #1 in which Ti is not present. It is surmised that this O may also be associated with Al, albeit in a different manner than the O I line in sample #1.

The identification of the F states is vague. The F III peaks are possibly related to fluorocarbon compounds. Literature values for F associated with Al and Si typically reside near 685-6 eV [82], which is likely associated with F I. The cause of the F II line is not known at this time. The N (1s) states are likely associated with C. The Al II line is likely due to oxides while the Al I line is in the region of fluoridated Al. The Si (2p) line near 102.8 eV is likely from SiO_2 while the line near 99 eV is most likely elemental Si. (Recall that XPS probes to a depth on the order of 5 nm.) The Ti (2p) line corresponds to an oxide. As previously noted, it appears that most of the original TiO_2 deposition on samples #2 has been removed by the vapor HF etching process.

Comparison of etch rate of oxides with wet etch HF method

Conventional method for releasing MEMS devices are still utilizing wet etch HF methods. The etch rate of ALD Al_2O_3 and TiO_2 in HF are measured and summarized in Table 32. The samples have the same deposition method explained in materials and methods section

of this paper. Thickness measurements were done using VASE Ellipsometer VB-400 (J.A. Woollam Co., Inc.) at Lehigh University. Etch rates were characterized in different HF solutions of 50%, 25%, 12.5 % and 6.25 % concentration. Etch rates were not measurable in 50% and 25% HF solutions for both samples as the oxides were removed very quickly. Based on the etch rates, TiO_2 is etched at a much slower rate than Al_2O_3 and this is also compatible with literature [74]. This suggests that TiO2 could be used as a protective layer while wet HF chemistry needs to be included in the processing. On the other hand, either of these oxides could be potential insulation layers compatible with vapor HF chemistry, because as it was previously shown in Table 26, both TiO2 and Al_2O_3 are not considerably etched. The fact that the ALD layers are not etched considerably in vapor HF verifies that they can be used as insulation layers for microelectronics applications.

Table 32. Etch rates of ALD Al_2O_3 and TiO_2 in liquid HF.

Wet Etch	**12.5 % HF**	**6.25 % HF**
Dip time	**5 seconds**	**5 seconds**
Deposition Temperature (C)	**100**	**100**
Etch rate of ALD Al_2O_3 (Å /sec)	> 168	> 168 *
Etch rate of ALD TiO_2 (Å /sec)	98	3.4

* Al_2O_3 sample with starting thickness of 838 A appears to be completely stripped during the short dip into different HF solutions.

One of the applications of insulation ALD layers could be for BioMEMS devices which operate in ionic medium. One example is an electrostatic actuator integrated on a BioMEMS for measuring mechanical properties of cell aggregates. In order for the operation of electrostatic actuator in ionic medium, higher frequency signals in MHz range are required. Electrolysis and electrochemical reactions in ionic medium could be prevented by application of ALD layers as insulation layers on electrodes.

5.12. Characterization of Micro-actuator

Characterization of micro-actuator was done using DC voltages to measure the displacement generated by actuation of comb drive actuators. The displacement translated to actuator shuttle that could be directly applied to a target is being measured. Characterization in air via AC voltage was performed to measure the resonant frequency and to determine the stiffness of the structure.

Characterization of actuator in DI water was investigated. For future applications in cell medium, an average finger spacing of 8 μm, will result in a critical frequency of 10 MHz. This means the actuator should be operated with more than 10 MHz signals in cell medium to avoid the effect of double layer in ionic medium. In order to improve the performance, the insulation layer should be added to protect the metal electrodes from delamination in ionic media.

5.13. DC Characterization of Actuator

Static displacement of micro-actuator was measured using DC voltages. As previously mentioned, the displacement is a result of electrostatic force generated by comb drive actuator pairs and is translated to the central part of the actuator. Comb drives in this design mechanically engage with the central part of actuator to move it forward.

DC characterization experimental set up incorporated a current limiting resistor, a digital voltmeter (Hewlett Packard, 34401A millimeter), a DC power supply (PR18-5 Kenwood Inc.), and a high voltage wideband amplifier (9100 Tabor Electronics Inc.). The actuator movement is recorded by live imaging software (Motic) and voltmeter readout is recorded by a LabVIEW program. Characterization experiments for 5 different displacements i.e. 100 μm, 90 μm, 77.5 μm, 65 μm, and 52.5 μm was performed. DC characterization diagram is shown in Fig. 90. Wafer level characterization was done using probe station (SuSS MicroTec) as shown in Fig. 91.

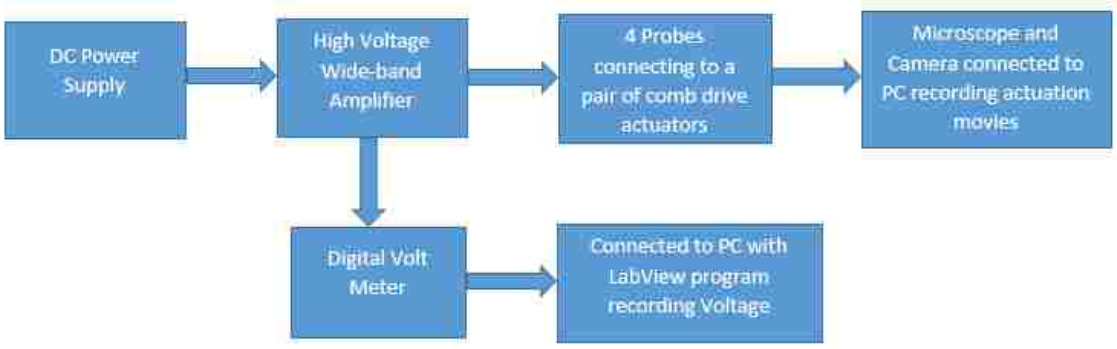

Figure 90. Diagram of simplified DC characterization set-up

In the experiments with the initial set-up, the DC power supply was connected to digital voltmeter (DVM) and the DVM was connected to a LabVIEW program through a GPIB port to desktop computer and voltages were recorded in a text file. The resistance between probes were measured to be around 20 kOhm and therefore 10 mA of current was needed that could not be provided by the original power supply. Therefore, a high voltage wide band amplifier was later used to amplify the voltage and current at the same time. A setup was designed to limit the current using a 1 kOhm resistor so that it would not damage the instruments.

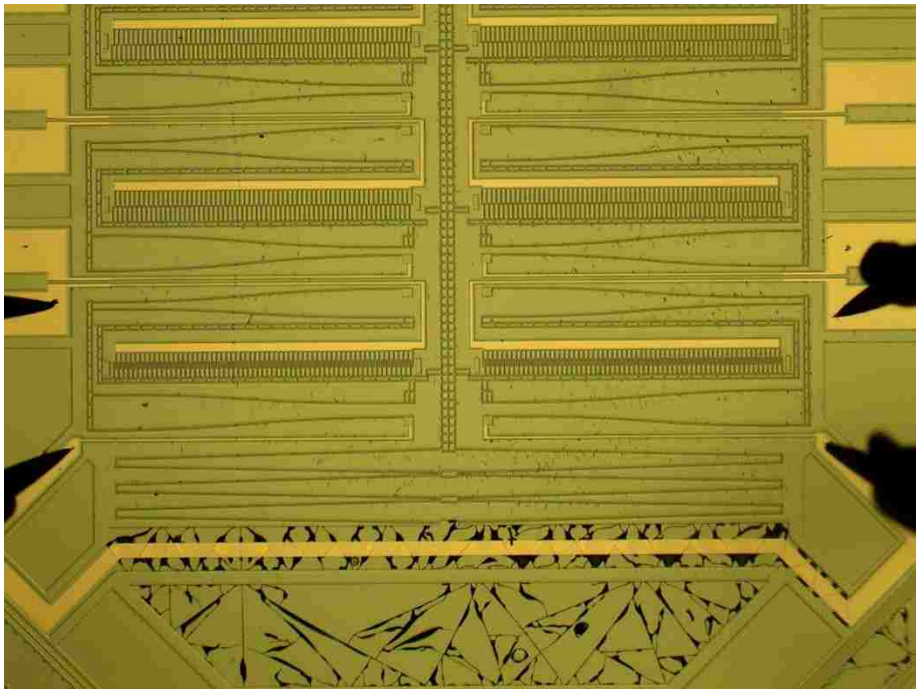

Figure 91. Experimental set up with four probes, the first pair of comb drive actuators was actuated here.

5.14. Characterization Procedure

DC characterization of actuator involves a few steps that is explained below.

1- Preparation of set up and probes on SuSS MicroTec

2- Taking a picture from actuator with 10 X lens before experiment

3- Making measurement of resistance between two probes before experiment

4- Reading the voltage across limiting resistor and therefore determine the current of limiting resistor

5- Start recording voltage-time measurements from DVM (Hewlett Packard, 34401A)

6- Start recording the video of actuator movement from Motic live imaging software right before the experiment

7- Running the characterization test, increasing DC voltage linearly from 0 Volts to 10 Volts by regulated DC power supply (PR18-5 Kenwood Inc.) connected to the high voltage wideband amplifier (9100 Tabor Electronics Inc.) and decrease the voltage back to zero

8- Taking a picture from actuator with 10 X lens after experiment and repeat 4

9- Analyzing data: MATLAB extraction of photos and Image J analysis of video for actuator movement, (Kinovea is the motion tracing software that was later used for analyzing the videos and generating displacement time figure)

10- Plotting voltage time from LabVIEW measurement data in Excel

5.15. DC Characterization Results

In the initial experiments, comb drive actuators were actuated separately to verify the performance. For instance, the comb drive corresponding to the smallest displacement was actuated with a semi-linear voltage up to 52.5 μm until anchor was touched, the actuator then moved back but hysteresis was observed (Figs. 92 and 93).

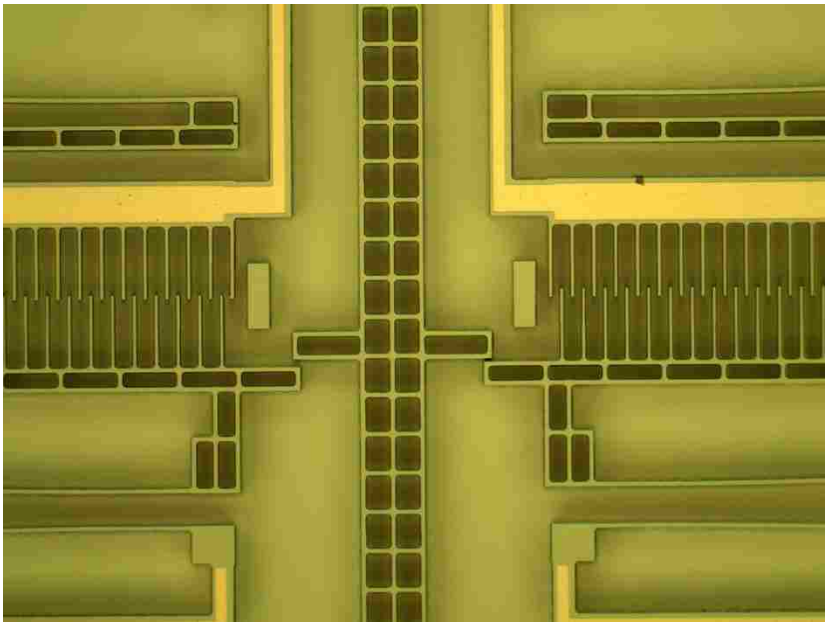

Figure 92. Hysteresis was observed after actuator went back to the initial state.

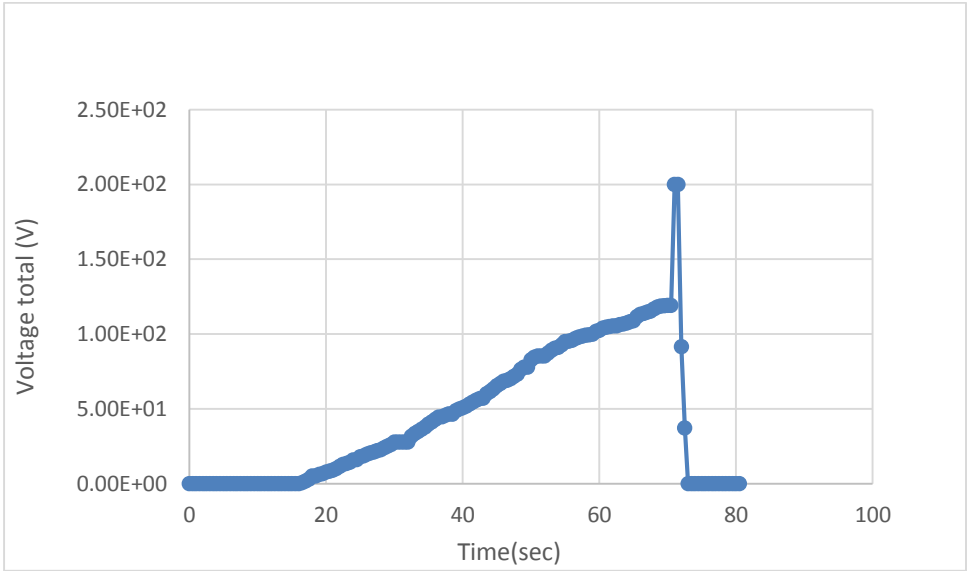

Figure 93. Voltage applied vs. time, the actuator on the right moved until hitting the anchor

In the following experiments, the pair of comb drive actuators was actuated and both actuators on the left and right moved together. An example of applied voltage and actuator movement is shown in Figs. 94 and 95 for the actuator corresponding to 52.5 µm.

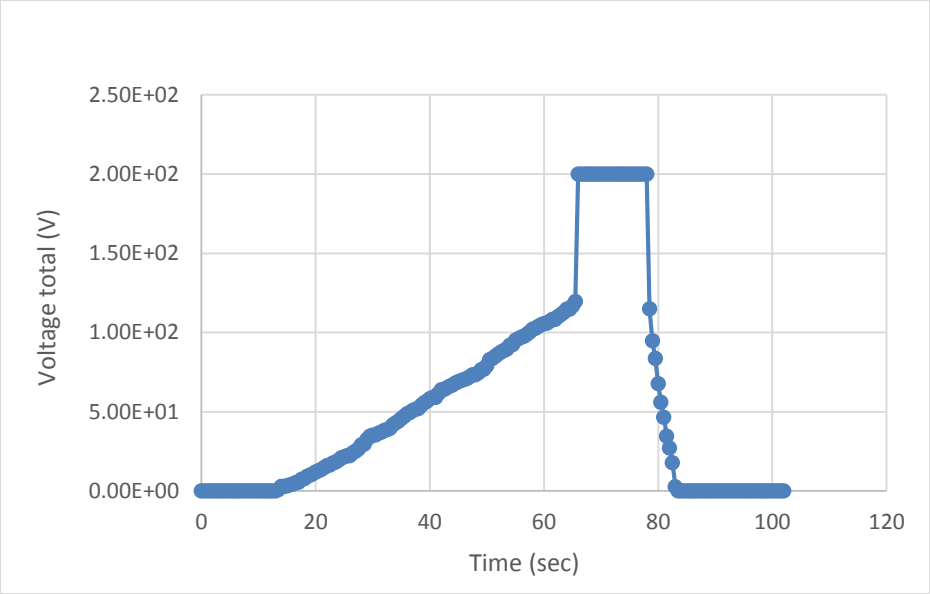

Figure 94. Total voltage applied vs. time, both actuators on the left and right were moving together.

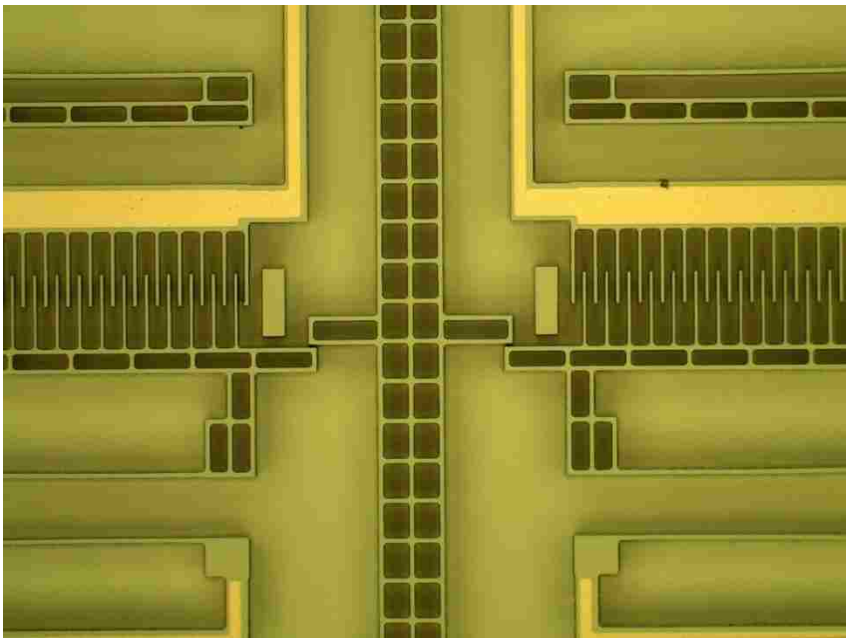

Figure 95. The first pair of comb drive actuators is shown after actuation for the displacement of 52.5 µm.

In the following experiments, bank of actuators on A06, A10, A11, D01, D02, D06 and D11 dies were characterized. Designed displacements of 52.5 µm, 65 µm and 77.5 µm, 90 µm and 100 µm were demonstrated on the bank of actuators. For instance, the 4th and 5th

full displacement corresponding to 90 µm and 100 µm were demonstrated on D01 (Figs. 96 and 97).

Some of the actuators moved less than full actuation. The cause was ranging from silicon grass contamination, part of unintentionally released anchor acting as a mechanical stop, or a broken spring that happened because of an artifact in lithography (Fig.98).
Also sometimes the actuator does not return to the initial state after actuation that might be due to charging [83]. This effect may be removed by low frequency AC actuation. The result of DC characterization is summarized in Table 33 and the detailed measurement results are given at the end of this chapter and in Appendix II.

Table 33: Characterization results summary

Inspected & Green Dies	Disp. 1, 52.5 µm	Disp. 2, 65 µm	Disp. 3, 77.5 µm	Disp. 4, 90 µm	Disp. 5, 100 µm
A06	Full actuation	Full actuation	Full actuation	Lithography artifact	Lithography artifact
A10	Mechanical obstacle	Full actuation	~ 0 µm	Broken Spring	Broken Spring
A11	N/A*	N/A	N/A	N/A	~ 67 µm
D01	~ 45 µm	Half way actuation	~ 60 µm	Full actuation	Full actuation
D02	Full actuation	~ 0 µm	~ 60 µm	~ 60 µm	~ 0 µm
D06	Full actuation	~ 10 µm	Full actuation	~ 24 µm	Full actuation
D11	~ 10 µm	~ 0 µm	~ 10 µm	~ 10 µm	0 µm

*A11 is designed for providing one type of displacement (100 µm).

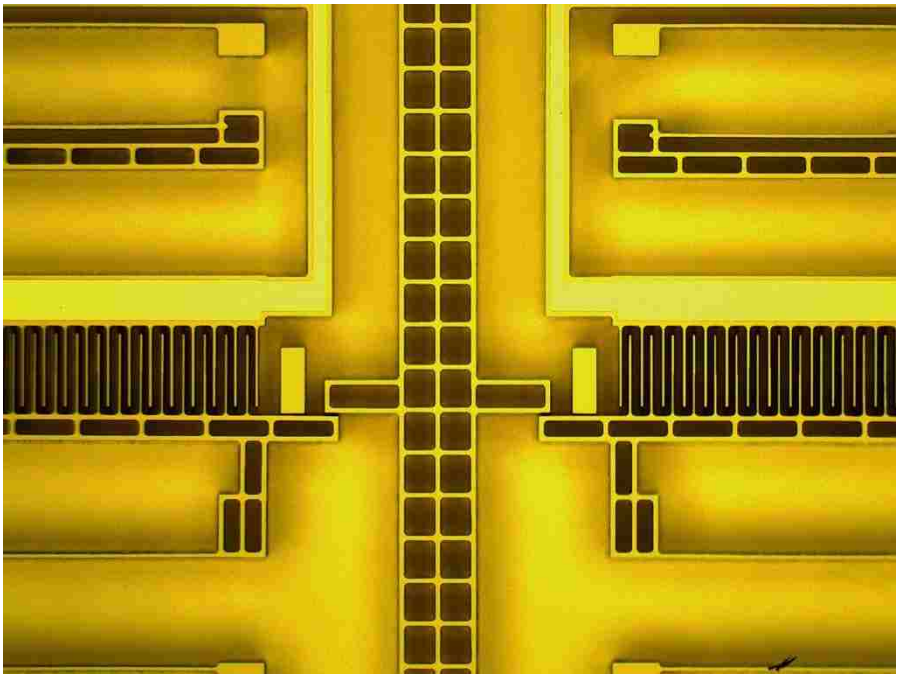

Figure 96. Full actuation for actuator pair on displacement 4 = 90 μm

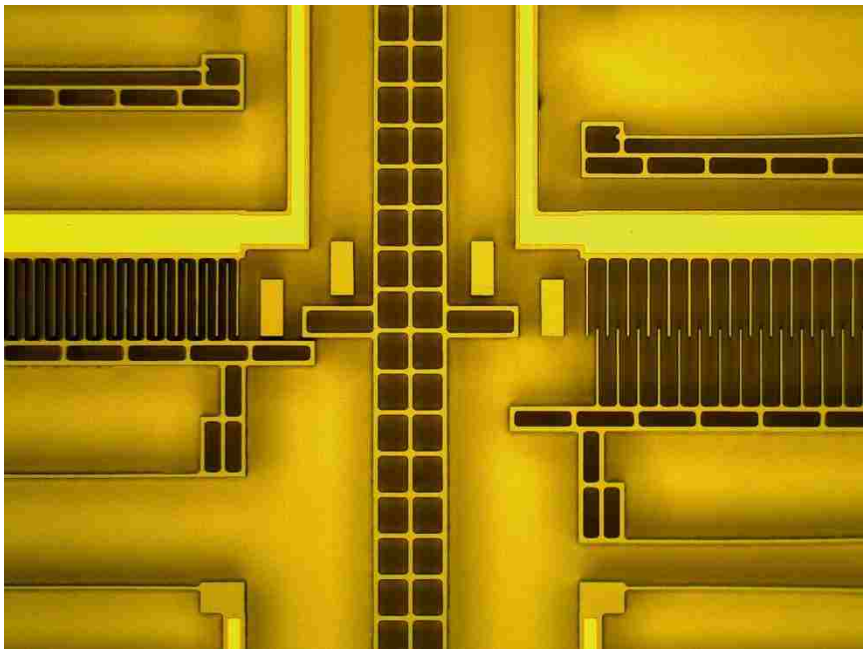

Figure 97. Full actuation for actuator on displacement 5 = 100 μm

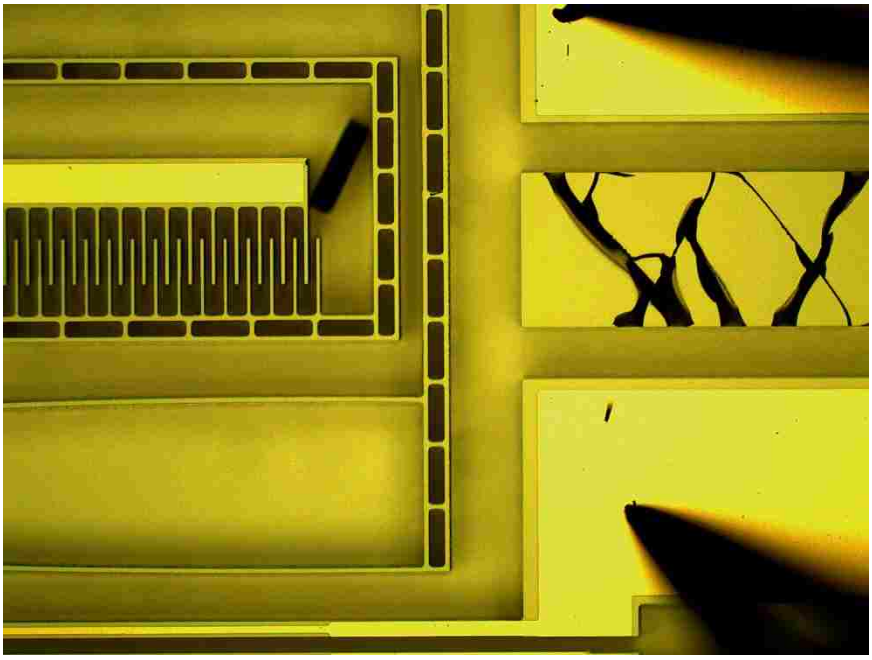

Figure 98. Actuator could not move further here due to part of silicon mechanically resisting it.

To analyze the data, a motion tracking software called Kinovea were utilized to track the motion of the actuator. This software works well when there is a high contrast between moving object and the background. Displacement vs. time was obtained from the output file from Kinovea. A text file from LabVIEW program was used to generate the voltage vs. time figure. The dies that were characterized along with their characteristics are listed in Table 34.

A comparison of modeling and experimental deflection is shown in Table 36. Experimental full actuation was observed in a lower voltage. Modeling displacement according to linear extrapolation would be 74 μm as opposed to displacement of 95 μm in experiment. Fabrication changes such as over-etching might be the cause of discrepancies between modeling and experimental results. Over etching of structures occurred because of the long DRIE time and resulted in narrower and more compliant beams in addition to a lighter structure.

Table 34: Selected dies for characterization and their corresponding actuator design parameters

Die Name	Min Si Width(μm)	AT Designed Displacement (μm)	AT Spring Width (μm)	AT Length (μm)	Comb Finger Spacing (μm)	Comb Finger Pairs	Spring length (μm)	Initial overlap (μm)
D01	8	Set	10	7861	8	70	2310	14
A06, A10, D02, D06	10	Set	12	7861	8	63	2310	10
D11	10	Set	12	7861	8	63	2310	10
A11	8	100	8	2961	8	70	2310	14

Table 35: DC characterization results for maximum voltage, measured displacement and corresponding designed displacement

Dies	Max Voltage (V)	Designed Displacement (μm)	Measured Displacement (μm)
A06_1	114	52.5	61.16
A06_3	119	77.5	85.3
A10_2	114	65	53.68
A11	58	100	67.12
D01_4	88.7	90	98.57
D01_5	69.7	100	108.02
D02_1	113	52.5	57.74
D02_4	71.6	90	59.56
D06_1	88.7	52.5	58.2
D06_3	98.82	77.5	98.13

Table 36. Comparison of modeling and experimental deflection

	Displacement (μm)	Voltage (V)	Voltage ^2 (V^2)
Modeling	130	150	22500
Modeling Linear Extrapolation	74	113	12769
Experimental	95	113	12769

Calibration of DC amplification

Calibration of DC amplification of high voltage amplifier was done in order to find the amplification characteristic for DC voltages. Fig.99) Power supply voltage is changed from 0 to 10 volts and the readout voltage is being measured. The voltage is almost linearly amplified. In the next step, voltages need to be applied for step voltage characterization experiment was calculated based on calibration.

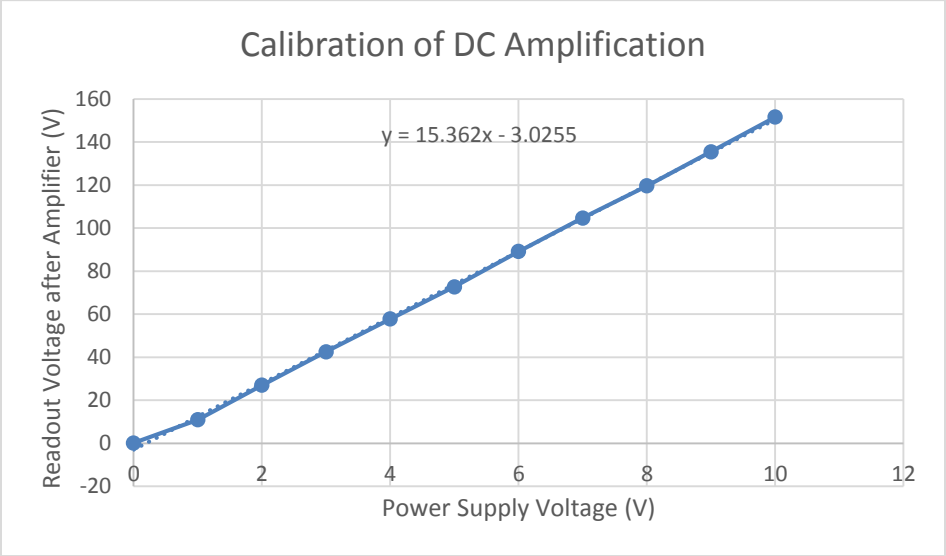

Figure 99. Calibration of DC amplification.

Detailed results for DC characterization with different types of voltages are given in the following section with more results included in Appendix II. Different type of voltages such as linear, delta and step voltages were applied and actuator displacement was recorded. The reverse displacement was also recorded when voltage decreased back to zero.

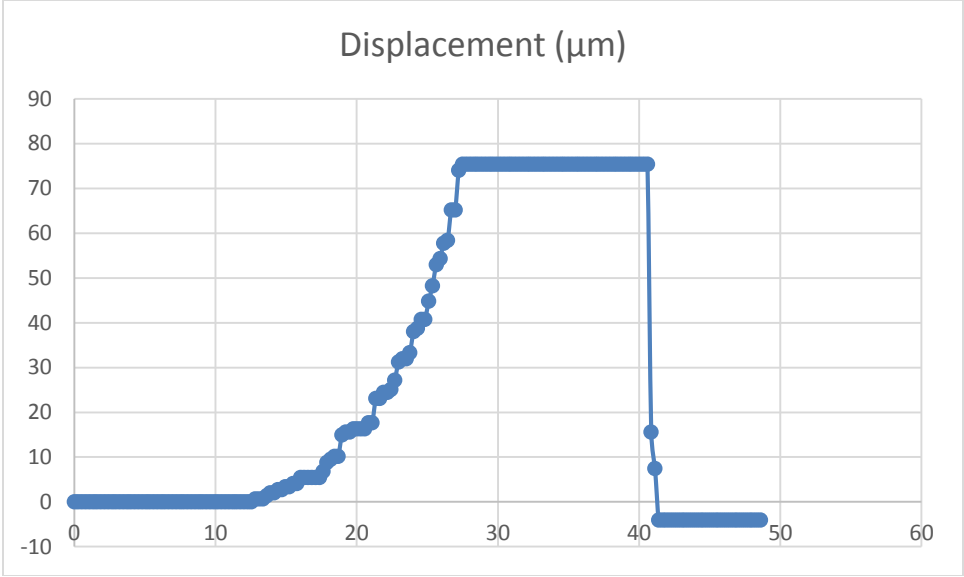

Figure 100. Displacement of actuator vs. time after applying linear DC voltage.

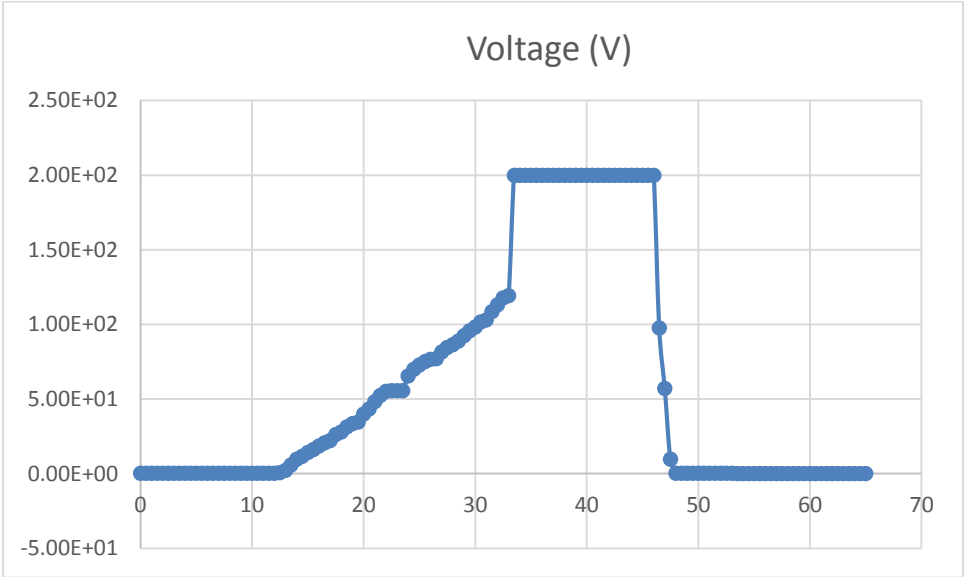

Figure 101. Linear DC voltage applied to comb drive actuator.

Usually actuator is stiffer in the initial trial and the response gets smoother in the following experiment. This may be attributed to the mechanical stiction or contamination below the free-standing structure.

Results for delta voltage characterization is given in Figs 102 and 103. A delta voltage was applied and the recorded displacement resembles a delta change as well. Delta voltage

causes an abrupt change in displacement and the response time is sufficiently fast for the application of device which is mechanical characterization experiments.

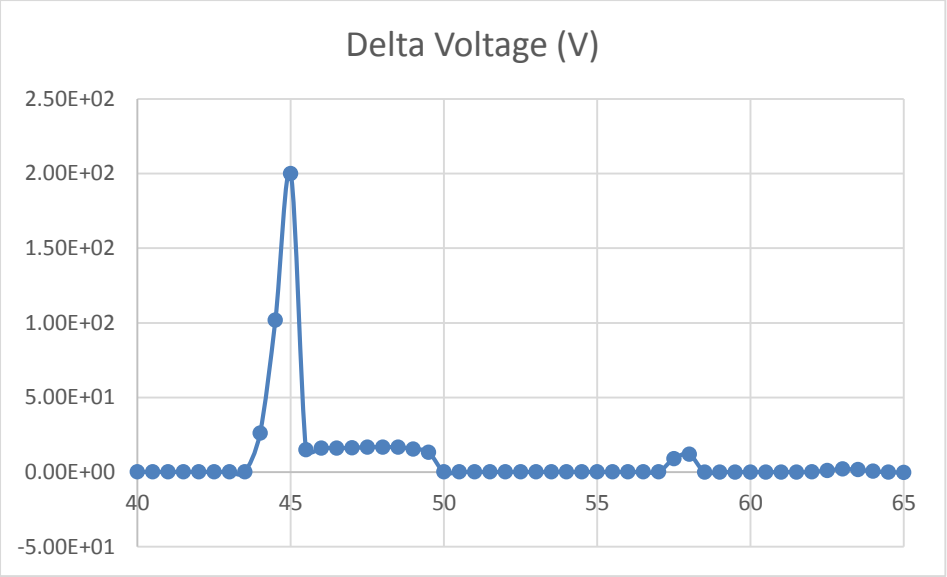

Figure 102. Delta DC voltage applied to actuator.

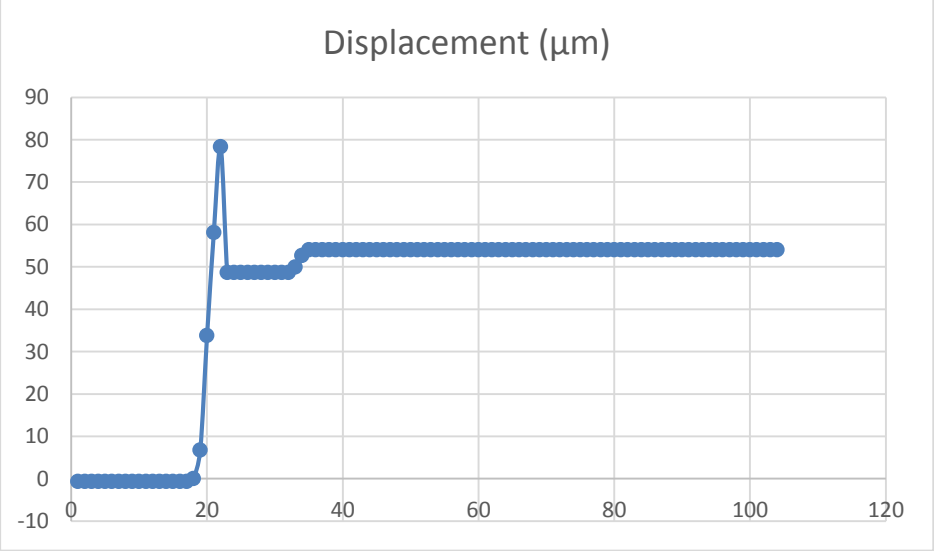

Figure 103. Displacement of actuator vs. time after applying delta DC voltage.

In the next series of characterization experiments, step voltages were applied and the displacements recorded. Displacement was then synchronized with voltage and was shown for both forward and reverse actuations. Step voltages were applied in 10 V step increments, starting from 0 V to 130 V. Each step was 10 seconds to 15 seconds in order

to synchronize displacement voltage more accurately. Then voltage was then decreased in a step fashion and displacement was recorded. Time were eliminated and displacement-voltage curves were obtained (Fig. 106). These curves are in agreement with the equation for displacement versus voltage which was given previously in (5) i.e. it is showing a second degree polynomial behavior for displacement vs. voltage. Also the displacement voltage curves are symmetric showing reliable forward and reverse displacement of the actuator.

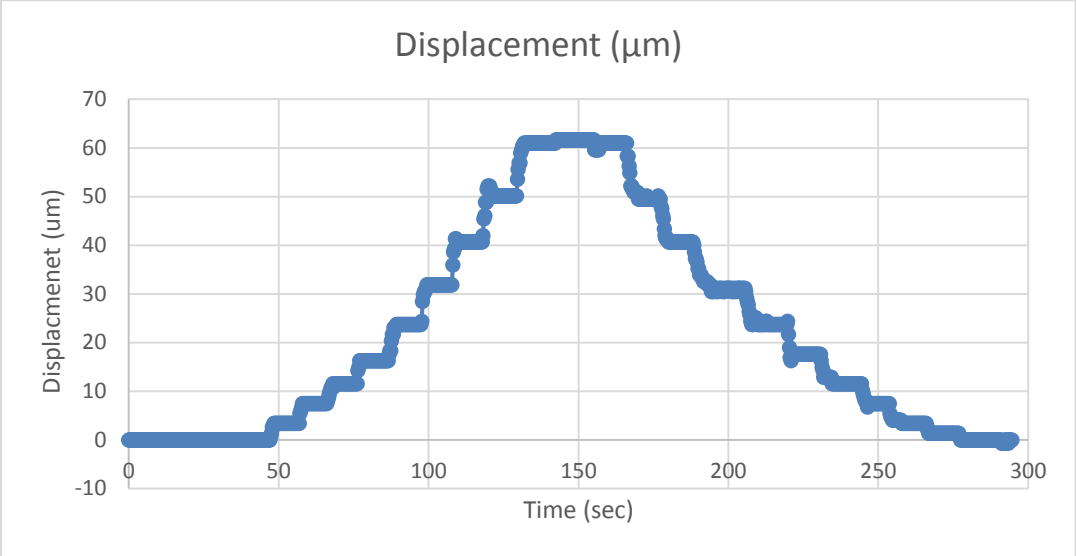

Figure 104. Displacement of actuator vs. time after applying step wise DC voltage.

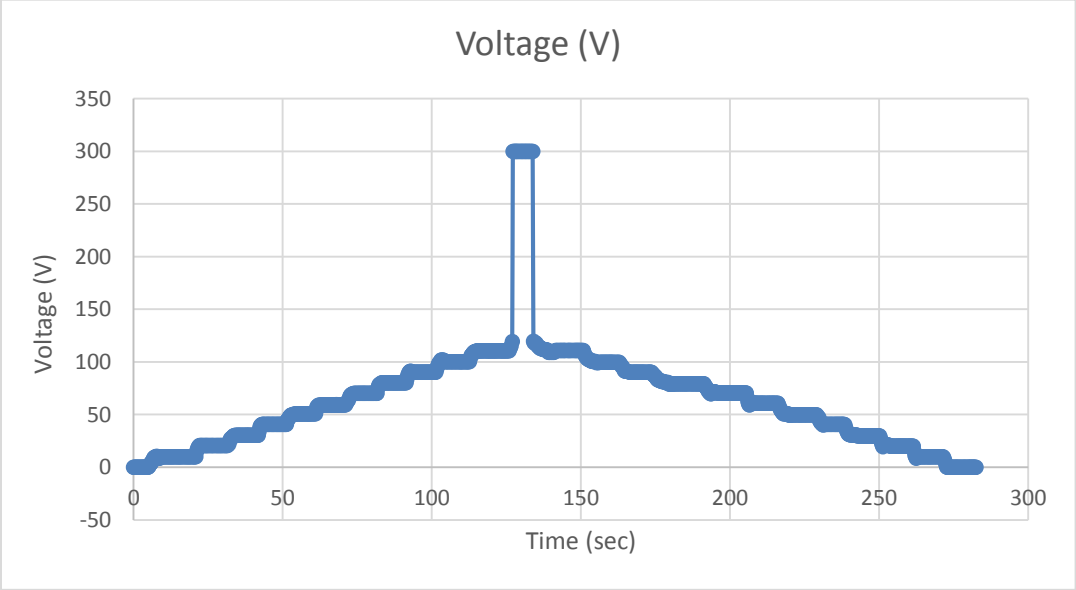

Figure 105. Step-wise DC voltage applied to actuator.

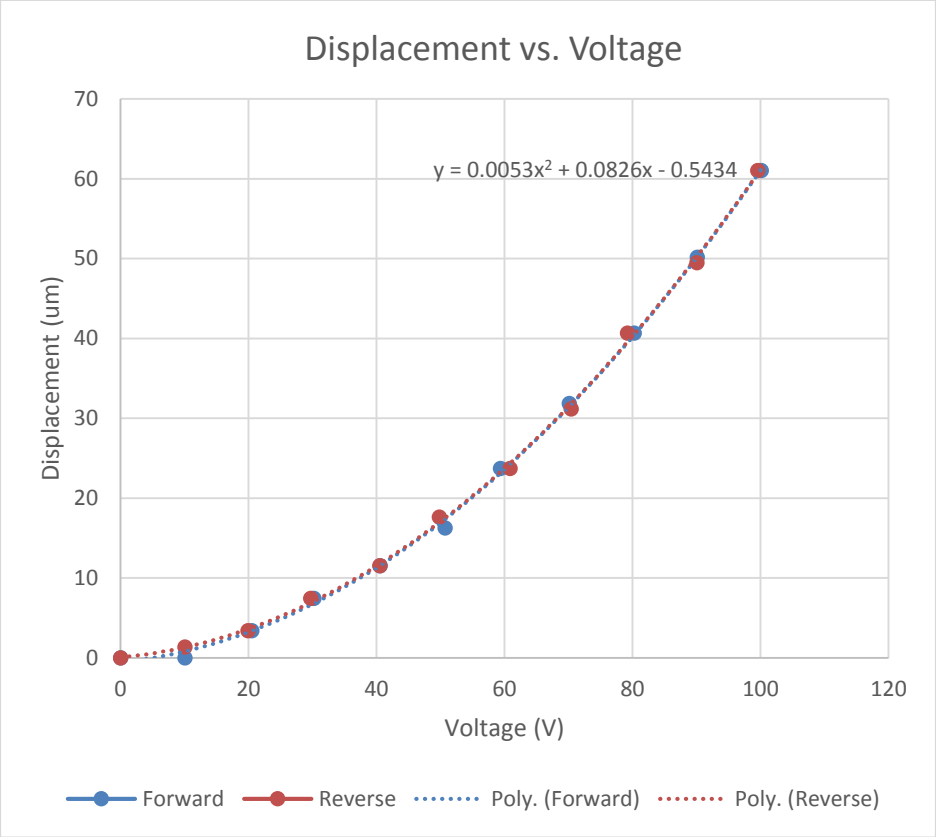

Figure 106. Displacement vs. voltage curve for forward and reverse actuation.

5.16. AC Characterization

AC Characterization of actuator was performed in air to determine the resonant frequency and stiffness of the actuator using a characterization setup with diagram shown in Fig. 107. AC characterization was also done in DI water, although a large displacement was demonstrated, there is a need for a protective layer to avoid electrolysis and electrochemical reactions. The details of these experiments are discussed in the following sections.

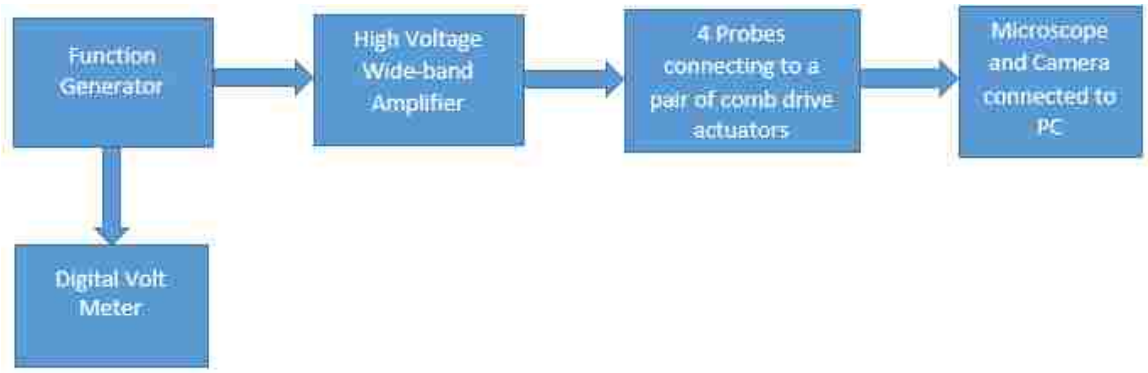

Figure 107. Simplified AC Characterization Diagram

Resonant Frequency Measurements

Resonant frequency was measured by sweeping AC voltages and the stiffness of the structure was determined. Frequency of AC voltage was swept in order to find the maximum oscillation amplitude which corresponds to the resonant frequency. Camera rate was 9990 frames per second. Electrodes were actuated with 3 Vp-p from function generator which is amplified by wide-band amplifier. Frequency was swept from 1 Hz to 1 kHz. The applied voltage was 9 Vp-p on function generator.

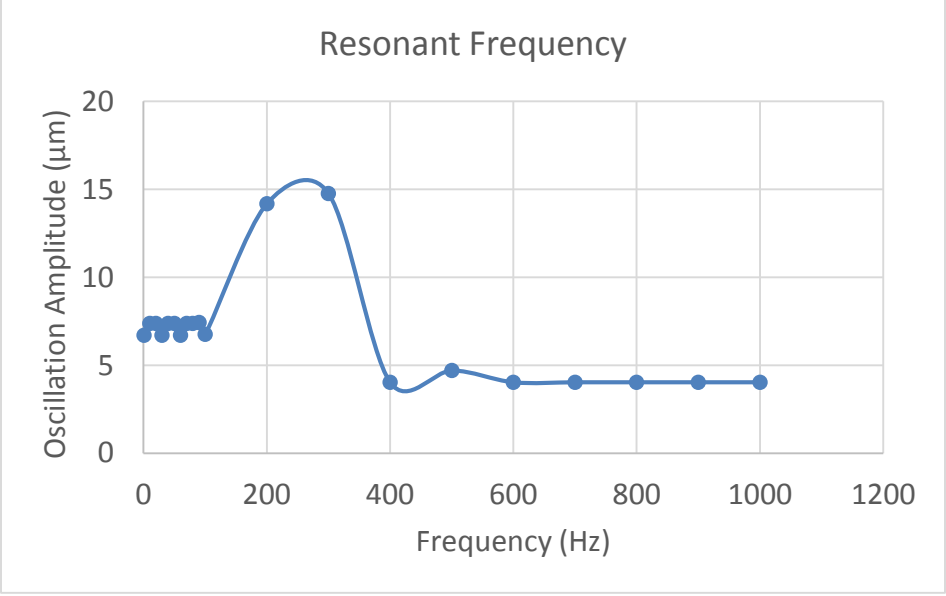

Figure 108. Oscillation amplitude for different frequency signals applied to actuator to measure resonance frequency.

In the next step, screening of the resonant frequency in the region of the maximum amplitude was performed. Frequency was swept from 100 Hz to 350 Hz with 25 Hz steps. The 3 Vp-p was utilized for this experiment. The maximum amplitude was located to be around 250 Hz. In the next experiment, frequency was swept with 5 Hz increments around 250 Hz and where the maximum amplitude was located. The resonant frequency was located at 244Hz based on the experiments. The total mass of the actuator was calculated and based on the resonant frequency, the spring constant of the system was derived. Results of AC characterization are given in Table 37.

Table 37. Spring constant of the actuator system.

Silicon Density (g/cm^3)	Total Actuator Mass (kg)	Resonant Frequency (Hz)	Spring Constant of Actuator System (N/m)
2.329	5.01153E-07	244	0.029837

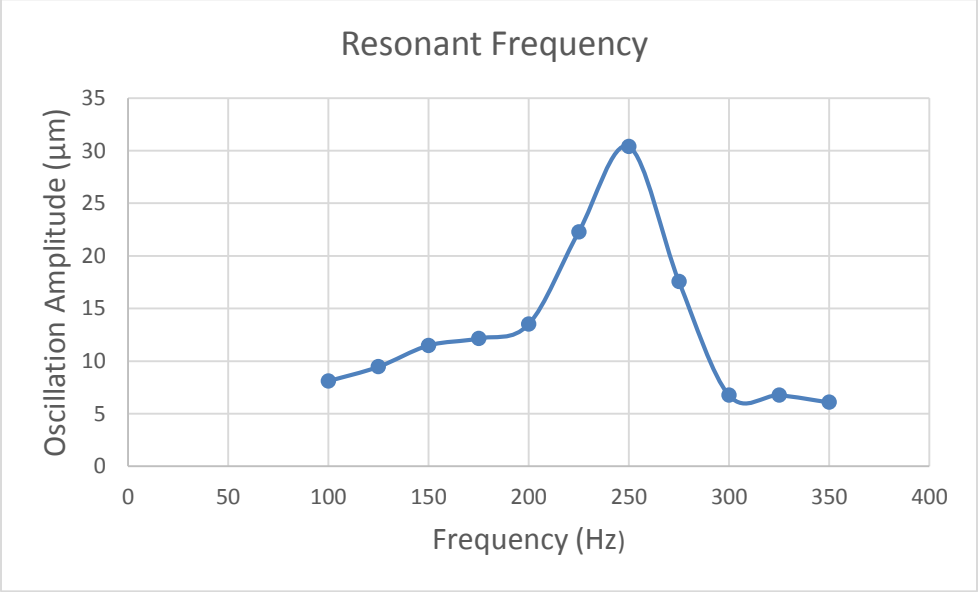

Figure 109. Oscillation amplitude for different frequency signals applied to actuator to measure resonance frequency with more accuracy.

A Feasible Tool for Cyclic Strain Actuation

The experiments proved the feasibility of the actuator to be used in cyclic strain experiments for mechanical characterization of cells or other viscoelastic targets. Pair of comb actuators were energized and oscillations could be controlled very well by a low

frequency such as 150 mHz and amplitude of 7-10 V from function generator which results to output voltage from 88 V to 107 V. Using this voltage, D02 fourth pair could be actuated up to 50 μm in cyclic motion and no hysteresis was observed as opposed to DC actuation. Also by reducing the amplitude in function generator from 10 V to 1 V, the actuator movement will stop right away, resulting in an accurate tool for performing cycling strain tests.

Characterization of Actuator in DI Water

The actuator corresponding to displacement 4 which equals 90 μm was characterized in DI water. The amplitude of oscillation in the air with same voltage was recorded to be 7.43 μm. The actuator moved in DI water at 100 Hz AC voltage frequency and 3 Vp-p source voltage but a lot of bubbles were created in a few seconds and prevented further actuation (Fig. 110). This phenomenon happened because of electrolysis and electrochemical corrosion. Since gold is electrochemically passive, the underlying chromium adhesion layer is being corroded in the solution [30]. Also after the experiment in DI water, damage and delamination of metal layer due to electrochemical corrosion was observed for this actuator.

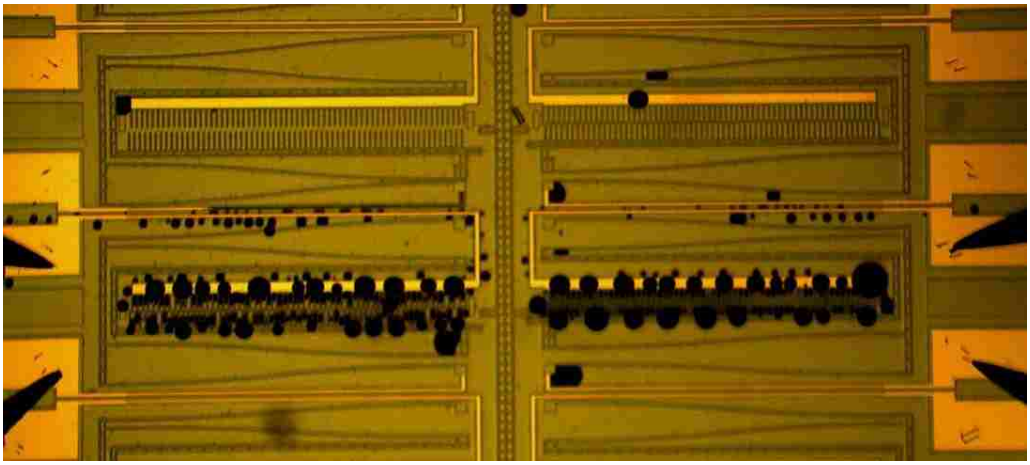

Figure 110. Formation of bubbles at frequency of 100 Hz in DI water.

In the next experiment with actuator corresponding to displacement 2, frequency was increased to 10 kHz and source voltage to 5 Vp-p. The actuator moved ~ 50 μm but the same bubbling happened that prevented actuator from further operation. Actuator

corresponding to displacement 5 was successfully actuated with increased frequency of 1MHz and bubbling did not happen (Fig. 111). Further increasing the frequency to the maximum limit of source (30 MHz) also resulted in bubbling problem and no movement was observed.

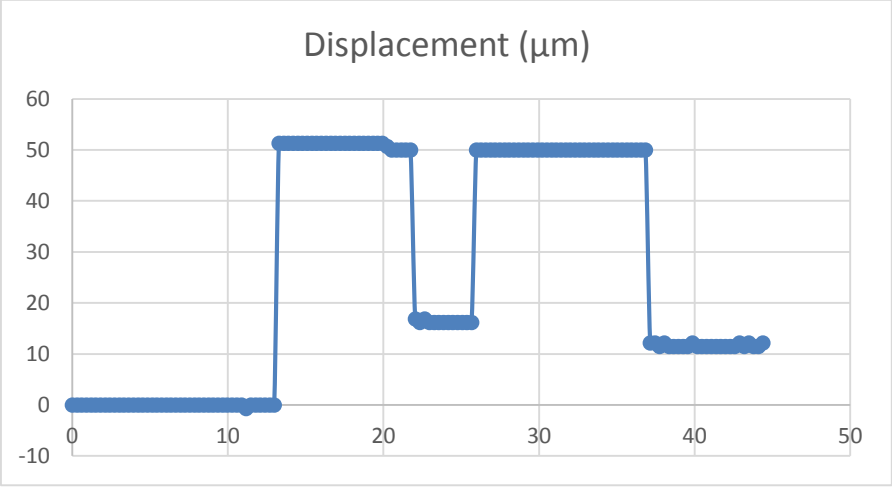

Figure 111. By increasing the frequency of voltage to 1 MHz no more bubbling was observed. Actuator forward and reverse displacement was verified in DI water though hysteresis was observed

6. Mechanical Properties of hMSC

Understanding of the biological response of cells to their biomechanical environment would enhance the knowledge of how cellular responses correlate to tissue level characteristics and how some diseases, such as cancer, grow in the body. Mechanical properties of human mesenchymal stem cells (hMSC) are particularly important in tissue engineering and research for the treatment of cardiovascular disease. We measured the elastic and viscoelastic properties of hMSC cells using a miniaturized custom-made BioMEMS device. We compared our results to the viscoelastic properties measured with other methods such as atomic force microscopy (AFM) and micropipette aspiration. Different models were applied to the experimental force data, including elastic, Kelvin and Standard Linear Solid (SLS) models, and the corresponding values were derived. The values were compared to the literature based on micropipette aspiration and AFM methods. We then utilized a tensegrity model, which represents major parts of internal structure of the cell and treats the cell as a network of microtubules and microfilaments, as opposed to a simple spherical blob. The results of this model were similar to the recorded experimental data.

Study of cell mechanobiology is also very beneficial to repair and tissue engineering strategies [84]. It was observed that normal cells and cancerous cells can exhibit different stiffness values [6] and it was hypothesized that higher deformability corresponds to more invasive cells [19], which can be a basis for their separation and detection [85, 86]. Furthermore, mechanical stimuli play an important role in basic cellular behavior, including proliferation, cell lineage, function and differentiation [87]. Since the mechanical properties of a cell is one of the important factors in determining its response to external mechanical forces [88], it is essential to characterize single cells to have a better understanding of the cellular mechanisms.

Viability and function of hMSC cells, which have promising use in gene therapy [89] and cardiac tissue engineering, are influenced by the presence of mechanical stimuli similar to other type of cells [4]. Furthermore, mechanobiology of differentiation can be better

understood by studying mechanical properties and inter-relations of hMSC cells. There is a hypothesis that chondrogenic or osteogenic differentiation might be caused by mechanical strain in undifferentiated hMSCs [9]. Mesenchymal stem cells are multipotent stromal cells. Stromal cells are connective tissue cells of any organ. Their interaction with tumor cells is known to play a major role in cancer growth and progression [90].

Modeling and analysis of single-cell responses to mechanical stimuli is the first step towards gaining knowledge about mechanical responses in tissue [91]. Several methods such as micropipette aspiration, AFM, cytoindentation, and magnetic beads have been developed to study mechanical properties of single cells and different models were applied to single cell responses to quantify their mechanical characteristics [10-13].

A miniaturized device such as a BioMEMS provides another way to characterize the single cells. This kind of device has the advantage of being smaller and easier to integrate onto a lab-on-a-chip with clinical use in addition to the possibility of using in for multiple experiments. We have utilized a BioMEMS device previously developed in our laboratory [2]. The device and its main components are shown in Fig. 112. The device incorporated a force sensor to measure the force, an electrostatic actuator to provide 1 μm to 6 μm displacement, a resistance temperature detector to measure the temperature, and a heater loop to maintain biological temperature. Its fabrication process and characterization have been previously described in [2]. We measured the mechanical characteristics of single hMSC cells *in vitro* using the mentioned BioMEMS device and an external piezo driver. Characterization of a single cell was done in ionic media.

The actuator design is depicted in Fig. 113. The actuator was based on electrostatic clamping between electrodes and was designed to provide displacements from 1 μm to 6 μm [2]. However, electrode clamping is not possible in ionic media due to charge screening effects. Therefore, an off-chip piezo driver was used to provide the displacement, and a piezoresistive force sensor was utilized to measure the reaction force. The goal of this study is to quantify biomechanical characteristics of single detached hMSC cells using elastic and viscoelastic models, in addition to a tensegrity model that partially represents the internal structure of the cell. We have studied detached cells in this study and therefore

eliminated the dependability of cells over cell cycle [92] that exists in other methods characterizing adherent cells. We compressed a single cell and measured the response on our device. We collected the data with LabVIEW and fit the data to different models in MATLAB. Our experimental and modeling methods for single cell characterization are explained in the following sections.

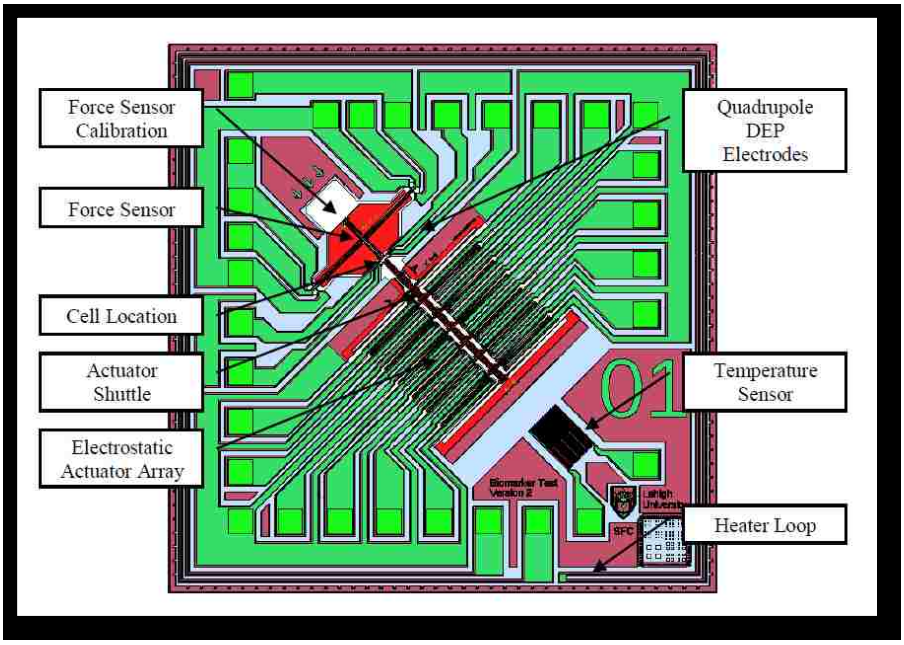

Figure 112. Previous generation of BioMEMS for single cell characterization [14].

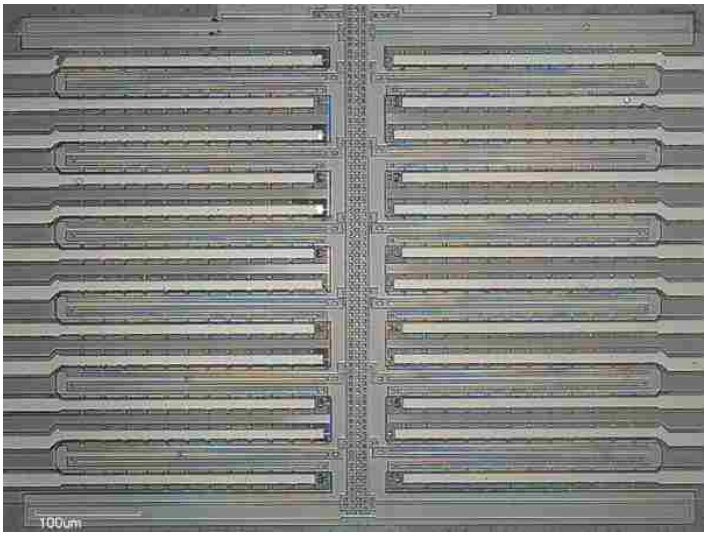

Figure 113.The actuator array in previous generation of BioMEMS for single cell characterization. The actuator was designed to provide 1 µm to 6 µm.

6.1. hMSC Cell Culturing Conditions

Cell lines were originated from bone marrow cells (Lonza), cryopreserved and cultured in a monolayer in 10 ml culture dishes. The dishes were incubated at 37^{o}C and 5% carbon dioxide (CO_2). Culture media consisted of low-glucose Dulbecco's modified eagle medium (DMEM), 10% fetal bovine serum (FBS) and penicillin antibiotic at 1%. Cells were harvested when there was a 90 % confluent monolayer on the culture dish. The cells used for the experiment had a passage number of n=4. For experiments involving cell compression, cells were placed in solution using trypsinization and were kept in suspension in cell medium during the duration of the experiment (<2 hours). A single-cell solution was prepared by using a diluted solution of two to three hundred cells/mL, and were kept at 37^{o}C during the experiment.

6.2. Single Cell Characterization Experiments

One of the methods for determining the mechanical characteristics of materials is stress relaxation [93]. Using our developed BioMEMS device, we were able to perform a stress relaxation on cells by applying a step compression and measuring the resulting force. Compressions were done for about 2 minutes and the cell was released afterwards. The hMSC cell was placed on the device between the sensor and actuator, as shown in Fig.114, and compressed by 20% of its diameter. The cell's diameter was measured before and after compression, with the data being incorporated into the fits from the models.

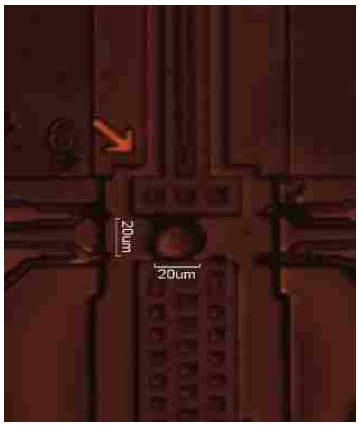

Figure 114. Single hMSC on device prior to a creep test.

The hMSC cells were cultured and used immediately after harvesting for experiment. The cells were diluted in hMSC cell medium to get single suspended cells solution. The forward motion was generated using an external piezo driver and was translated to the on-chip actuator by using a probe tip. The resulting force was measured using a piezoresistive on-chip sensor. Acquired at a sampling rate of 40 kHz and a sample window of 500 ms, the amplified signal was then filtered with a 4th-order infinite impulse response (IIR) bandpass Butterworth filter in LabView. The applied and measured deformation through the piezo driver is shown in Fig. 115. The corresponding force-time curve is shown in Fig. 116. A drift, possibly due to thermal noise, was observed in this data, but was eliminated from the force data.

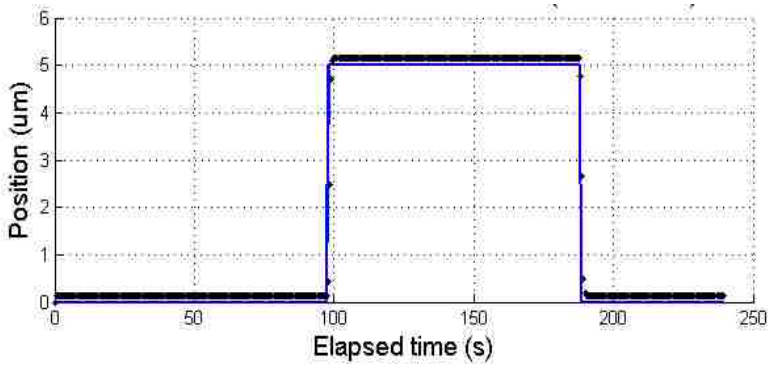

Figure 115. Controlled (blue line) and measured (black dots) deformation applied to the cell versus time.

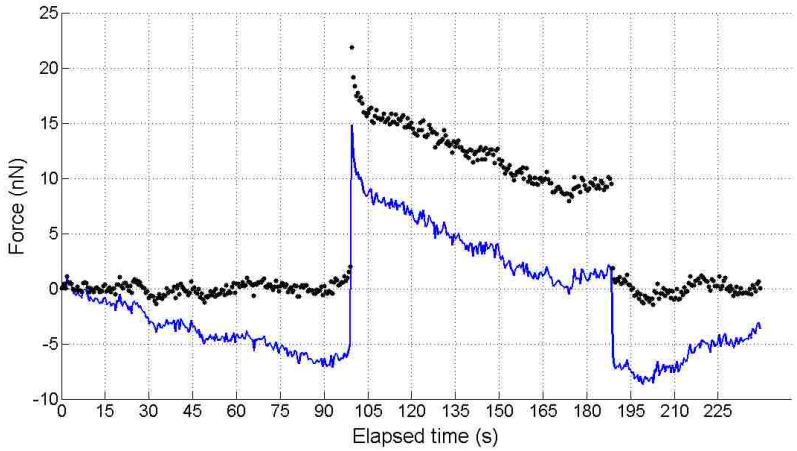

Figure 116. Raw force data (back-dotted line), and force data after compensating for the drift (blue line).

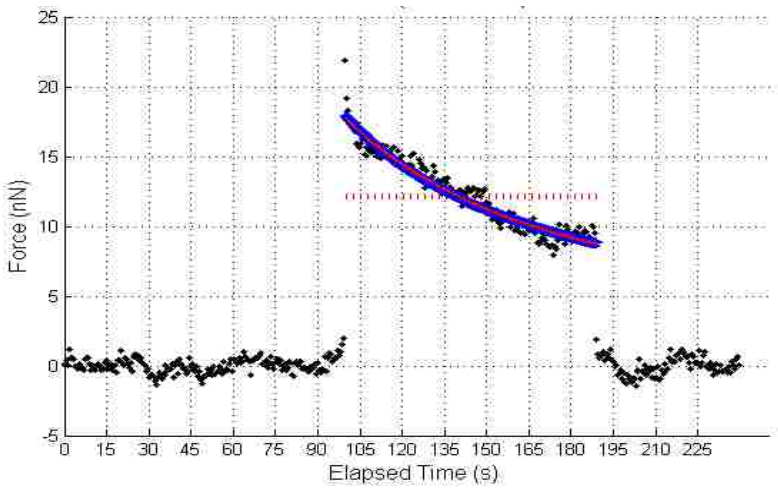

Figure 117. Experimental data (black-dotted line), elastic fit (red-dashed line) and viscoelastic fits i.e. Kelvin model (blue-solid line) and SLS model (pink-solid line) are depicted. The viscoelastic models visually coincide and fit the data closely.

6.3. Elastic and Viscoelastic Models

Displacement application and stress relaxation response measurements were used to determine the elastic and viscoelastic properties of hMSC cells. Three different fits were used to generate mechanical properties from experimental data. The linear-elastic model considers the cell to be a spherical solid with homogenous, elastic properties governed by Hooke's law [94]. The elastic fit and viscoelastic fits, including the Kelvin model and SLS models for a typical force response, are included in Fig. 117. Drift was removed from the data before modeling. Young's modulus by elastic model was determined to be 205Pa. The equation describing force of the Kelvin model can be written as the following:

$$f(t) = \frac{4}{3}\left(\frac{1}{\frac{1}{E1}+\frac{1}{E2}\left(1+e^{-\frac{t}{\tau}}\right)}\right)R^{0.5}\nabla d^{1.5} \quad \text{where } \tau = \frac{\eta}{E2} \tag{47}$$

where E1, E2 and η are parameters in the Kelvin model which, depicted in Fig. 118, generated an E1 modulus of 398.4Pa, an E2 modulus of 32.9Pa and a viscosity of 3.3e4 Pa-s. (R^2=87%).

The force expression for SLS model can be written as the following:

$$f(t) = \frac{4}{3}\left(\frac{1}{\left(\frac{1}{E1+E2}\right)+\frac{E2}{E1}\left(\frac{1}{E1+E2}\right)\left(1-e^{-\frac{t}{\tau}}\right)}\right)R^{0.5}\nabla d^{1.5} \text{ where } \tau = \frac{\eta}{E2} \quad (48)$$

where E1, E2 and η are parameters in the SLS model which, shown in Fig. 119, produced an elastic modulus of 397 Pa for E2, 2.8e-4 Pa for E1 and a viscosity of 3.4e4 Pa-s (R^2=88%). The very small value for E1 could be because the model did not represent the peak of data at the beginning perfectly. The applied strain was equal or less than 20 % of the diameter of the cell, therefore linear viscoelastic regime was still applicable. For the cells in our study, and also in the literature, the SLS model closely exhibits the cell response [91].

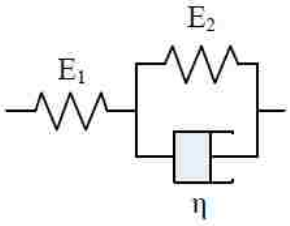

Figure 118. Kelvin Model.

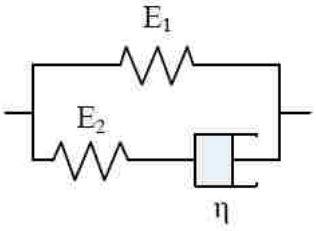

Figure 119. SLS Model.

6.4. Results and Discussion

The feasibility of mechanically testing suspended single hMSC cells using step compression was demonstrated. Elastic and viscoelastic properties of hMSC cells were extracted using three different models. The derived biomechanical properties are listed in Table 38. The average Young's modulus by the elastic model was determined to be

0.69kPa. The Kelvin model generated an average E1 modulus of 1.18kPa, an E2 modulus of 0.064kPa and an average relaxation time constant of 517.1s. Fitting the force-deformation curve to the SLS model, produced an average E1 modulus of 0.022kPa, a modulus of 1.15kPa for E2, and a relaxation time constant of 29.9s.

Table 38. Elastic and Viscoelastic Properties of hMSC Cells Measured by Step Compression.

		a) Elastic Model	b) Kelvin Model	c) SLS Model
Elastic	**E (kP**a)	0.240±0.030	-	-
Viscoelastic	**E1 (kPa)**		0.780±0.330	0.00013±0.00012
	E2 (kPa)	-	0.020±0.010	0.780±0.330
	τ (s)	-	1007±992	29.4±28.5
	Viscosity (kPa-s)	-	22.7±8.96	23.0±9.54

The measured values are average ± standard deviation. R^2 values for the fits were in the range of 88 % to 49%. τ is defined in equations (47) and (48).

Other methods, such AFM, micropipette aspiration and optical methods have been developed to measure the biomechanical characteristics of single hMSC cells. Results of AFM and micropipette aspiration methods are compared in Table 39. The reported values from previous studies were interpreted with the SLS model in order to eliminate variations because of different models. Our findings are generally in agreement with previous reports on the biomechanical properties of hMSCs measured with the other techniques, but there are also differences (See Table 39 for comparison). The reported values from the AFM method for cell modulus are larger than our values, likely due to the larger applied displacement in AFM [16, 17]. The micropipette aspiration method determined a lower Young's modulus and viscosity than AFM and our method [18, 20]. The differences in results may be caused by cell source, culture environment, culturing substrate, testing device and method.

It should be noted that the adherent cells in previous reports exhibited different mechanical properties and in most cases were stiffer [17]. This may be the reason why the spherical hMSC cells in our study showed lower modulus values in comparison to the attached cells

in other methods such as AFM. This might also be the cause of smaller reported values for the micropipette aspiration method, as the cells were also suspended in that method. It is also possible that this could be due to the absence of stress fibers in the suspended state.

One of the benefits of interrogating cells in the suspended state is the ability to represent the alternate extreme mechanical extracellular environment relevant to cell delivery, allowing for the investigation of fundamental cellular mechanisms such as post-detachment remodeling and rheology. Additionally, cells show less passage-dependent trends in mechanical behavior, suggesting this approach could be a more robust biomarker [92].

Due to differences in methods used, applied displacements, cell culture surface and cell preparation, a direct comparison between these types of experiments is difficult, with variations existing among the results of the same method.

Table 39. Comparison of Biomechanical Properties of hMSC Cells Obtained via Different Methods, our results are included in the Step Compression column on the right.

		a) AFM [19]		**b) AFM** [16]	**c) Micropipette Aspiration** [18]	**d) Step Compression**
	Cell Shape	Spherical	Spread	Spherical	Spread	Spherical
Elastic	**E (kP**a)	2.50±1.80	3.20±2.20	2.00±0.50	-	0.240±0.030
Viscoelastic	**E_1 (kPa)**	0.47±0.52	2.20±1.90	-	0.250±0.080	0.00013±0.00012
	E_2 (kPa)	4.82±0.83	2.03±0.45	-	0.340±0.280	0.780±0.330
	τ (s)	9.60±11.30	10.1±16.8	-	7.92±1.48	29.4±28.5
	Viscosity (kPa-s)	46.3±19.29	20.5±15.68	-	2.71±1.63	23.0±9.54

6.5. Modeling the Viscoelastic Cell Behavior Using Tensegrity

Tensegrity is a structural principle based on the use of isolated components, consisting of a set of compression and tension members arranged in such a way that the compressed members do not touch each other and the pre-stressed tensile members delineate the system spatially. This allows for the whole structure to be in the mechanical equilibrium. Starting with pioneering work of Ingber [95], a number of researchers have utilized this powerful approach to model cell behavior. The six-strut tensegrity model was used to predict the static elastic modulus of cells [96]. A cell is modeled as a network of interconnected tension-bearing elements, such as actin filaments, and compression-bearing elements, such as microtubules, to provide shape and stability to the entire cell [97]. Several models are based on the idea that the mechanical behavior of a cell mainly depends on the filamentous structure, or cytoskeleton, by means of its components, microtubules, microfilaments and intermediate filaments, which form an integrated network. A number of models have been developed using numerical and computational tools [98]. Some models treat the cytoskeleton as a pre-stressed cable network in order to predict the elastic properties and emerging forces by deforming the model mechanically [99], while another mechanical model was proposed by Maurin [100] to investigate the form-finding structure of a cytoskeleton by using a granular structure, representing the interconnected network of filaments in the cytoskeleton. The tensegrity cell model utilized here consists of thirty components, including six struts representing microtubules and twenty-four cables representing microfilament of the cytoskeleton (Fig. 120).

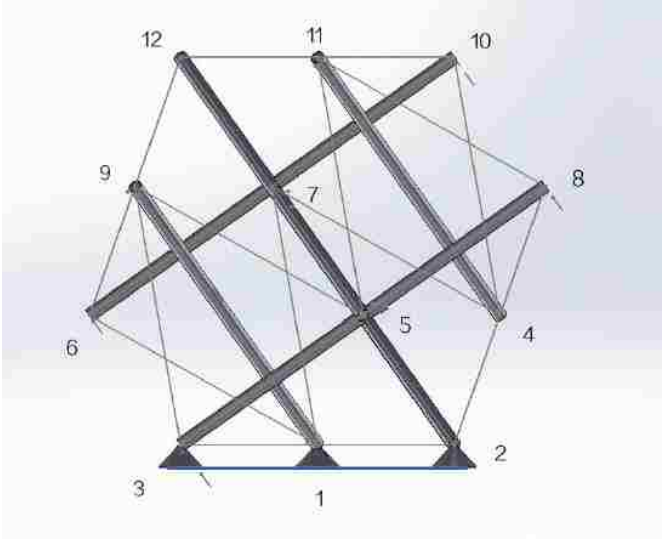

Figure 120. Cytoskeletal tensegrity model. The thick bars represent 3 pairs of mutually parallel microtubules (struts) and thin lines represent microfilaments (cables).

Typically, one node needs to be attached to the surface to simulate the focal adhesion. Rest of the nodes are free, allowing for morphing or geometry change when external or internal forces are applied to the cell. ANSYS Mechanical APDL[1] was used as a finite element analysis tool to calculate internal forces and deformations in each of the thirty elements (cables and struts) due to the applied external excitation.

In this study, a 30-member tensegrity structure is used to simulate a cell's viscoelastic behavior. The mechanical properties of microtubules and microfilaments were assigned on the basis of the experiment implemented by Mickey et al.[101]. In our study, most of the parameters of cells' properties were based on this experiment, but the value of the cross section was enlarged to assure that the whole structure is stable under the external force. For the elastic case, the physical and mechanical properties of the cellular members are displayed in Table 40.

[1] ANSYS, Inc., Canonsburg, PA, USA

Table 40. Physical and Mechanical Properties of the Cellular Members in the Cell Model.

Properties	Micro-tubules	Micro-filaments
Radius (nm)	36.0	18.00
Cross-sectional area (nm^2)	4070	1017
E (GPa) (Elastic modulus)	1.20	2.60
Poison's ratio	0.300	0.300

We modeled stiffer micro-tubules as internal elastic members while more flexible micro-filaments are modeled as internal viscoelastic members of the cell, resulting in a viscoelastic response for the whole cell. In ANSYS, one can model viscoelastic behavior by utilizing a Prony series, which describes the Wiechert model (Fig. 121).

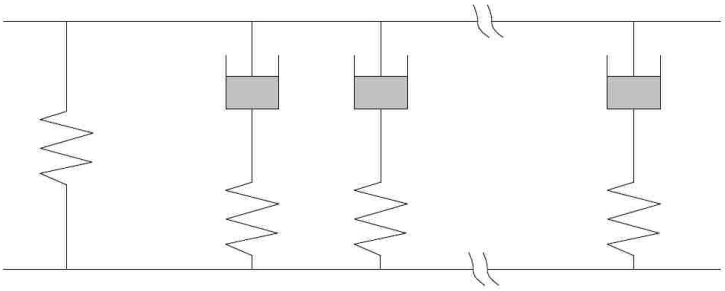

Figure 121. Schematic of the Wiechert model.

The Wiechert model is composed of a spring in parallel with an infinite set of Maxwell units i.e. spring-dashpot elements. The Wiechert model containing only one set of spring-dashpot element represents the SLS model. This model was used in the experimental data curve-fitting. The mathematical representation for a Prony series is given in (49):

$$E(t) = E_0 + \sum_{n=1}^{\infty} E_n \exp(-\frac{t}{\tau}) \tag{49}$$

Using a one-term Prony series, E(t) can be written as the following:

$$E(t) = E_1 + E_2 \exp(-\frac{t}{\tau}) \tag{50}$$

As shown from the SLS model that was previously derived for the single cell, E_1 = 0.022 kPa, E_2 = 1.15 kPa and τ = 29.9 s. We treated the previously determined viscoelastic values for a single cell as the starting values for mechanical properties of the viscoelastic microfilament members inside the cell. Therefore, we can write the E (t) as (51):

$$E(t) = 0.022 + 1.15 * \exp(-\frac{t}{29.9}) \tag{51}$$

Denoting the relative shear modulus as α^G , and the relaxation time constant as τ, the ANSYS input parameters were calculated as follows:

$E_0 = E_1 + E_2 = 0.022 + 1.15 = 1.172$ (52)

$$\alpha_1^G = \frac{E_2}{E_0} = 0.98 \tag{53}$$

$$\tau = 29.9\ (s) \tag{54}$$

The transient analysis was used to model the behavior of a cell under the constant deformation of 5 microns. The pre-stress was applied [102, 103] and the top surface nodes, i.e. nodes 10, 11 and 12, were given a displacement of 5 microns in the negative z direction. From the experimental data, the total elapsed time of the test was 90 seconds, the initial force was about 18nN and the final force was about 9nN, thus the ratio of initial force to final force was 2. From the results obtained by the tensegrity viscoelastic model, the elapsed time for the applied displacement is 90 seconds, the starting force is about 13.5 nN and the final force is about 8.2 nN, producing a ratio of starting force to the final force of 1.65. It should be mentioned that the parameters derived here on the basis of the SLS model represent viscoelastic behavior of the whole cell. The tensegrity model needs viscoelastic properties for each microfilament, thus these values do not have to be the same. In order to closely match the experimental results, the experimental average values of elastic modulus and relaxation time constant were modified (Table 41). These changes are within the standard deviation range of the measured values.

Table 41. Comparison of Modified and Experimental Parameters.

	Experimental value	Modified value
Elastic modulus of micro-tubules (GPa)	1.200*	1.536
α (microfilaments)	0.98	0.98
τ (s) (microfilaments)	29.9	20.9

*[101]

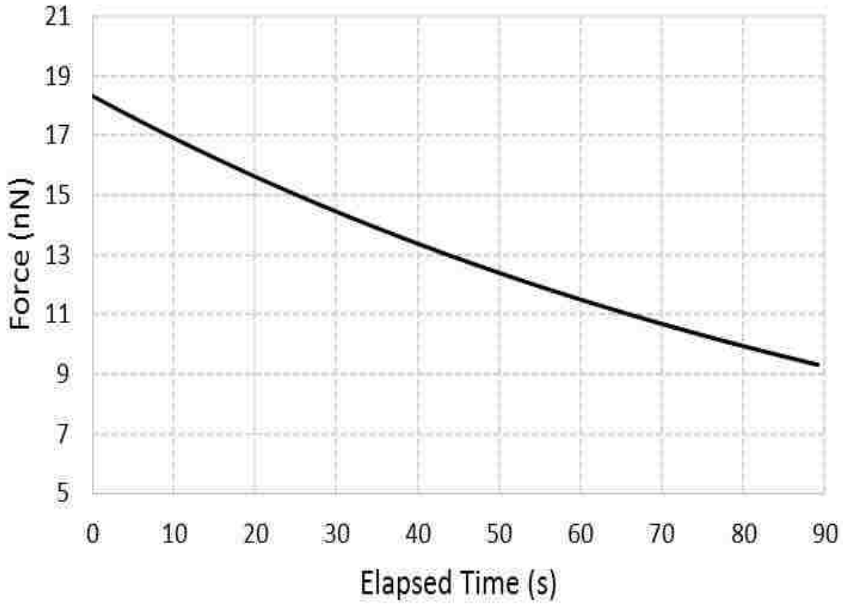

Figure 122. Reaction force versus time (with modified parameters).

Using the modified values (Table 40) as input into our model, one can obtain a modified curve (Fig. 122) that shows a starting force at 18 nN and the final force at 9 nN. These values more closely represent the experimental data.

The experimental data together with SLS and tensegrity models are presented in Fig.123. The first approach assumes the cell is a single homogenous object and the tensegrity modeling method simulates mechanical behavior of the cell considering the mechanical characteristics of internal components such as microfilaments or microtubules. The difference between the experimental data, SLS and tensegrity models is relatively small and can be attributed to inaccuracies in the mechanical properties of the microfilaments

and microtubules used in the current model and to the low number of components used to model viscoelastic cell behavior. Also other internal members such as nuclei were not being considered here and could be added in the future to make the model more accurate.

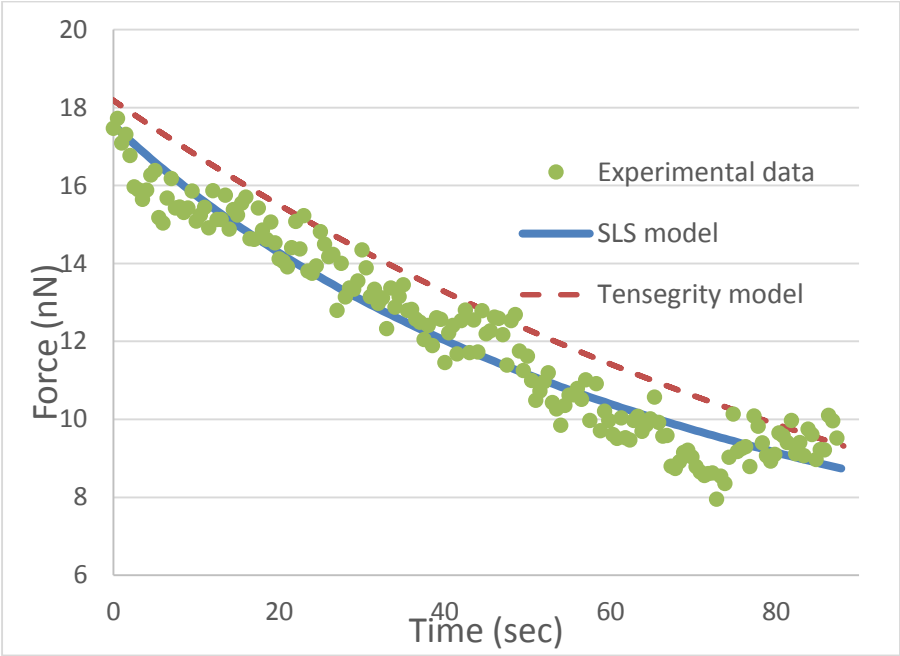

Figure 123. Comparison of the force generated by tensegrity model, which considers viscoelastic. parameters of internal structure of the cell, versus SLS model that models the cell as a continuum.

Overall, our results for hMSC viscoelastic properties are close to the reported values. Since biomechanical properties can also act as a biomarker representing a special type of tissue [17], this method may also have applications in the sorting and classification of different cell types. Furthermore, studying mechanical properties of hMSC cells can have a great impact on cartilage regeneration and cartilage tissue engineering, leading to a cure for heart disease [104]. This approach utilizes a miniaturized device and is cost effective in comparison with AFM and could be arrayed to characterize more cells at the same time.

Elastic, viscoelastic and tensegrity models were utilized to describe mechanical behavior of hMSC cells. Cells exist in extracellular matrices inside the body and they need to conform to various surfaces and change their shape. In order to model the cell mechanical behavior and interactions within different surfaces, it is necessary to study viscoelastic

properties of the cells, taking internal structure into account. To study a cell's viscoelastic behavior more realistically, it internal structure was partially simulated by a tensegrity model. By comparing the simulation results with the experimental results, the plot obtained by the computational model matched the curve obtained by the experiment. The tensegrity model has the potential to be improved by including the effect of more internal members of the cell and therefore more accurately modelling the mechanical behavior of living cells. In conclusion, this study presents experimental data of mechanical properties of hMSC cells measured by using as BioMEMS device and shows the feasibility of the SLS model and the tensegrity approach in representing the viscoelastic behavior of a single detached hMSC cell. The cell was modeled both as a continuum by SLS model and as a network of microtubules and microfilaments with tensegrity. In the future, the tensegrity approach can be used to model the cell's motion and mechanical behavior in collective cell migration, which can have potential applications in cancer studies and tissue engineering. In the future work, we would like to validate the model for single cells also for cell aggregates.

6.6. Force-Deformation Models

In order to meet the design specifications, the required force range for characterization of EBs was calculated according to the literature values for Young's modulus of hMSC cells and the equation for force-deformation.

For explaining the behavior of viscoelastic spherical objects such as cells under compression, a model based on the standard linear solid model and Hertz contact mechanics is developed [105]. Based on this model, force and displacement are related as follows:

$$F = \frac{4}{3}\frac{E}{1-v^2}R^{0.5}d^{1.5} \tag{55}$$

where E is Young's modulus, v is Poisson's ratio, d is displacement and R is radius of the cell. This equation used to find the reaction force in the following table and graphs. The average size of EBs is ranging from 250 μm to 290 μm in diameter. Because of high aspect

ratio of device and fabrication limitations, we have primarily designed our system for smaller size of 250 µm diameter size. Force-deformation was plotted for an embryoid body diameter of 250 µm in Fig. 124 for the Young's modulus range in literature [16, 20].

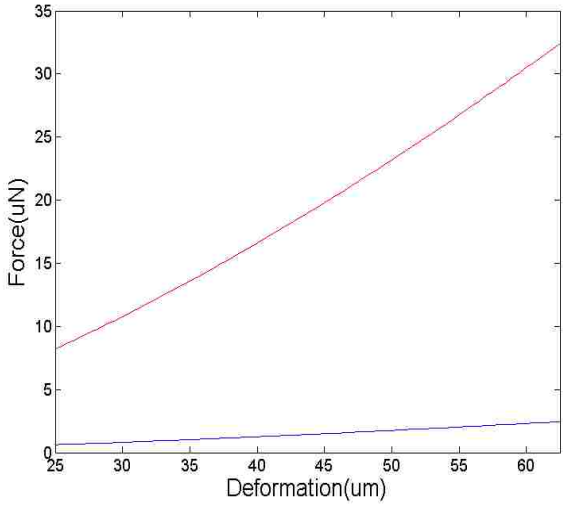

Figure 124. Force-deformation using standard linear solid model and Hertz model for an embryoid body with diameter of 250 µm, E_Minimum=0.25 kPa (blue) and E_Maximum=3.3 kPa (red)

Different Young's moduli were reported from different methods of characterization [16, 20]. Based on Young's modulus for hMSC single cells from literature, forces needed to compress the embryoid body were calculated using equation 55. Assuming the same Young's modulus for embryoid bodies as single hMSC cell, forces for 10% and 25% displacement for different diameters of the embryoid bodies based on values from different methods for measuring cell stiffness such as AFM and micropipette aspiration are given in Table 42 and Table 43. These forces are believed to be needed to be provided by the designed actuator in order to compress the embryoid bodies.

Table 42: Force range based on AFM method (Young's modulus of 0.6 kPa to 3.3 kPa) [16]

Predicted force	Diameter = 250 μm
10% deformation	1.49 μN - 5.89 μN
25% deformation	8.2 μN - 32.4 μN

Table 43: Force range based on micropipette aspiration method (Young's modulus of 0.25 kPa to 1.18 kPa) [20]

Predicted force	EB Diameter = 250 μm
10% deformation	0.62 μN - 2.46 μN
25% deformation	2.93 μN - 11.6 μN

The summary of the corresponding design specifications is given in Table 44. The force range was determined based on the Young's modulus range from Table 42 and Table 43. The maximum required force is determined based on the reaction force and displacement needed for characterization.

Table 44: Design specifications for EB characterization system

Diameter of Embryoid Body (μm)	Displacement (μm)	Device Height (μm)	Minimum Feature Width (μm)	Young's Modulus Range* (kPa)	Force (μN)
250	25	150	8	0.25 - 3.3	0.6 - 2.5
250	62.5	150	8	0.25 - 3.3	8.2 - 32.4

* [16, 20]

Conclusion and Outlook

In this research, a micro-electro-mechanical-system for measuring the mechanical properties of cell aggregates was designed and developed. A novel high aspect ratio micro-actuator that can provide five predefined large displacements up to 100 μm was designed and modeled using finite element analysis. Five displacements include 52.5 μm, 65 μm, 77.5 μm, 90 μm and 100 μm which correspond to 5% to 25% of a cell aggregate with diameter of 250 μm. 40 μm is added to these numbers because the gap for target placement is 290 μm and the device needs to move 40 μm to touch the cell aggregate first.

A fabrication process was successfully developed for etching the high aspect ratio structure. This included both DRIE recipe and photolithography recipe for a thick masking layer of photoresist. A deep etching recipe for fabrication of high aspect ratio MEMS with different trench sizes down to 8 μm was developed and process was tuned to remove the silicon grass contamination. Aspect ratio of device was 20 and the mask consists of features and trenches with different sizes including 8 μm trenches to 250 μm wide areas.

Static and dynamic characterization was performed for the bank of comb drive actuators. Five designed displacements up to 100 μm were successfully demonstrated by the actuator in the air and a large displacement of 50 μm was recorded for the first time by electrostatic actuation in DI water. By addition of insulation layer with ALD alumina for the metal electrodes, this actuator may be characterized in ionic medium in the future. The fabrication process method for addition of the insulation layer is discussed in the fabrication and characterization chapter of this dissertation. In AC characterization experiments, resonant frequency of this actuator was measured to be 244 Hz and the stiffness of the structure was accordingly determined.

The etch rate of Al_2O_3 and TiO_2 thin films deposited by ALD in vapor HF was for the first time characterized and material characterization of etched oxides in vapor HF was performed using XPS method. ALD method has advantages in comparison with other deposition techniques. This method provides a conformal coverage for high aspect ratio devices and can be performed at relatively low temperatures as opposed to other techniques

such as Chemical Vapor Deposition (CVD). ALD layers may be used as protective and insulation layers for microelectronics and specifically BioMEMS applications enabling operation of biomedical tools in ionic environments. The measured etch rate of ALD layers in wet etching method is much larger than the vapor HF method. This shows vapor HF release is more compatible with ALD layers than wet etching process. In the future we will investigate the effect of deposition temperature and annealing on the etch rate of ALD layers.

A quadrupole electrode configuration for contactless positioning of cell aggregates was integrated into the system. The application of these DEP electrodes which utilize MHz voltages for trapping of microspheres and single fibroblast cells were modelled and experimentally verified. In the future, the performance needs to be validated for trapping cell aggregates.

This device currently provides large displacements which are needed to characterize a viscoelastic target such as a cell aggregate in the air and has the capability to perform in DI water. In the future, more improvement of the tool will be needed to provide required deflections in ionic medium, since the cells need to be characterized while they are inside ionic cell medium. Ionic screening and electrochemical problems may arise in ionic medium and they may be avoided by high frequency actuation and electrode insulation. Further performance improvements of the actuator, increasing repeatability and reliability also involves developing a process to avoid DRIE undercut and to enhance quality of sidewalls. In the future, the biomedical application of the device in measuring mechanical properties of cell aggregate could be further investigated. This novel microactuator can provide actuation for other application such as micro-optics and microfluidics in addition to biomedical applications.

References

[1] M. D. Vahey and J. Voldman, "Isodielectric separation and analysis of cells," *Single-Cell Analysis: Methods and Protocols,* pp. 53-63, 2012.

[2] S. Tatic-Lucic and M. Gnerlich, "Implementation of BioMEMS for determining mechanical properties of biological cells," in *MRS Proceedings,* 2012, pp. mrsf11-1415-ii05-01.

[3] J. Guck, S. Schinkinger, B. Lincoln, F. Wottawah, S. Ebert, M. Romeyke, D. Lenz, H. M. Erickson, R. Ananthakrishnan and D. Mitchell, "Optical deformability as an inherent cell marker for testing malignant transformation and metastatic competence," *Biophys. J.,* vol. 88, pp. 3689-3698, 2005.

[4] D. Li, J. Zhou, F. Chowdhury, J. Cheng, N. Wang and F. Wang, "Role of mechanical factors in fate decisions of stem cells," *Regenerative Medicine,* vol. 6, pp. 229-240, 2011.

[5] J. B. Wyckoff, J. G. Jones, J. S. Condeelis and J. E. Segall, "A critical step in metastasis: in vivo analysis of intravasation at the primary tumor," *Cancer Res.,* vol. 60, pp. 2504-2511, May 1, 2000.

[6] E. L. Baker, R. T. Bonnecaze and M. H. Zaman, "Extracellular matrix stiffness and architecture govern intracellular rheology in cancer," *Biophys. J.,* vol. 97, pp. 1013-1021, 2009.

[7] H. Yu, C. Y. Tay, W. S. Leong, S. C. W. Tan, K. Liao and L. P. Tan, "Mechanical behavior of human mesenchymal stem cells during adipogenic and osteogenic differentiation," *Biochem. Biophys. Res. Commun.,* vol. 393, pp. 150-155, 2010.

[8] M. F. Pittenger, A. M. Mackay, S. C. Beck, R. K. Jaiswal, R. Douglas, J. D. Mosca, M. A. Moorman, D. W. Simonetti, S. Craig and D. R. Marshak, "Multilineage potential of adult human mesenchymal stem cells," *Science,* vol. 284, pp. 143-147, Apr 2, 1999.

[9] G. Friedl, H. Schmidt, I. Rehak, G. Kostner, K. Schauenstein and R. Windhager, "Undifferentiated human mesenchymal stem cells (hMSCs) are highly sensitive to mechanical strain: transcriptionally controlled early osteo-chondrogenic response in vitro," *Osteoarthritis and Cartilage,* vol. 15, pp. 1293-1300, 2007.

[10] R. M. Hochmuth, "Micropipette aspiration of living cells," *J. Biomech.,* vol. 33, pp. 15-22, 2000.

[11] R. Mahaffy, S. Park, E. Gerde, J. Käs and C. Shih, "Quantitative analysis of the viscoelastic properties of thin regions of fibroblasts using atomic force microscopy," *Biophys. J.*, vol. 86, pp. 1777-1793, 2004.

[12] D. Shin and K. Athanasiou, "Cytoindentation for obtaining cell biomechanical properties," *Journal of Orthopaedic Research*, vol. 17, pp. 880-890, 1999.

[13] A. R. Bausch, F. Ziemann, A. A. Boulbitch, K. Jacobson and E. Sackmann, "Local measurements of viscoelastic parameters of adherent cell surfaces by magnetic bead microrheometry," *Biophys. J.*, vol. 75, pp. 2038-2049, 1998.

[14] M. Gnerlich, "Microelectromechanical Actuator and Sensor System for Measuring the Mechanical Compliance of Biological Cells," 2011.

[15] C. L. Mummery, J. Zhang, E. S. Ng, D. A. Elliott, A. G. Elefanty and T. J. Kamp, "Differentiation of human embryonic stem cells and induced pluripotent stem cells to cardiomyocytes: a methods overview," *Circ. Res.*, vol. 111, pp. 344-358, Jul 20, 2012.

[16] D. Docheva, D. Padula, C. Popov, W. Mutschler, H. Clausen-Schaumann and M. Schieker, "Researching into the cellular shape, volume and elasticity of mesenchymal stem cells, osteoblasts and osteosarcoma cells by atomic force microscopy," *J. Cell. Mol. Med.*, vol. 12, pp. 537-552, 2008.

[17] E. M. Darling, M. Topel, S. Zauscher, T. P. Vail and F. Guilak, "Viscoelastic properties of human mesenchymally-derived stem cells and primary osteoblasts, chondrocytes, and adipocytes," *J. Biomech.*, vol. 41, pp. 454-464, 2008.

[18] Wenxiao Pan, E. Petersen, Ning Cai, Gang Ma, Jian Run Lee, Zhiqin Feng, Kin Liao and K. W. Leong, "Viscoelastic properties of human mesenchymal stem cells," in *2005 IEEE Engineering in Medicine and Biology 27th Annual Conference*, 2005, pp. 4854-4857.

[19] E. M. Darling, S. Zauscher, J. A. Block and F. Guilak, "A Thin-Layer Model for Viscoelastic, Stress-Relaxation Testing of Cells Using Atomic Force Microscopy: Do Cell Properties Reflect Metastatic Potential?" *Biophys. J.*, vol. 92, pp. 1784-1791, 2016/07, .

[20] F. Guilak, J. R. Tedrow and R. Burgkart, "Viscoelastic properties of the cell nucleus," *Biochem. Biophys. Res. Commun.*, vol. 269, pp. 781-786, 2000.

[21] N. Moghimi, D. R. Decker and S. Tatic-Lucic, "Modeling and measurement of dielectrophoretic force and 2-D trajectories of microspheres in quadrupole electrode configuration," in *Sensors, 2012 IEEE*, 2012, pp. 1-4.

[22] A. Gooray, G. Roller, P. Galambos, K. Zavadil, R. Givler, F. Peter and J. Crowley, "Design of a MEMS ejector for printing applications," *J Imaging Sci Technol,* vol. 46, pp. 415-421, 2002.

[23] L. Lu, K. S. Ryu and C. Liu, "A magnetic microstirrer and array for microfluidic mixing," *J Microelectromech Syst,* vol. 11, pp. 462-469, 2002.

[24] M. E. S Shoji and, "Microflow devices and systems," *J Micromech Microengineering,* vol. 4, pp. 157, 1994.

[25] T. Gregory and A. Kovacs, "Micromachined transducers sourcebook," *Kovacs, WCB McGraw-Hill,* pp. 19-154, 1998.

[26] D. J. Beebe, J. S. Moore, J. M. Bauer, Q. Yu, R. H. Liu, C. Devadoss and B. Jo, "Functional hydrogel structures for autonomous flow control inside microfluidic channels," *Nature,* vol. 404, pp. 588-590, 2000.

[27] M. A. Unger, H. P. Chou, T. Thorsen, A. Scherer and S. R. Quake, "Monolithic microfabricated valves and pumps by multilayer soft lithography," *Science,* vol. 288, pp. 113-116, Apr 7, 2000.

[28] T. L. Sounart, T. A. Michalske and K. R. Zavadil, "Frequency-dependent electrostatic actuation in microfluidic MEMS," *J Microelectromech Syst,* vol. 14, pp. 125-133, 2005.

[29] D. J. Bell, T. Lu, N. A. Fleck and S. M. Spearing, "MEMS actuators and sensors: observations on their performance and selection for purpose," *J Micromech Microengineering,* vol. 15, pp. S153, 2005.

[30] V. Mukundan and B. L. Pruitt, "MEMS Electrostatic Actuation in Conducting Biological Media," *Journal of Microelectromechanical Systems : A Joint IEEE and ASME Publication on Microstructures, Microactuators, Microsensors, and Microsystems,* vol. 18, pp. 405-413, 04/01, 2009.

[31] T. L. Sounart, T. A. Michalske and K. R. Zavadil, "Frequency-dependent electrostatic actuation in microfluidic MEMS," *J Microelectromech Syst,* vol. 14, pp. 125-133, 2005.

[32] D. J. Bell, T. Lu, N. A. Fleck and S. M. Spearing, "MEMS actuators and sensors: observations on their performance and selection for purpose," *J Micromech Microengineering,* vol. 15, pp. S153, 2005.

[33] V. Giurgiutiu, C. A. Rogers and Z. Chaudhry, "Energy-based comparison of solid-state induced-strain actuators," *J Intell Mater Syst Struct,* vol. 7, pp. 4-14, 1996.

[34] (14 Feb. 2011). *Comparison of EAPs with Other Actuator Technologies* [Jet Propulsion Laboratory (JPL)]. Available: http://ndeaa.jpl.nasa.gov/nasa-nde/lommas/eap/actuators-comp.pdf.

[35] D. Sameoto, T. Hubbard and M. Kujath, "Operation of electrothermal and electrostatic MUMPs microactuators underwater," *J Micromech Microengineering,* vol. 14, pp. 1359, 2004.

[36] H. V. Panchawagh, D. Serrell, D. S. Finch, T. Oreskovic and R. L. Mahajan, "Design and characterization of a BioMEMS device for in-vitro mechanical stimulation of single adherent cells," in *ASME 2005 International Mechanical Engineering Congress and Exposition,* 2005, pp. 19-25.

[37] V. Mukundan and B. Pruitt, "Differential electrode design for electrostatic actuator in conducting media," in *The 14th International Conference on Solid-State Sensors, Actuators and Microsystems,* 2007, .

[38] W. C. Tang, T. H. Nguyen, M. W. Judy and R. T. Howe, "Electrostatic-comb drive of lateral polysilicon resonators," *Sensors and Actuators A: Physical,* vol. 21, pp. 328-331, 1990.

[39] L. Lin, C. Nguyen, R. T. Howe and A. P. Pisano, "Microelectromechanical filters for signal processing," in *Micro Electro Mechanical Systems, 1992, MEMS'92, Proceedings. an Investigation of Micro Structures, Sensors, Actuators, Machines and Robot. IEEE,* 1992, pp. 226-231.

[40] V. P. Jaecklin, C. Linder, N. F. de Rooij, J. M. Moret, R. Bischof and F. Rudolf, "Novel polysilicon comb actuators for xy-stages," in *Micro Electro Mechanical Systems, 1992, MEMS '92, Proceedings. an Investigation of Micro Structures, Sensors, Actuators, Machines and Robot. IEEE,* 1992, pp. 147-149.

[41] C. Kim, A. P. Pisano and R. S. Muller, "Silicon-processed overhanging microgripper," *J Microelectromech Syst,* vol. 1, pp. 31-36, 1992.

[42] D. Loconto and R. Muller, "High-sensitive micromechanical electrostatic voltmeter," in *Proc. 7th Int. Conf. Solid-State Sens. Actuators, Transducers' 93 (Yokohama, Japan, 1993),* 1993, pp. 878-881.

[43] E. J. Garcia and J. J. Sniegowski, "Surface micromachined microengine as the driver for micromechanical gears; sponsor org.: USDOE, washington, DC (united states)," in 1995, .

[44] Y. Gerson, S. Krylov, B. Ilic and D. Schreiber, "Design considerations of a large-displacement multistable micro actuator with serially connected bistable elements," *Finite Elements Anal. Des.,* vol. 49, pp. 58-69, 2012.

[45] R. Legtenberg, A. Groeneveld and M. Elwenspoek, "Comb-drive actuators for large displacements," *J Micromech Microengineering,* vol. 6, pp. 320, 1996.

[46] V. Jaecklin, C. Linder, N. De Rooij, J. Moret and R. Vuilleumier, "Optical microshutters and torsional micromirrors for light modulator arrays," in *Micro Electro Mechanical Systems, 1993, MEMS'93, Proceedings an Investigation of Micro Structures, Sensors, Actuators, Machines and Systems. IEEE.* 1993, pp. 124-127.

[47] O. Tabata, R. Asahi, N. Fujitsuka, M. Kimura and S. Sugiyama, "Electrostatic driven optical chopper using SOI wafer," in *Technical Digest, Transducers '93, 7th International Conference on Solid-State Sensors and Actuators,* 1993, pp. 124-127.

[48] P. Y. Chen and R. S. Muller, "Microchopper-modulated IR microlamp," in *Proc. IEEE Solid-State Sens. Actuators Workshop,* Hilton Head Island, SC, 1994, pp. 239-242.

[49] J. D. Grade, H. Jerman and T. W. Kenny, "Design of large deflection electrostatic actuators," *J Microelectromech Syst,* vol. 12, pp. 335-343, 2003.

[50] T. Beléndez, C. Neipp and A. Beléndez, "Large and small deflections of a cantilever beam," *European Journal of Physics,* vol. 23, pp. 371, 2002.

[51] V. Mukundan, "Electrostatic Actuators in Aqueous Ionic Media for Applications in Cell Mechanics," 2009.

[52] N. Gadish and J. Voldman, "High-throughput positive-dielectrophoretic bioparticle microconcentrator," *Anal. Chem.,* vol. 78, pp. 7870-7876, 2006.

[53] R. S. Thomas, H. Morgan and N. G. Green, "Negative DEP traps for single cell immobilisation," *Lab on a Chip,* vol. 9, pp. 1534-1540, 2009.

[54] S. Minnikanti, D. Reyes, R. C. Aguilar, J. Pancrazio, M. Gaitan and N. Peixoto, "Microfluidic based contactless dielectrophoretic device: Modeling and analysis," in *2010 Annual International Conference of the IEEE Engineering in Medicine and Biology,* 2010, pp. 6506-6509.

[55] A. Rosenthal and J. Voldman, "Dielectrophoretic traps for single-particle patterning," *Biophys. J.,* vol. 88, pp. 2193-2205, 2005.

[56] M. Frenea, S. Faure, B. Le Pioufle, P. Coquet and H. Fujita, "Positioning living cells on a high-density electrode array by negative dielectrophoresis," *Materials Science and Engineering: C,* vol. 23, pp. 597-603, 2003.

[57] Z. R. Gagnon, "Cellular dielectrophoresis: applications to the characterization, manipulation, separation and patterning of cells," *Electrophoresis,* vol. 32, pp. 2466-2487, 2011.

[58] C. H. Kua, Y. C. Lam, I. Rodriguez, C. Yang and K. Youcef-Toumi, "Cell motion model for moving dielectrophoresis," *Anal. Chem.,* vol. 80, pp. 5454-5461, 2008.

[59] J. Voldman, "Dielectrophoretic traps for cell manipulation," in *BioMEMS and Biomedical Nanotechnology*Anonymous Springer, 2006, pp. 159-186.

[60] N. G. Green and H. Morgan, "Separation of submicrometre particles using a combination of dielectrophoretic and electrohydrodynamic forces," *J. Phys. D,* vol. 31, pp. L25, 1998.

[61] D. J. Griffiths, Ed., *"Introduction to Electrodynamics" 3rd Ed.* Upper Saddle River, NJ: Prentice-Hall, 1999.

[62] L. F. Shampine, I. Gladwell and S. Thompson, Eds., *Solving ODEs with MATLAB.* New York: Cambridge University Press, 2003.

[63] G. Fuhr, T. Müller, T. Schnelle, R. Hagedorn, A. Voigt, S. Fiedler, W. M. Arnold, U. Zimmermann, B. Wagner and A. Heuberger, "Radio-frequency microtools for particle and live cell manipulation," *Naturwissenschaften,* vol. 81, pp. 528-535, 1994.

[64] F. Drake, G. Pierce and M. Dow, "Measurement of the dielectric constant and index of refraction of water and aqueous solutions of kcl at high frequencies," *Physical Review,* vol. 35, pp. 613, 1930.

[65] (2012). *Video of trapping a mouse fibroblast cell (NIH3T3)*. Available: http://www.lehigh.edu/~nem210/.

[66] (2012). *Intorduction of silicon deep reactive ion etching (DRIE) process*. Available: http://mnm.physics.mcgill.ca/system/files/Introduction+of+DRIE+process.pptx.pdf.

[67] B. Jong, H. Jansen, M. Boer and G. Krijnen, "Tailored etch-profiles of high aspect ratio trenches to prevent voids after refill with LPCVD SiRN," 2005.

[68] P. Dixit and J. Miao, "Effect of Clamping Ring Materials and Chuck Temperature on the Formation of Silicon Nanograss in Deep RIE," *Journal of the Electrochemical Society,* vol. 153, pp. G771-G777, August 01, 2006.

[69] P. Dixit and J. Miao, "Effect of SF 6 flow rate on the etched surface profile and bottom grass formation in deep reactive ion etching process," *Journal of Physics: Conference Series,* vol. 34, pp. 577, 2006.

[70] K. Jung, W. Song, H. W. Lim and C. S. Lee, "Parameter study for silicon grass formation in Bosch process," *Journal of Vacuum Science & Technology B,* vol. 28, pp. 143-148, 2010.

[71] S. Leopold, C. Kremin, A. Ulbrich, S. Krischok and M. Hoffmann, "Formation of silicon grass: Nanomasking by carbon clusters in cyclic deep reactive ion etching," *Journal of Vacuum Science & Technology B,* vol. 29, 2011.

[72] H. Kim and W. Maeng, "Applications of atomic layer deposition to nanofabrication and emerging nanodevices," *Thin Solid Films,* vol. 517, pp. 2563-2580, 2009.

[73] M. Leskelä and M. Ritala, "Atomic layer deposition chemistry: recent developments and future challenges," *Angewandte Chemie International Edition,* vol. 42, pp. 5548-5554, 2003.

[74] R. L. Puurunen, J. Saarilahti and H. Kattelus, "Implementing ALD layers in MEMS processing," *ECS Transactions,* vol. 11, pp. 3-14, 2007.

[75] C. F. Herrmann, F. W. DelRio, D. C. Miller, S. M. George, V. M. Bright, J. L. Ebel, R. E. Strawser, R. Cortez and K. D. Leedy, "Alternative dielectric films for RF MEMS capacitive switches deposited using atomic layer deposited Al 2 O 3/ZnO alloys," *Sensors and Actuators A: Physical,* vol. 135, pp. 262-272, 2007.

[76] W. Ashurst, Y. Jang, L. Magagnin, C. Carraro, M. Sung and R. Maboudian, "Nanometer-thin titania films with SAM-level stiction and superior wear resistance for reliable MEMS performance," in *Micro Electro Mechanical Systems, 2004. 17th IEEE International Conference on.(MEMS),* 2004, pp. 153-156.

[77] N. D. Hoivik, J. W. Elam, R. J. Linderman, V. M. Bright, S. M. George and Y. Lee, "Atomic layer deposited protective coatings for micro-electromechanical systems," *Sensors and Actuators A: Physical,* vol. 103, pp. 100-108, 2003.

[78] T. Mayer, J. Elam, S. George, P. Kotula and R. Goeke, "Atomic-layer deposition of wear-resistant coatings for microelectromechanical devices," *Appl. Phys. Lett.,* vol. 82, pp. 2883-2885, 2003.

[79] Y. Lee, K. Park, J. Lee, C. Lee, H. J. Yoo, C. Kim and Y. Yoon, "Dry release for surface micromachining with HF vapor-phase etching," *J Microelectromech Syst,* vol. 6, pp. 226-233, 1997.

[80] A. Witvrouw, B. Du Bois, P. De Moor, A. Verbist, C. A. Van Hoof, H. Bender and C. Baert, "Comparison between wet HF etching and vapor HF etching for sacrificial oxide removal," in *Micromachining and Microfabrication*, 2000, pp. 130-141.

[81] C. D. Wagner and G. Muilenberg, *Handbook of X-Ray Photoelectron Spectroscopy*. Perkin-Elmer, 1979.

[82] (September 15, 2012). *NIST X-ray Photoelectron Spectroscopy Database* [NIST Standard Reference Database 20, Version 4.1]. Available: https://srdata.nist.gov/xps/.

[83] J. Engelen, "Optimization of Comb-Drive Actuators," 2011.

[84] D. Schumann, R. Kujat, M. Nerlich and P. Angele, "Mechanobiological conditioning of stem cells for cartilage tissue engineering," *Biomed. Mater. Eng.*, vol. 16, pp. S37-S52, 2006.

[85] W. Xu, R. Mezencev, B. Kim, L. Wang, J. McDonald and T. Sulchek, "Cell stiffness is a biomarker of the metastatic potential of ovarian cancer cells," *PloS One*, vol. 7, pp. e46609, 2012.

[86] S. Suresh, "Nanomedicine: elastic clues in cancer detection," *Nature Nanotechnology*, vol. 2, pp. 748-749, 2007.

[87] B. N. Mason, J. P. Califano and C. A. Reinhart-King, "Matrix stiffness: A regulator of cellular behavior and tissue formation," in *Engineering Biomaterials for Regenerative Medicine*Anonymous Springer, 2012, pp. 19-37.

[88] P. A. Janmey and D. A. Weitz, "Dealing with mechanics: mechanisms of force transduction in cells," *Trends Biochem. Sci.*, vol. 29, pp. 364-370, 2004.

[89] J. Chan and P. Lam, "Human mesenchymal stem cells and their paracrine factors for the treatment of brain tumors," *Cancer Gene Ther.*, vol. 20, pp. 539-543, 2013.

[90] B. S. Wiseman and Z. Werb, "Stromal effects on mammary gland development and breast cancer," *Science*, vol. 296, pp. 1046-1049, May 10, 2002.

[91] N. D. Leipzig and K. A. Athanasiou, "Unconfined creep compression of chondrocytes," *J. Biomech.*, vol. 38, pp. 77-85, 2005.

[92] J. M. Maloney, D. Nikova, F. Lautenschläger, E. Clarke, R. Langer, J. Guck and K. J. Van Vliet, "Mesenchymal stem cell mechanics from the attached to the suspended state," *Biophys. J.*, vol. 99, pp. 2479-2487, 2010.

[93] Y. Zhou, L. Yang and Y. Huang, *Micro-and Macromechanical Properties of Materials.* CRC Press, 2013.

[94] M. L. Rodriguez, P. J. McGarry and N. J. Sniadecki, "Review on cell mechanics: experimental and modeling approaches," *Appl. Mech. Rev.,* vol. 65, pp. 060801, 2013.

[95] D. E. Ingber, "Cellular tensegrity: defining new rules of biological design that govern the cytoskeleton," *J. Cell. Sci.,* vol. 104, pp. 613-613, 1993.

[96] D. Stamenović and M. F. Coughlin, "A quantitative model of cellular elasticity based on tensegrity," *J. Biomech. Eng.,* vol. 122, pp. 39-43, 2000.

[97] N. Wang, K. Naruse, D. Stamenovic, J. J. Fredberg, S. M. Mijailovich, I. M. Tolic-Norrelykke, T. Polte, R. Mannix and D. E. Ingber, "Mechanical behavior in living cells consistent with the tensegrity model," *Proc. Natl. Acad. Sci. U. S. A.,* vol. 98, pp. 7765-7770, Jul 3, 2001.

[98] D. Stamenović and D. E. Ingber, "Models of cytoskeletal mechanics of adherent cells," *Biomechanics and Modeling in Mechanobiology,* vol. 1, pp. 95-108, 2002.

[99] M. F. Coughlin and D. Stamenović, "A prestressed cable network model of the adherent cell cytoskeleton," *Biophys. J.,* vol. 84, pp. 1328-1336, 2003.

[100] B. Maurin, P. Cañadas, H. Baudriller, P. Montcourrier and N. Bettache, "Mechanical model of cytoskeleton structuration during cell adhesion and spreading," *J. Biomech.,* vol. 41, pp. 2036-2041, 2008.

[101] F. Gittes, B. Mickey, J. Nettleton and J. Howard, "Flexural rigidity of microtubules and actin filaments measured from thermal fluctuations in shape," *J. Cell Biol.,* vol. 120, pp. 923-934, Feb, 1993.

[102] A. Voloshin, "MODELING CELL MOVEMENT ON A SUBSTRATE WITH VARIABLE RIGIDITY," .

[103] E. Yalcintas, J. Hu, Y. Liu and A. Voloshin, "Modeling Cell Spreading and Alignment on Micro-Wavy Surfaces," *CMES: Computer Modeling in Engineering & Sciences,* vol. 98, pp. 151-180, 2014.

[104] C. L. Mummery, J. Zhang, E. S. Ng, D. A. Elliott, A. G. Elefanty and T. J. Kamp, "Differentiation of human embryonic stem cells and induced pluripotent stem cells to cardiomyocytes: a methods overview," *Circ. Res.,* vol. 111, pp. 344-358, Jul 20, 2012.

[105] W. Lu, K. Tung, S. Hung, J. Shiau and K. Hwang, "Compression of deformable gel particles," *Powder Technol,* vol. 116, pp. 1-12, 2001.

Appendix I

Fabrication Instructions

Starting Materials

1. 6 inch SOI wafers
    - 2 μm buried oxide layer,150 μm device layer and 500 μm handle layer
    - Device resistivity 0.001 – 0.005 Ω-cm

Native Oxide Removal

1. Dilute HF approximately 50:1 mix by volume
   (Typically mixed in a 600 ml polyethylene beaker with 600 ml water and small amount of HF)

2. HF dip for 35 seconds until water zips off the back indicating that native oxide is removed

3. Rinse in DI water

4. Blow dry with nitrogen

Metal Layer Photoresist Patterning (Mask 1-Metal Mask)

1. Dehydration
   Bake 3 min on the hotplate at 180 C

2. Spin-coat HMDS
    a. HMDS Program 1, 3000 RPM, 30 sec
    b. Bake 1 min on hot-plate at 170 C
    c. Let cool 15 min

3. Spin-coat negative photoresist
    a. negative tone lift-off photoresist AZ nLOF 2020 target thickness 2 μm
    b. Program 2, 2000 RPM, 30 sec

4. Softbake
    a. Bake 30 sec on hot-plate at 50 C and 1 min on hot-plate at 110 C
    b. Let cool an hour

5. Mask Exposure
    a. Warm-up the machine and load Mask 1 in projection system
    b. Expose wafer at 48 mJ via aperture 1 (account for major changes in humidity or temperature for adjusting the exposure accordingly by keeping a log)

6. Post Exposure Bake
    a. Bake 1 min on hot-plate at 110 C
    b. Allow enough time 40 min-an hour based on humidity for rehydration

7. Develop
    a. AZ 300 MIF developer full strength
    b. Submerge in beaker for 2 min and agitate with gentle swirling motion

8. Rinse & dry
    a. Rinse in DI water
    b. Blow dry with nitrogen

9. Inspection (optical microscope)
    a. Test structures located on test dies in the center and edges of the wafer are a good indicator of photolithography accuracy
    b. If failure, strip in AZ 400T and repeat photoresist patterning.

Metallization and Lift-Off

1. Using e-beam evaporator:
   500 Å (50 nm) Chrome
   2500 Å(250 nm)Gold
   100 Å (10 nm) Chrome
   (Note: titanium cannot be substituted for chrome due to HF release step)

2. Lift-off
    a. 2 hours in heated AZ 400 T at 80 C (1 hour in first bath, 1 hour in second bath)
    b. Rinse in DI water
    c. Blow dry with nitrogen

Device Layer Photoresist Patterning (Mask 2-Device Mask)

1. Dehydration

a. Bake 3 min on the hotplate at 180 C

2. Spin-coat HMDS
    a. HMDS Program 1, 3000 RPM
    b. Bake 1 min on hot-plate at 170 C
    c. Let cool for 5 min

3. Spin-coat positive tone photoresist
    a. SPR220, target thickness 11 μm
    b. Program 9, 1500 RPM, 30 sec

4. Softbake
    a. Bake 2 min on hot-plate at 50 C and 5 min on hot-plate at 110 C
    b. Rehydration and resist relaxation for a day to avoid resist bubbling

5. Mask Exposure
    a. Warm-up the machine and load Device Mask in projection system
    b. Expose wafer at 48 mJ via aperture 1 (account for major changes in humidity or temperature for adjusting the exposure accordingly by keeping a log)
    c. Rehydration for a day to avoid resist cracking

6. Post Exposure Bake
    a. Bake 2 min on hot-plate at 50 C and 5 min on hot-plate at 110 C
    b. Rehydration for 2-3 hours

7. Develop
    a. AZ 300 MIF developer full strength
    b. Submerge in beaker for 3 min and agitate with gentle swirling motion until the pattern is clear of resist (This resist is very thick and development is trackable with eyes)

8. Rinse & dry
    a. Rinse in DI water
    b. Blow dry with nitrogen

9. Inspection (optical microscope)
    a. Test structures located on test dies in the center and edges of the wafer are a good indicator of photolithography accuracy

b. If failure, strip in AZ 400T and repeat photoresist patterning.

Deep Reactive Ion Etching

1. LOWROUGHNESS Process using Adixen AMS 100 I-Speeder
   This process lasts about 2 hours and etches about 150µm deep in 8µm trench and etch will stop on buried oxide layer

   a. It is recommended to clean the chamber with 30 min oxygen plasma cleaning before the etch. Also conditioning the chamber with a dummy wafer is recommended to avoid silicon grass
   b. Clean the back of the wafer from any remaining photoresist with acetone, this will improve the seal of the wafer
   c. Vent the load luck and place the wafer on wafer holder
   d. Pump down the load lock
   e. Select transfer wafer from load lock to chamber on the program
   f. Wait and inspect that wafer is in place inside chamber
   g. Select Go Process, the process will begin with bringing the substrate to the set temperature first. After wards, SF6 and C4F8 plasmas will switch for etching and passivation cycles respectively. SF6 plasma is purple and C4F8 plasma is blue, the color that can be seen from chamber window indicates which cycle is in progress.
   h. After completion of the etch, the handle bring wafer from chamber to load-lock automatically.
   i. Vent the chamber and take the wafer out.

2. Photoresist strip
   a. Oxygen plasma cleaning can be used to remove part of the hardened resist, if the resist remains try wet strip
   b. 30 min in AZ400T heated on hot-plate at 80 C (standard 2-bath method) Do not agitate like normal wafer – small cantilever structures will break.
   c. Rinse in DI water
   d. Blow dry with nitrogen

3. Inspect
   a. If there is residue remaining after wet strip, try oxygen plasma cleaning until there is no residue

ALD Deposition

Deposition of 10 nm ALD Alumina on the wafer

Insulation Layer Photoresist Patterning (Mask3- Insulation Mask)

1. Lamination of dry resist at Dev Corp, the dry negative tone photoresist will be laminated with lamination machine using pressure and heat on top of the wafer
2. Patterning dry photoresist at Lehigh

Pad Etch

Note that Chromium Etchant is acidic and produces toxic fumes.

1. Work with the etchant where there is white light.
2. Prepare a beaker with DI water
3. Place the wafer in the Chromium Etchant and wait 40 to 60 seconds
    a. The pads will suddenly change from silver color to gold color
    b. Remove the wafer as soon as all pads are visibly gold and transfer immediately to the water bath
    c. Do not over-etch or the insulation layer will delaminate!
4. Rinse carefully in DI water.
5. Blow dry gently with nitrogen

Wafer Dicing

Since the structure is high aspect ratio (aspect ratio of ~ 19) and fragile beams are present, laser dicing is the best approach to preserve the structure. Furthermore, there will be no residue and no need to protect with photoresist. Wet chemical processing might be damaging to the narrow beams at this point.

Device Release via Vapor HF

1. uEtch Vapor HF (SPTS Inc.) tool was used for releasing the device.
2. Standard recipe with etch rate of 0.1 μm per min
3. The device will require 50 minutes of etching
4. It is recommended to calculate the time for etch according to the DRIE footing and allow for a margin before complete etching to avoid over-etching and releasing anchors
5. Probe the structure under microscope to determine if it is released (force sensor transducers are the last section to release based on the design)

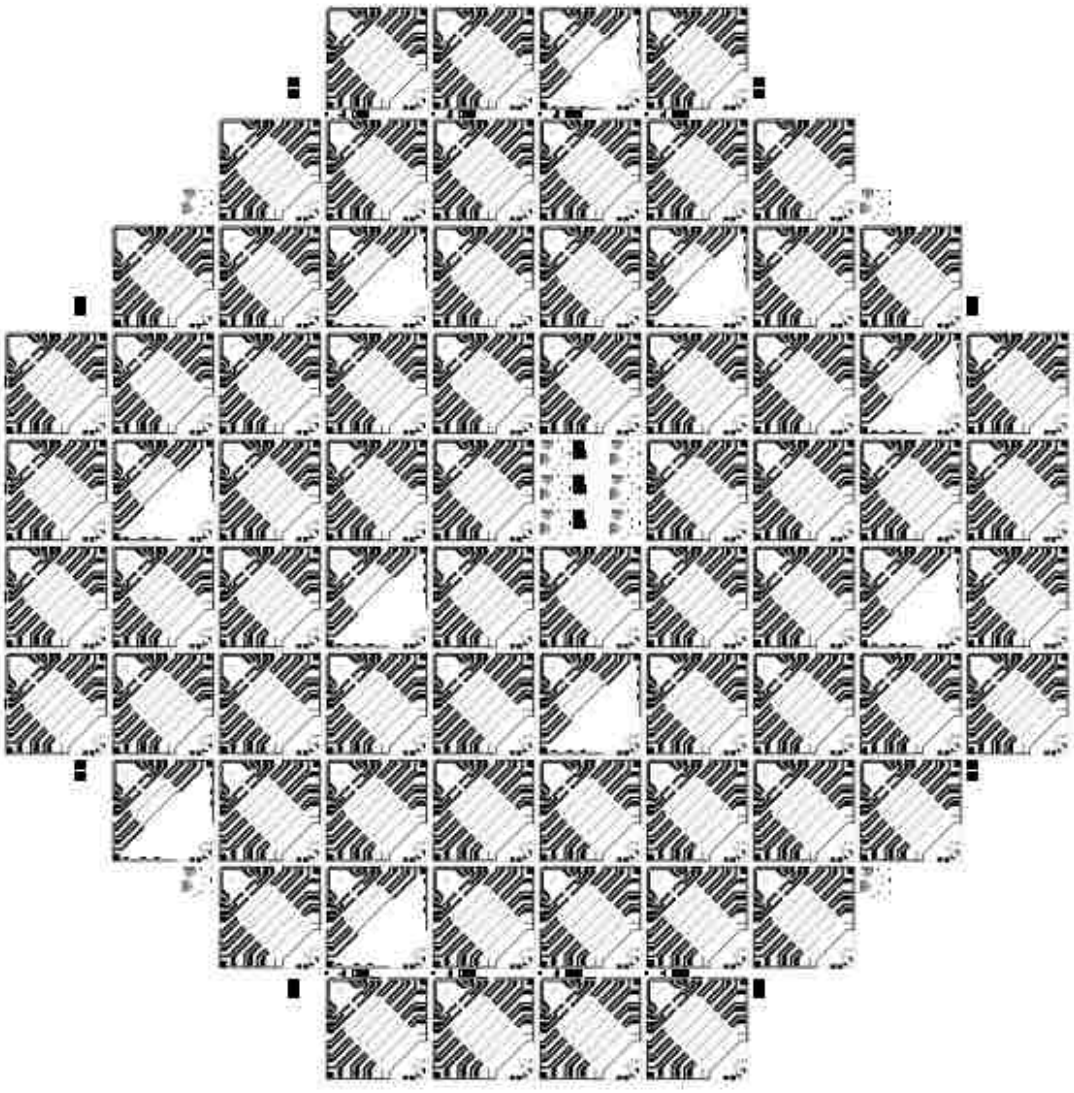

Figure 125. Mask1_Metal Mask.

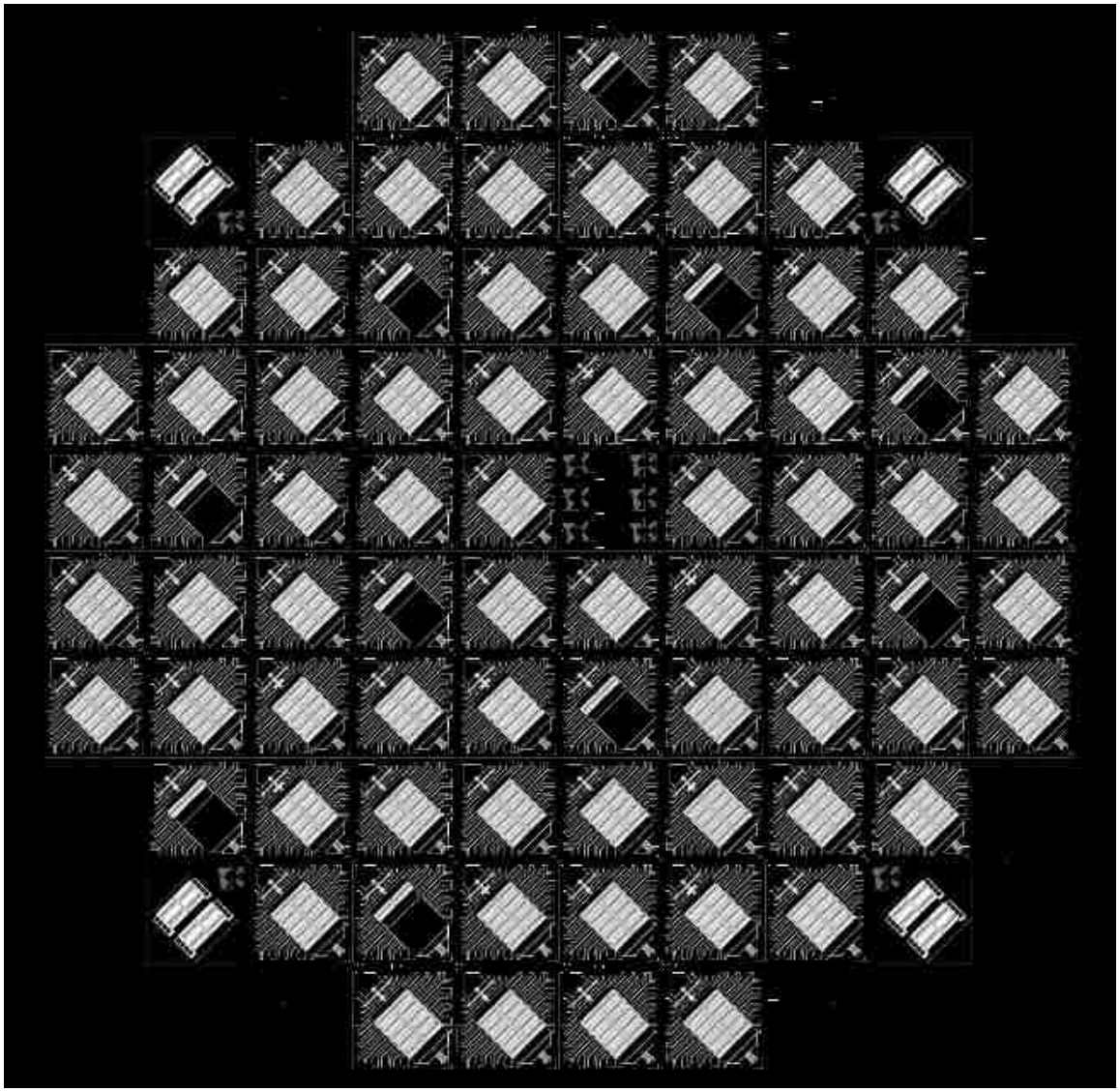

Figure 126. Mask2_Device Mask (revised version).

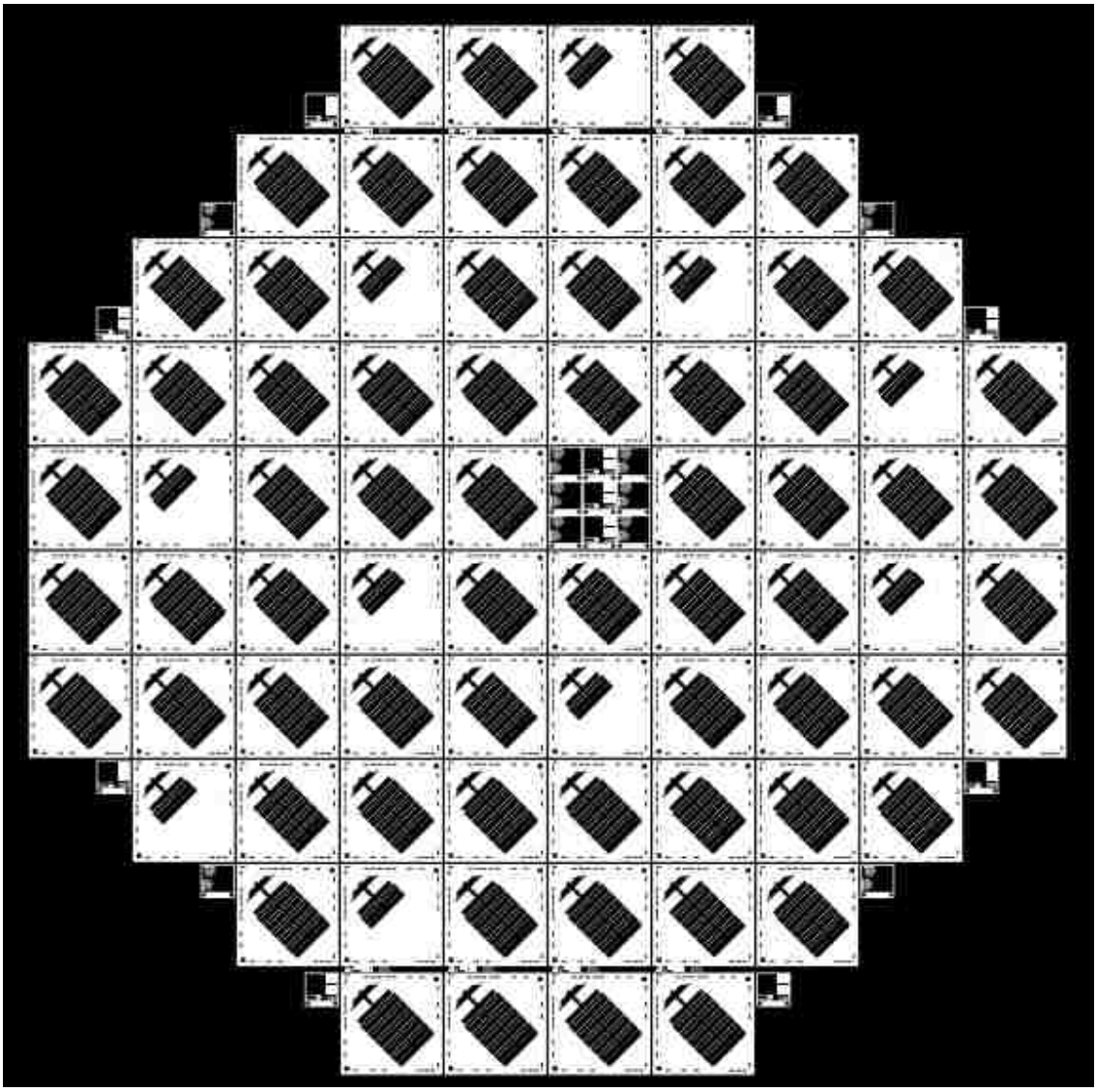

Figure 127. Mask3_Isolation Mask

Appendix II

Supplemental Figures of Experimental Data

Static displacement and corresponding applied dc voltage versus time is given for actuators in different dies.

(X axis is time in seconds for all the following figures)

A06_1

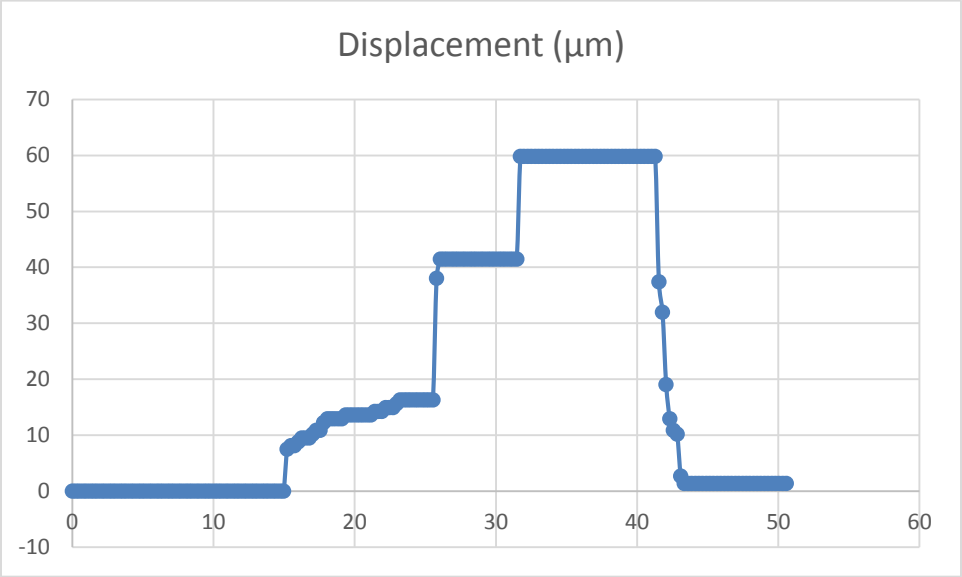

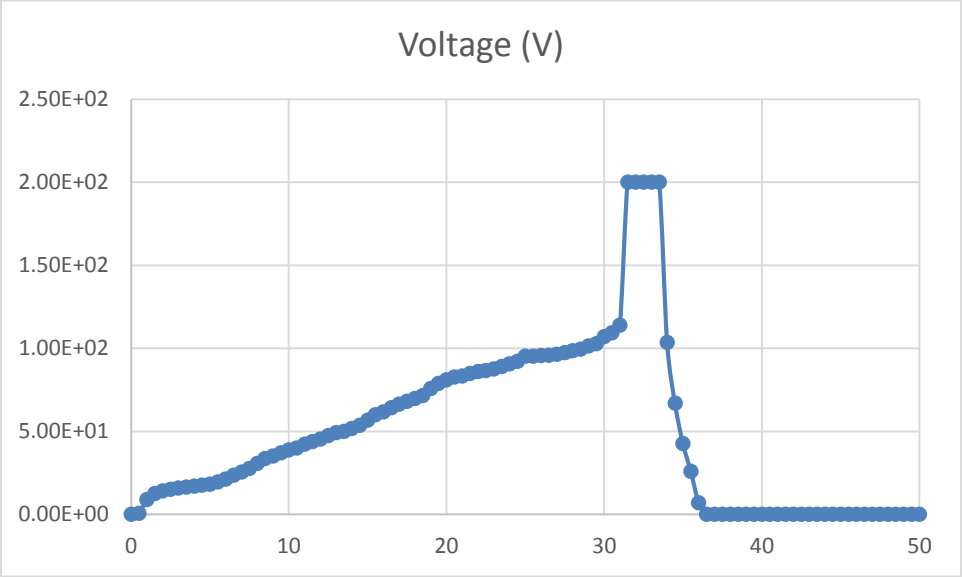

A06_3 Trial 1
Hysteresis was observed.

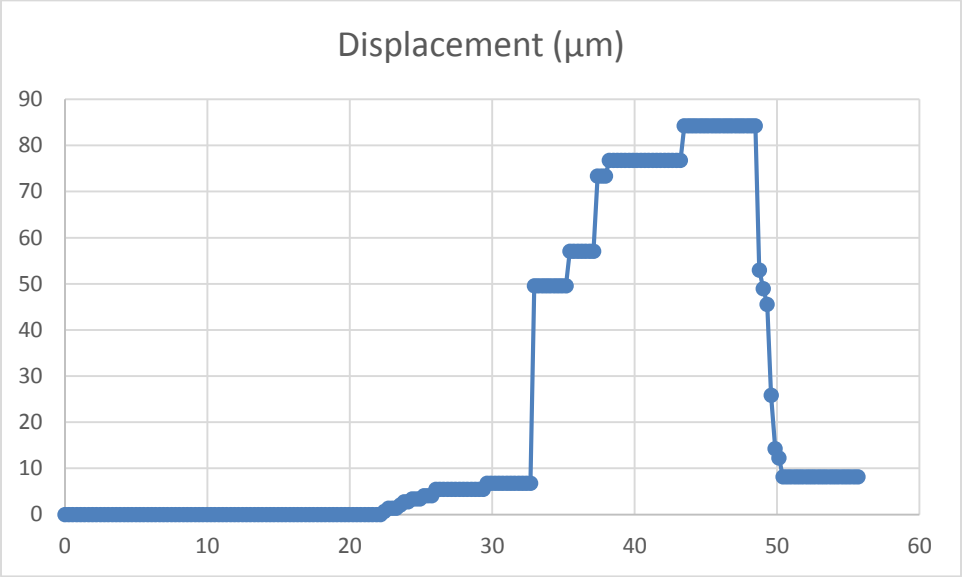

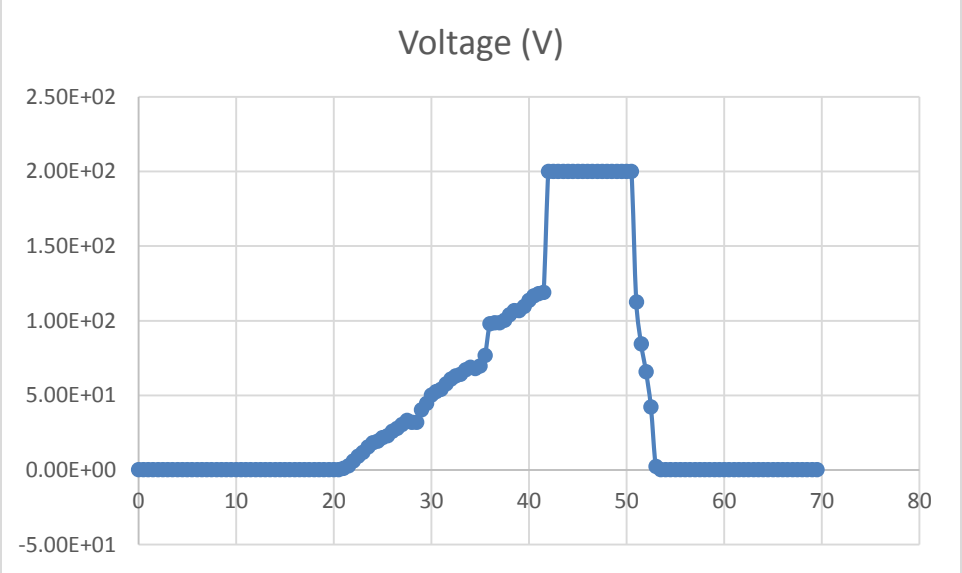

A06_3 Trial 2

The displacement curve was smoother in the second trial and about 4 µm of hysteresis was removed when the actuator went back to its initial state. The reason that the first time that actuator was moving, displacement is a stepped curve might be slight mechanical obstacles underneath the movable structure.

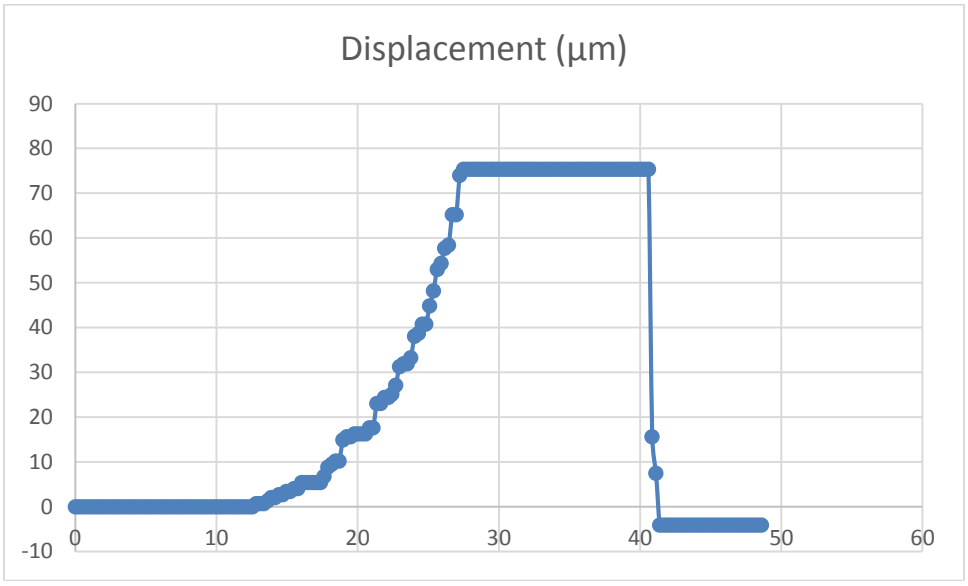

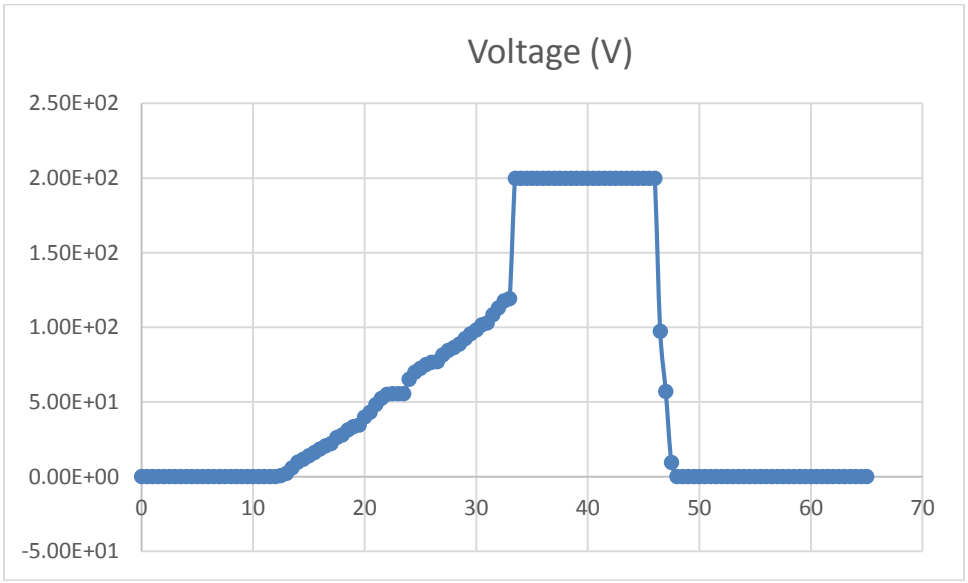

A06_4 trial 1

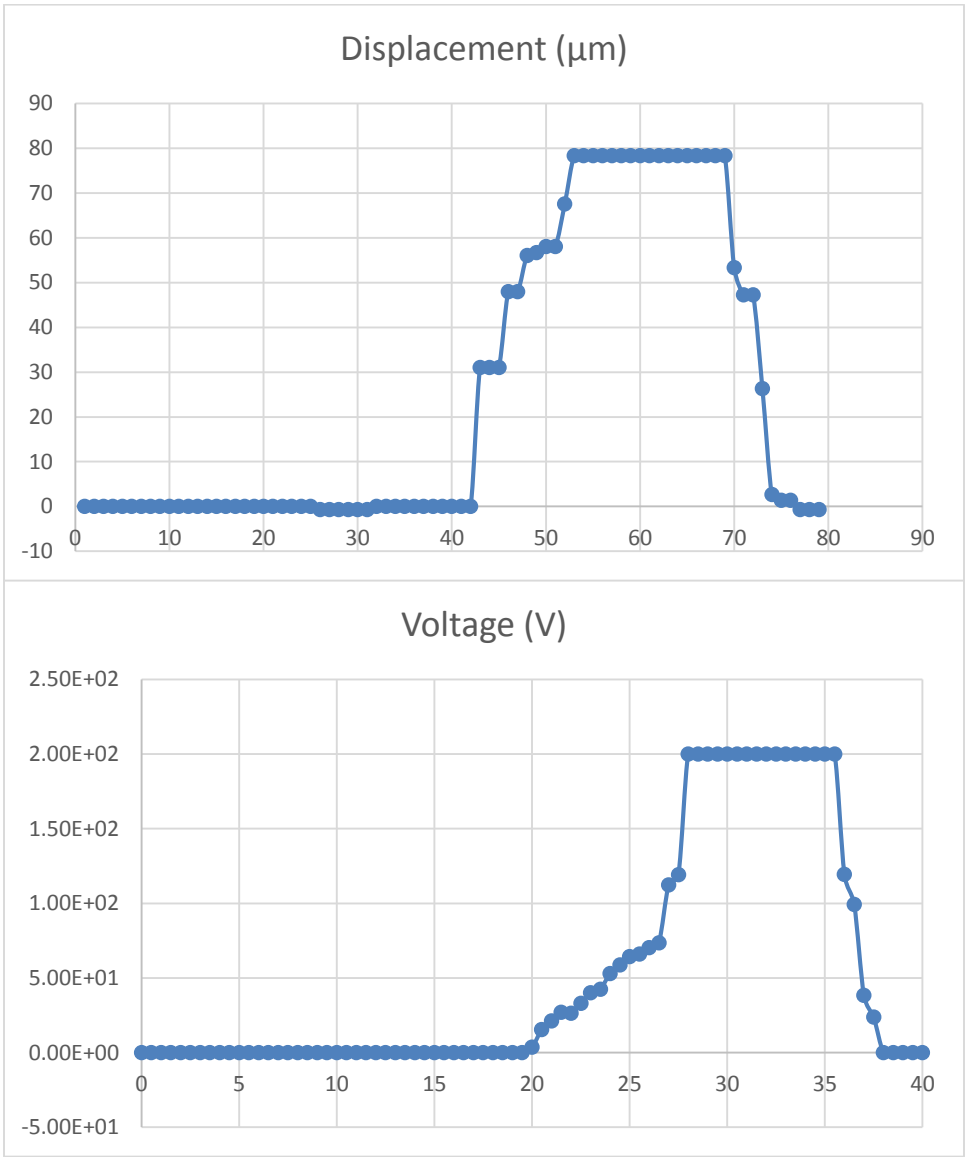
Displacement (µm)
90
80
70
60
50
40
30
20
10
0
-10
0
10
20
30
40
50
60
70
80
90
Voltage (V)
2.50E+02
2.00E+02
1.50E+02
1.00E+02
5.00E+01
0.00E+00
-5.00E+01
0
5
10
15
20
25
30
35
40

A06_4 trial 2
A delta voltage was tried and the displacement looked like a delta as well.

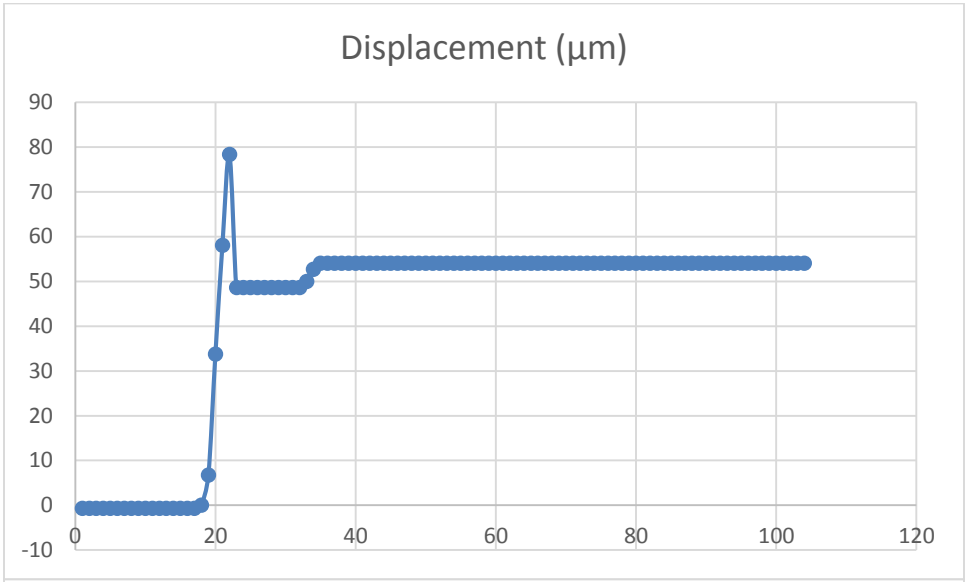

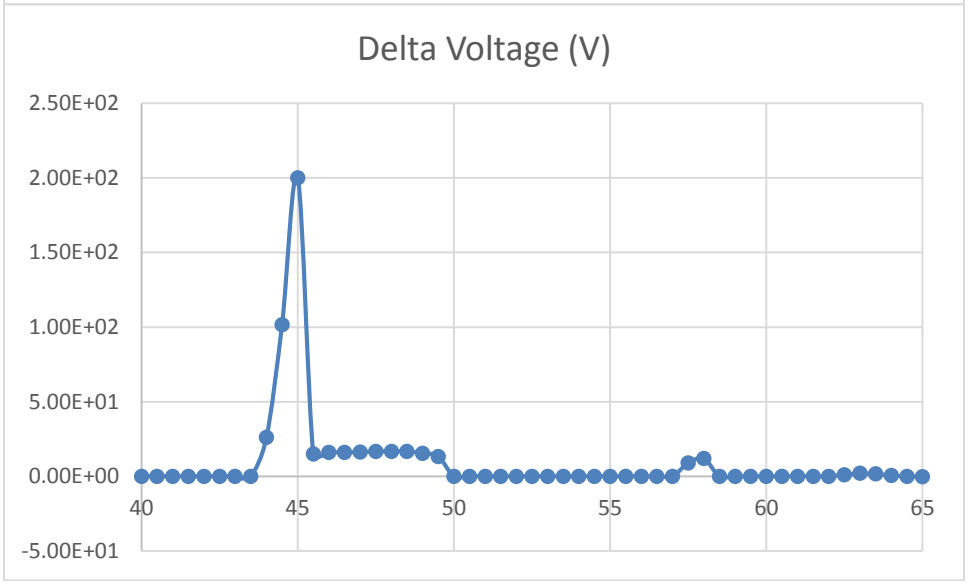

A10_2

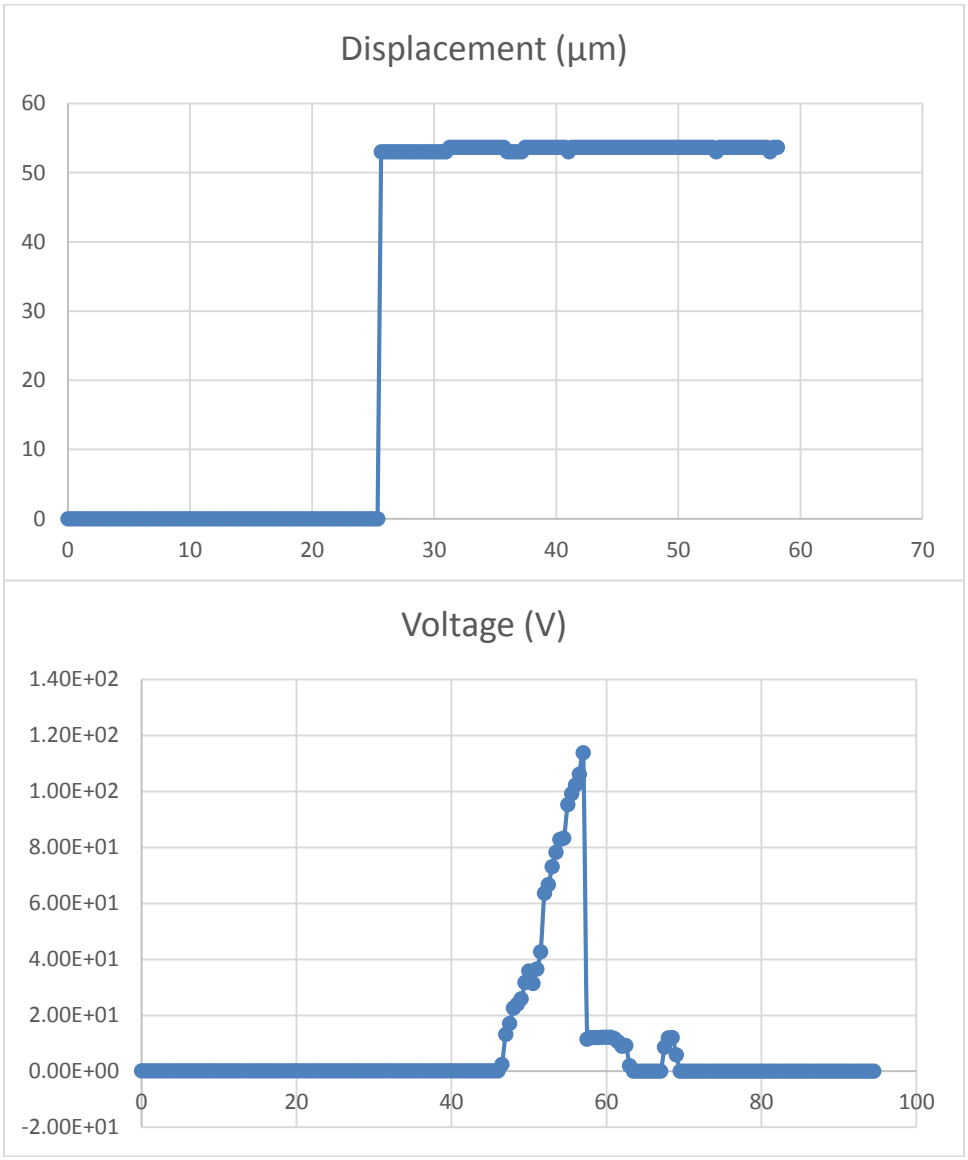
Displacement (µm)
60
50
40
30
20
10
0
0
10
20
30
40
50
60
70
Voltage (V)
1.40E+02
1.20E+02
1.00E+02
8.00E+01
6.00E+01
4.00E+01
2.00E+01
0.00E+00
-2.00E+01
0
20
40
60
80
100

A11

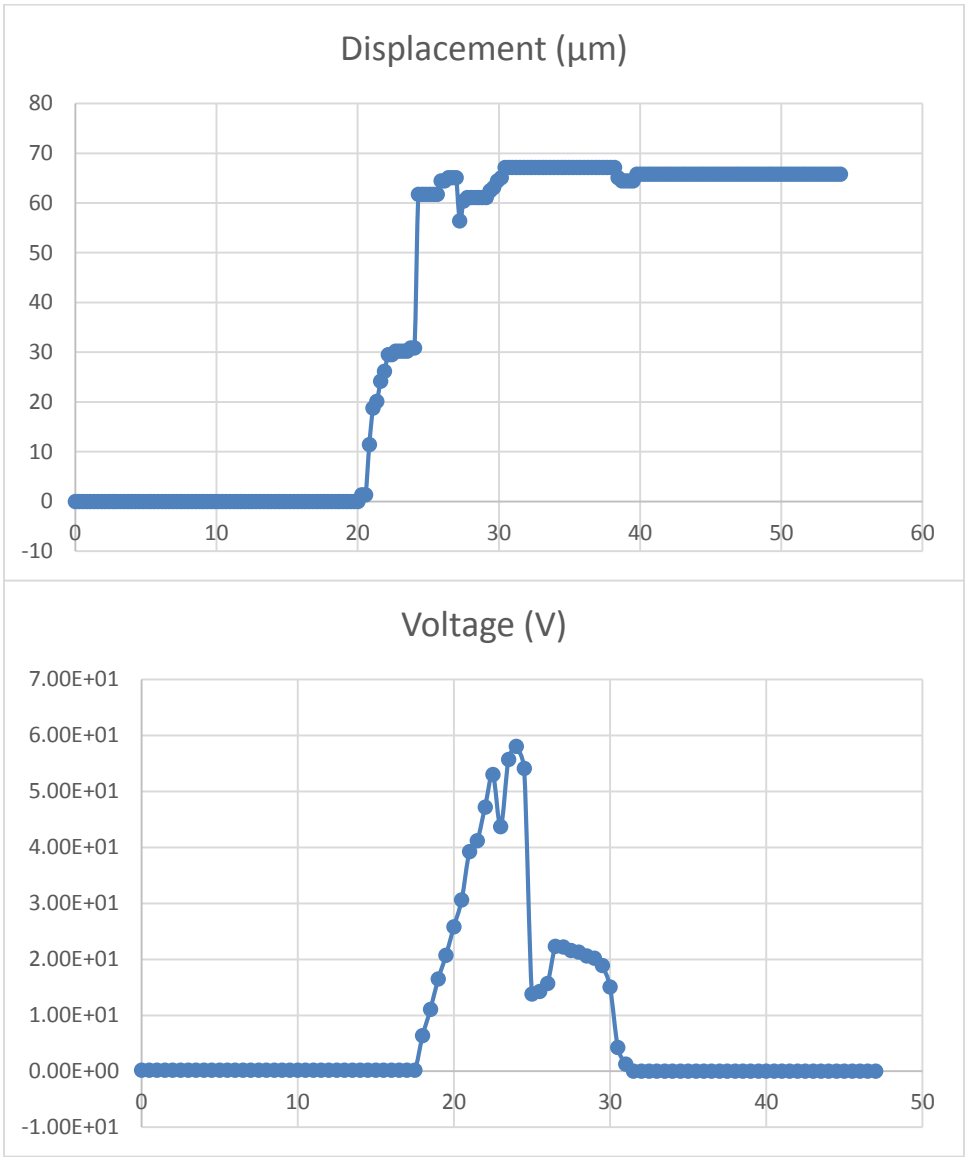
Displacement (µm)
80
70
60
50
40
30
20
10
0
-10
0
10
20
30
40
50
60
Voltage (V)
7.00E+01
6.00E+01
5.00E+01
4.00E+01
3.00E+01
2.00E+01
1.00E+01
0.00E+00
-1.00E+01
0
10
20
30
40
50

D01_1

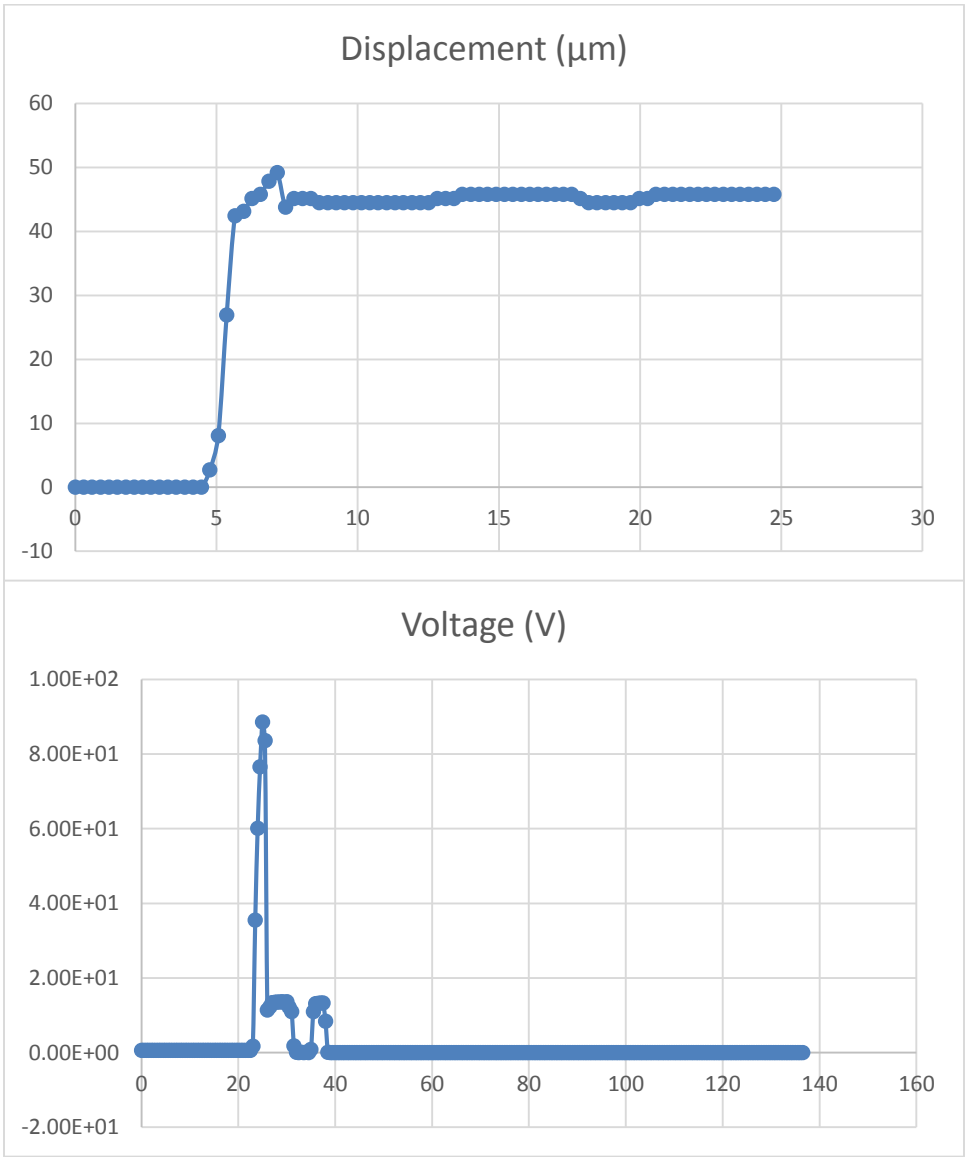
Displacement (µm)
60
50
40
30
20
10
0
-10
0
5
10
15
20
25
30
Voltage (V)
1.00E+02
8.00E+01
6.00E+01
4.00E+01
2.00E+01
0.00E+00
-2.00E+01
0
20
40
60
80
100
120
140
160

D01_2

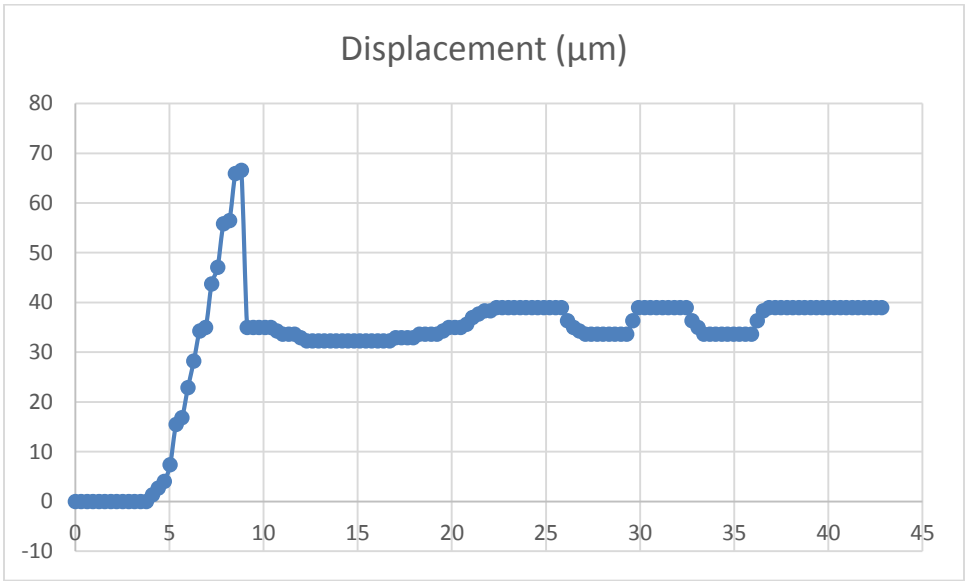
Displacement (µm)
80
70
60
50
40
30
20
10
0
-10
0
5
10
15
20
25
30
35
40
45

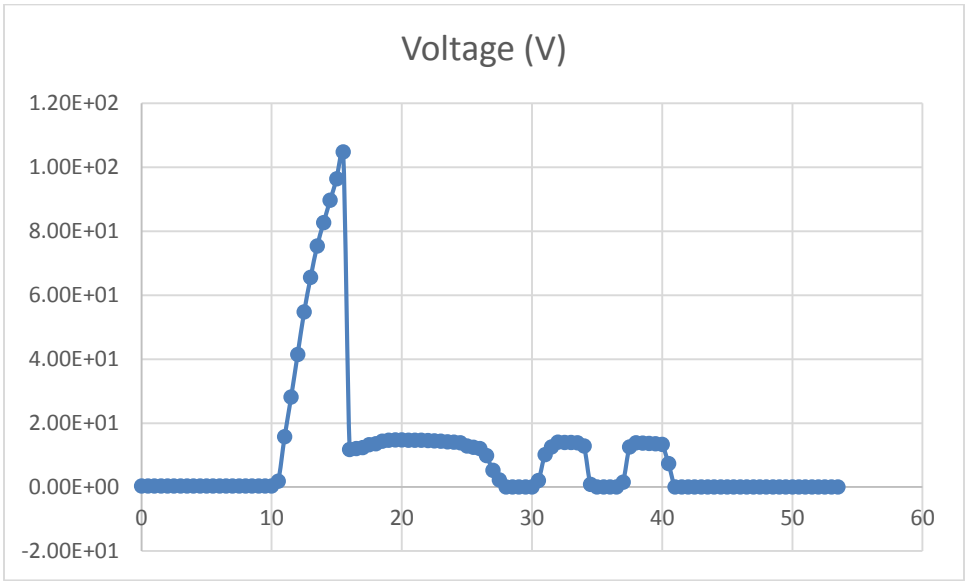
Voltage (V)
1.20E+02
1.00E+02
8.00E+01
6.00E+01
4.00E+01
2.00E+01
0.00E+00
-2.00E+01
0
10
20
30
40
50
60

D01_3

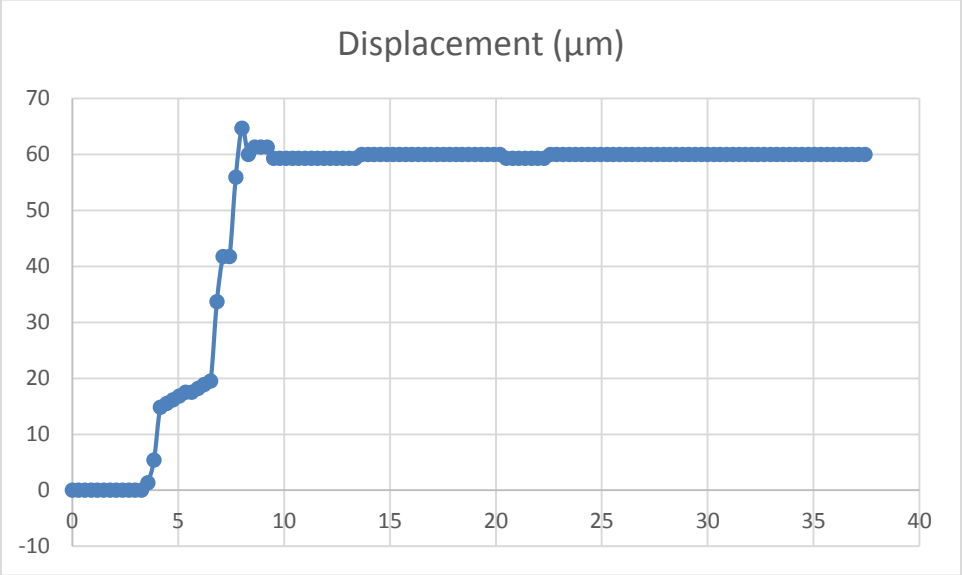
Displacement (µm)
70
60
50
40
30
20
10
0
-10
0
5
10
15
20
25
30
35
40

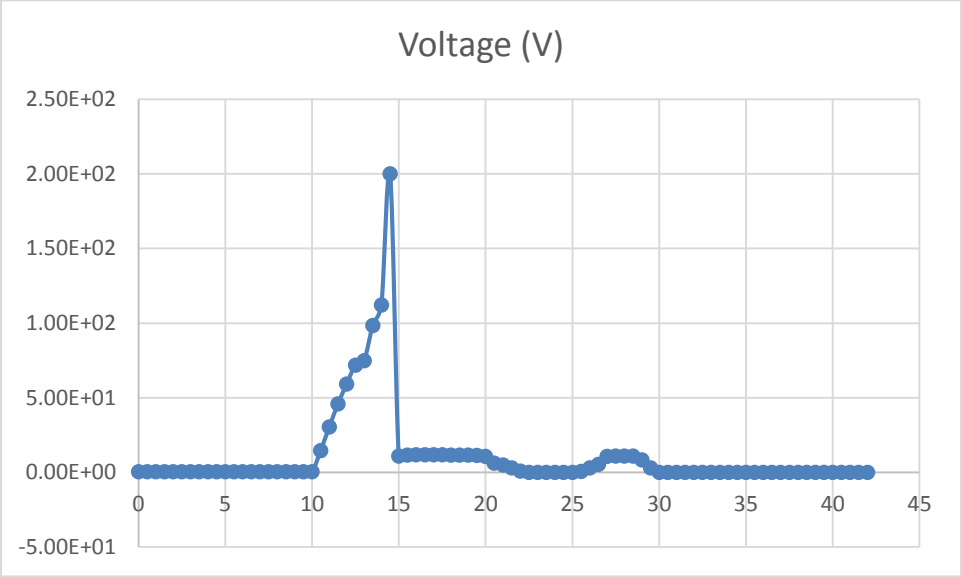
Voltage (V)
2.50E+02
2.00E+02
1.50E+02
1.00E+02
5.00E+01
0.00E+00
-5.00E+01
0
5
10
15
20
25
30
35
40
45

D01_4

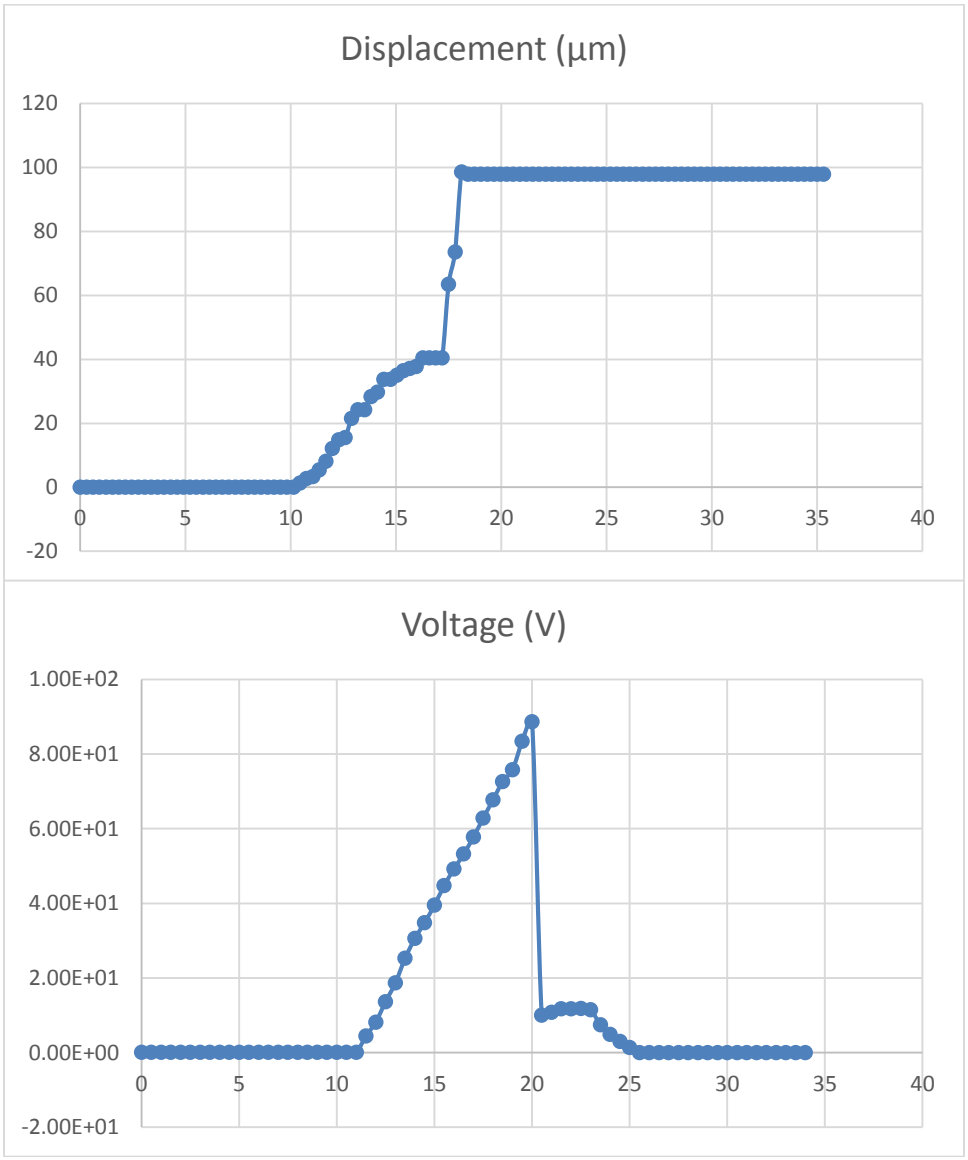
Displacement (µm)
120
100
80
60
40
20
0
-20
0
5
10
15
20
25
30
35
40
Voltage (V)
1.00E+02
8.00E+01
6.00E+01
4.00E+01
2.00E+01
0.00E+00
-2.00E+01
0
5
10
15
20
25
30
35
40

D01_5

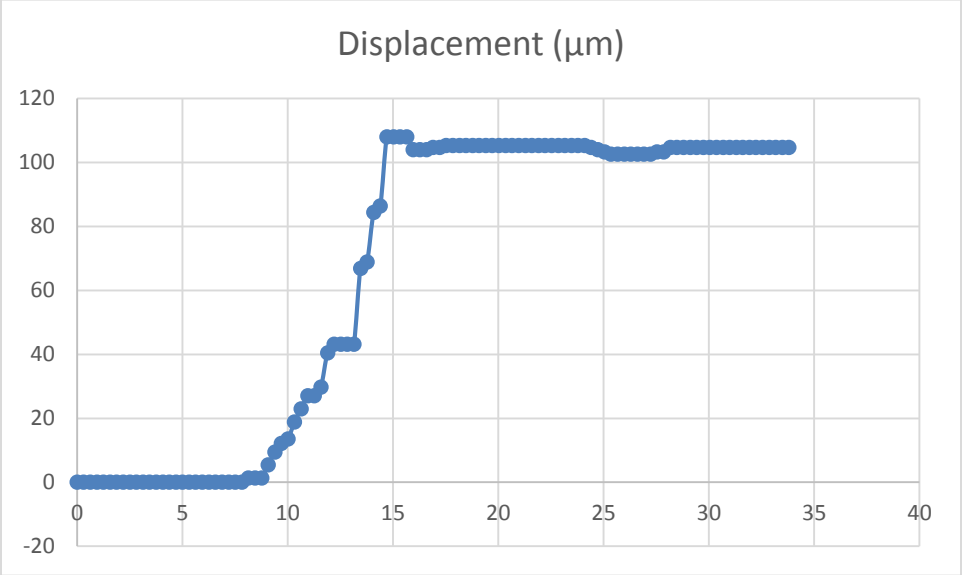
Displacement (µm)
120
100
80
60
40
20
0
-20
0
5
10
15
20
25
30
35
40

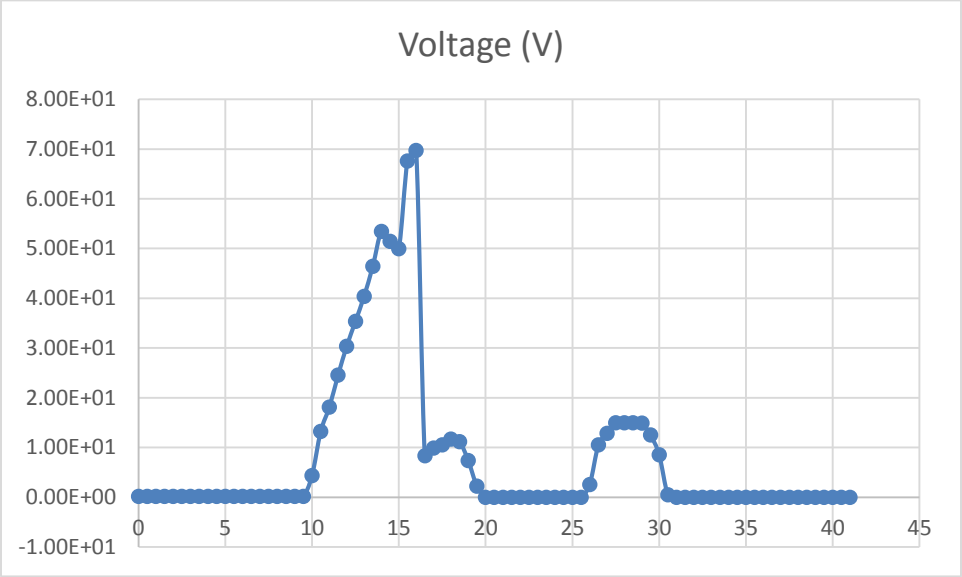
Voltage (V)
8.00E+01
7.00E+01
6.00E+01
5.00E+01
4.00E+01
3.00E+01
2.00E+01
1.00E+01
0.00E+00
-1.00E+01
0
5
10
15
20
25
30
35
40
45

D02_1

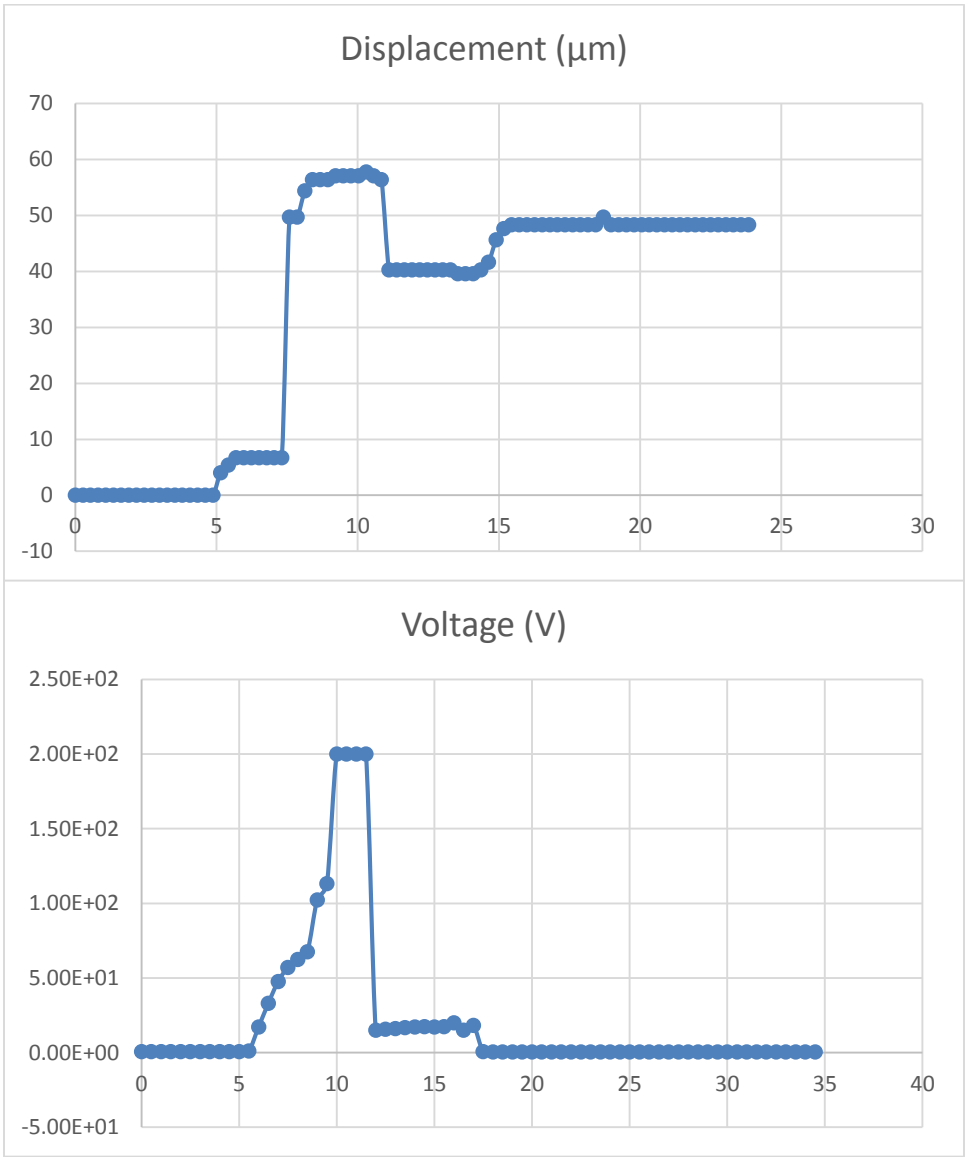
Displacement (µm)
70
60
50
40
30
20
10
0
-10
0
5
10
15
20
25
30
Voltage (V)
2.50E+02
2.00E+02
1.50E+02
1.00E+02
5.00E+01
0.00E+00
-5.00E+01
0
5
10
15
20
25
30
35
40

D02_4

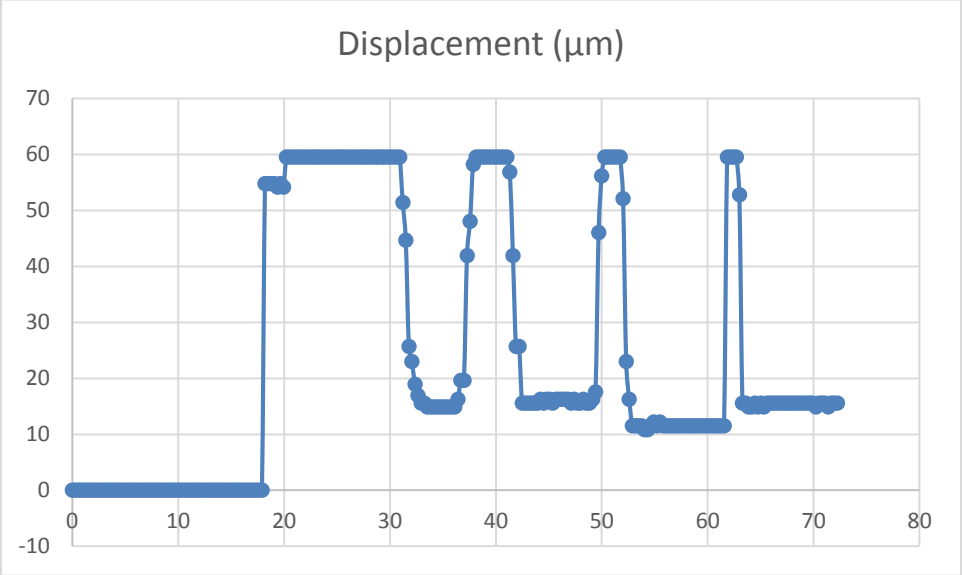
Displacement (µm)
70
60
50
40
30
20
10
0
-10
0
10
20
30
40
50
60
70
80

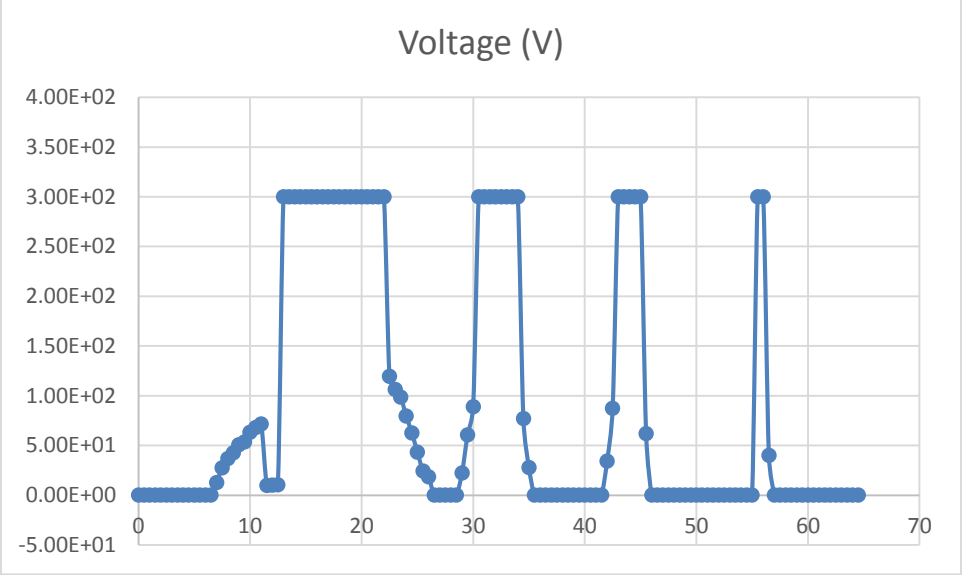
Voltage (V)
4.00E+02
3.50E+02
3.00E+02
2.50E+02
2.00E+02
1.50E+02
1.00E+02
5.00E+01
0.00E+00
-5.00E+01
0
10
20
30
40
50
60
70

D06_1

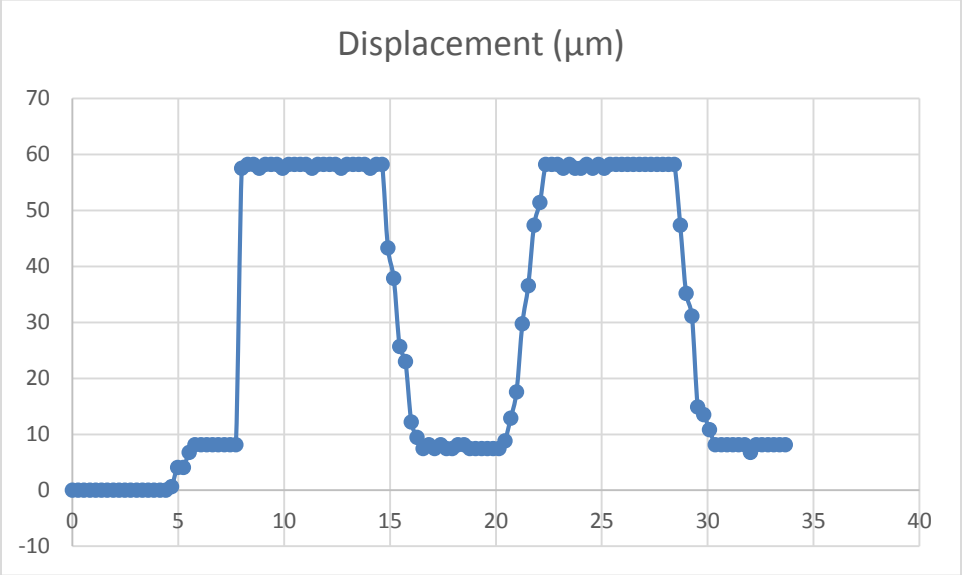
Displacement (µm)
70
60
50
40
30
20
10
0
-10
0
5
10
15
20
25
30
35
40

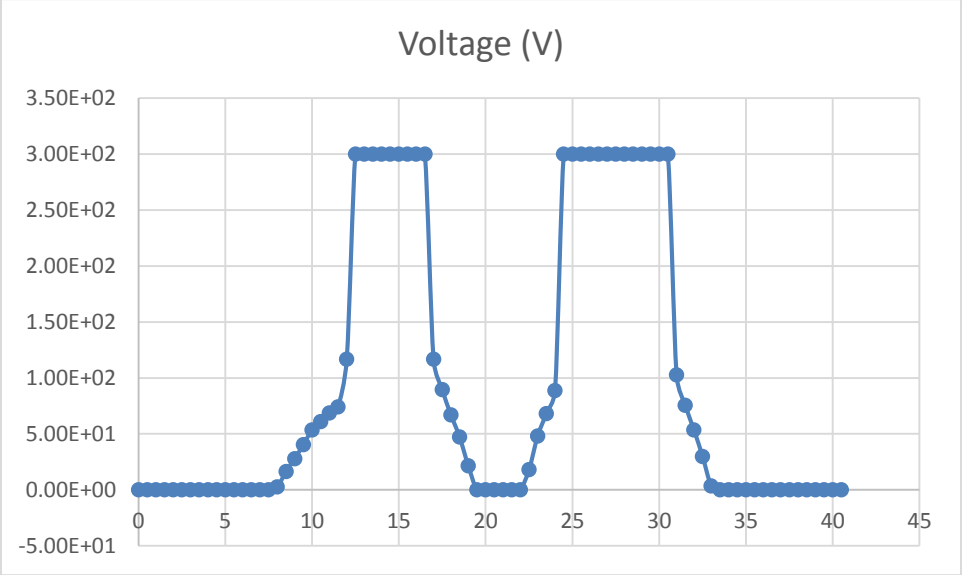
Voltage (V)
3.50E+02
3.00E+02
2.50E+02
2.00E+02
1.50E+02
1.00E+02
5.00E+01
0.00E+00
-5.00E+01
0
5
10
15
20
25
30
35
40
45

D02_1

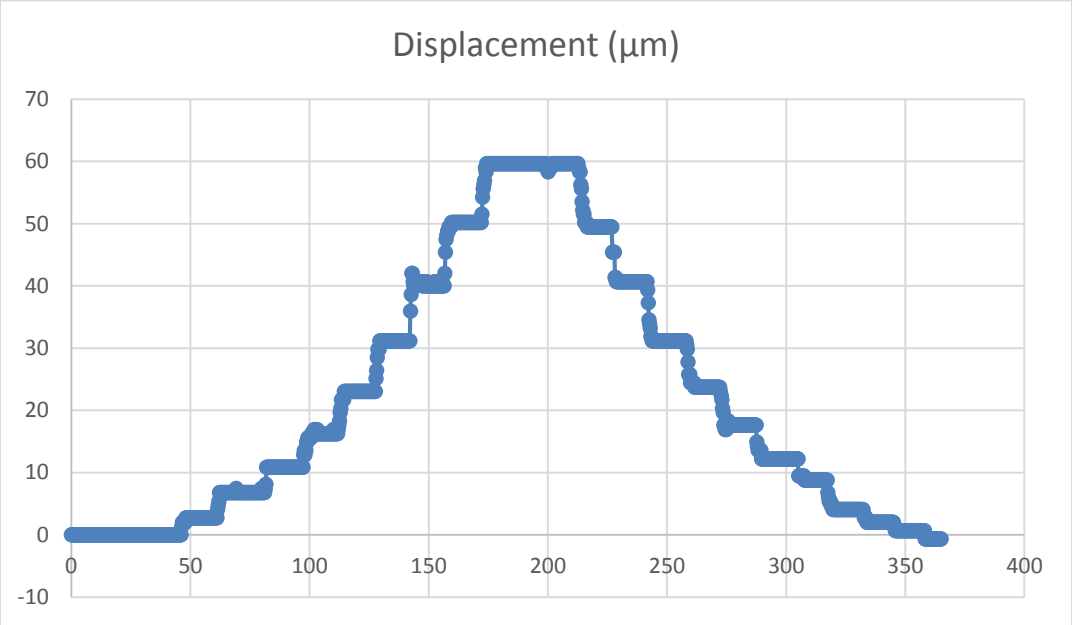
Displacement (µm)
70
60
50
40
30
20
10
0
-10
0
50
100
150
200
250
300
350
400

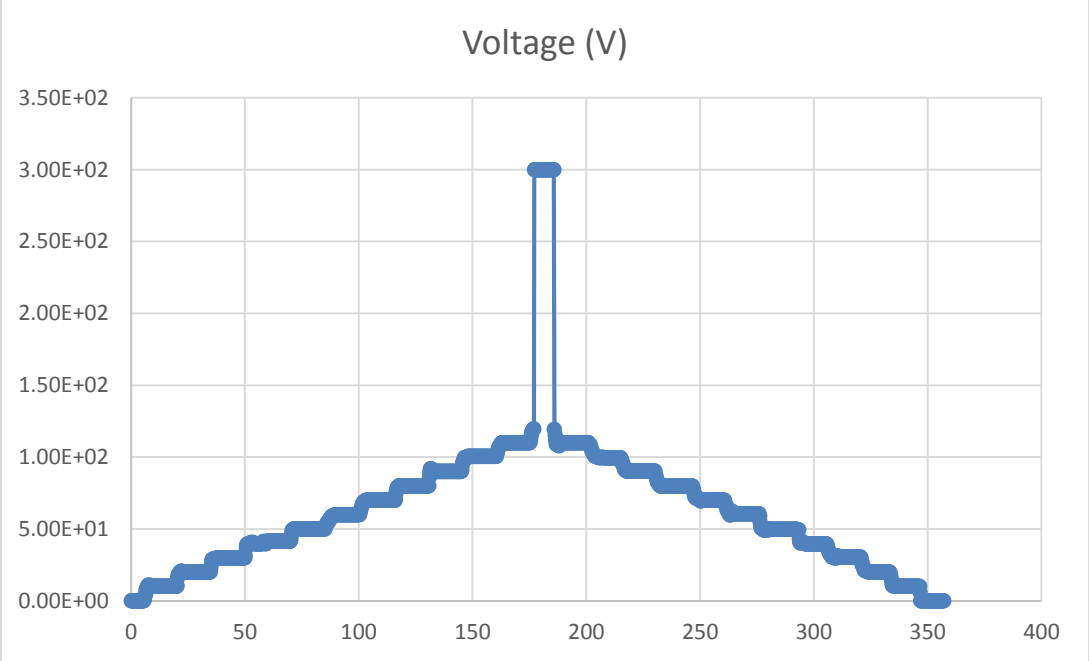
Voltage (V)
3.50E+02
3.00E+02
2.50E+02
2.00E+02
1.50E+02
1.00E+02
5.00E+01
0.00E+00
0
50
100
150
200
250
300
350
400

The displacement voltage curve is given in the following figure.

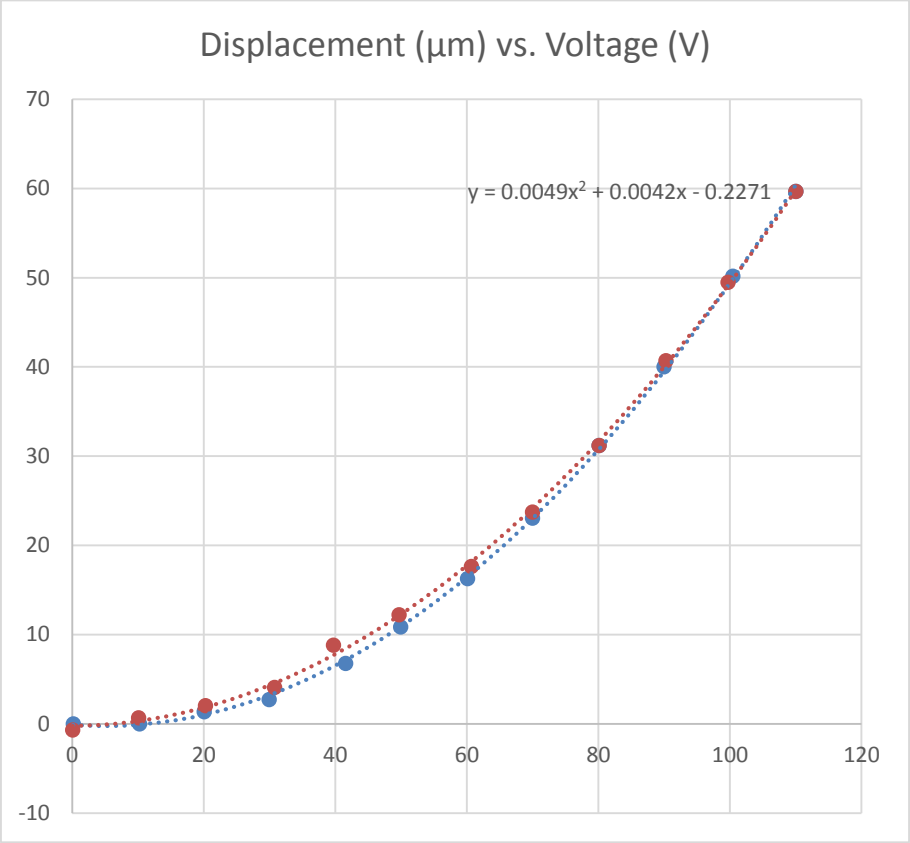

Vita

Negar Moghimi was born in Arak, Iran. Her parents are Reza Moghimi and Shahnaz Hashemi. She pursued her education in National Organization for Development of Exceptional Talents High School in Arak, Iran and graduated with highest honors. She ranked 132 in national college entrance exam with over one million and two thousand participants and was admitted to University of Tehran. She graduated with honors from University of Tehran with a Bachelor of Science in Electrical Engineering with focus on Electronics in 2010.

She joined MEMS group in ECE department at Lehigh University in 2010 and started her PhD under supervision of Professor Tatic-Lucic. She received Master of Science in Electrical Engineering from Lehigh university at 2013. During her graduate studies, she has done research projects in MEMS, microfluidic, microfabrication, and semiconductor.

During her undergraduate and graduate studies, she has been awarded scholarship and fellowships such as Faculty of Engineering Scholarship at University of Tehran, Sherman Fairchild Fellowship and Dean's Fellowship at Lehigh University. She is a student member of IEEE and IMAPS.

Publications

N. Moghimi, S. Jedlicka, and S. Tatic-Lucic, "Micro-Electro-Mechanical System for Measuring Mechanical Properties of Cell Aggregates", IMAPS 11th International Conference on Device Packaging Proceedings, Vol. 2015, No. DPC, pp. 001701-001720.

N. Moghimi, D. Richard Decker, S. Tatic-Lucic, "Modeling and Measurement of Dielectrophoretic Force and 2-D Trajectories of Microspheres in Quadrupole Electrode Configuration", IEEE Sensors 2012, DOI: 10.1109/ICSENS.2012.6411508.

N. Moghimi, J. Neumann, K. Lebouitz, N. Strandwitz, H. Luftman, S. Jedlicka, and S. Tatic-Lucic, "Characterization of ALD TiO_2 and Al_2O_3 thin films after vapor HF treatment", in submission, 2017.

N. Moghimi, R. P. Vinci, and S. Tatic-Lucic, "Large Deflection High Aspect Ratio Electrostatic MEMS Actuator for Mechanical Characterization of Cell Aggregates", in submission, 2017.